UNIVERSITY OF MANITOBA

# Development of Microneedle Array Electrodes for Transcutaneous Neural Stimulation and Recording Applications

by

Ramin Soltanzadeh

A Thesis submitted to the Faculty of Graduate Studies of

The University of Manitoba

in partial fulfillment of the requirements of the degree of

DOCTOR OF PHILOSOPHY

Biomedical Engineering

Winnipeg, MB

# Abstract

Transcutaneous electrical nerve stimulation is one of the physical neuromodulation methods that stimulate a nerve and potentially its adjacent nerve fibers. To make this method more effective, it would be of value to design new electrodes that only target a specific nerve and prevent the co-stimulation of an adjacent nerve.

In this dissertation, different scenarios of tissue and blood capillary placements were analyzed through multiphysics simulation of a 3D model and the best microneedle array electrode was suggested as a new electrode for nerve stimulation. These studies showed that the design of the microneedle array plays a critical role in presenting a uniform electric field to a target nerve and the resulting performance benefits. Analysis showed that microneedle array electrodes can increase the distinguishability between a target nerve fiber and its adjacent nerve fibers up to 10% compared to conventional surface electrodes. Uniform electric field, effective thermal behaviour and consistent current density in different depths of tissue are the other advantages of using microneedle electrodes for stimulation. Different stimulation parameters were investigated and the analysis showed that the geometry of the microneedles on top of the electrodes, such as their tip-to-tip pitch, their numbers and shape can affect performance.

Microneedle arrays were fabricated and used for experimental verification of performance benefits. One study explored polymer microneedles molded from a polycarbonate master. They were coated with titanium and titanium-nitride to increase the mechanical strength, and molybdenum (which is a biocompatible metal) to increase the conductivity of the structure. In clinical study it was found that they enhanced the tissue-electrode interface parameters, such as decreasing the resistance and increasing the double-layer capacitance. In another study, low cost

microneedle arrays were printed using 3D printing technology. In a clinical study comparing with the molded microneedles, it was found that the 3D printed ones had better high frequency performance (such as for EMG), and the molded microneedles performed better for low frequency signals (such as for EEG).

# Acknowledgments

I would like to express my sincere gratitude to Dr. Cyrus Shafai for giving me the opportunity to study and work at the University of Manitoba and NSFL (Nano System Fabrication Laboratory). I am sincerely grateful for his continuous support of my Ph.D. study and related research, for his patience, motivation, and immense knowledge. His guidance helped me in all the time of research and writing of this thesis. Truly, I learned a lot not only in the science part from him, but the professionalism as well.

I am very grateful to Dr. Brian Blakley for his advice, scientific support and time that spent to help me on provisional animal studies.

I am very thankful to Dr. Neda Anssari and Dr. Behzad Mansouri who helped me in clincal experiments and allowed that I use their facilities to evaulate my work clinically.

I would like to acknowledge Dr. Pradeepa Yahampath for his advice and also taking time for reviewing my research all through this work.

I would like to thank Dr. Sherif Sherif for his helpful advice and his time that spent on reading and reiviewing my work.

My sincere thanks also go to Dwayne Chrusch for teaching me practical skills in the cleanroom. I am very thankful to Glen Kolansky, Zoran Trajkoski, Sinisa Janjic, Mount-First Ng, Guy Jonatschick, Daryl Hamelin and Cory Smit for their technical support. I also thank Keverly Malawski for her support.

I would like to express my appreciation to Dr. Moussavi as my primary mentor and the director of Biomedical Engineering Graduate program.

Last but not least, I have to thank Dr. Magdy Younse, Mr. Earl Gardnier, Mr. Dawson Reimer, Mr. Darren Decock and my other colleagues in Cerebrahealth Company that helped me at work to save my time and finish my study.

*I dedicate this thesis to all the Biomedical Engineers who try to save lives with their knowledge and by developing medical technologies and to my family: my lovely wife, Elnaz, and my parents who did a lot for my success.*

# Contents

# List of Figures

# List of Tables

# Notations and Abbreviations

The following notations and abbreviations are used in the thesis:

| List | Description |
|---|---|
| $\sigma_J$ | Current Density Variance |
| ∇ | Divergence |
| µs | Microsecond |
| 2D | two-dimension |
| 3D | three-dimension |
| AL | Acupuncture-Like |
| Al | Aluminium |
| AP | Action Potential |
| Ar | Argon |
| Au | Gold |
| BMI | Body Mass Index |
| $Cl^-$ | Chloride Ion |
| $C_n$ | Capacitance Membrane |
| CNS | Central Nervous System |
| Cr | Chromium |
| DRIE | Deep Reactive Ion Etching |
| EIT | Electrical Impedance Tomography |
| FE | Finite Element |
| GG | Genioglossal |
| $G_n$ | Electrical Conductance of the nerve membrane (Unit: S/m) |
| HAR | High Aspect Ratio |
| HF | High Frequency |
| HGN | Hypoglossal Nerve |

| | |
|---|---|
| Hz | Hertz |
| IVF | in-vitro fertilization |
| $J$ | Current Density (Unit: A/cm$^3$) |
| kPa | Kilo Pascal |
| $l$ | Length |
| LF | Low Frequency |
| MEMS | Micro-Electro-Mechanical System |
| MMA | Methyl Methacrylate |
| MNA | Microneedle Array |
| Mo | Molybdenum |
| MPa | Mega Pascal |
| ms | Millisecond |
| $N_2$ | Nitrogen |
| NSFL | Nano System Fabrication Laboratory |
| $p$ | Pressure (Unit: Torr) |
| PDMS | Polydimethylsiloxane |
| PNS | Peripheral Nervous System |
| Poisson's Ratio ($\nu$) | The ratio of lateral strain and axial strain. $\nu$ = lateral strain / axial strain (Unitless) |
| PR | Photoresist |
| RIE | Reactive Ion Etching |
| $R_n$ | Coupling Resistance (Unit: Ω) |
| SA | Sinoatrial |
| SAR | Specific Absorption Ratio |
| SC | Stratum Corneum |
| SD | Standard Deviation |
| Si | Silicon |
| $SiO_2$ | Silicon Dioxide |

| | |
|---|---|
| SNR | Signal-Noise-Ratio |
| SNS | Somatic Nervous System |
| T | Temperature (Unit: K or $^{\circ}$C) |
| TENS | Transcutaneous Electrical Nerve Stimulation |
| Thermal Conductivity | The amount of heat per unit time per unit area that can be conducted through a plate of unit thickness of a given material. (unit = W/m·K) |
| Ti | Titanium |
| UA | Upper Airway |
| V | Potential |
| v | Voltage |
| VN | Vagus Nerve |
| Young's modulus ($E$) | The ratio of stress and strain in the linear range of the stress and strain curve of the material. $E$ = stress / strain (unit = Pa) |
| $\lambda$ | Space Constant (Unit: m) |
| $\rho$ | Density (Unit: kg/m$^3$) |
| $\sigma$ | Conductivity (Unit: S/m) |

# 1

# Introduction

## Summary

The nervous system controls all the voluntary and involuntary actions in the body. Modification in the performance of an organ can be enabled via manipulation of that organ's nervous system. Transcutaneous electrical nerve stimulation (TENS) is a non-invasive method that has been used for nervous system stimulation of different organs. Recent studies showed that TENS can positively affect chronic syndromes. However, the efficiency of the surface electrodes is not enough to target a specific nerve fiber. Therefore, effective protocols and electrodes are required if a specific nerve fiber is the target of the stimulation. In this dissertation, the performance of microneedle electrodes is investigated for both neural recording and stimulation.

## 1.1. Introduction

In the human body, the nervous system controls voluntary and involuntary procedures. Therefore, in many situations, any interference in an organ's function can result from corresponding manipulation of the nervous system. Depending on the severity of the action, this interference might be too invasive or completely non-invasive. For example, implanting a heart pacemaker is considered as an invasive procedure where an electrical stimulator is embedded inside the thorax cavity to regulate the heart pulses. In contrast, the transcutaneous electrical nerve stimulation (TENS), which can be used to treat limb pain mostly, is known as a non-invasive technique (Wark et al., 2013).

TENS has been applied to many situations. Therefore, many studies have been conducted to use TENS to treat different chronic syndromes like bladder dysfunction and sleep apnea. For example, in (Chwieśko-Minarowska et al., 2016), TENS was used during wakefulness to stimulate the hypoglossal nerve (HGN), and the effect of this on its activity during sleep was assessed. The HGN innervating the upper airway (UA) muscles and genioglossal (GG) muscle which controls the patency of the UA. Replacing the TENS technique with the conventional apnea treatment (Kezirian et al., 2010) is a significant improvement from invasive to non-invasive treatment. The other example is using TENS in controlling the muscles that contribute in controlling the bladder (Bristow et al., 1996). In a pilot study (Nakamura et al., 1986), it was shown that the transcutaneous sacral nerve electrical stimulation caused improvements in the muscles performance that control the bladder. Interestingly, the recent clinical studies showed that the TENS had exceptional clinical effects on the patients with bladder dysfunctions and increased their bladder capacity (Fall, 2018, Peters, 2017, Nitti et al., 2017).

TENS is not applicable in all clinical situations. In cases where a specific nerve is the target of stimulation, invasive procedures and implanting the stimulator electrodes on that specific nerve is unavoidable. For example, stimulating the sinoatrial (SA) node of the heart is one of the invasive nerve stimulation procedures in which the electrodes of the stimulator should be placed on the heart by a surgeon. Stimulating vagus nerve (VN) is another invasive example. The left and right VN stimulation are either approved or possible treatment for epilepsy refractory or treatment-resistant depression and the heart failure (Howland, 2014). Since the VN is a deep nerve, it is not possible to stimulate it with TENS techniques. Therefore, TENS is limited to the superficial branches of VN (Howland, 2014).

Besides TENS, current injection and stimulating the tissues can be used in electrical impedance tomography (EIT) which is an imaging modality. EIT is based on measuring the electrical impedance difference between different tissues. To find this difference, one should stimulate the tissue with current and calculate the voltage across the tissue. Therefore, the procedure is similar to what happens in the TENS. However, in TENS, it is not necessary to measure the voltage across the target tissue.

Conventional TENS techniques have different disadvantages. The most important disadvantage of existing TENS methods is their poor spatial precision. In the other words, if there are two adjacent nerves, both of them will be receive almost the same amount of current density, and so stimulating only one is not possible. For example, in the HGN stimulation, exciting the branches of the nearby VN is inventible because of its proximity to the HGN. Therefore, more precise studies are required to design a system with higher spatial resolution. Also, depending on the organ that is stimulated, the depth of current penetration is different.

In many stimulation applications, like EIT, the impedance between the electrodes and the skin is mentioned as the biggest problem in exciting the tissue and recoding the response (Hua et al., 1993). In the former studies, problems like current singularities along the electrode edges that cause non-uniform current density and consequently tissue burning was addressed (Wiley and Webster, 1982). In order to make a uniform current density underneath of stimulation electrodes, Song et al., suggested a structural change in the electrodes based on a precise mathematical model (Song et al., 2011). However, in this dissertation this topic is explored in detail, contrasting the performance of surface electrodes with arrays of microneedle electrodes. The microneedle arrays offer the opportunity of specific electric field shaping over the skin contact, and so provide the potential to make more effective electrodes, both better thermal results and uniform current density inside the tissue compared to conventional electrodes.

## 1.2. Objectives

This thesis aims to solve some of the limitations of TENS, by exploring new designs for the stimulation electrodes particularly for long-term stimulation applications. Also, the characteristics of the designed and fabricated electrode when they are used as recorders were investigated. These new designs are based on the painless microneedle arrays that can minimally pierce the skin. In many TENS practicing cases, the conventional stimulation electrodes are placed on the epidermis of the skin and the current is applied to the tissue. However, the practitioners often neglect to consider the amount of power that is applied to excitable and unexcitable tissues underneath of the electrodes. As mentioned above, in many treatment cases, the treatment protocol is based on stimulating a specific nerve. Although it is not possible to avoid stimulating adjacent nerves at the

same time, it is possible to decrease the effect of cross-stimulation of undesired tissues by using microneedle electrodes.

This thesis studies the effectiveness of microneedle electrodes for TENS, and compares to standard surface electrodes. First, the performance of microneedle electrodes is modelled and compared to conventional smooth electrodes. Second, different parameters of the microneedle electrodes are explored to see how they affect the depth of current penetration and the distinguishability of the electrical field inside the tissue. From this, it can be understood how much current density is present in different adjacent tissues to a specific organ and at different depths from the surface of the skin. Finite element modeling (FEM) is employed in this thesis to investigate different stimulation parameters, in addition to experimental work.

The results of these studies are also of interest for the EIT impedance tomography research, where the skin impedance is noticeable problem in getting high signal to noise ratio (SNR). Minimally piercing the skin can enhance the SNR of the captured signal for EIT image reconstruction. Although this study is only focusing on the TENS parameters enhancement, EIT can be counted as one of the other applications for microneedle electrodes.

## 1.3. Thesis Outline

In order to complete the objectives, thesis consists of modeling, fabrication and clinical measurements of both microfabricated and 3D printed microneedle array electrodes.

**Background:** The anatomy of the peripheral nerve and the skin are reviewed in chapter 2, so as to enable discussion of the efficiency of the types of electrodes. Also, the TENS method is explained in detail and the physiological perspective is discussed. In the last part of chapter 2, the structure of different conventional electrodes for the TENS purpose is reviewed.

**Modeling:** In chapter 3, a 3D finite element model was developed and different parameters of stimulations with microneedle array electrodes and surface electrodes were investigated on that model. Chapter 4 follows this, presenting different models of the microneedle array electrodes were investigated to find the best design of the microneedle array for stimulation with high distinguishability. Findings of chapter 4 about shape, height and number of microneedles on the surface of the electrodes were used in the clinical measurement that is described in chapter 7.

**Fabrication Background:** In chapter 5, different methods were investigated to fabricate microneedle arrays. Different important parameters and common microneedle experiments for different applications are discussed.

**Fabrication (Method 1):** The fabrication process of a short microneedle electrodes based on SU-8 etching is discussed in chapter 6. It is also shown that by etching the SU-8, it is difficult to build high density and high aspect ratio structures. The technique of coating thick layers of SU-8 on a silicon wafer is described in this chapter.

**Fabrication (Method 2) and Clinical Evaluation:** Chapter 7 discusses the fabrication and simulation model of a molded metal coated SU-8 microneedle electrodes. Clinical experiments showed that the performance of these microneedle array electrodes in TENS is better than that of conventional smooth surface electrodes. Based on the electrode-tissue-interface electrical model, the parameters of stimulation, such as faradaic and double layer capacitor was estimated. The estimated parameters showed that stimulation through microneedle arrays can decrease the harmful irreversible faradaic current while they are increasing the capacitance of the double layer capacitor between the active electrode and tissue.

**Fabrication (Method 3) and Clinical Evaluation:** Chapter 8 compares the structure and performance of the microfabricated microneedles of chapter 7, with metal coated 3D printed from

methyl methacrylate (MMA) (which is the main material of Formlab$^{TM}$ Clear Resin V4) microneedles. It was shown that the microfabricated microneedle arrays have sharp edges and can penetrate easier and deeper than the 3D printed ones. Also, it was shown that the capability of the microfabricated microneedles in stimulation and recording the low frequency signals is more than the 3D printed microneedle electrodes.

Finally, chapter 9 presents the conclusions for the work and possible future studies are discussed.

## 1.4. Contributions

The 3D finite element model of chapter 3 is a new work that explores the different parameters of nerve stimulation, contrasting microneedle array electrodes and surface electrodes. This chapter is conditionally accepted in *International of Numerical Methods in Biomedical Engineering*. Chapter 4 is a unique study that discuss important design parameters of MNA electrodes, and relates to their performance. This can be potentially be a journal paper. Chapter 5 presents a broad and detailed review of fabrication methods for microneedles. This chapter would be valuable for readers interested in exploring this topic. Chapter 7 presents experimental testing of microneedle electrodes, and this work was published in the Springer journal *Biomedical Microdevices.* Chapter 8 presents microneedles fabricated by 3D printing, and explores and contrasts their performance with the needles of Chapter 7 in clinical trials. This work was submitted to the *Journal of Future Medicine: 3D Printing in Medicine* and is currently under review.

## References

BRISTOW, S., HASAN, S. & NEAL, D. 1996. TENS: a treatment option for bladder dysfunction. International Urogynecology Journal, 7, 185-190.

CHWIEŚKO-MINAROWSKA, S., MINAROWSKI, Ł., SZEWCZAK, W. A., CHYCZEWSKA, E. & KURYLISZYN-MOSKAL, A. 2016. Efficacy of daytime transcutaneous electrical stimulation of the genioglossus muscle in patients with obstructive sleep apnea syndrome. European Archives of Oto-Rhino-Laryngology, 273, 3891-3895.

FALL, M. 2018. Use of Transcutaneous Electrical Nerve Stimulation in the Management of Bladder Pain Syndrome. Bladder Pain Syndrome–An Evolution. Springer.

HOWLAND, R. H. 2014. Vagus nerve stimulation. Current behavioral neuroscience reports, 1, 64-73.

HUA, P., WOO, E. J., WEBSTER, J. G. & TOMPKINS, W. J. 1993. Finite element modeling of electrode-skin contact impedance in electrical impedance tomography. IEEE Transactions on Biomedical Engineering, 40, 335-343.

KEZIRIAN, E. J., BOUDEWYNS, A., EISELE, D. W., SCHWARTZ, A. R., SMITH, P. L., VAN DE HEYNING, P. H. & DE BACKER, W. A. 2010. Electrical stimulation of the hypoglossal nerve in the treatment of obstructive sleep apnea. Sleep medicine reviews, 14, 299-305.

MOORE, K. L., AGUR, A. M. & DALLEY, A. F. 2002. Essential clinical anatomy, Lippincott Williams & Wilkins Philadelphia.

NAKAMURA, M., SAKURAI, T., TSUJIMOTO, Y. & TADA, Y. 1986. Bladder inhibition by electrical stimulation of the perianal skin. Urologia internationalis, 41, 62-63.

NITTI, V. W., DMOCHOWSKI, R., HERSCHORN, S., SAND, P., THOMPSON, C., NARDO, C., YAN, X., HAAG-MOLKENTELLER, C., ANDREOU, C. & EGERDIE, R. 2017. OnabotulinumtoxinA for the treatment of patients with overactive bladder and urinary incontinence: results of a phase 3, randomized, placebo controlled trial. The Journal of urology, 197, S216-S223.

PETERS, K. 2017. Use of Transcutaneous Electrical Nerve Stimulation. Bladder Pain Syndrome–An Evolution, 131.

SONG, Y., LEE, E., WOO, E. J. & SEO, J. K. 2011. Optimal geometry toward uniform current density electrodes. Inverse Problems, 27, 075004.

WARK, H., SHARMA, R., MATHEWS, K., FERNANDEZ, E., YOO, J., CHRISTENSEN, B., TRESCO, P., RIETH, L., SOLZBACHER, F. & NORMANN, R. 2013. A new high-density (25 electrodes/mm2) penetrating microelectrode array for recording and

stimulating sub-millimeter neuroanatomical structures. Journal of neural engineering, 10, 045003.

WILEY, J. D. & WEBSTER, J. G. 1982. Analysis and control of the current distribution under circular dispersive electrodes. IEEE Transactions on Biomedical Engineering, 381-385.

# 2

# A Review on Peripheral Nervous System and Skin Anatomy and Different Transcutaneous Nerve Stimulation Protocols


## Summary

The human nervous system consists of central and peripheral nervous systems. In order to stimulate a peripheral nerve fiber effectively, one should know the anatomy and mechanism of peripheral nervous system properly. In addition, having knowledge about the skin anatomy and its mechanical properties is critical in order to optimize the nerve stimulation procedures. In this chapter, a short review on the anatomy of the peripheral nervous system and the skin layer is presented. Also, the physiology of transcutaneous electrical nerve stimulation and its different protocols are reviewed.

## 2.1. Introduction to Peripheral Nerve Anatomy

The human nervous system consists of two major structural parts: 1) Central Nervous System (CNS) and 2) Somatic Nervous System (SNS). The CNS includes the brain, brain stem, spinal cord and the SNS consists of a variety of the voluntary/involuntary and sensational branches of cranial nerve, spinal nerves and their roots and branches. The neuromuscular junctions are classified in the SNS group. The Peripheral Nervous System (PNS) and the somatic part of the CNS are forming the SNS (Moore et al., 2002). Fig. 2.1 shows the role of the SNS and PNS in human body briefly.

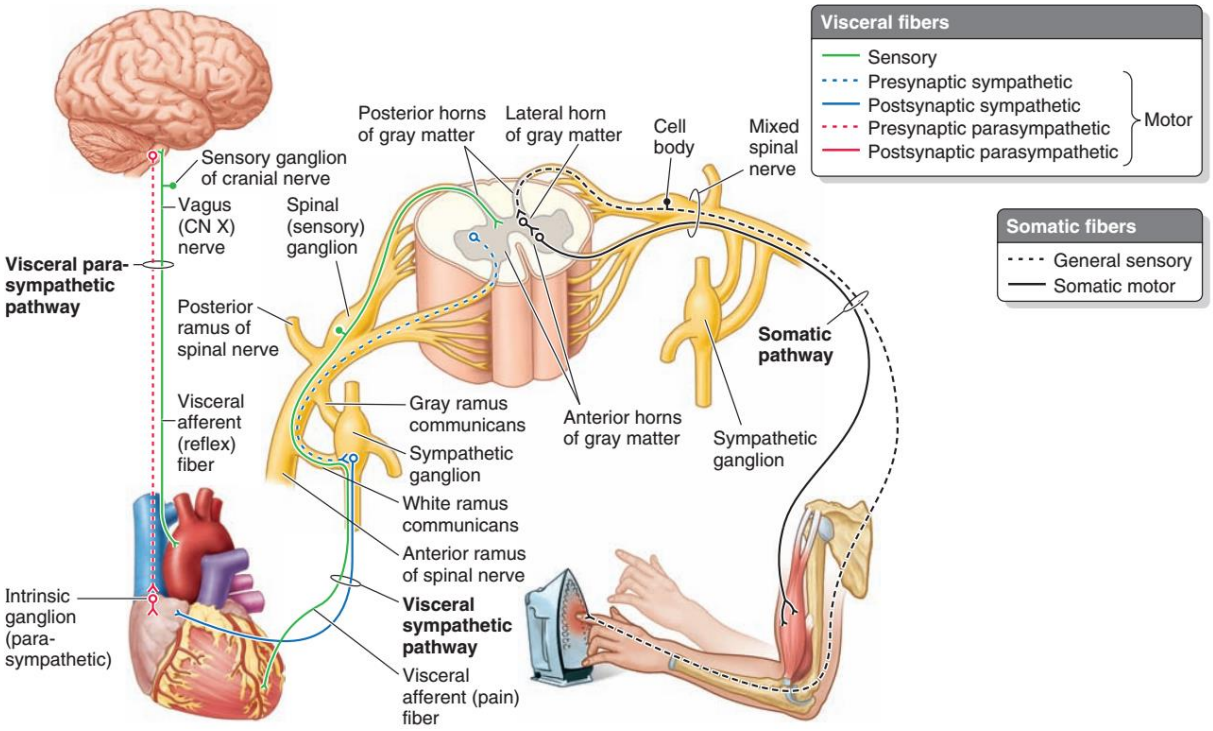


**Fig. 2.1.** A brief sketch of SNS and PNS and their roles in body (Moore et al., 2002) [Used with permission]

Fig. 2.1 shows that the nerve fibers are initiating from the spinal cord. It is divided into anterior (ventral) root that consists of the motor (efferent) fibers, and the posterior (dorsal) fibers that deliver the sensory information through the sensory fibers (afferent) to the sensory receptors of the CNS (Moore et al., 2002).

The PNS includes the nerve fibers and nerve cell bodies that convey information to the CNS and back to the PNS (Moore et al., 2002). Peripheral nerves are traveling through the peripheral structures like a bundle. These nerve fibers are isolated from the blood vessels by the connective tissues. As shown in Fig. 2.2, there are two different types of the nerve fibers in the PNS (Moore et al., 2002) :

1) Myelinated nerve fibers in which a series of the Schwann cells (a part of neuroglia cells) surround a nerve axon and build myelin for that axon.
2) Unmyelinated nerve fibers enwrapped in the cytoplasm of a single Schwann cell that do not produce any myelin around the axon. The cutaneous nerve fibers are mostly from this type (Moore et al., 2002).

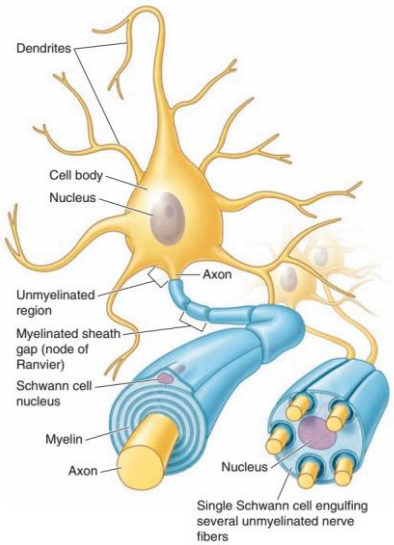


**Fig. 2.2.** Myelinated and unmyelinated nerve fibers (Moore et al., 2002) [Used with permission]

In Fig. 2.2, it can be seen that in the myelinated axons, there are some points that are not covered by myelin. These regions are called Ranvier nodes that play important role in the action potential conduction along a nerve axon fiber (D'Este et al., 2017, Rasband et al., 1999, Rasband et al., 1998). The Ranvier nodes are placed approximately every 1 μm along the axon (Hubbard, 2012).

In the PNS nerve fibers, the main functional part of the nerve fibers are their axons (Hubbard, 2012, Moore et al., 2002). Since the peripheral nerves are supported and protected by different layers of connective tissues, they are very strong and elastic (Moore et al., 2002). The length of the axons in the nerve fibers depends on their role in the body. For example, the nerve fibers in the limbs have long axons compare to the other organs. Also, the peripheral axons can be stretched to considerable length (Swenson, 2006). Therefore, an axon would be the majority part of a nerve that is involved in the peripheral limb stimulation. In the other words, the impulse response of the peripheral nerve axons affects the results of the any type of stimulation. The physiology of the axon and its impulse response are described below.

## 2.2. Introduction to Skin Anatomy

Electrical current should pass through the skin in order to access peripheral nerves. Therefore, it is worthwhile to know more about different layers of skin. The skin is the largest organ of the human body that covers and protects all the limbs and external organs of the body. Also, the skin plays the role as a containment for the important liquids in the body like the blood and water, it regulates the temperature of the body through sweating, and contains blood vessels and fat. Many open-end nerves exist in the skin that contribute to sense sensation (Moore et al.,

2002). Fig. 2.3 shows that the skin has three major layers: epidermis, dermis and subcutaneous tissue. The stratum corneum (SC) is the first layer of the epidermis. The SC has the highest electrical impedance. It is formed by tough layers of keratin (Moore et al., 2002).

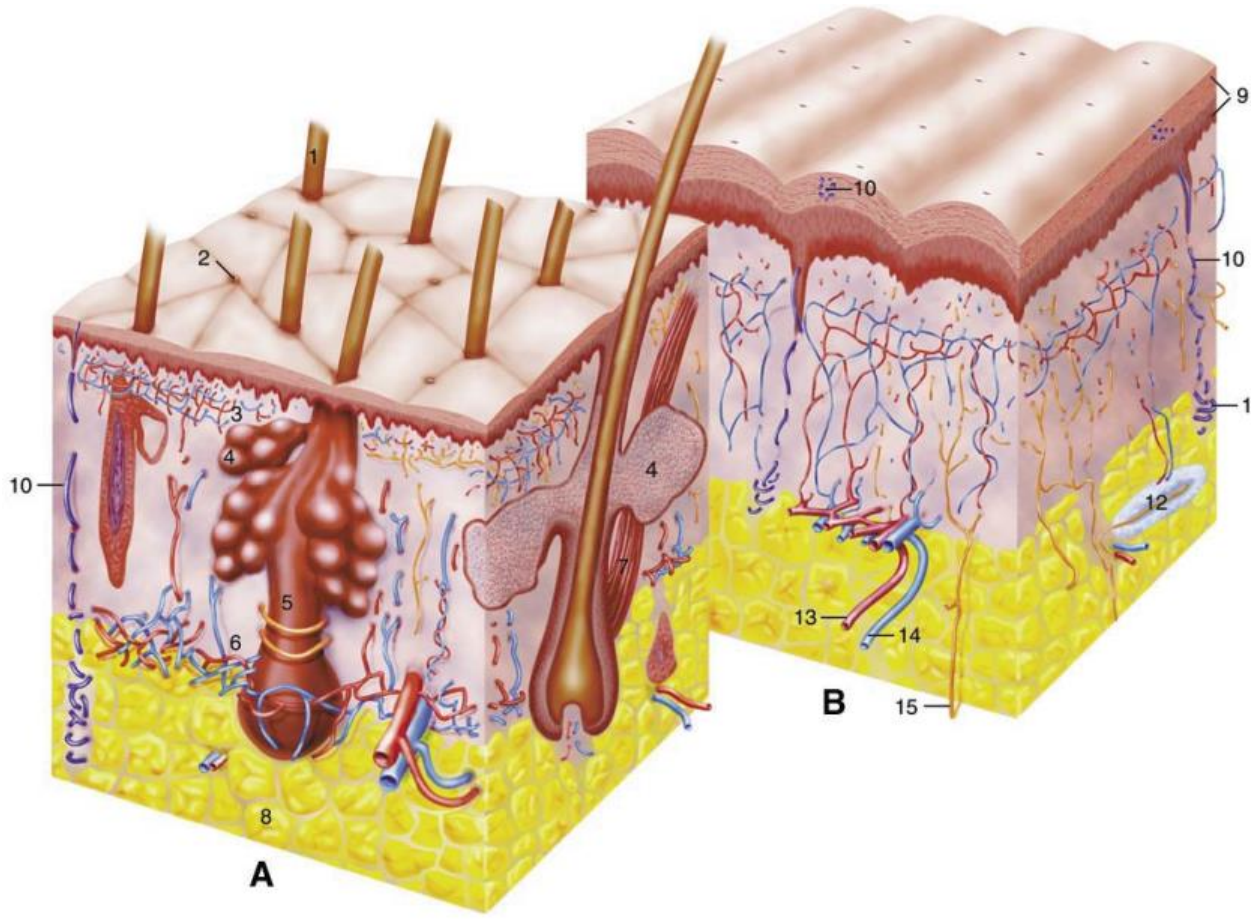


1. Hair shaft
2. Opening of sweat duct
3. Subpapillar neurovascular plexus
4. Sebaceous gland
5. Hair follicle
6. Deep cutaneous neurovascular plexus
7. Piloarrector muscle
8. Adipose tissue of subcutis
9. Epidermis
10. Sweat duct
11. Sweat gland
12. Pacinian corpuscle
13. Artery
14. Vein
15. Nerve

**Fig. 2.3.** Different layers of (A) a hairy thin skin and (B) hairless thick skin (Kálmán and Csillag, 2005) [Used with permission]

Former anatomical studies showed that the thickness of the SC in different people and in different organs is different (Ya-Xian et al., 1999). For example, the number of SC layers (mean ± standard deviation(SD)) in the neck is 10 ± 2 and in the hand palms it is 47 ± 24 (Ya-Xian et al., 1999). Consequently, the electrical resistance of the skin in different area of the body is different (Ahn et al., 2008).

There are no blood vessel in the epidermis and this layer of skin is fed by the capillaries from the vessels in the underlying layer which is dermis (Moore et al., 2002). Also, most of the open-end nerve fibers are located in the dermis. However, some of these nerve fibers penetrate through the epidermis and reach closer to the outer layer of the skin (Moore et al., 2002). The nerves in the dermis are somatosensory nerves and play role in gathering information via touching or sensing the temperature and etc. (Moore et al., 2002). The dermis mainly consists of *elastic fibers* that strengthen the skin. Between the dermis and the subcutaneous tissue, there are connective tissue and a layer of fat (Moore et al., 2002). However, the majority of the adipose tissue (or fat tissue) is accumulated in the subcutaneous tissue. Therefore, the thickness of the subcutaneous tissue is varying based on the individuals' nutrition plans (Moore et al., 2002). The subcutaneous tissue contains the vessels and the cutaneous nerve fibers. This layer of the skin is separated from the muscle underneath by deep fascia (Hansen, 2018, Moore et al., 2002).

As mentioned above, the thickness of the skin differs from one person to another. However, to model the skin in 3-dimensions (3D), the average thickness of each layer was estimated in this thesis. In (Sandby-Moller et al., 2003), it was reported that the thickness of SC in the forearm, and shoulder are 18.3 ± 4.9 µm and 11.0 ± 2.2 µm respectively among 71 studied participants. Also, in the same study, it was mentioned that the epidermis thickness is 56.6 ± 11.5 µm and 70.3 ± 13.6 µm in the forearm and shoulder respectively. In a skin model that was developed by another study

(Chizmadzhev et al., 1998), it was assumed that the thickness of the SC has 15-20 µm thickness. Also, in the same article, it was assumed that the thickness of the epidermis is from 50 µm to 70 µm. The thickness of the different layers of the skin affects the skin resistance which will be discussed in detail in the following chapters. Noteworthy, in all the body organs, the SC has the highest impedance compared to the other skin layers (Chizmadzhev et al., 1998, Keller and Kuhn, 2008). Therefore, bypassing the SC will facilitate the closing of the electrical circuit through the nerve fiber for any treatment (e.g. TENS) or diagnostic (e.g. EIT) purposes.

## 2.3. Mechanical properties of the Skin

The performance of microneedle electrodes depends on the depth of their penetration. Theoretically, it is assumed that the microneedles pierce the SC and reach the next layer of the epidermis. However, in practice, skin is an elastic tissue and the penetration depth of the microneedle electrodes depends on the force that is applied on them. Therefore, one should be familiar with the mechanical properties of the skin tissue to estimate how deep the electrodes can pierce the skin. Former studies showed that the Young's modulus of the SC and the layers underneath are 26 MPa and 136 kPa respectively (Yuan and Verma, 2006). Also, the Poisson ratio of the SC and the layers underneath was estimated as 0.49 (Magnenat-Thalmann et al., 2002). Kong et al., simulated the microneedles' insertion into skin and used 34 kPa for hypodermis in their simulation (Kong et al., 2011). Also, in the same study, it was shown that the small tip diameter of the solid microneedles and the area of their base affects the insertion force of the microneedles.

## 2.4. Background on the Transcutaneous Electrical Nerve Stimulation

Based on the American Physical Therapy Association, TENS is the skin surface application of the electrical stimulation to control the pain particularly in the limbs (Sluka and Walsh, 2003). The history of stimulating the nerve from the skin surface to manage the pain goes back to ancient Egypt and Roman (Gildenberg, 2006). For example, people in those days used electric fish as the source of electric current, and they put them on the skin, where their discharges caused electric current in the tissue and reduction of pain. The goal of TENS is inhibiting the pain neurotransmitter secretion by changing the electrical charge around the nerve. The electrical current changes the balance of the electrical field around the axon of a peripheral nerve and this inhibits pain (Johnson and Bjordal, 2011). However, the clinical effectiveness of TENS is controversial (Johnson, 2014). In the former investigations, it is shown that the effectiveness of TENS depends on many parameters such as the settings of the stimulation (i.e. the delay between the stimulation and rest portions, the intensity and the frequency of the stimulation signal and the times that the stimulation is repeated) (DeSantana et al., 2008, Chandran and Sluka, 2003). These parameters are the ones that affect the neuromodulation procedure. In (Chandran and Sluka, 2003), it was shown that by an organized daily TENS schedule, the results of the treatment was shown up in the $4^{th}$ day. In another study, a clinical trial was run on a large number of the patients (around 1000 individuals) with neuropathic pain and it was realized that the TENS in long-term usage is useful either as a preliminary or secondary treatment (Somers and Clemente, 2006). Effectiveness of TENS depends on the applied protocol and this is discussed below.

## 2.5. Physiological Perspective of the TENS

Tissues are categorized into excitable and non-excitable cells. Based on definition, any cell that can generate an *action potential (AP)* is called an excitable cell; otherwise it is a non-excitable cell (Hall, 2015). Only a few tissues in the body, like the nerve fibers, are excitable tissue (Hall, 2015). By applying electrical current to a nerve, the electrical field will cause a reaction from the axon hillock which is located at the beginning of the axon and is indicated in Fig. 2.2 by "*Axon"*. Conventionally, the stimulation signal in TENS is separated into low frequency (LF) and high frequency (HF) components, which are less than 10 Hz and more than 50 Hz respectively (DeSantana et al., 2008, Vance et al., 2014). TENS affects the mechanism of both central and peripheral nervous systems (DeSantana et al., 2008). In general, HF TENS affects the peripheral sensory nervous system and LF TENS has impact on the motor neurons (DeSantana et al., 2008). However, animal studies show that both HF and LF reduce the dorsal horn neuron cell activities, which is a part of the central nervous system (Lee et al., 1985, Garrison and Foreman, 1997). Furthermore, it was shown that the HF decreases the sensitization of pain in the central nervous system by releasing glutamate as an excitatory neurotransmitter (Ma and Sluka, 2001). On the other hand, it is shown that LF TENS can block some of the peripheral opioid receptors that prevent pain sensation (called analgesia). These peripheral opioid receptors cannot be reached by HF TENS and only LF TENS can block them (Santos et al., 2013, Sabino et al., 2008, Vance et al., 2014). Therefore, one may conclude that both HF and LF TENS play a role in decreasing the input of the afferent nerve fibers and reduce their excitability (Vance et al., 2014).

The intensity of the stimulation signal is another important parameter in TENS. Regardless of the frequency, high intensity stimulation may excite the motor neurons and this is not painful (DeSantana et al., 2008). However, the threshold of motor neuron excitability varies from one

person to another, and it depends on different parameters such as skin moisture, nerve fiber performance, body mass index (BMI) of the patients, and others. These parameters determine the type of protocol that is applied in order to use TENS for different treatment goals.

The stimulation signal used for TENS is a rectangular constant current (or voltage) pulse signal. In terms of phase, the stimulation signal may be mono or biphasic. A biphasic stimulation signal might be either symmetric or asymmetric rectangle signal. In the biphasic stimulations, the cell's membrane is exposed to the positive current (or voltage depending on the type of stimulation) and partially negative current after stimulation. This biphasic exposure will reduce the recovery time of the cell after it generates an action potential. Therefore, by using biphasic stimulation signals, it is possible to increase the magnitude and the frequency of stimulation (Scheiner et al., 1990). In order to reduce the hazard of pH increase, it is recommended that imbalanced stimulation signals have higher cathodic portion than the anodic portions (Scheiner et al., 1990). It is worthwhile to mention that an imbalanced rectangular single is a signal who's duty cycle is not 50%. Fig. 2.4 shows different biphasic stimulation waveforms.

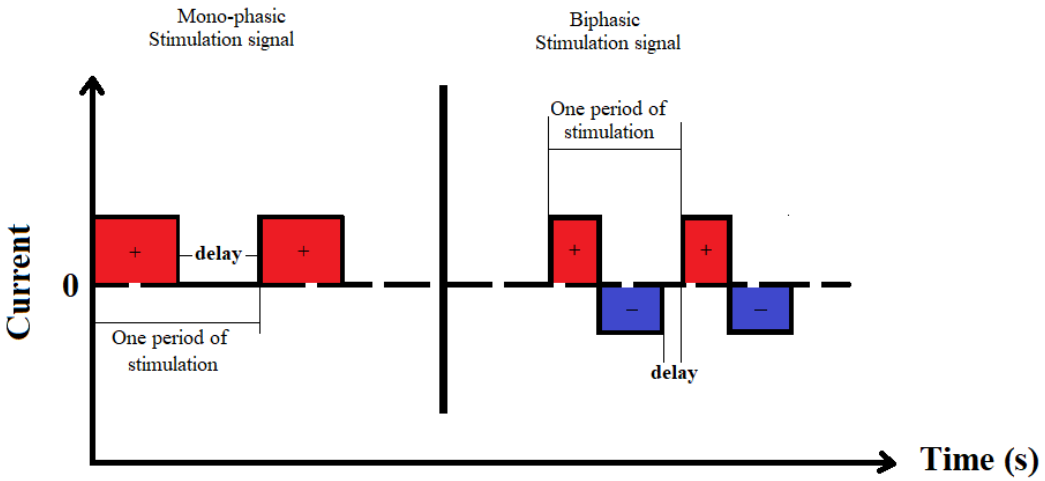


**Fig. 2.4.** Monophasic and Biphasic stimulation signals

Depending on the type stimulation signal, between 30 mA to 100 mA of current may pass through a tissue that causes a tingling feeling inside the stimulated tissue. The duration and frequency of the stimulation pulse changes the amount of delivered charge to the tissue. The combination of the stimulation signal duration and frequency will result in three different TENS stimulation protocols: conventional, acupuncture-like (AL), and burst mode. Frequencies of conventional and AL stimulation protocols are respectively similar to the HF and LF stimulation signals. Burst mode stimulation is a modulation of the HF on LF stimulation signals. The pulse duration of the stimulation signal in conventional, AL, and burst protocols is different. In conventional TENS, the duration of the stimulation signal is between 50-80 µs. In the AL protocol, the duration of the stimulation signal is around 200 µs, but the intensity of the AL is larger than in the conventional and burst stimulation protocols (Garrison and Foreman, 1997). Fig. 2.5 shows the stimulation signal for the different described TENS protocols.

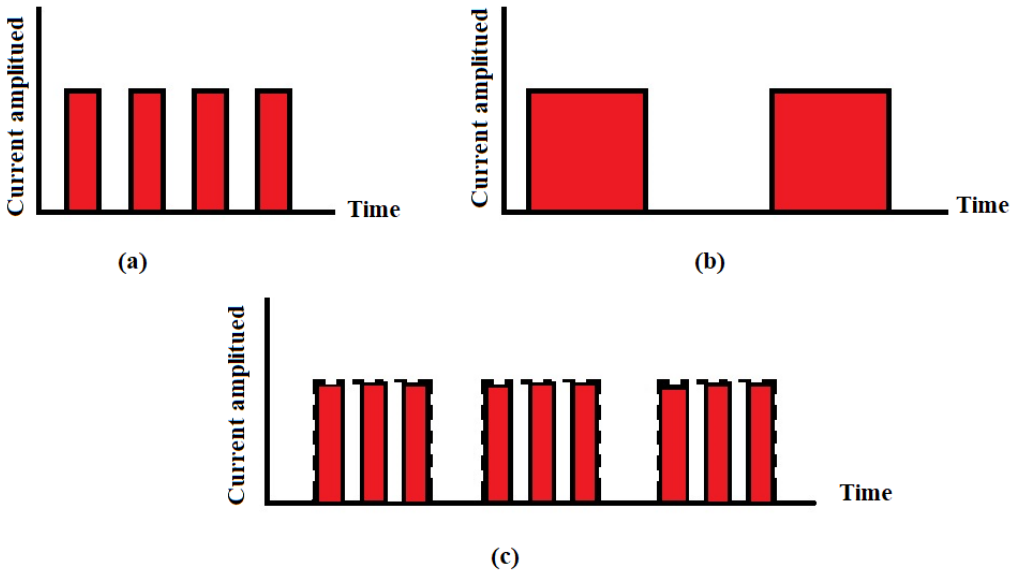


**Fig. 2.5.** Different TENS protocols: (a) Conventional (b) AL (c) Burst mode (Garrison and Foreman, 1997)

In summary, it can be understood that by bypassing the skin, low stimulation signals are able to pass to the inner tissues and reach nerves. This can be particularly beneficial for the AL stimulation method, as it will be benefit from electrodes that minimally or completely penetrate the skin. Skin penetration is also needed in order to stimulate the deep tissues like nerves. Both low and high frequency stimulation will involve the inhibitory mechanism of the nervous system, and decrease acute or chronic pains. This mechanism can be further applied to include syndromes such as overactive bladder and sleep apnea.

## References

AHN, A. C., COLBERT, A. P., ANDERSON, B. J., MARTINSEN, Ø. G., HAMMERSCHLAG, R., CINA, S., WAYNE, P. M. & LANGEVIN, H. M. 2008. Electrical properties of acupuncture points and meridians: a systematic review. Bioelectromagnetics, 29, 245-256.

CHANDRAN, P. & SLUKA, K. A. 2003. Development of opioid tolerance with repeated transcutaneous electrical nerve stimulation administration. Pain, 102, 195-201.

CHIZMADZHEV, Y. A., INDENBOM, A. V., KUZMIN, P. I., GALICHENKO, S. V., WEAVER, J. C. & POTTS, R. O. 1998. Electrical properties of skin at moderate voltages: contribution of appendageal macropores. Biophysical Journal, 74, 843-856.

D'ESTE, E., KAMIN, D., BALZAROTTI, F. & HELL, S. W. 2017. Ultrastructural anatomy of nodes of Ranvier in the peripheral nervous system as revealed by STED microscopy. Proceedings of the National Academy of Sciences, 114, E191-E199.

DESANTANA, J. M., WALSH, D. M., VANCE, C., RAKEL, B. A. & SLUKA, K. A. 2008. Effectiveness of transcutaneous electrical nerve stimulation for treatment of hyperalgesia and pain. Current rheumatology reports, 10, 492.

GARRISON, D. & FOREMAN, R. 1997. Effects of prolonged transcutaneous electrical nerve stimulation (TENS) and variation of stimulation variables on dorsal horn cell activity in cats. European journal of physical medicine & rehabilitation, 7, 87-94.

GILDENBERG, P. L. 2006. History of electrical neuromodulation for chronic pain. Blackwell Publishing Inc Malden, USA.

HALL, J. E. 2015. Guyton and Hall textbook of medical physiology e-Book, Elsevier Health Sciences.

HANSEN, J. T. 2018. Netter's Clinical Anatomy E-Book, Elsevier Health Sciences.

HUBBARD, J. 2012. The peripheral nervous system, Springer Science & Business Media.

JOHNSON, M. 2014. Transcutaneous electrical nerve stimulation: review of effectiveness. Nursing Standard (2014+), 28, 44.

JOHNSON, M. I. & BJORDAL, J. M. 2011. Transcutaneous electrical nerve stimulation for the management of painful conditions: focus on neuropathic pain. Expert review of neurotherapeutics, 11, 735-753.

KÁLMÁN, M. & CSILLAG, A. 2005. The skin and other diffuse sensory systems. Atlas of the sensory organs. Springer.

KELLER, T. & KUHN, A. 2008. Electrodes for transcutaneous (surface) electrical stimulation. Journal of Automatic Control, 18, 35-45.

KONG, X., ZHOU, P. & WU, C. 2011. Numerical simulation of microneedles' insertion into skin. Computer methods in biomechanics and biomedical engineering, 14, 827-835.

LEE, K. H., CHUNG, J. M. & WILLIS JR, W. D. 1985. Inhibition of primate spinothalamic tract cells by TENS. Journal of neurosurgery, 62, 276-287.

MA, Y.-T. & SLUKA, K. 2001. Reduction in inflammation-induced sensitization of dorsal horn neurons by transcutaneous electrical nerve stimulation in anesthetized rats. Experimental brain research, 137, 94-102.

MAGNENAT-THALMANN, N., KALRA, P., LEVEQUE, J. L., BAZIN, R., BATISSE, D. & QUERLEUX, B. 2002. A computational skin model: fold and wrinkle formation. IEEE Transactions on Information Technology in Biomedicine, 6, 317-323.

MOORE, K. L., AGUR, A. M. & DALLEY, A. F. 2002. Essential clinical anatomy, Lippincott Williams & Wilkins Philadelphia.

RASBAND, M. N., TRIMMER, J. S., PELES, E., LEVINSON, S. R. & SHRAGER, P. 1999. K+ channel distribution and clustering in developing and hypomyelinated axons of the optic nerve. Journal of neurocytology, 28, 319-331.

RASBAND, M. N., TRIMMER, J. S., SCHWARZ, T. L., LEVINSON, S. R., ELLISMAN, M. H., SCHACHNER, M. & SHRAGER, P. 1998. Potassium channel distribution, clustering, and function in remyelinating rat axons. Journal of Neuroscience, 18, 36-47.

SABINO, G. S., SANTOS, C. M., FRANCISCHI, J. N. & DE RESENDE, M. A. 2008. Release of endogenous opioids following transcutaneous electric nerve stimulation in an experimental model of acute inflammatory pain. The Journal of Pain, 9, 157-163.

SANDBY-MOLLER, J., POULSEN, T. & WULF, H. C. 2003. Epidermal thickness at different body sites: relationship to age, gender, pigmentation, blood content, skin type and smoking habits. Acta Dermato Venereologica, 83, 410-413.

SANTOS, C. M., FRANCISCHI, J. N., LIMA-PAIVA, P., SLUKA, K. A. & RESENDE, M. A. 2013. Effect of transcutaneous electrical stimulation on nociception and edema induced by peripheral serotonin. International Journal of Neuroscience, 123, 507-515.

SCHEINER, A., MORTIMER, J. T. & ROESSMANN, U. 1990. Imbalanced biphasic electrical stimulation: muscle tissue damage. Annals of biomedical engineering, 18, 407-425.

SLUKA, K. A. & WALSH, D. 2003. Transcutaneous electrical nerve stimulation: basic science mechanisms and clinical effectiveness. The Journal of pain, 4, 109-121.

SOMERS, D. L. & CLEMENTE, F. R. 2006. Transcutaneous electrical nerve stimulation for the management of neuropathic pain: the effects of frequency and electrode position on prevention of allodynia in a rat model of complex regional pain syndrome type II. Physical therapy, 86, 698-709.

SWENSON, R. S. 2006. Review of clinical and functional neuroscience. Dartmouth Medical School. Retrieved November, 18, 2012.

VANCE, C. G., DAILEY, D. L., RAKEL, B. A. & SLUKA, K. A. 2014. Using TENS for pain control: the state of the evidence. Pain management, 4, 197-209.

YA-XIAN, Z., SUETAKE, T. & TAGAMI, H. 1999. Number of cell layers of the stratum corneum in normal skin–relationship to the anatomical location on the body, age, sex and physical parameters. Archives of dermatological research, 291, 555-559.

YUAN, Y. & VERMA, R. 2006. Measuring microelastic properties of stratum corneum. Colloids and Surfaces B: Biointerfaces, 48, 6-12.

# 3

# Investigation of Transcutaneous Electrical Nerve Stimulation Improvements with Microneedle Array Electrodes based on Multiphysics Simulation

## Summary

This chapter investigates microneedle array electrodes for transcutaneous electrical nerve stimulation, and compares their performance with conventional surface electrodes. A 3D model of tissue was developed for finite element multiphysics simulations. Investigations included current density in different depths of a tissue, space constant under electrodes, specific absorption ratio of tissue, distinguishability of stimulation, temperature rise and blood flow. Results showed that microneedle electrodes have up to 10% higher distinguishability than the surface electrodes. Furthermore, it was found that stimulation using microneedle electrodes provides more robust and uniform current density at different tissue depths compared to the surface electrode stimulation. Microneedle electrodes showed enhanced stimulation parameters, particularly for targeting a specific nerve in a specific depth of a tissue.

## 3.1. Introduction

In the human body, the nervous system is controlling all the voluntary and involuntary procedures. Therefore, in many situations, any interference in an organ's performance needs manipulation of the nervous system. Depending on the severity of the action, this interference might be too invasive or completely non-invasive. For example, implanting a heart pacemaker, that is embedding a stimulator electrode in contact with the heart to regulate the heart pulses, is considered as an invasive procedure. Hearing cortex stimulator and some particular deep brain stimulator (e.g. for controlling the Parkinson Diseases) can be mentioned as the invasive stimulators too. In contrast, transcutaneous electrical nerve stimulation which is used to treat limb pain and also some rehabilitation protocols is known as a non-invasive technique. By improving the technology, the ideal treatment procedures are proceeding toward techniques that are harmless and have no side effects on patients. Therefore, many studies have been conducted using methods such as TENS to treat different chronic syndromes like bladder dysfunction and sleep apnea, which involve neuromodulative theory in treatment. For example, in (Chwieśko-Minarowska et al., 2016), TENS was used during wakefulness and the assessments showed better performance of the hypoglossal nerve (HGN) during sleep. It is worthwhile to mention that the HGN innervates the upper airway (UA) muscles, including genioglossal (GG) muscle, which controls the patency of the UA. The other example is using TENS in controlling the muscles that contribute to controlling the bladder (Bristow et al., 1996, McGee et al., 2015). Interestingly, the recent clinical studies showed that TENS had exceptional clinical effects on patients with bladder dysfunctions and increased their bladder capacity (Fall, 2018, Nitti et al., 2017, Peters, 2018).

Based on the American Physical Therapy Association, TENS is the skin surface application of the electrical stimulation to control pain particularly in the limbs (Sluka and Walsh, 2003). The

conventional TENS techniques stimulates the peripheral nerve (PN) usually with low-intensity and high-frequency (>50 Hz) electrical current. There are other types of the TENS, such as acupuncture-like TENS (AL-TENS) which stimulates the PN using high-intensity and low-frequency (<10 Hz) (Johnson and Bjordal, 2011). Regardless of the TENS protocol, the outcome of the stimulation depends on electrode position and type, and the intensity of the stimulation. On the one hand, particularly in the implantable electrodes, the mechanical strength and electrical impedance of the implanted electrodes are very important parameters (Recio and Schneider, 2011). On the other hand, in the conventional TENS application, the placement of the electrodes is critical in order to create the desired current density in a targeted tissue. Although the electrical impedance of the skin is not uniform in the body, it was shown that increasing the stimulation intensity and frequency can compensate for the high impedance of the skin (Vance et al., 2015, Howell et al., 2015). However, analysis in a former study showed that using surface electrodes for TENS may lead to skin burns in long term applications because of differences in the impedance of the first layer of skin in different parts of body, and in different persons (Soltanzadeh et al., 2018, Patriciu et al., 2001, Keller and Kuhn, 2008). Therefore, the development of new types of TENS electrodes that can bypass the skin's impedance and target a specific tissue with high selectivity would be worthwhile.

In this chapter, the relationship between different parameters of an MNA (such as the number of needle spikes) was investigated to explore the effect on the current density at different depths in tissue, the temperature of the tissue during stimulation, and the effect of stimulation on blood flow. Since blood and nerve fibers have high conductivity compared to other tissues inside the body, the presence of blood capillaries or other nerve fibers will significantly affect the electric field and current density at different depths of the tissue. Therefore, the mentioned parameters

were simulated in different scenarios. Fig.3.1 shows the different scenarios that were considered in this study.

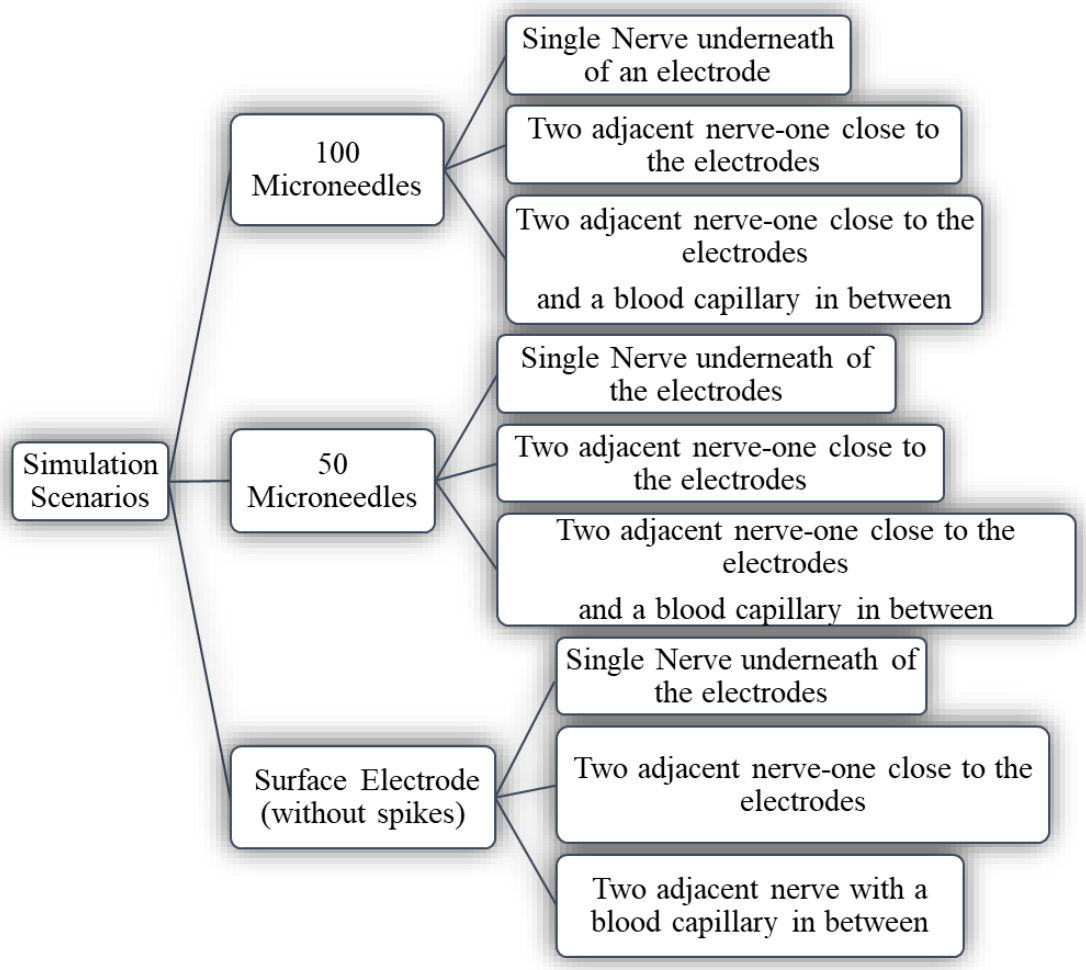


**Fig. 3.1.** Different simulation scenarios

Investigating the relationship between the structural parameters of MNAs and the selectivity of a specific target nerve compared to adjacent nerves (thereby reducing co-stimulation) was one of the goals of this study, and is called "*distinguishability"*(Graham and Adler, 2006, Gaggero, 2011). In order to analyze the impact of these parameters on the nerve fibers and adjacent tissues, a passive 3-dimension (3D) model was developed and studied in the finite element (FE) software

COMSOL Multiphysics 5.3a. By using the simulation results, the space constant of the stimulation caused by both surface and MNA electrodes was estimated. Also, it was demonstrated that the presence of other tissues with higher conductivity than the subcutaneous tissue (such as blood and the other nerves) affects current density and electrical field inside the tissue.

## 3.2. Methods and Materials

The model of Fig. 3.2 further expands on the work of (Soltanzadeh et al., 2018). It shows the developed 3D multilayer model of the skin, which consists of two nerves (target and adjacent) and a blood-filled capillary that is located between the nerves. This multilayer tissue model is based on the study by (Moore et al., 2013). The properties of the different model layers are shown in Table 3.1.

The electrical properties of each layer were mostly adopted from former study (Elder and Yoo, 2018) and COMSOL AC/DC library and thermal and fluid properties were adopted from COMSOL material library and (Panescu et al., 1995, Comsol, 2011). Different physics properties of each model layer are shown in Table 3.1. It is worthwhile to mention that the blood electrical properties are varying in different frequency bands (Abdalla et al., 2010). Since the fluid physics was only studied for the blood, dynamic viscosity was only required for the whole blood (including cells and plasma) in this model and it was considered $3.5\times10^{-3}$ (Pa·s) (Gore et al., 2018).

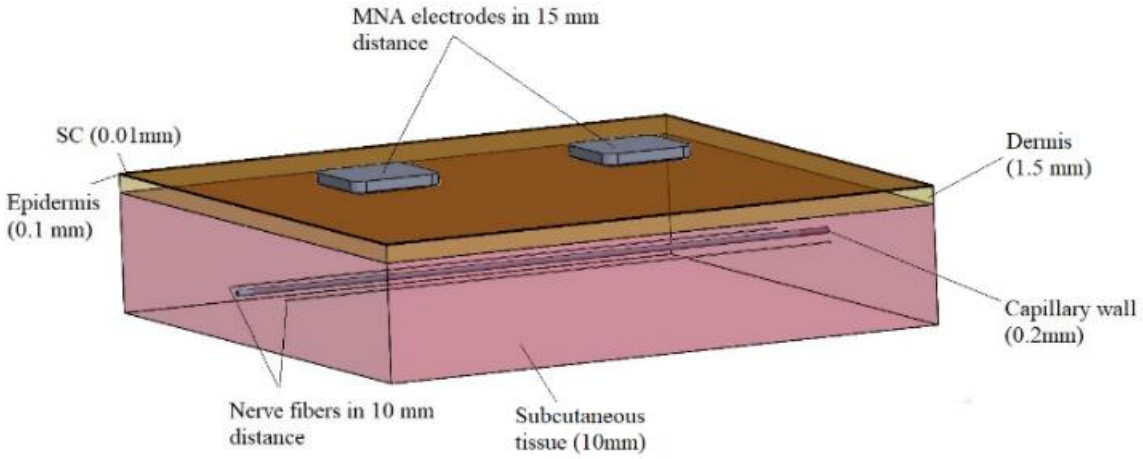


(a)

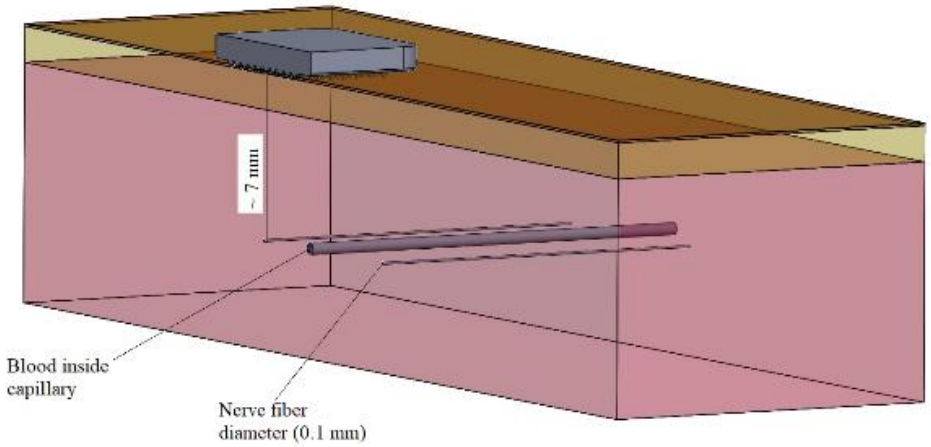


(b)

**Fig. 3.2.** (a) Developed 3D multilayer model of the skin, and (b) its cross-section (the values in parenthesis are thickness of each layer)

In the first simulation scenario, it was assumed that only one-third of an MNA with pyramid microneedle spikes on its surface (the length of each spike was ~450 μm) pierced the skin. The skin thickness is not uniform in all limbs (Olatunji, 2011). Therefore, because of different mechanical resistance, the depth of penetration is different in different parts of the body. In order

to make the simulation scenarios more realistic, it was assumed that the MNA is not piercing completely through, and only two-third of the length of the array is penetrating inside the skin. However, because the MNAs' tips will not pass the dermis layer, the assumption of whole length of the MNA piercing will not change the results considerably. The partially penetrating assumption was applied on the MNA electrodes with different number of the microneedle spikes (50 and 100), and for a conventional surface electrode (without any spikes on it). Fig.3.3 shows the 3D view of the electrodes that were used in the simulation scenarios.


**Fig. 3.3.** Different modelled electrode cases: 50 MNs, 100 MNs, and surface electrode (Dimensions are in mm).

**Table 3. 1.** Electrical and thermal properties of the skin

| Layer name | Electric Physics | | Bioheat Physics | |
|---|---|---|---|---|
| Stratum Corneum and Epidermis | Electrical Conductivity | $1.67\times10^{-4}$ (S/m) | Thermal Conductivity | 0.209 (W/m·K) |
| | Relative permittivity | $3\times10^{4}$ | Heat capacity | 2500 (J/kg·K) |
| | | | Density | 1000 ($kg/m^3$) |
| Dermis | Electrical Conductivity | $1.4\times10^{-3}$ (S/m) | Thermal Conductivity | 0.37 (W/m·K) |
| | Relative permittivity | $6\times10^{3}$ | Heat capacity | 3391 (J/kg·K) |
| | | | Density | 1109 ($kg/m^3$) |
| Subcutaneous tissue* | Electrical Conductivity | $3.03\times10^{-2}$ (S/m) | Thermal Conductivity | 0.21 (W/m·K) |
| | Relative permittivity | $2.5\times10^{4}$ | Heat capacity | 2348 (J/kg·K) |
| | | | Density | 911 ($kg/m^3$) |
| Nerve fibers* (myelinated) | Electrical Conductivity | $1.1\times10^{-7}$ (S/m) | Thermal Conductivity | 0.21 (W/m·K) |
| | Relative permittivity | $2.5\times10^{4}$ | Heat capacity | 2348 (J/kg·K) |
| | | | Density | 911 ($kg/m^3$) |
| Capillary walls | Electrical Conductivity | 0.095 (S/m) | Thermal Conductivity | 0.543 (W/m·K) |
| | Relative permittivity | $8.5\times10^{4}$ | Heat capacity | 3212 (J/kg·K) |
| | | | Density | 960 ($kg/m^3$) |
| Blood | Electrical Conductivity | $8.5\times10^{-6}$ (S/m) | Thermal Conductivity | 0.492 (W/m·K) |
| | Relative permittivity | $2.4\times10^{4}$ | Heat capacity | 4180 (J/kg·K) |
| | | | Density | 1060 ($kg/m^3$) |

**Note:** Since the nerve fibers are surrounded by subcutaneous tissue, most of their physical parameters are close to the subcutaneous tissue parameters.

### 3.2.1. Electrical Physics

*Electrical physics (Electric Current module)* is the physics that was used to analyze the simulation model. This model was used to calculate the potential distribution in a conductive medium where the inductance effect is not significant (Comsol, 2011). The electrical physics was modeled based on the Eq. 1.

$$-\nabla.(\sigma\nabla \mathrm{V} - \boldsymbol{J_e}) = 0 \quad (1)$$

where V is the potential (V), σ is conductivity (S/m) and $J_e$ is an external current density. In this study, it was assumed that stimulation is based on constant voltage. Therefore, to study the potential distribution inside tissue and current density in different depth of the tissue, a 1 ms width monopolar pulse with 20V amplitude electric potential was applied between the two MNA electrodes and the other boundaries were connected to ground (Fig. 3.4).

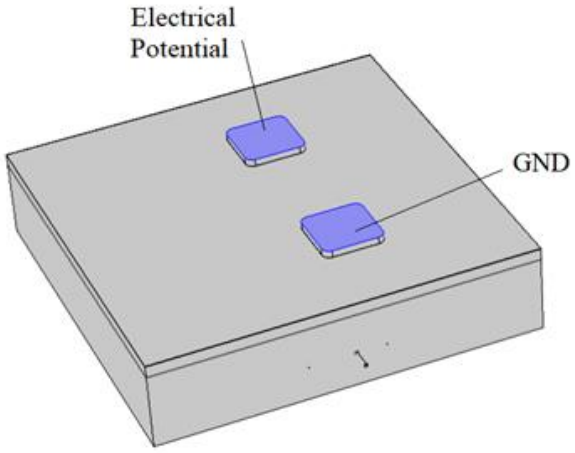


**Fig. 3.4.** Boundary condition of the electrical physics

It is worthwhile to mention that the purpose of this simulation study is finding the difference(s) between TENS through conventional surface electrodes and the MNAs. Hence, in all the scenarios it is assumed that the stimulation amplitude is high enough to excite the nerve. It was assumed that the nerve fiber itself does not generate any action potential over time and it is modeled as a passive

cable (Gabbiani and Cox, 2017). Using the simulation output, the space constant of different stimulation electrodes, specific absorption rate (SAR) and temperature change at each layer of the tissue were calculated through the FE results.

### 3.2.2. Estimating Space Constant

Based on the above model assumptions, each nerve membrane is divided into small compartments that are isopotential per segment but the voltage of each comportment is different. With this assumption, neuroscientists model a nerve fiber membrane like an electrical circuit shown in Fig. 3.5 (Gabbiani and Cox, 2017, Warman et al., 1992) where the loops of 1 to n represent the isopotential compartments, $C_n$ is the capacitance across the nerve membrane, $G_n$ is the electrical conductance of the nerve membrane and $V$ is the voltage difference across the nerve membrane in rest.

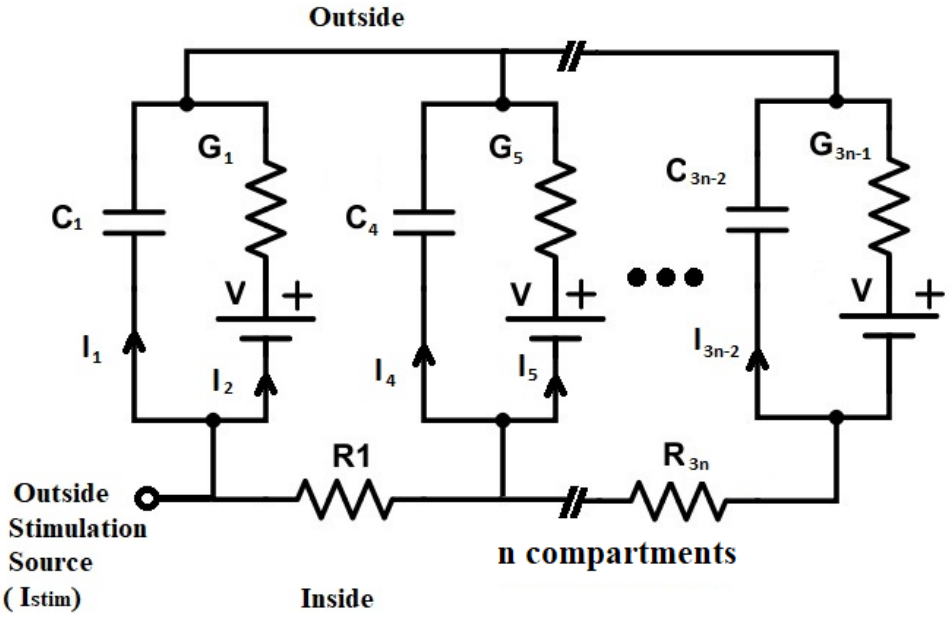


**Fig. 3.5.** Electrical model of a passive nerve fiber.

Since the model is a passive one, *V* can be called the membrane rest voltage. Physiologically, the major voltage difference in the rest state is coming from chloride ions ($Cl^-$). Thus, *V* can also be called $V_{Cl}$ (Gabbiani and Cox, 2017). If it is assumed that the length of the modeled nerve fiber is $\ell$, the length of each segment would be $dx=\ell/n$. Also, each segment is coupled with the adjacent one via the coupling resistor $R_n$ (which is the electrical resistance of the cell cytoplasm). Furthermore, the structural definition of space constant, $\lambda$, can be calculated using Eq. 2 (Gabbiani and Cox, 2017, Gow and Devaux, 2008).

$$\lambda \equiv \sqrt{\frac{\pi a^2 dx}{R_n G}} \tag{2}$$

where *a* is the radius of the nerve fiber. Measuring $\lambda$ in practice is not practical in alive tissue. Therefore, it was investigated how to estimate $\lambda$ with the circuit model in Fig. 3.5.

In Fig. 3.5, the voltage of each compartment is *v(x,t)* changing by both time and distance of the compartments where $0 \le x \le l$. For the *n*th segment, $v(\left(\frac{n-1}{2}\right)dx, t)$ is the voltage difference across the segment *n*. Based on the described condition and the assumption that the current is injected to the first component, the loop equation for each segment can be written as Eq. 3.

$$C_m(2\pi a dx)\frac{\partial v}{\partial t}\left(\frac{dx}{2}, t\right) + Gv\left(\frac{dx}{2}, t\right) - \frac{\pi a^2}{R_a}\frac{v\left(\frac{3dx}{2}, t\right) - v\left(\frac{dx}{2}, t\right)}{dx} = I_{stim}(t) \tag{3}$$

For any interior point inside the nerve, called *x*, Eq. 3 can be written as Eq. 4 where $dx \to 0$.

$$\lim_{dx\to 0}[\tau\frac{\partial v}{\partial t}(x,t) + v(x,t) - \lambda^2\frac{v(x+dx,t)-2v(x,t)+v(x-dx,t)}{dx^2}] = 0 \tag{4}$$

Therefore, Eq. 4 can be simplified as Eq. 5

$$\tau\frac{\partial v}{\partial t}(x,t) + v(x,t) - \lambda^2\frac{\partial^2 v}{\partial x^2}(x,t) = 0;\ \ 0 < x < \ell\ ,\ t > 0 \tag{5}$$

where $\tau = RC$ is the time constant and $\lambda$ is the space constant. In steady-state situation, where $t\to\infty$, Eq. 4 is rewritten as Eq. 6 in which the time derivative is ignored.

$$\lambda^2 \frac{\partial^2 v(x)}{\partial x^2} = v(x) \tag{6}$$

From Eq.6, $\lambda = \sqrt{\frac{\partial^2 v(x)}{\partial x^2 v(x)}}$ which shows the *space constant* of a nerve fiber. Although the space constant depends on the physical characteristics of a nerve (such as nerve fiber diameter Eq. 2), Eq. 2-5 show how the stimulation parameters and the amount of potential delivered at different points of a nerve will affect $\lambda$ too. To investigate the effect of MNAs on the spatial parameter of stimulation, the developed model was solved in a stationary study based on Eq. 4 by applying the input pulse that was explained in the beginning of the electrical physics section. The voltage and $\frac{\partial^2 v}{\partial x^2}$ were estimated from simulated model and inserted in Eq. 5 to find $\lambda$ along the nerve. It is worthwhile to mention that the Eq. 6 supports the conclusion of the other study in which Rattay developed a model and showed that the effectiveness of the nerve fiber stimulation is depending on the second derivative of the external voltage around the nerve fiber (Rattay, 1986). Although the name of the space constant is inducing a constant value, based on what is defined in Eq. 6, it is following the finding of Rattay. In the other words, the space constant parameter is the second derivative of the potential difference that is normalized by the voltage along the nerve. Since the variation of this parameter is constant along a nerve, for each nerve fiber depends on its morphology, it is known as space constant. More discussion about the results are provided in section 3 of this chapter.

### 3.2.3. Estimating Specific Absorption Rate in Different Depths of the 3D model

In order to investigate differences between MNA and surface electrodes performances, current density is a crucial factor. Current density in a specific depth reveals the energy that is applied to that depth. Thus, one can estimate how much energy is absorbed in an specific layer

based on SAR that is calculated by Eq. 7 depends on the current density at that layer (Panescu et al., 1995).

$$SAR = \frac{|J^2|}{2\sigma\rho} \tag{7}$$

where $J$ is the norm of current density in an specific depth, $\sigma$ is electrical conductance and $\rho$ is the density of that depth respectively. SAR was calculated based on the parameters that were obtained from numerical simulation.

### 3.2.4. Estimating the distinguishability of two adjacent nerves

In a situation where there are two (or more) nerves besides each other, there is possibility to have co-stimulation while one wants to simulate only a specific nerve fiber among them. Hypothetically, if the current injected by the electrodes is such that it was more localized, it could be possible to target one nerve without co-stimulation of the other adjacent nerve(s). To explore this, the distribution of energy inside the tissue was investigated for both the surface electrode and MNAs.

Distinguishability is a parameter that shows how much of the energy is distributed towards the target compare to an adjacent nerve (Gaggero, 2011). The method for calculating distinguishability is similar to the one for calculating signal-to-noise ratio (SNR) in signal processing (Johnson, 2006). The concept of distinguishability is close to *selectivity* as is defined in (Grill and Mortimer, 1995). The concept of distinguishability can also be used to investigate how to enable more localized studies in electrical impedance tomography (EIT), as electrodes with more localized interrogation of tissue would better discriminate between adjacent tissues.

Distinguishability is calculated based on the effectiveness coefficient (EC) that is defined in Eq. 8.

$$EC = \frac{median[J]}{\sigma_J} \tag{8}$$

where the *median[J]* is the median value and $\sigma_J$ is the standard deviation of the normal current density along a nerve. When the stimulation is more targeted toward a specific nerve, *EC* of the target nerve ($EC_{stim}$) should be higher than the adjacent nerve's one ($EC_{adj}$). The values of current density along two target and adjacent nerves were obtained from the results of simulation in different scenarios.

## 3.3. Thermal Physics

Applying electrical current to a living tissue will end to increase the temperature of the tissue. This temperature rising happens more in the connective tissues with no blood vessel in the vicinity. In this study, the temperature changes in different layers of the developed 3D model was investigated, and calculated from the result of the multiphysics simulation based on Eq. 9 (Davalos et al., 2005, Comsol, 2011).

$$\delta_{ts}\rho C\frac{\partial T}{\partial t} + \nabla.(-k\nabla T) = \rho_b C_b \omega_b (T_b - T) + Q_{Ext} \tag{9}$$

where $\delta_{ts}$ is a time-scaling coefficient; $\rho$ is the tissue density (kg/m$^3$); C is the tissue's specific heat (J/(kg·K)); and k is its thermal conductivity (W/(m·K)). On the right side of the Eq.9, $\rho_b$ gives the blood's density (kg/m$^3$); $C_b$ is the blood's specific heat (J/ (kg·K)); $\omega_b$ is its perfusion rate (1/s); $T_b$ is the arterial blood temperature (K); while $Q_{Ext}$ is the heat sources from electric source (W/m$^3$). The initial temperature of all the boundaries was set on 37 $^\circ$ C.

Also, the relationship between SAR (calculated from Eq. 7) and temperature of the specific layer of tissue, can be calculated from Eq. 10 (Panescu et al., 1995):

$$SAR = c.\frac{T(t)-T_0}{2.t} \quad (10)$$

where *c* is the thermal capacity of the specific layer of tissue, $T_0$ is the initial temperature and *T(t)* is temperature of that layer in time *t.*

## 3.4. Fluid physics

In this study, it was assumed that the blood enters from one side (inlet) of the capillary and flows out from another side (outlet) of the blood capillary. In the former studies, the blood flow speed in capillary was measured about 1.14 mm/s (Ivanov et al., 1981). The creeping flow physics was studied only on the blood and capillary based on Eq. 11.

$$\nabla.[-PI + \mu(\nabla u + (\nabla u)'] = 0 \; ; \nabla.u = 0. \quad (11)$$

where *P*, is the pressure, $\mu$ , is the viscosity and *u* is velocity of the blood. Blood flow is affected by temperature. In a living tissue, when temperature is increased locally, the blood flow will increase at that area to remove the heat (Pennes, 1948, Pennes, 1998, Petrofsky et al., 2009, Petrofsky et al., 2011). Assuming that the heat transfer from blood to tissue is uniform and consistent regardless of the tissue type, the relationship between heat and blood flow rate can be modeled by Eq. 12 (Pennes, 1948).

$$h_b = V.s\,(\theta_a - \theta) \quad (12)$$

where $h_b$ is rate of heat transfer from blood to tissue, *V* is the blood volume, *s* is time, $\theta_a$ is arterial temperature and $\theta$ is the surrounding tissue temperature. From Eq. 10, it is obvious that increasing the tissue temperature will result in blood temperature elevation and increase the blood flow locally and in the entire of the limb or organ eventually.

## 3.5. Meshing

The model was segmented into tetrahedral elements, in order to simulate the described physics on the developed 3D model (Fig. 2). Since the model consists of small feature in some points and large part in the rest, the meshing procedure was divided into *coarser* and e*xtra-fine* categories. In the coarser category, element sizes are varied between minimum values of 2 mm to 1 cm. In contrast, in the extra-fine category, the elements were smaller and varied between 80 µm to 1.8 mm. On average, the developed 3D model was meshed into 539,476 elements. One should keep this in mind that because the distinguishability was calculated based on a comparison between the current density of the target and adjacent nerves, the size of the meshes did not affect the calculated parameters. Therefore, once the independency of the results from the size of the meshes was proved by some studies, all the scenarios were investigated based on the described mesh setting.

## 3.6. Results

The results of this study are separated into analytic and simulation sections. The organization of the results is based on the physics. In each physic, there are some parameters that were calculated based on the outcome of the simulation and the calculation method was earlier discussed in Methods and Materials (section 3.2). The result of each physic in multiphysics simulation was calculated based on the equation of that physic. All the physics of the described model were segregated and the equations of the physics were calculated simultaneously. The model was run in a time-dependent study with the length of 1 ms and the steps of 0.1 ms.

### 3.6.1. Electrical Physics

In this physics, first current density of each layer of the skin, which was calculated from the model for different scenarios (Fig. 3.1), is presented. In the next step, space constant, SAR and distinguishability of the scenarios of Fig. 3.1 are calculated based on the outcomes of the simulations.

### 3.6.2. Current Density

A single pulse was applied like what was explained in section 3.2.1 (1 ms width and 20V amplitude) in different scenarios of Fig. 3.1. The current density in different depths of the tissue was simulated in the 3D model. In order to demonstrate the average current density over stimulation time in different depths of the developed 3D model properly, two different cross-sections of the model were considered. These two cross-sections were taken from points A and B in Fig 3.6a.

From the current density graphs of both A and B cutlines, it can be seen that the current density drastically drops in dermis layer. According to the values of Table 3.1, the dermis layer possesses a lower relative permittivity ($\varepsilon$) than the epidermis and subcutaneous tissue which explains the drop in the current density. Because of this low $\varepsilon$, less electrical charge will sit on the dermis compared to the epidermis and subcutaneous tissue. This causes low current density between epidermis and subcutaneous and consequently the valleys in the graphs of Fig. 3.6.

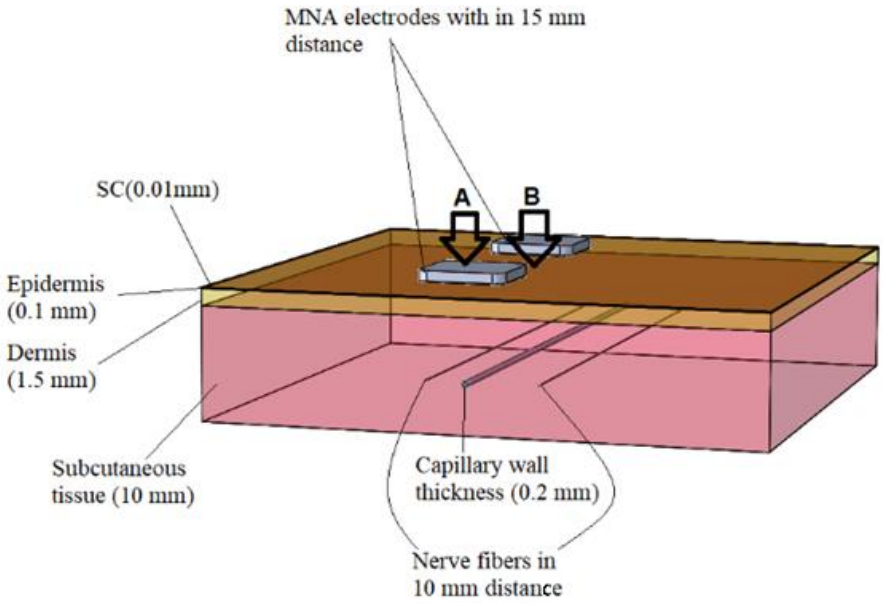


**Note:** The Capillary and nerve fibers are in 7mm depth from the skin surface

(a)

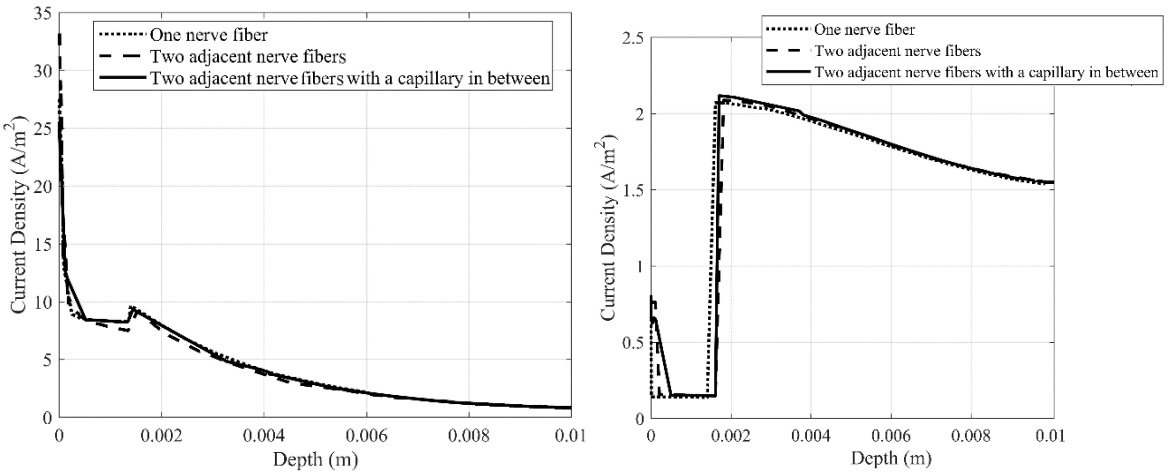


(b)

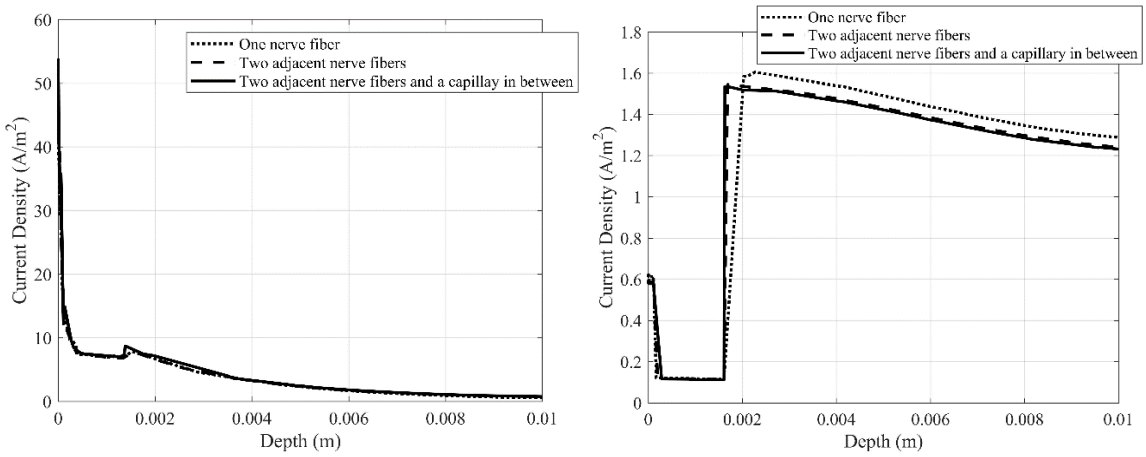


(c)

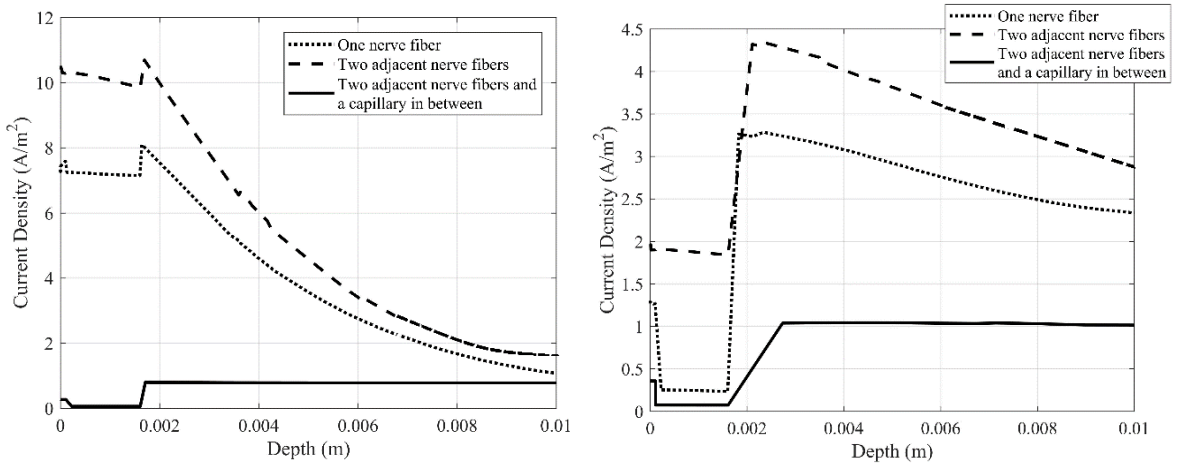


(d)

**Fig. 3.6.** (a) The two cutlines (A and B) across which the current density in different depths of the 3D modeled tissue was measured (b) Current density in different depths of cutline A (left) and B (right) for an electrode with 100 microneedles (c) Current density in different depth of cutline A (left) and B(right) for an electrode with 50 microneedles (d) Current density in different depth of cutline A (left) and B(right) for a surface electrode.

#### 3.6.2.1. Estimating Space Constant

Based on the cable theory, the practical definition of space constant is defined as the distance that electrical potential can travel along a nerve (Rall, 2011). In Eq. 6, it was shown that the space constant depends on the variation of the voltage respect to the distance ($x$) along a nerve fiber. The voltage, that a nerve fiber receives, depends on many factors like presence or absence of adjacent nerve and blood capillary. These tissues affect the electrical field and consequently the voltage along the nerve. Fig. 3.7 shows the space constant in different scenarios of the simulation that picked the values of the voltage below the electrodes in different depths (cutline A of Fig. 3.6a). It can be inferred that the microneedle electrodes have almost similar space constant. However, because of the blood capillary that causes a charge barrier between the nerves, space constant of stimulation through surface electrode is significantly higher than the microneedle electrodes. It is worthwhile to mention that in Fig. 3.7, the space constant was calculated in different depths to estimate the effectiveness of the stimulation on the nerve fibers that might be located in different depths from the skin surface.

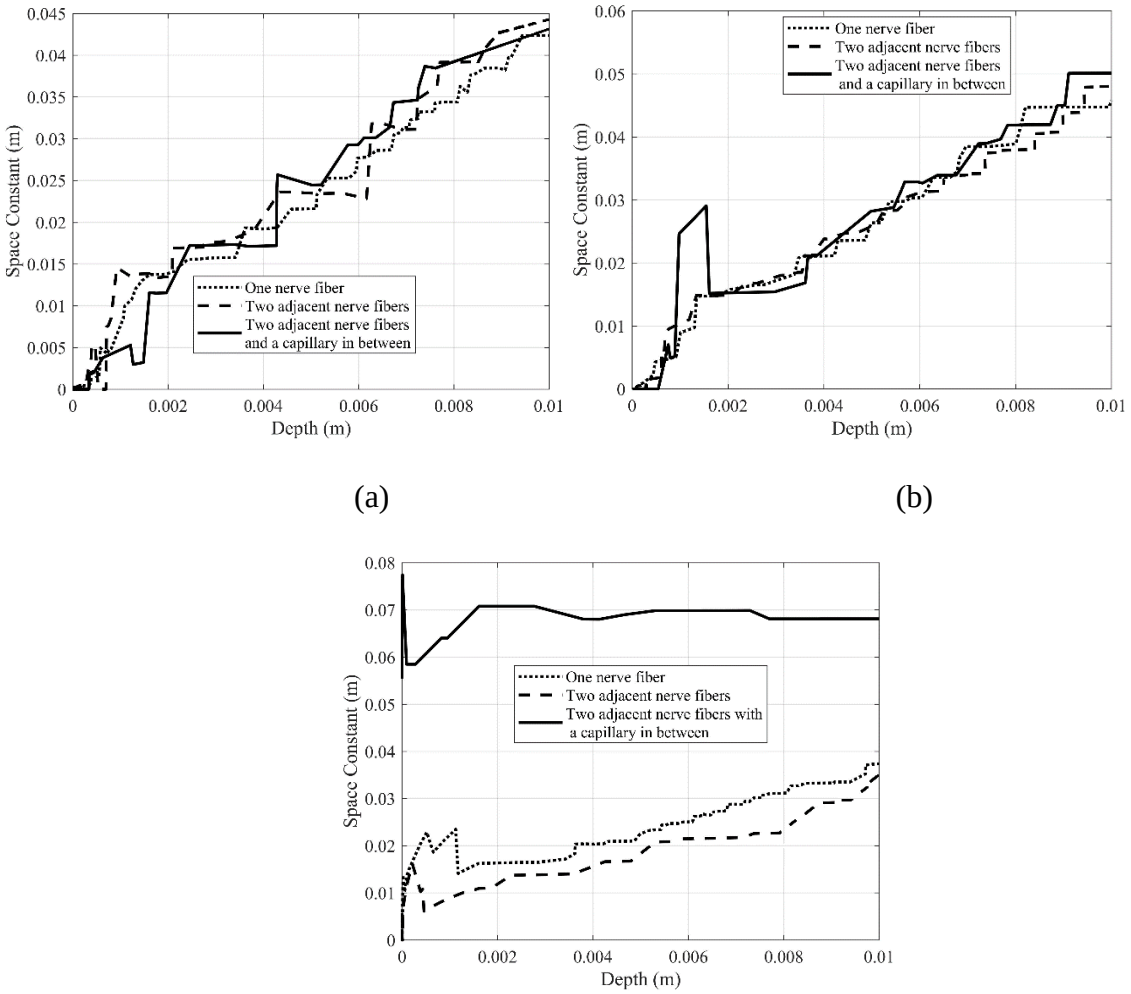


**Fig. 3.7.** Space constant in cutline A for (a) 100 microneedle electrode, (b) 50 microneedle electrode, (c) surface electrode.

### 3.6.2.2. Estimating Specific Absorption Rate in Different Depth

SAR is an index that should be considered in a specific range while an alive tissue is exposed to any type of electrical or electromagnetic stimulation (Kiminami et al., 2008). In order to measure this index in different studied scenarios, the developed model was cut through horizontal planes where the nerve fibers and the blood capillary were located. Following this, the maximum SAR during stimulation time along the nerve fibers (target and adjacent farther fibers) and capillary wall

were shown in Fig 3.8. In Fig 3.8a, the horizontal plane cut is shown. Also, the target nerve is directly underneath the stimulating electrodes, and the farther nerve is the one that is not supposed to be stimulated. The graphs show how the applied energy impacts both nerve fibers at the same time.

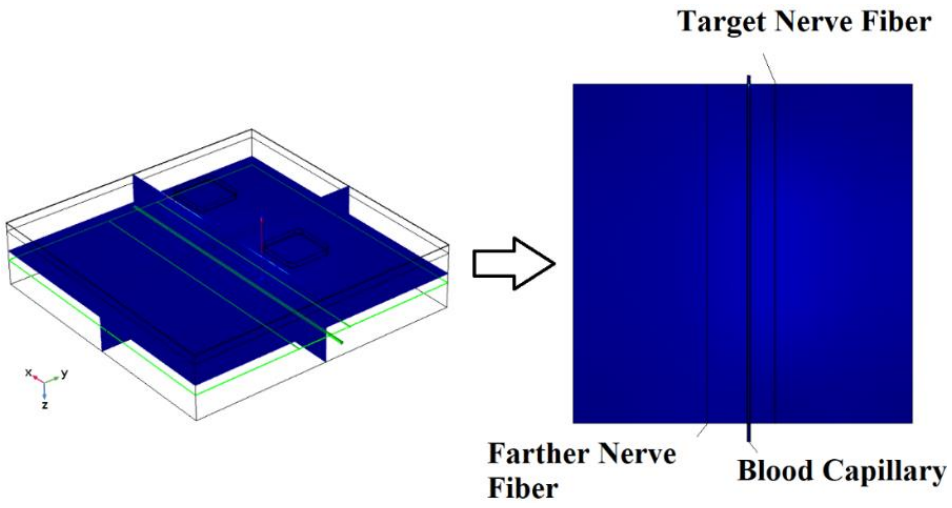


(a)

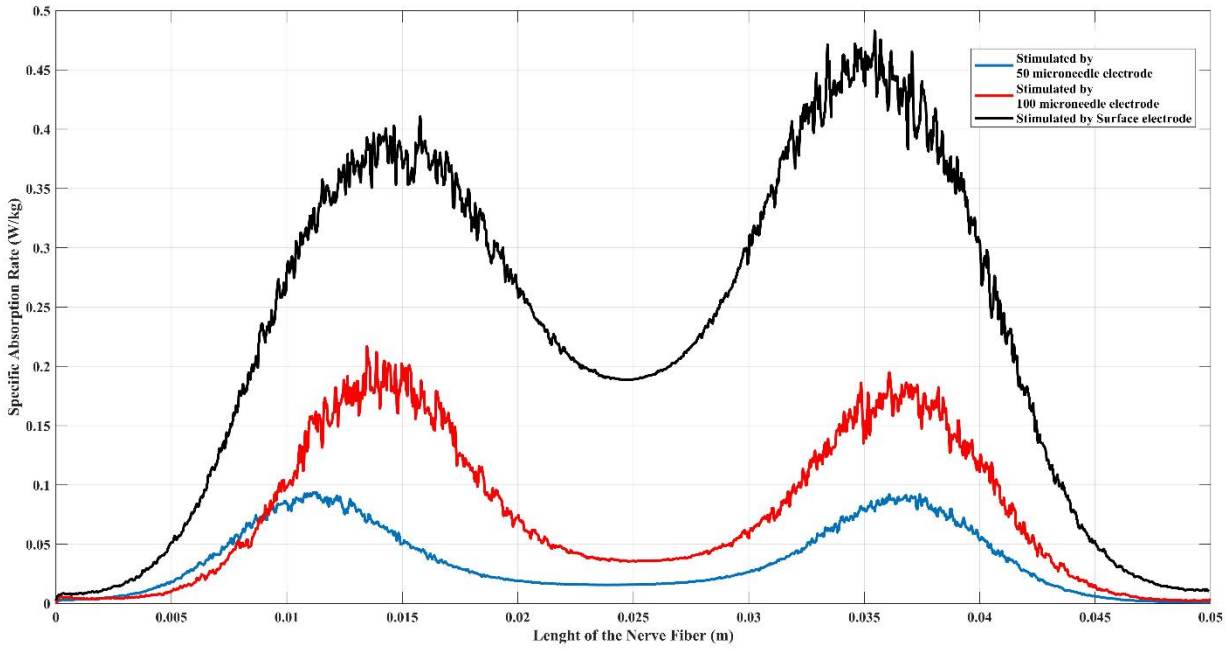


(b)

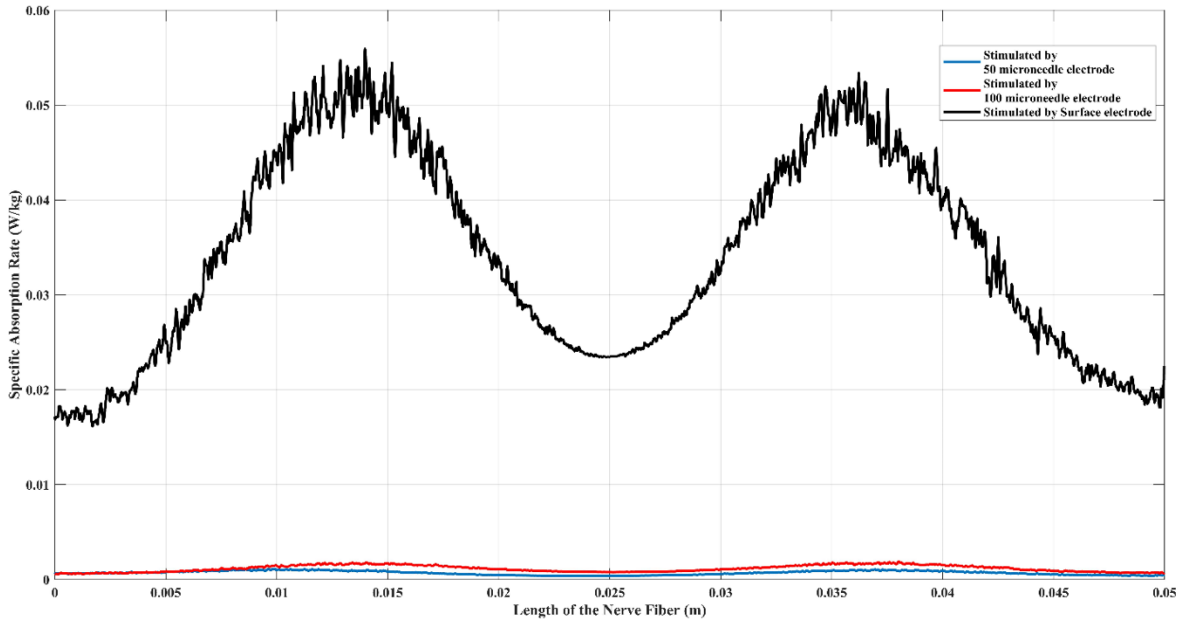


(c)

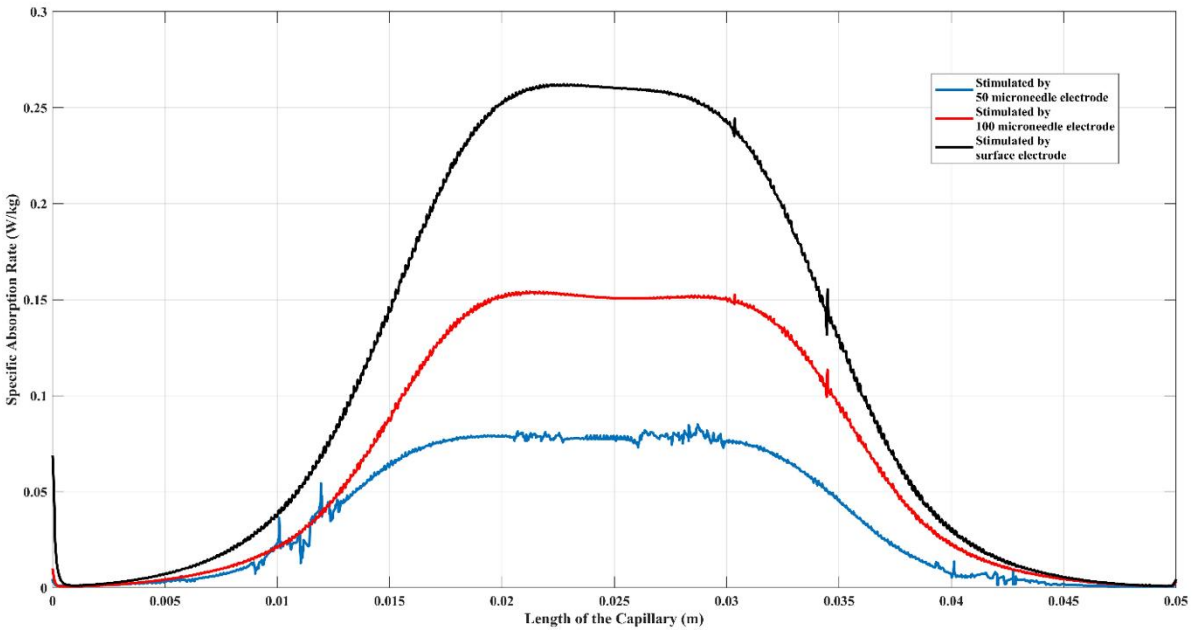


(d)

**Fig. 3.8.** (a) Horizontal plane of the model and SAR in (b) target nerve fiber (c) farther adjacent nerve fiber (d) capillary wall.

From Eq. 7, one can speculate that the SAR is high in the layers with low density and conductance. It means that these layers absorb more energy and their temperatures increase with prolonging the stimulation time. However, this increase should be restricted over time and should not exceed an specific range. The maximum amount of the SAR that is allowed by the medical device standard (IEC 60601-2-33 and FDA) is less than 3.2 W/kg for head and neck and less than 10 W/kg for any other localized area in the body (Commission, 2010). In the graphs of Fig. 3.8, it is shown that all the stimulations are in the acceptable range. However, as the SAR graphs show (Fig. 3.8), stimulation via microneedle electrodes transfers more energy to the target nerve compare to the other electrodes.

### 3.6.2.3. Estimating Distinguishability

It was shown in Eq. 8 that the distinguishability is a statistical feature that is related to the current density. Fig. 3.9 shows the mean and standard error of the current density along the two nerve fibers in the model.

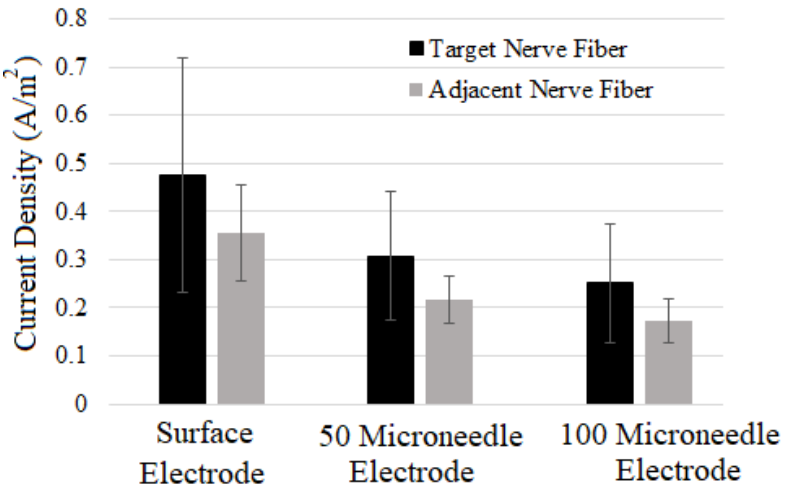


**Fig. 3.9.** Mean and standard deviation of the time-average of current density over stimulation period along the nerve fibers in the developed 3D model.

Calculating EC factors shows that the distinguishability of the microneedle electrodes is more that the surface electrodes. Fig. 3.9 bar chart is showing the ratio between the EC factors of the main target nerve and the adjacent farther nerve when they were stimulated with different types of electrodes. From the bars in Fig. 3.10 one can understand that the microneedle electrodes are more distinguishable than the surface electrodes. Also, it can be inferred that the 100 pyramidal microneedle electrode can be more distinguishable than the other types of electrodes.

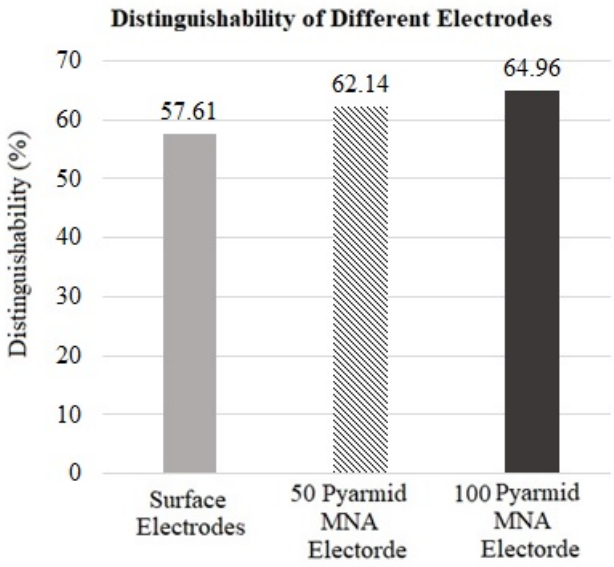


**Fig. 3.10.** Distinguishability percentage between a target nerve and adjacent nerve when different electrodes were used for stimulation.

The electric field of the model in different scenarios was calculated in order to investigate the reason of distinguishability increase. As shown in Fig 3.11a, a cross-section of the model and the stimulator electrodes was picked and the average of vertical electric field ($E_z$) over stimulation time was calculated. The graph of Fig. 3.11b shows how the microneedle electrodes will increase the directive electrical field that ends to higher distinguishably than the surface electrodes.

The reason for the $E_z$ difference in different electrodes can be shown in the electrode-tissue interface of the model. Fig. 3.12 shows the $E_z$ at the interface for the surface and 100 microneedle electrodes. It shows that the microneedle electrodes can generate a uniform electric field along the z-axis. Therefore, the $E_z$ component of the applied electric field will have higher amplitude compare to the other components in the microneedle stimulations.

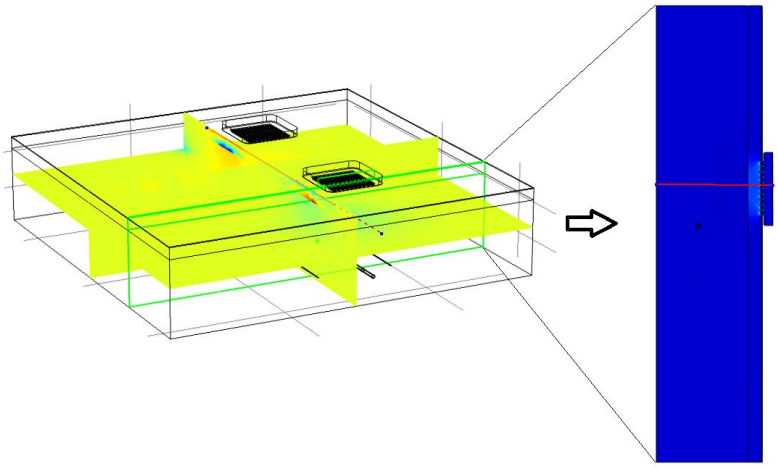

(a)

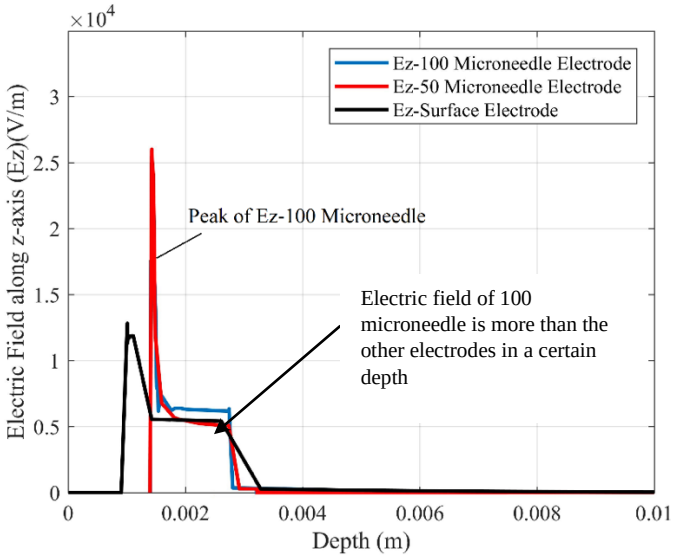


(b)

**Fig. 3.11.** Electrical field in (a) vertical cut of the model, and (b) Ez in different depths along redline of figure (a).

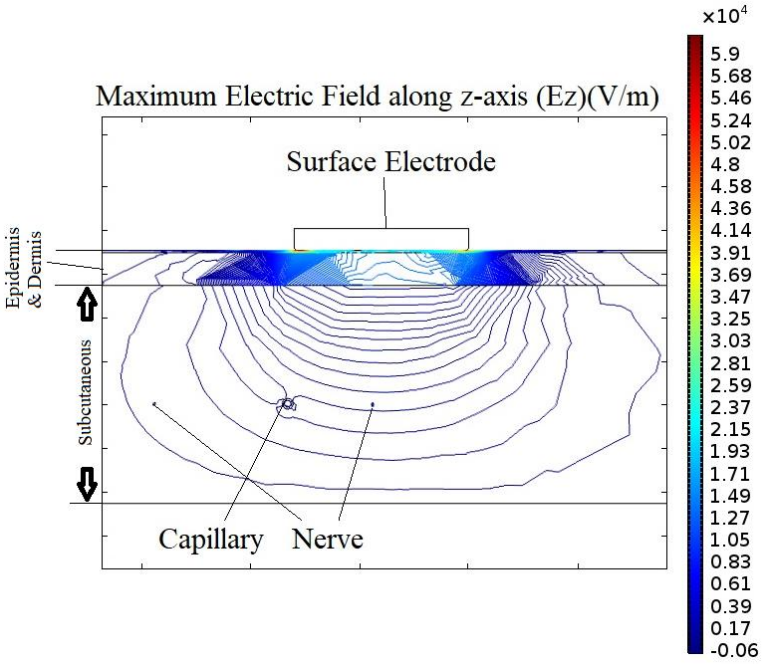


(a)

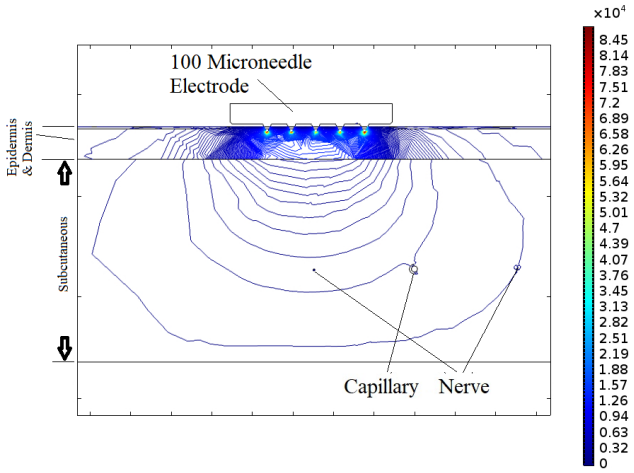


(b)

**Fig. 3.12.** Electrical field along z-axis (Ez) in (a) surface electrode (b) 100 microneedle electrode.

### 3.6.3. Thermal Physics

The thermal physics simulation was done to investigate the temperature change of the modeled tissue during pulsatile stimulation. It was shown in Eq. 9 that the temperature difference of different layers in a living tissue during stimulation depends on the thermal capacity of each layer. Referring to the values of Table 3.1, the thermal capacity of different layers of the tissue is high. High thermal capacity decreases the temperature difference in each layer. The simulation results support the fact that the temperature rise in tissue caused by the pulsatile electrical stimulation is negligible. Fig. 3.13 shows the temperature of different layers of a tissue that was stimulated by different types of electrodes.

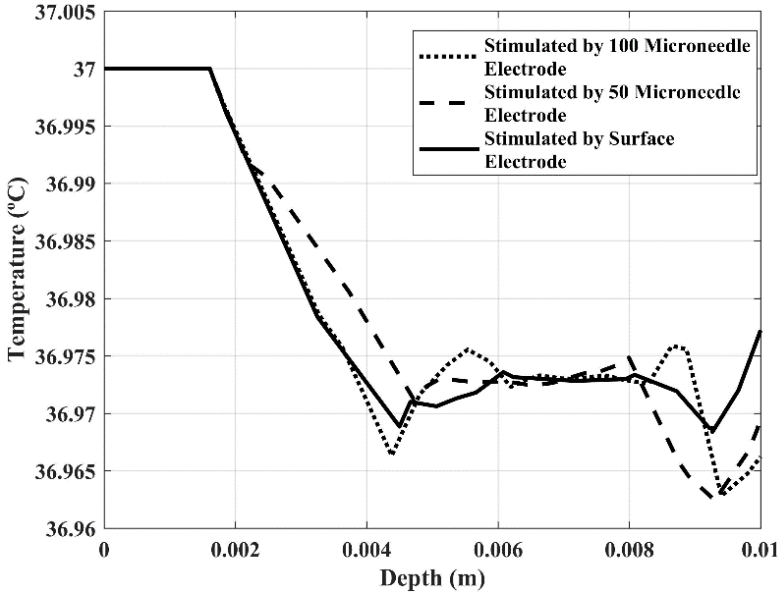


**Fig. 3.13.** Temperature of the modeled tissue in different depths during stimulation.
(Note: The initial temperature was 37º C on the surface of the model and it decreases in the inner layer because of higher thermal capacitance than the surface layers.)

Thermal analysis is not limited to the temperature of different layers of the stimulated tissue. The amount of dissipated heat under the electrodes is very crucial. If the generated heat by the electrodes is accumulated, it may burn the top layer of the skin. In order to investigate the amount

of dissipated heat, a horizontal cut plane is investigated through the tissue located underneath of the surface and 100 microneedle electrode. Fig. 3.14 shows that the amount of dissipated heat under both types of electrodes.

### 3.6.4. Flow Physics

Flow physics was only studied for the blood capillary in the developed model. It was assumed that the initial blood velocity is 1.14 mm/s (Ivanov et al., 1981). Fig. 3.15 shows that how the surface electrode will increase the blood flow velocity compared to the other types of microneedle electrodes.

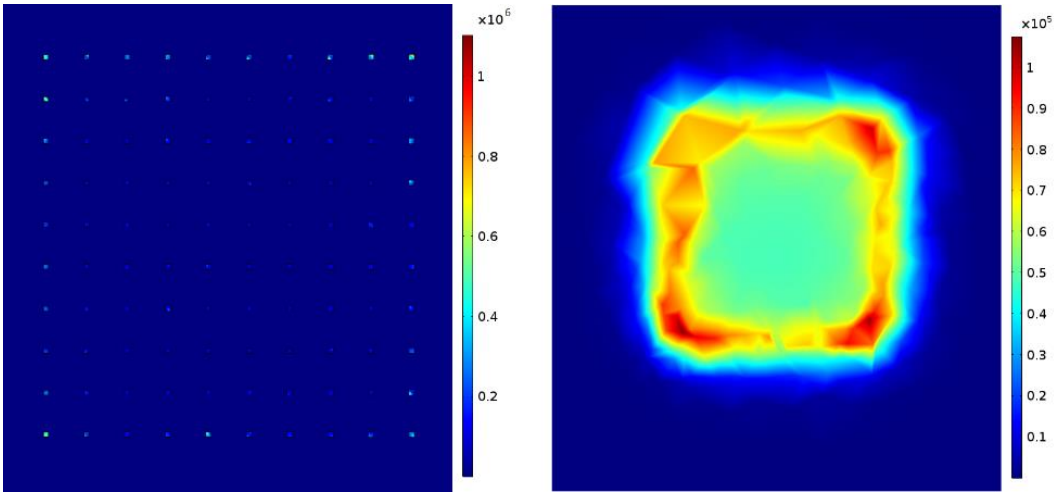


(a) (b)

**Fig. 3.14.** (a) Maximum planar cut of the volumetric dissipated heat underneath of working electrodes; input: 20 V and 1 ms stimulation pulse width in fabricated MNPs model (Average over stimulation time: $4\times10^5$ W/mm$^3$ on some spots). (b) Smooth surface electrode (Average over stimulation time: $10^5$ W/mm$^3$).

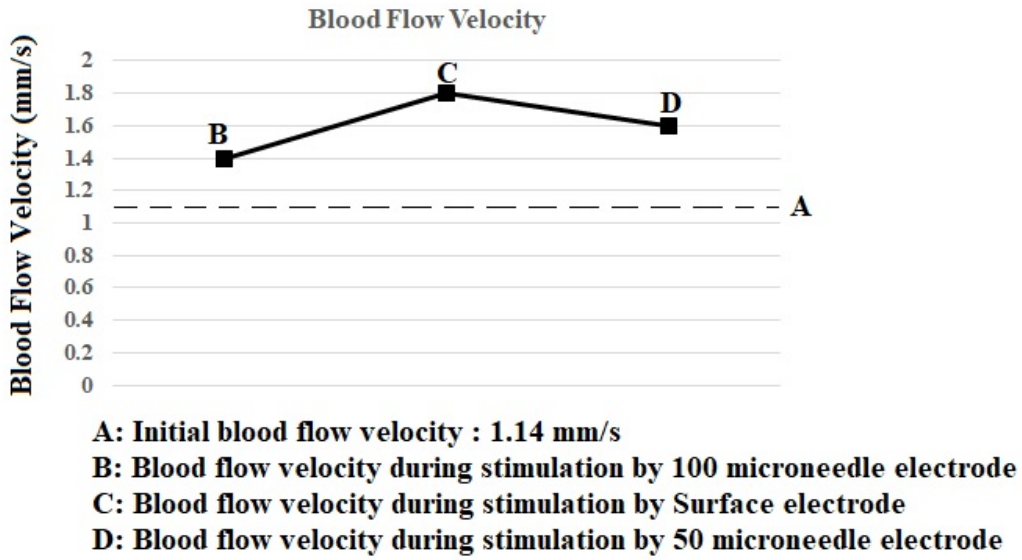


**Fig. 3.15.** Blood flow velocity during stimulation by different types of electrodes.

It was shown in Eq. 12 that the blood flow velocity depends on the temperature difference. Also, Fig. 3.13 illustrates that the temperature difference is not significant while the tissue is stimulated. Therefore, it is not expected to have a considerable change in blood flow velocity during stimulation with different types of electrodes in a short period of time. However, prolonging the stimulation time will increase the temperature difference and blood flow velocity consequently.

## 3.7. Discussion

TENS is recently being considered as a treatment for chronic syndromes. Therefore, enhancing its parameters, like distinguishability to target an specific nerve, is valued. In this study, different electrodes were investigated to determine their performance for TENS. The TENS parameters were investigated through 3 different physics: electrical, thermal and flow. Since, all the studied physics affect each other, a multiphysics study was run on a developed 3D model. The model was stimulated by 3 different electrodes in different simulation scenarios (Fig. 3.1).

Current density at different depths of the tissue is one of the parameters that plays a critical role in nerve stimulation. As it is shown in the graphs of Fig. 3.6, below the microneedle electrodes the current density at different depths is considerably higher than the surface electrodes, regardless of existence or absence of another nerve or blood capillary. However, the current density is not changing consistently in different depths while the model was stimulated by surface electrodes and different tissues with different conductivities were existed. Although the surface electrodes cannot deliver robust current density in different depths, more current density was generated is generate by surface electrodes compare to the MNAs. Also, it can be inferred that increasing the number of the microneedles on the surface of the electrodes would increase the current density slightly, particularly at a depth of ~1 cm below the electrodes. The fact that makes the MNAs performance outstanding is that the MNAs pierce the skin and bypass the SC which causes a higher current density at an specific location, while the surface electrodes spread the electric field over a larger area. One should keep this in mind that because the surface electrodes have more contact surface than the MNAs, they generate more electrical field in a large area. Therefore, the current density that surface electrodes generate in all the tissues at different depths is higher than the situation that the tissue is stimulated by the MNAs.

Adding microneedles on the electrode surface will slightly increase the surface area of the electrode. The 100-microneedle, 50-microneedle and surface electrodes have 115 $mm^2$, 72.7 $mm^2$ and 63.14 $mm^2$ area respectively. Due to the pyramidal shape of the microneedle spikes, the resistance against piercing the skin will increase by increasing the depth of penetration. Therefore, the electrodes do not completely pierce the skin, and so the effective contact area of the microneedle electrodes would be less than their total surface area. In the other words, the effective contact surface of the MNAs would be less than their total surface area and the conventional

surface electrodes obviously. This effective contact surface reduction is similar to decreasing the size of electrodes in (Geuze, 1983, Ksienski, 1992) that will lead to high tissue-electrode resistance and more uniform electric field underneath of an electrode consequently.

In the graphs of cutline B in Fig. 3.6, it can be seen that current density drastically drops across the dermis layer but this cannot be seen in the cutline A graphs. Aforementioned, the dermis layer has lower relative permittivity compared to the other layers. Therefore, lower electrical charge will sit on this layer compared to the other layers. This effect cannot be seen in the cutline A graphs because it was immediately underneath of the electrodes where the current density is inherently high. This is supporting the idea that increasing the local current density around a particular nerve will increase the stimulation selectivity (Djilas et al., 2011).

The reason for exploring the different scenarios of the nerve fibers and blood capillary, was to find a robust MNA design that can generate a uniform current density and has a consistent result in the various scenarios. The graphs of Fig. 3.6 showed that both 100- and 50-microneedle electrodes have fairly consistent results in the different scenarios, particularly underneath of the electrodes. Their distinguishability (Fig. 3.9) is higher than the surface electrodes while their current density is lower (Fig. 3.8). Furthermore, it was shown in the graphs of Fig.7 that the space constant in the microneedle electrodes is relatively higher than the surface electrodes. It can be seen when the surface electrodes were used for stimulation, the presence of tissues with high conductivity (like blood capillary and another nerve fiber) significantly affected electric field, current density and the space constant consequently. However, the presence or absence of any other tissue did not affect the stimulation parameters in the scenarios that MNAs were used as the simulator electrodes. It is worthwhile to mention that the space constant was used as a stimulation

parameter in this study because it shows the normalized second derivative of the voltage across the target nerve fibers (Rattay, 1986).

In Fig. 3.13 it was shown that the temperature inside the tissue did not change considerably at different depths. Therefore, there is not any concern about tissue burning during short time stimulation. However, it should be considered as a serious hazard during long term stimulation or longer pulse than what was studied in this simulation. Although it is shown in Fig. 3.14 that the maximum dissipated energy on the tip of the MNAs is higher than the surface electrodes, the risk of tissue burning can be mitigated by fabricating the tip of the needles more curvature (Tungjitkusolmun et al., 2000). Furthermore, according to the graph of Fig. 3.15, blood flow increases in surface electrode stimulation more than 100- and 50-microneedle electrode stimulation.

Overall, one may conclude that depending on the application, either 100 microneedle or surface electrodes can be used in TENS. If a specific nerve needs to be stimulated and more current density uniformity is required, the 100 microneedle electrodes can provide more distinguishability and robust uniform current density but less strength compared to the surface electrodes with a same stimulation setup. Furthermore, if increasing the blood flow velocity is required, one may choose the surface electrodes for stimulation. However, the effectiveness of each of them on the long term application, particularly for specific syndromes like overactive bladder, should be investigated clinically.

## 3.8. Conclusion

In this study, a 3D model of tissue was developed and finite element multiphysics simulations, including electrical, thermal and flow physics, were run on it. Different parameters, like the current density in different depths of the tissue, the space constant under electrodes, specific absorption rate of the tissue, distinguishability of the stimulation, temperature rise of the tissue and the blood flow under the electrodes, were investigated in the model in different scenarios. For each scenario the model was stimulated in the mentioned physics with 100 microneedle, 50 microneedle, and surface electrodes.

Simulations showed that the microneedle electrodes can increase the distinguishability of stimulation. Performing stimulation through microneedle electrodes will provide a relatively robust current density at different depths of the tissue, compared to conventional surface electrodes. It was shown that increasing the number of microneedles on the electrodes, increases the distinguishability of stimulation. However, because of localizing the electrical field, microneedle electrodes showed reduced current density. Furthermore, this study indicates that if the purpose of the TENS is increasing the blood flow velocity, surface electrodes would be superior to microneedle electrodes.

## References

ABDALLA, S., AL-AMEER, S. & AL-MAGAISHI, S. 2010. Electrical properties with relaxation through human blood. Biomicrofluidics, 4, 034101.

BRISTOW, S., HASAN, S. & NEAL, D. 1996. TENS: a treatment option for bladder dysfunction. International Urogynecology Journal, 7, 185-190.

CHWIEŚKO-MINAROWSKA, S., MINAROWSKI, Ł., SZEWCZAK, W. A., CHYCZEWSKA, E. & KURYLISZYN-MOSKAL, A. 2016. Efficacy of daytime transcutaneous electrical stimulation of the genioglossus muscle in patients with obstructive sleep apnea syndrome. European Archives of Oto-Rhino-Laryngology, 273, 3891-3895.

COMMISSION, I. E. 2010. International standard, medical equipment—IEC 60601-2-33: particular requirements for the safety of magnetic resonance equipment for medical diagnosis. Geneva, Switzerland: International Electrotechnical Commission.

COMSOL, A. 2011. AC/DC Module–User's Guide. COMSOL, 3, 151.

ELDER, C. W. & YOO, P. B. 2018. A finite element modeling study of peripheral nerve recruitment by percutaneous tibial nerve stimulation in the human lower leg. Medical engineering & physics, 53, 32-38.

FALL, M. 2018. Use of Transcutaneous Electrical Nerve Stimulation in the Management of Bladder Pain Syndrome. Bladder Pain Syndrome–An Evolution. Springer.

GABBIANI, F. & COX, S. J. 2017. Mathematics for neuroscientists, Academic Press.

GAGGERO, P. O. 2011. Miniaturization and distinguishability limits of electrical impedence tomography for biomedical application. Université de Neuchâtel.

GORE, S., MAZUMDER, B. & BIT, A. 2018. Effects of Inclination of Micro-capillary on Blood-Viscosity of Diseased Blood in Presence of Metallic Ball. BioNanoScience, 1-16.

GOW, A. & DEVAUX, J. 2008. A model of tight junction function in central nervous system myelinated axons. Neuron glia biology, 4, 307-317.

GRAHAM, B. & ADLER, A. 2006. Objective selection of hyperparameter for EIT. Physiological measurement, 27, S65.

GRILL, W. M. 1999. Modeling the effects of electric fields on nerve fibers: influence of tissue electrical properties. IEEE Transactions on Biomedical Engineering, 46, 918-928.

IVANOV, K., KALININA, M. & LEVKOVICH, Y. I. 1981. Blood flow velocity in capillaries of brain and muscles and its physiological significance. Microvascular research, 22, 143-155.

JOHNSON, D. H. 2006. Signal-to-noise ratio. Scholarpedia, 1, 2088.

JOHNSON, M. I. & BJORDAL, J. M. 2011. Transcutaneous electrical nerve stimulation for the management of painful conditions: focus on neuropathic pain. Expert review of neurotherapeutics, 11, 735-753.

KIMINAMI, K., IYAMA, T., ONISHI, T. & UEBAYASHI, S. 2008. Novel specific absorption rate (SAR) estimation method based on 2-D scanned electric fields. IEEE Transactions on Electromagnetic Compatibility, 50, 828-836.

MCGEE, M. J., AMUNDSEN, C. L. & GRILL, W. M. 2015. Electrical stimulation for the treatment of lower urinary tract dysfunction after spinal cord injury. The journal of spinal cord medicine, 38, 135-146.

MOORE, K. L., DALLEY, A. F. & AGUR, A. M. 2013. Clinically oriented anatomy, Lippincott Williams & Wilkins.

NITTI, V. W., DMOCHOWSKI, R., HERSCHORN, S., SAND, P., THOMPSON, C., NARDO, C., YAN, X., HAAG-MOLKENTELLER, C., ANDREOU, C. & EGERDIE, R. 2017. OnabotulinumtoxinA for the treatment of patients with overactive bladder and urinary incontinence: results of a phase 3, randomized, placebo controlled trial. The Journal of urology, 197, S216-S223.

PANESCU, D., WHAYNE, J. G., FLEISCHMAN, S. D., MIROTZNIK, M. S., SWANSON, D. K. & WEBSTER, J. G. 1995. Three-dimensional finite element analysis of current density and temperature distributions during radio-frequency ablation. IEEE Transactions on Biomedical Engineering, 42, 879-890.

PENNES, H. H. 1948. Analysis of tissue and arterial blood temperatures in the resting human forearm. Journal of applied physiology, 1, 93-122.

PENNES, H. H. 1998. Analysis of tissue and arterial blood temperatures in the resting human forearm. Journal of applied physiology, 85, 5-34.

PETERS, K. M. 2018. Use of Transcutaneous Electrical Nerve Stimulation in the Management of Bladder Pain Syndrome: 2017 Update. Bladder Pain Syndrome–An Evolution. Springer.

PETROFSKY, J., BAINS, G., PROWSE, M., GUNDA, S., BERK, L., RAJU, C., ETHIRAJU, G., VANARASA, D. & MADANI, P. 2009. Does skin moisture influence the blood flow response to local heat? A re-evaluation of the Pennes model. Journal of medical engineering & technology, 33, 532-537.

PETROFSKY, J., PALUSO, D., ANDERSON, D., SWAN, K., YIM, J. E., MURUGESAN, V., CHINDAM, T., GORAKSH, N., ALSHAMMARI, F. & LEE, H. 2011. The contribution of skin blood flow in warming the skin after the application of local heat; the duality of the Pennes heat equation. Medical engineering & physics, 33, 325-329.

RALL, W. 2011. Core conductor theory and cable properties of neurons. Comprehensive physiology, 39-97.

RECIO, A. C. & SCHNEIDER, A. C. 2011. Electrical Stimulation. Pain Procedures in Clinical Practice (Third Edition). Elsevier.

SLUKA, K. A. & WALSH, D. 2003. Transcutaneous electrical nerve stimulation: basic science mechanisms and clinical effectiveness. The Journal of pain, 4, 109-121.

SOLTANZADEH, R., AFSHARIPOUR, E., SHAFAI, C., ANSSARI, N., MANSOURI, B. & MOUSSAVI, Z. 2018. Molybdenum coated SU-8 microneedle electrodes for transcutaneous electrical nerve stimulation. Biomedical microdevices, 20, 1.

VANCE, C. G., RAKEL, B. A., DAILEY, D. L. & SLUKA, K. A. 2015. Skin impedance is not a factor in transcutaneous electrical nerve stimulation effectiveness. Journal of pain research, 8, 571.

WARMAN, E. N., GRILL, W. M. & DURAND, D. 1992. Modeling the effects of electric fields on nerve fibers: determination of excitation thresholds. IEEE Transactions on Biomedical Engineering, 39, 1244-1254.

# 4

# Analysis of the Effects of Different Models and Microneedle Array Designs on the Parameters of the Transcutaneous Nerve Stimulation

## Summary

This chapter is about investigations on microneedle array electrodes for transcutaneous electrical nerve stimulation, and comparing their performance with conventional surface electrodes. A 3D model of tissue was developed for finite element multiphysics simulations. Investigations included current density in different depths of a tissue, space constant under electrodes, specific absorption ratio of tissue, distinguishability of stimulation, temperature rise and blood flow. Results showed that microneedle electrodes have up to 10% higher distinguishability than the surface electrodes. Furthermore, it was found that stimulation using microneedle electrodes provides more robust current density at different tissue depths compared to the surface electrode stimulation. Microneedle electrodes showed enhanced stimulation parameters, particularly for targeting a specific nerve in a specific depth of a tissue.

## 4.1. Introduction

The effect of microneedle arrays (MNAs) on different parameters of transcutaneous electrical nerve stimulation (TENS) was investigated the simulation scenarios of chapter 3. It was shown that the MNAs can increase the distinguishability of between a target nerve and an adjacent nerve while the two nerve fibers are besides each other. Also, based on the simulation results, it was proved that the space constant of the MNAs is independent of the depth of penetration and the existence or absence of a blood capillaries between them. All these advantages of the MNAs happen while the specific absorption ratio (SAR) of the MNAs in different parts of a model remains lower than for surface electrodes. While the parameters for the MNA designs were shown to be superior, possible causes of the performance improvement was not investigated. Furthermore, it was not investigated what parameter(s) are important to make an MNA more efficient in nerve stimulation. In this chapter, the physical reasons that may relate to the better performance of the MNAs is investigated, by exploring different models and designs. These investigations also reveal what MNA design features provide best performance for transcutaneous nerve stimulation.

The only change that is applied on the model of chapter 3 is to include the effect of the stratum corneum (SC) on the performance of the stimulation electrodes. The design features that are explored for the MNAs consist of changing the shape (pyramid and cone), pitch (distance between the microneedle spikes tip-to-tip) and the base area of each microneedle. It is proved that the pitch of the microneedle spikes plays a very critical role in the stimulation distinguishability for the case of two adjacent nerve fibers. However, it does not mean that changing the number of the microneedle spikes has no effect of the distinguishability. Another finding showed that the shape of the microneedle spikes does not any significant effect on the distinguishability and the SAR.

## 4.2. The Effect of SC Removal on the Results of Electrical Simulation

In the study of chapter 3, the surface electrodes were placed on the exterior of the skin, while the MNA pierced the SC layer. In this section it is investigated whether placing the surface electrodes below the SC layer would give similar improvement to the MNA case. The simulation was re-done but now with the condition that the surface electrodes are place underneath the SC layer. It should be mentioned that in practice, usually the SC can be partially removed by scrubbing the skin with an alcohol pad. However, this method cannot remove the SC consistently on the entire of the surface.

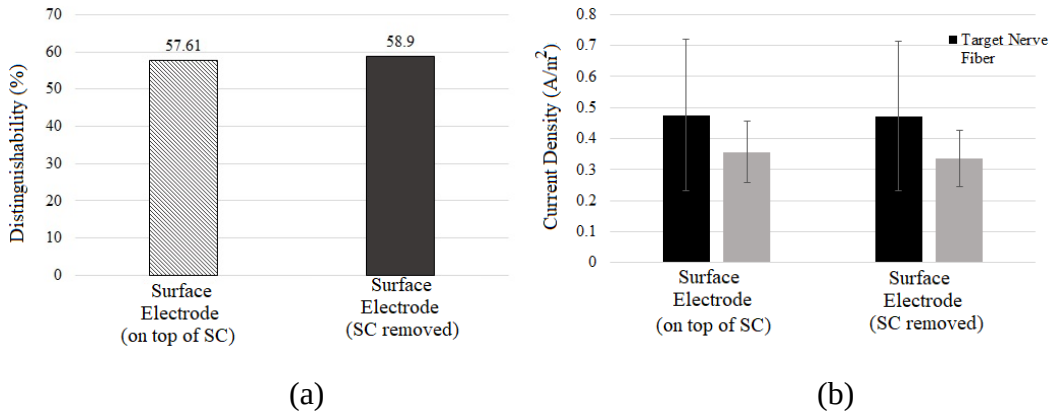


(a) (b)

**Fig. 4.1.** (a) Distinguishability in two scenarios of with and without SC. (b) Mean and standard deviation (error bar) of current density along target and adjacent nerve fibers.

Fig. 4.1 shows the effects of bypassing the SC on the current density and the distinguishability (calculated based on Eq. 8 in Chapter 3) of the surface electrodes with and without SC. Fig. 4.1b shows that the current density does not change significantly along the nerve fibers by removing the SC. However, in Fig. 4.1a one observes that the distinguishability is improved. The reason is that by removing a layer with relatively high relative electric permittivity, the capacitance of the tissue will decrease. Therefore, the amount of current that is delivered to the

tissues in different depths will decrease slightly. By reducing the capacitance, the current leakage to the area around the electrode will decrease and target nerve will grab more amount of current than the adjacent nerve. Therefore, the distinguishability will increase slightly.

## 4.3. The Effect of Microneedles Base and Tip Area on the Result of Electrical Simulation

Increasing the base size of the MNAs was another parameter that was investigated. The base of the microneedles was increased from 0.45×0.45 mm to 0.5×0.5 mm in the 50 microneedle electrode patch. Although the base area of the needles was increased, the needle length and wall angle (26°) was kept constant. Therefore, the area of the final tip then increases up to almost two times. It should be mentioned that by increasing the width of the tips, the penetration depth will decrease in practice. However, in the developed model, it was assumed that the depth of penetration is not affected and only two-third of the needle's length will pierce the skin. Fig. 4.3 shows the electric field inside the tissue when it was stimulated with MNAs with 0.45×0.45 mm and 0.5×0.5 mm based microneedles.

In Fig 4.3, it can be seen that the electric field of the MNAs with the large tip area (110×110 µm where the base area is 500×500 µm) is slightly less than the one with small tip area (60×60 µm where the base area is 450×450 µm). This is to be expected.

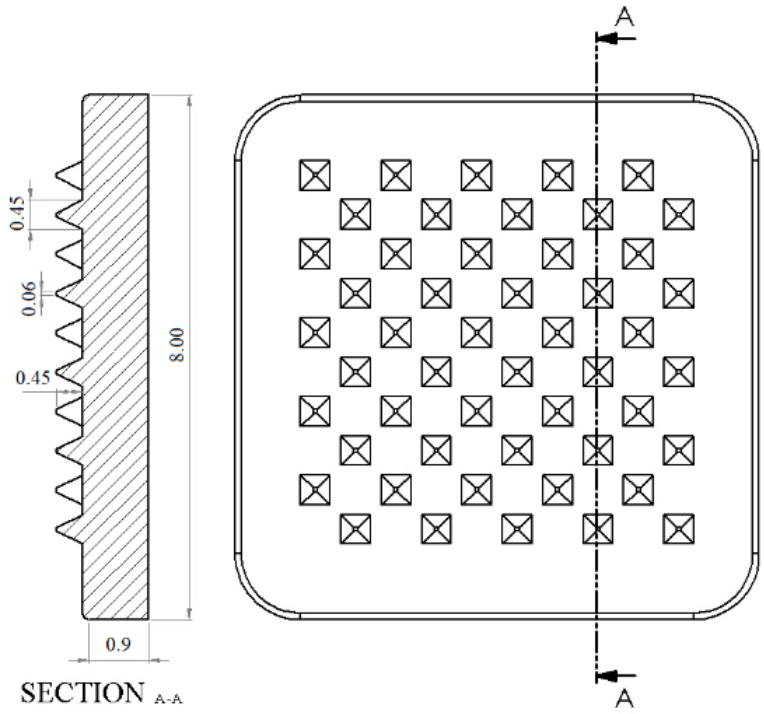


(a)

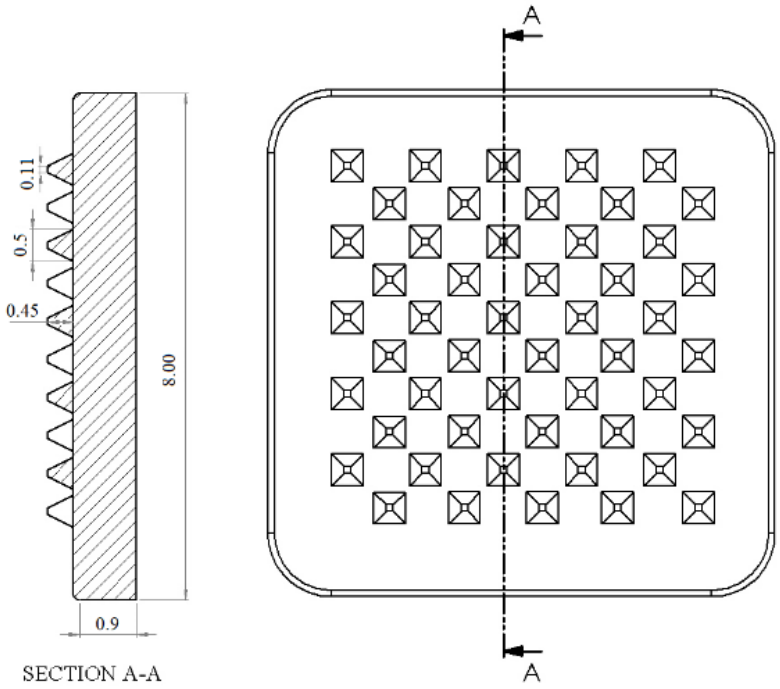


(b)

**Fig. 4.2.** MNA with the base needle of (a) 450 µm and 60×60 µm tip (b) 500 µm and 110×110 µm tip (Note: all dimensions are in mm)

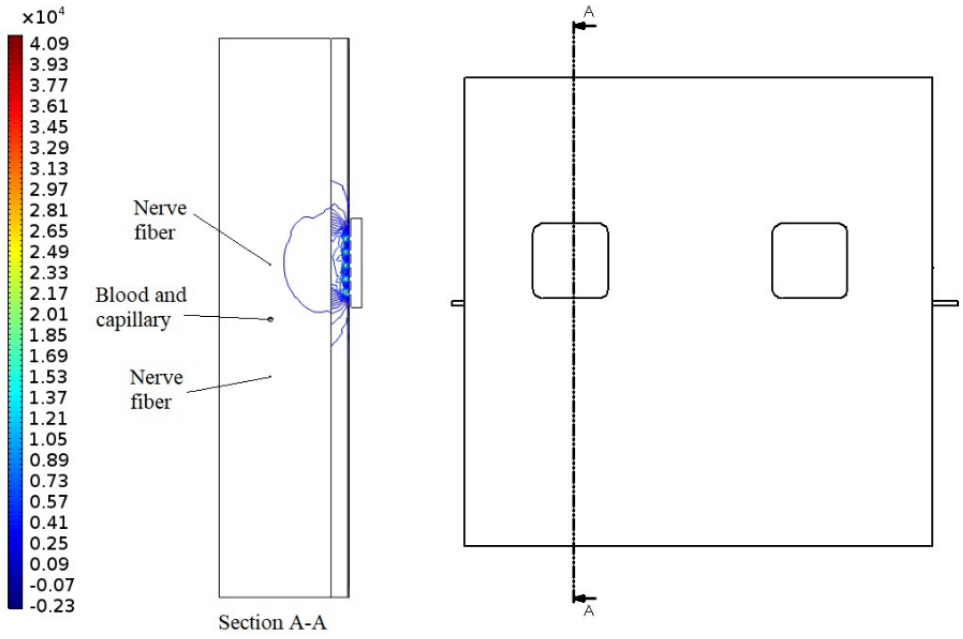


(a)

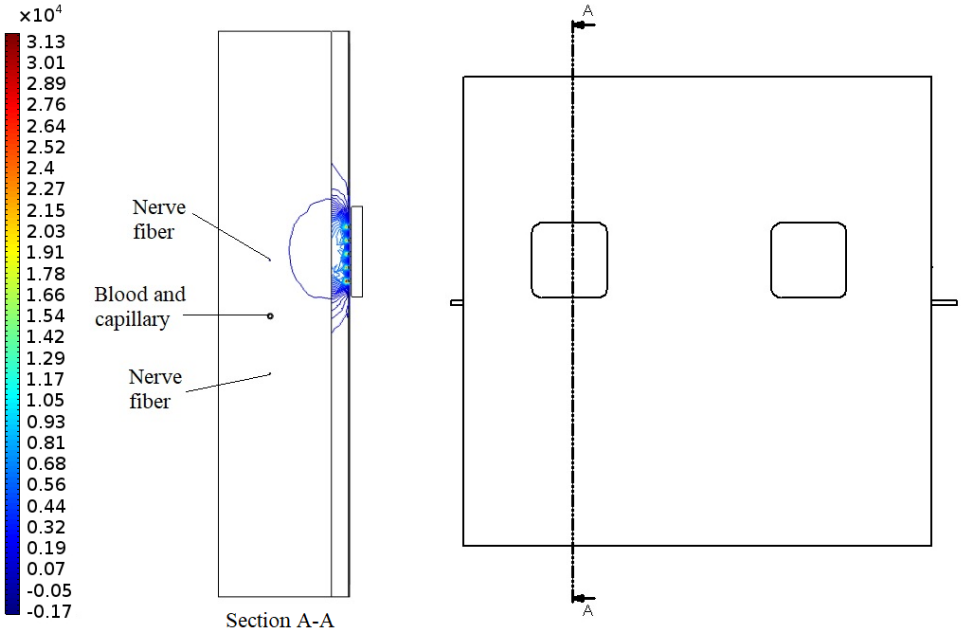


(b)

**Fig. 4.3.** A comparison between the averages of electric field over stimulation time in (a) MNA with 50 microneedle with 450×450 µm microneedle bases (b) MNA with 50 microneedles with 500×500 µm microneedle bases.

In Fig. 4.4, it can be seen that neither distinguishability nor the current density change significantly by changing the base and tip areas. It is worthwhile to mention that the horizontal tip-to-tip pitch of the needles is 1.2 mm, the distance between each row is 0.6 mm and the diagonal tip-to-tip pitch is 0.8 mm.

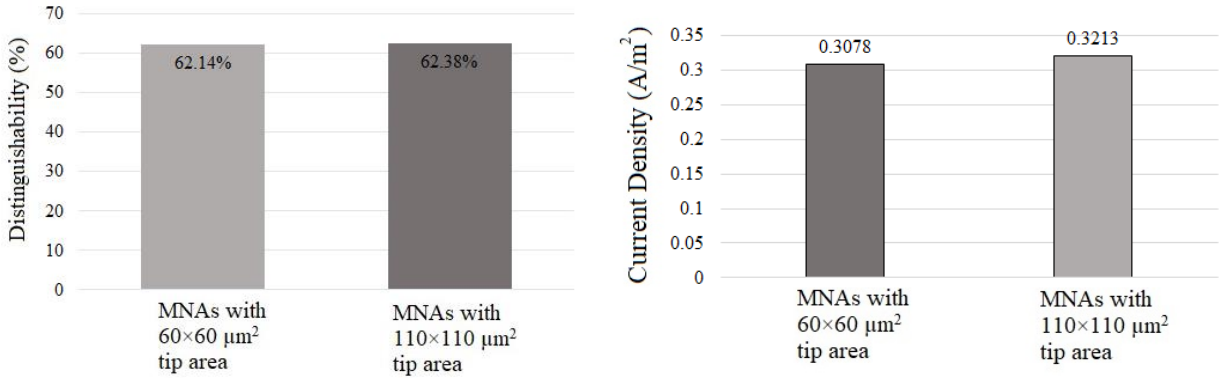


(a) (b)

**Fig. 4.4.** (a) Distinguishability (b) current density of two different MNAs

## 4.4. The Effect of Microneedles Shapes, Pitches and Numbers on the Result of Electrical Simulation

In this section the shape of the MNAs, their numbers, and the distance between them on an 8×8 mm surface is investigated. In all the simulations, pyramidal and conical shapes of the needles are studied. Fig. 4.5, shows a schematic of conical MNA that contains 100 conical microneedles.

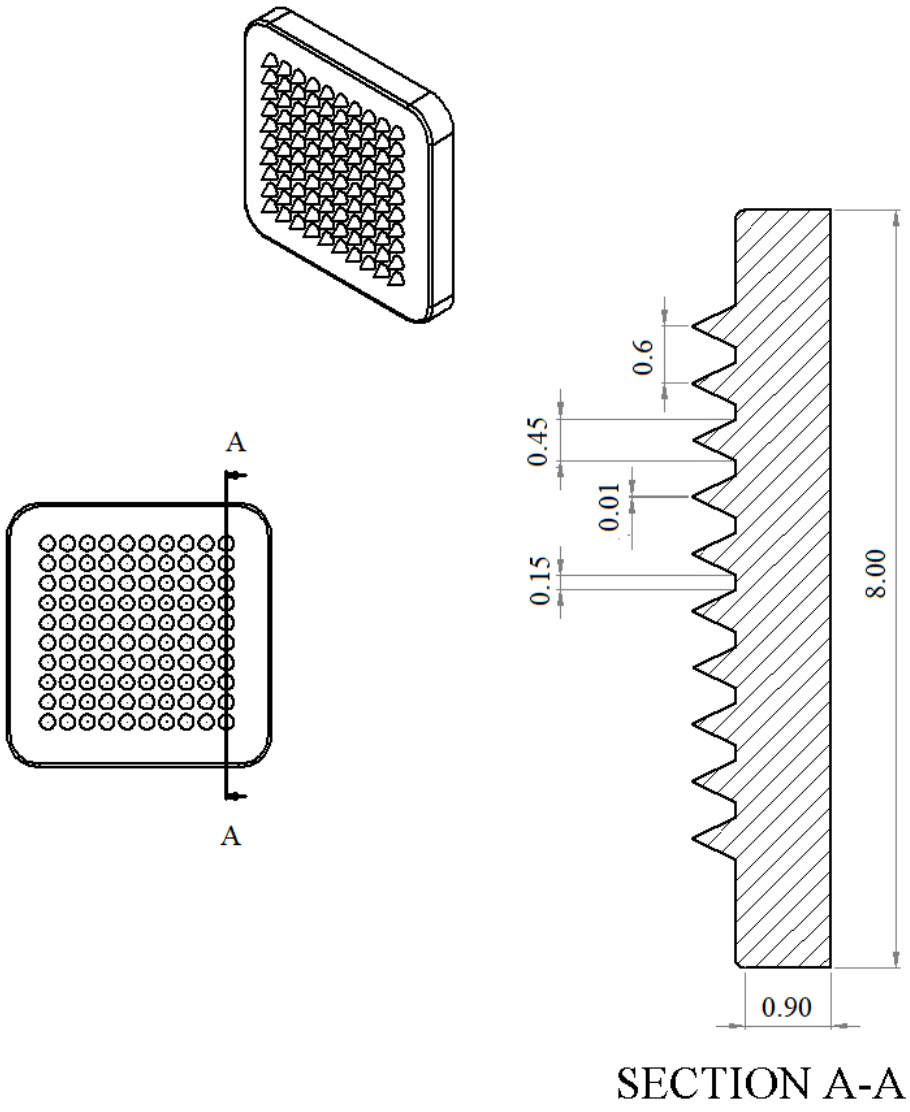


**Fig. 4.5.** Simulated conical MNA (all dimensions are in mm)

Table 4.1 presents different simulations scenarios. In each scenario, only one parameter was changed and its effect on the distinguishability and the maximum SAR along the nerve is shown. It can be seen that the tip-to-tip pitch of the microneedles on the surface of an MNA plays an important role in the distinguishability. Decreasing the pitch to a certain level will increase the distinguishability. However, placing the microneedles too close to each other will decrease the

distinguishability. In the other words, decreasing the tip-to-tip pitch of the needles will result in a large number of needles on a specific area, and this eventually corresponds to the case of a surface electrode that has infinite spatial resolution. For example, these effects can be seen for the case of the conical MNAs, with the distinguishability increasing when reducing the pitch from 0.7 to 0.6, and the distinguishability decreasing when reducing the pitch from 0.6 to 0.5. According to the percentage of the area the MNs occupied on a patch, it can be understood that there might be a spatial cut-off pitch for the best distinguishability in each application that can be studies based on the type of application and the depth of the target nerve.

**Table 4.1.** A comparison between the distinguishability and average current density of different simulation scenarios

| Needle Shape | Tip-to-Tip Pitch (mm) | Distinguishability (%) | Average of current density on the target nerve ($A/m^2$) | Number of needles | Length (mm) | Tip size (µm) | MN area |
|---|---|---|---|---|---|---|---|
| Cone 0.45 mm diameter | 0.7 | 59.73 | 0.3357 | 100 | 0.45 | 69.36 | 0.829268293 |
| | 0.6 | 63.73 | 0.2958 | 100 | 0.45 | 69.36 | 0.62249727 |
| | 0.5 | 63.14 | 0.2794 | 100 | 0.45 | 69.36 | 0.527120495 |
| Pyramid 0.45×0.45 mm | **0.62** | **64.96** | **0.2518** | **100** | **0.45** | **60×60** | 0.655260284 |
| | 1.2 | 62.13 | 0.3211 | 50 | 0.45 | 60×60 | 0.633600291 |
| Pyramid 0.3×0.3 mm | 0.7 | 60.96 | 0.3033 | 100 | 0.3 | ~10×10 | 0.792864944 |
| | 0.6 | 63.61 | 0.2718 | 100 | 0.3 | ~10×10 | 0.622861303 |
| | 0.5 | 65.18 | 0.2220 | 100 | 0.3 | ~10×10 | 0.419366582 |
| | **0.4** | **65.49** | **0.1681** | **100** | **0.3** | **~10×10** | 0.27684747 |
| | 0.4 | 64.71 | 0.2181 | 144 | 0.3 | ~10×10 | 0.402074991 |
| | 0.4 | 61.4 | 0.2939 | 256 | 0.3 | ~10×10 | 0.722424463 |
| Surface | NA | 57.61 | 0.4757 | 0 | NA | NA | 1 |

From Table 4.1, one may conclude that the MNA with a 100 microneedles has the highest distinguishability compare to the others. However, the pitch for these MNAs was almost 0.60 mm in the pyramidal MNAs.

Since an MNA substrate has a confined area, it is hard to keep the pitch constant and increase the microneedles quantity more than a certain number. Therefore, increasing the number of needles more than specific number results in a corresponding lowering of the tip-to-tip pitch. In order to investigate the effect of the microneedles number on the distinguishability, a small model of the microneedles with 0.3×0.3 mm base size was studied too. The length of these needles was lower that the ones with 0.45×0.45 mm because their wall angle was kept constant while the base size was increased. The tip-to-tip pitch of the microneedles in an MNA was 0.4 mm and the number of the microneedles were changed in different simulation scenarios. The results support the reason that was discussed about the MNAs with larger base and showed that increasing the number of needles up to certain amount, like decreasing the tip-to-tip pitch of the needles down to specific distance, will increasing the distinguishability. However, beyond that threshold, the distinguishability of the MNAs will decrease. Furthermore, fabricating the MNAs with small base area was not easy. Therefore, these scenarios were not studied experimentally.

In a comparing conical and pyramidal microneedles, it can be seen that the pyramidal MNAs can be more effective when all the other parameters in an MNA are identical. The reason is that the electric field at the tip of pyramidal needles is greater than for the conical ones. This is discussed further in section 4.5. Regardless of the shape, pitch, and the number of microneedles in an MNA, it can be seen that the distinguishability in the MNAs is better than the surface electrodes. Although the average of current density in the surface electrodes is higher than for the MNAs, the

reduced distinguishability results in almost same current density present on the adjacent and target nerves.

## 4.5. Discussion and Conclusion

This chapter showed that the pitch of the microneedles on the surface of an MNA plays a critical role on the distinguishability and effectiveness of an MNA. In order to find the reason, the electric field below emanating from the electrodes was investigated.

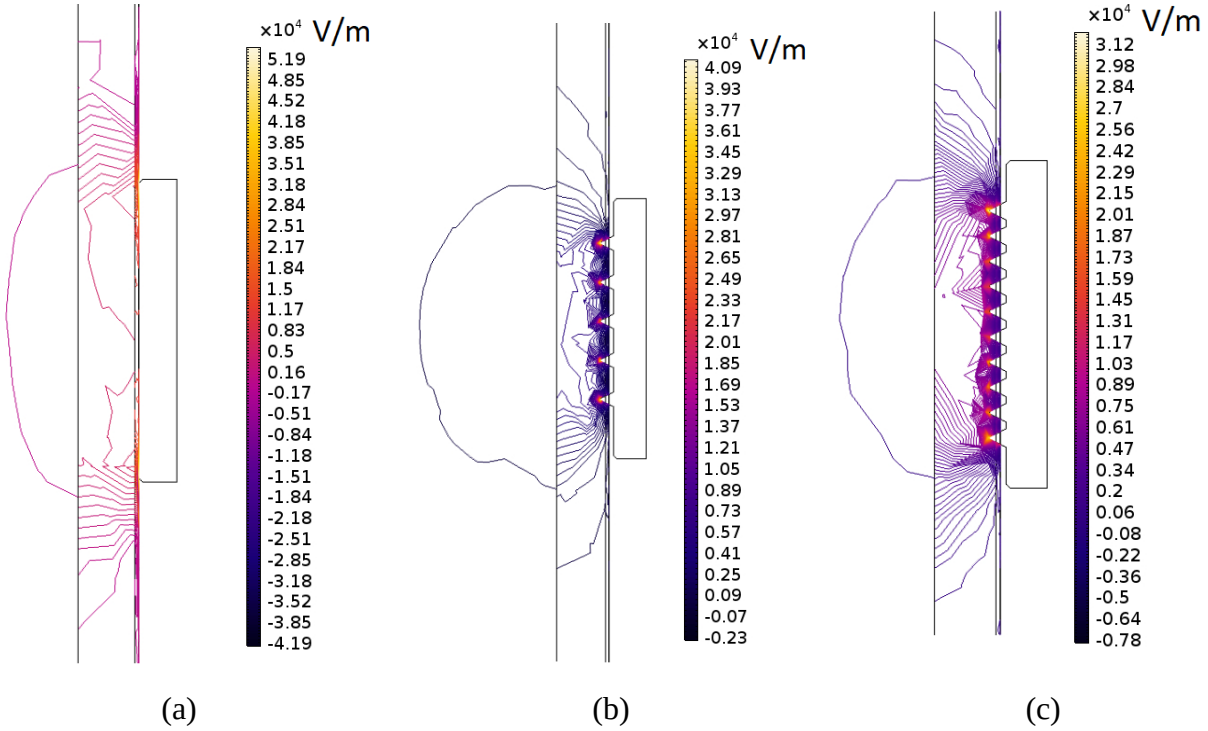


(a) (b) (c)

**Fig. 4.6.** Z-axis Electric field in the interface of the electrode and two first layers of skin in (a) surface electrode (b) 50 microneedle electrode (c) 100 microneedle electrode.

The z-axis component of the electric field ($E_z$) underneath of a surface electrode, a 50-microneedle MNA and a 100-microneedle MNA are shown in Fig. 4.6. In all cases, it can be seen that the electric field on the edges of the electrode is more than the central areas. However, one can see that the density of the electric field at the tip of the microneedles is considerably higher

than the surface electrode. Between the microneedles in the middle an electrode, it can be understood that the strength of the electric field is higher for MNA cases, and higher from 100 vs. 50 MNA case. This can be a reason for the distinguishability improvement. Though, increasing the tip-to-tip pitch will bring more skin between the needles and causes more contact surface which leads to high current density in different depths. Reducing the number of needle spikes, while the pitch is kept constant, due to reduction of contact surface and penetration, will reduce both the current density and distinguishability. However, increasing the number of microneedles too high will result in a behaviour that is similar to that of a surface electrode. Loosely speaking, a roughly opposite relationship between distinguishability and current density (average of all frequencies) can be seen in all the simulation scenarios. Also, results showed that the best distinguishability can be achieved when the tip-to-tip pitch is around 0.62 mm and the number of microneedles on the surface is around 100 for an 8×8 mm MNA pyramidal MNA.

The length of the needles is the other parameter that affects the stimulation parameters, particularly distinguishably. The MNAs with 450 µm and 300 µm length were analyzed in this study. The MNA with microneedles longer than 450 µm may hit the percutaneous pain nerves during insertion (depending on the skin thickness). However, needles less than 300 µm may not be able to bypass the stratum corneum layer. Besides the piercing concerns, fabrication difficulties are the concerns that one may encounter in building the MNAs. Since the MNAs are the high aspect ratio structures, their microfabrication processes are not easy to implement. More details about fabrication difficulties are reviewed in chapters 5 and 6.

Overall, if one wants to adapt the simulation parameters of this chapter with tissue-electrode-interface circuit, it can be seen that long microneedle spike will decrease the resistance (R) and capacitance (C) between the electrode and tissue. In oppose to long microneedle spikes, the short

ones will increase both C and R while C will increase more than R by shortening the microneedles height. Also, the size of the area where microneedles are distributed on is very crucial; larger microneedle area will increase C and R but C elevation is more than R.

From results of Table 4.1, one may conclude that the best implementable structure can be MNAs with ~0.45 mm and ~0.6 mm tip-to-tip pitch and with 100 microneedles. An MNA with the suggested structure was built and its performance is compared experimentally with the surface electrodes in chapter 7.

# 5

# A Review on Microfabrication of Different Types of Microneedles


## Summary

This chapter is a review on various fabrication and replication methods of different types of microneedles and their applications. The microneedles are classified into single and array types, and different structural material and fabrication methods of each group were reviewed. Since the fabrication method may depend on the application, the application and test procedure are discussed in separate sections. From this review, one may understand that the easiest way to build a microneedle array is by using polymers like SU-8, which is a negative tone photoresist.

## 5.1. Introduction

Microneedles (MNs) are in the frontline of many different versatile fields in biomedical engineering. The application of MNs was investigated in epidermis drug delivery, bio-signal recording and electrical stimulation of excitable nerves. As the technology advanced, the base materials of MNs changed. The early MNs were fabricated by heating and stretching glass pipes (Chaen et al., 1989). Most of the studies between 1980 and 1990 explored single MN fabrication. Single MNs are usually used for recording from a specific nerve, cell, or sarcomere of a muscle (Reitboeck, 1983, Jahnke, 1982). Therefore, it is worthwhile to consider single MN fabrication methods as a topic in the review of MN fabrication. In the first decade of 2000, most of studies explored MN fabrication based on micro-electromechanical systems (MEMS) techniques (Henry et al., 1998, Zahn et al., 2000, Stoeber and Liepmann, 2000, Shikida et al., 2004, Griss et al., 2002). By combining bulk and surface processing, Lin et al. fabricated a type of hollow MN that can be considered as the first attempt to use MNs for drug delivery (Lin and Pisano, 1999b, Lin and Pisano, 1999a). Afterwards, many other research groups researched fabrication methods of different designs of MNs for different applications (Eriksson, 1997, Smart and Subramanian, 2000, Brazzle et al., 2000). It was almost in the same decade that polymers started being used in MEMS labs as structural materials. Since working with polymers is easier than silicon, these materials replaced silicon in different microfabrication studies.

SU-8 is a negative photoresist polymer that is used in the MEMS industry to fabricate different structures (Lorenz et al., 1997). Because of its high mechanical strength and simple lithography methods, SU-8 was used in many different high aspect ratio (HAR) microfabrication studies including MN fabrication (Shirtcliffe et al., 2004, Park et al., 2004). Furthermore, polymer MNs can be fabricated from degradable materials like polylactic acid, polyglycolic acid, and their

co-polymers (Park et al., 2005, Sullivan et al., 2008). Biocompatibility and biodegradability opened new areas in the field of drug delivery through MNs. Also, polymers were used as the sacrificial layers or the material of the micro-molds in many studies (Becker and Heim, 2000, Soltanzadeh et al., 2018). Polymers like polydimethylsiloxane (PDMS) and polymethyl methacrylate (PMMA) are common materials in micromolding of HAR structures. (Kuo and Chou, 2004, Bystrova and Luttge, 2011, Moon et al., 2005). Therefore, polymeric MNs are a major study in the MN area.

In this review, various fabrication and replication methods of different types of MNs and their applications are discussed. Moreover, in different articles, various experiments were introduced to test MNs. Fig. 5.1 shows briefly how this review is organized. As it is illustrated, single MN and MN array electrodes are known as different classes of MNs. Based on these two categories, the fabrication, application, and assessment experiment methods of single and arrays of MNs are discussed separately. The time trend of the fabrication studies showed that most of the studies were concentrating on MN arrays, and single MNs were studied only in a few recent investigations (Lee et al., 2018).

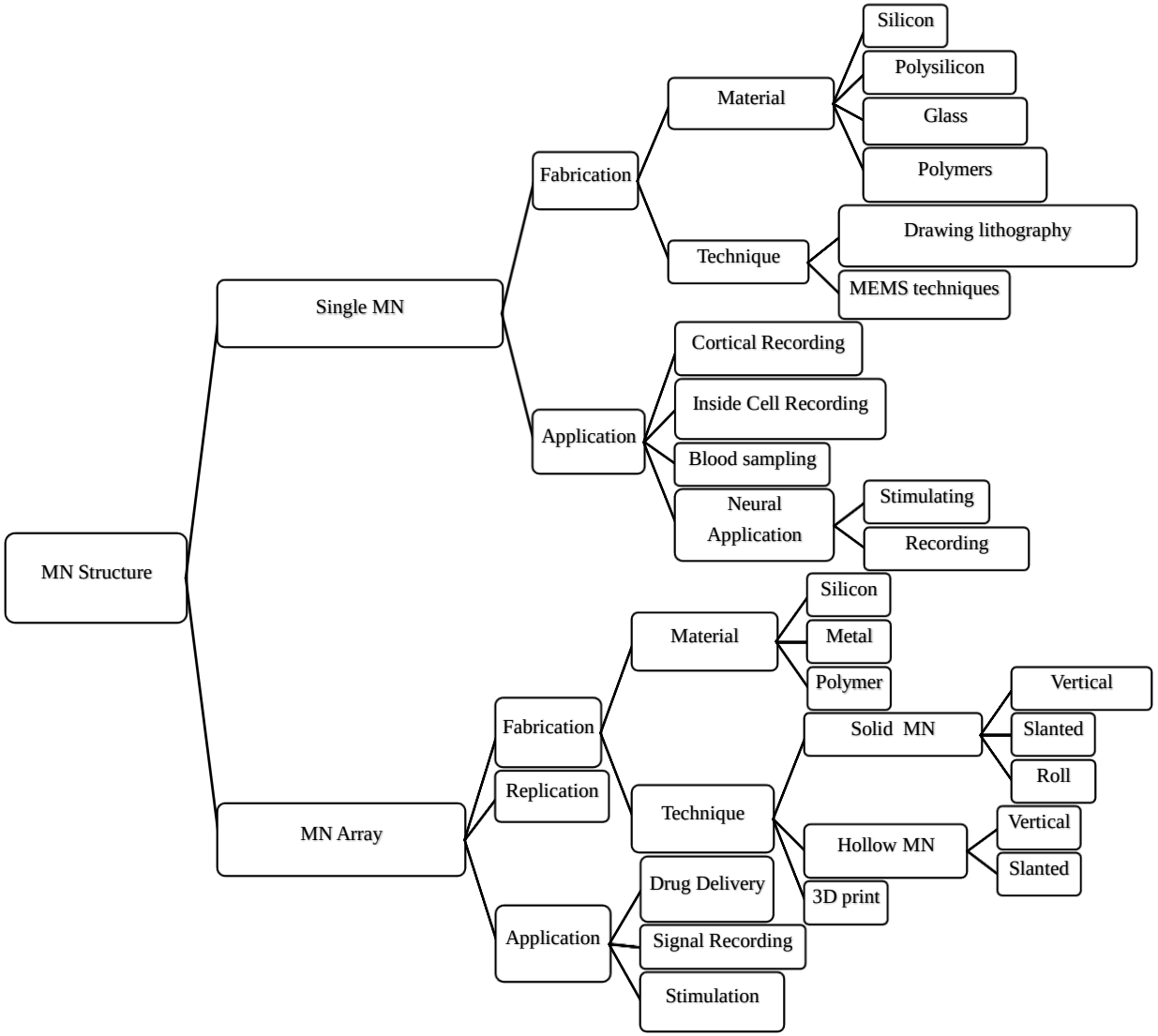


**Fig. 5.1.** Different categories of the application, fabrication and the experiments on the MNs

## 5.2. Single Microneedle

Single MNs are the popular type of the electrodes for recording inside cellular membrane. In some studies, they were used for drug delivery purposes. In terms of fabrication, different materials have been used as the base material for single MNs. In this section, different fabrication techniques and applications of single MN fabrication are reviewed. Depending on the type of application, different evaluation experiments are described.

### 5.2.1. Single Microneedle Fabrication Techniques

#### 5.2.1.1. Glass Single Microneedle Fabrication

Pulling glass rods, with a precise mechanical puller, is the common way to fabricate the solid single MNs (Römgens et al., 2014, Martanto et al., 2006, Brown and Flaming, 1974). To build hollow single MN, glass pipettes are narrowed by a precisely controlled puller while its middle is heated by either an electrical heater or a laser beam (Wang et al., 2006, Mahadevan, 2011, Chowdhury, 1969). One of the pipette puller devices is P-97 from the Sutter Instrument ® company (shown in Fig. 5.2.a) (Osterele, 2011). In the glass pulling techniques, the diameter of the MN is varied based on the location that the MN is cut and the initial diameter of the micropipettes. Fig.5.2.b and Fig. 5.3 shows MN tips with different diameters that have been cut at different locations of a puller micropipette.

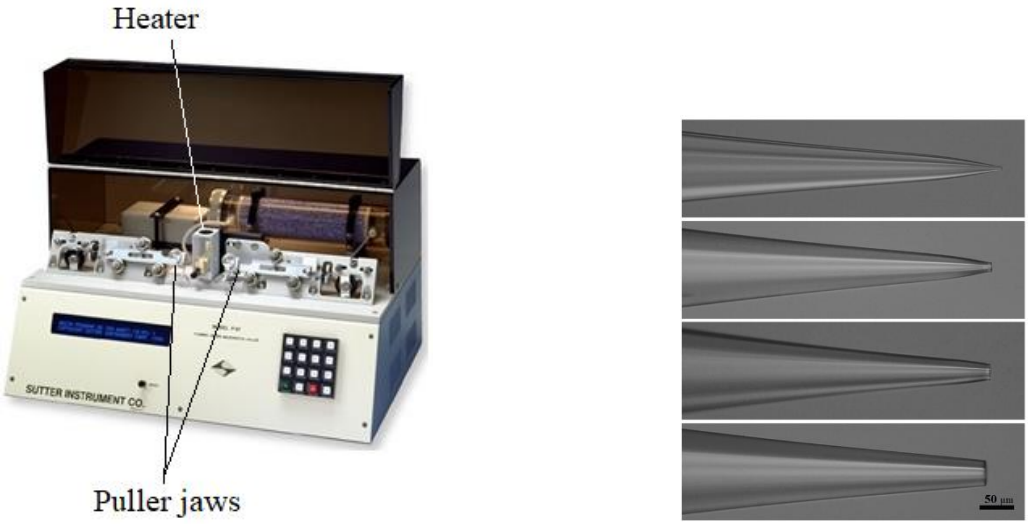


(a) (b)

**Fig. 5.2.** (a) P-97 (Suttern Instruments®) Micropipette puller (Osterele, 2011) [Used with permission] (b) Glass MN with different tip diameters (Römgens et al., 2014) [Used with permission]

In the applications were the MNs were needed to be conductive, a fine wire string was passed through the inner area of the formed micropipette (Levick, 1972). However, this technique takes up the area inside the fabricated micropipette and is not efficient particularly when the microinfusion is happening simultaneously.

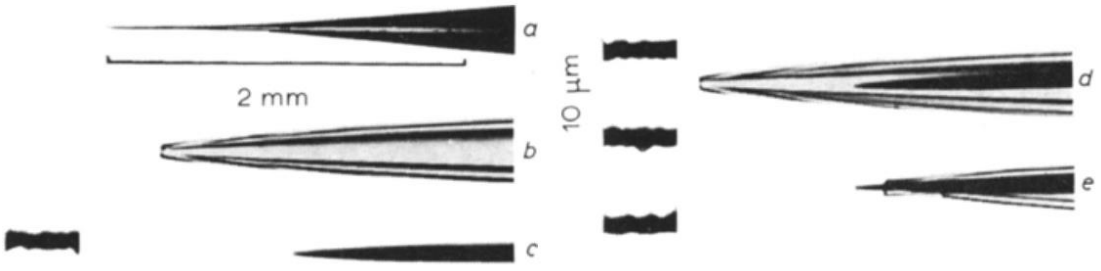


**Fig. 5.3.** (a,e,d) Glass MN with tungsten wire in it (b) tapered glass MN (c) tungsten micro-wire (Levick, 1972) [Used with permission]

The use of microfabrication techniques simplified the fabrication of MNs and the ability to coat them with different metals. Therefore, with advancing micro-electromechanical systems (MEMS) fabrication methods, many studies started to investigate single MN fabrication from silicon and the other common MEMS materials.

### 5.2.2.2. Silicon Single Microneedle Fabrication

Loosely speaking, MEMS methods involve combinations of bulk and surface processes that fabricate a specific geometry from silicon and its derivatives (Lin and Pisano, 1999b, Held et al., 2010). The advantage of fabricating MNs from silicon is that a proper substrate is already provided to fabricate other needle's accessories. For example, in (Lin and Pisano, 1999b), as shown in Fig. 5.4, several micropumps were built together with the needle itself, in order to control the rate of fluid injection through the fabricated MN.

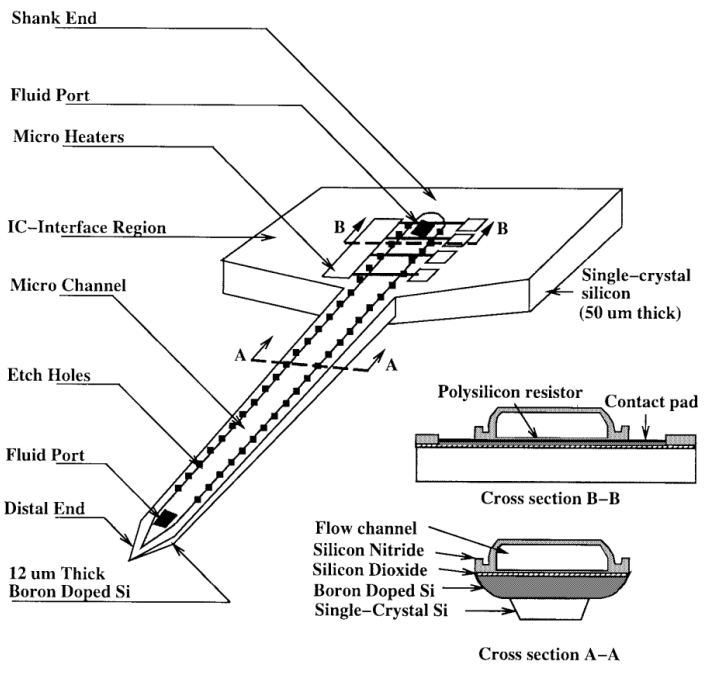


**Fig. 5.4.** The schematic of the fabricated silicon process MN (Lio et al, Silicon-processed- MNs, Journal of Microelectromechanical Systems) IEEE copyright line © 2011 IEEE

Single MNs were used for measurements inside cells or cortical brain measurements. As another example, in (Sawahata et al., 2016), a single fine silicon wire electrode with a 3 µm diameter tip and 160 µm length was fabricated and used to record the in-vivo brain activity of rodents. The researchers used vapor-liquid-solid (VLS) method in this study to grow a single silicon MN on top of a frame on top of a printed circuit board (PCB). In this study, gold (Au) was used as the metal catalyst in the VLS technique (Wagner and Ellis, 1964, Trentler et al., 1995, Wu and Yang, 2001). Fig. 5.5 shows the single MN grown on locations of the silicon substrate where the Au and the silicon dioxide ($SiO_2$) were etched. In order to increase the mechanical strength of the needle, a layer of titanium (Ti) with a thickness of 50 nm was sputtered on the grown needle. Also, to enable a biocompatible electrode, platinum (Römgens et al.) was sputtered on top of the Ti with a thickness of 150 nm. Afterwards, all the needle's body was insulated with parylene-C (Sawahata et al., 2016). In the last step, the area between the MNs was diced by laser and each MN (or more than one of them depending on the application) was used separately.

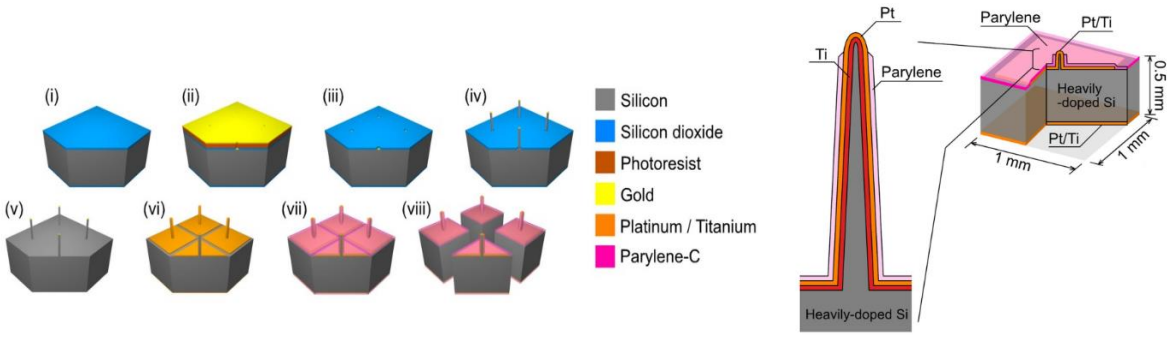


(a) (b)

**Fig. 5.5.** (a) Fabrication procedure of the single MN with VLS technique (b) The schematic of the finished MN (Sawahata et al., 2016).

The above described methods are for hollow and solid MNs respectively. There are other MEMS techniques, like deep reactive ion etching (DRIE), that were employed to build the MNs. However, those techniques are expensive and were commonly used to fabricate MN arrays. These are discussed in section 5.3.1.

#### 5.2.2.3. Polymer Single Microneedle Fabrication

Polymers are categorized into three different classes: 1) fibers, 2) plastics, and 3) elastomers (Liu, 2007). Polymers have been substituted for silicon in many investigations since the 1990s (Liu, 2007). Although silicon has a higher Young's modulus than polymers and can provide superior mechanical strength, in some cases it is brittle (Sharpe et al., 2001, Sharpe Jr and Bagdahn, 2004). Polymers, particularly the elastomers, are more flexible materials than silicon. One of the advantages of using polymers is their various forming methods. As an example, with simple lithography it is possible to fabricate high aspect ratio (HAR) structures with SU-8, which is a common *"photopatternable epoxy",* and used as a photoresist in optical lithography (del Campo and Greiner, 2007, Liu, 2007). Some polymers, like polydimethylsiloxane (PDMS), are solidified by heat curing. PDMS is one of most applicable elastomers for micro- and nano- molding (Liu, 2007, Kim et al., 2002, Zhang et al., 2006). Polycarbonate, polyimide, acrylics, biodegradable polymers (like polyvinylpyrrolidone (PVP), carboxymethylcellulose (CMC), and sodium hyaluronate (HA)) and polyurethane are the other polymers that have been used in MN fabrication procedures either as the main material or as sacrificial ones (Liu, 2007, Kim et al., 2012, Kim et al., 2013).

SU-8 as a negative photoresist was introduced in 1989 by IBM (Lorenz et al., 1997). This photopolymer epoxy consists of 8 epoxy groups. It has revolutionized the MEMS fabrication

technology particularly for fabricating the HAR structures (Lorenz et al., 1998). SU-8 can be easily coated with different thicknesses on relatively rough surfaces. The adhesion of different metals to SU-8 was investigated and it has been shown that the adhesion strength of metals like titanium, copper (Cu) and chromium (Cr) on SU-8 is suitable for MN fabrication (Dai et al., 2005). Also, it has been shown that SU-8 does not trigger the immune system while implemented subcutaneously and so it can be considered as a biocompatible material (Nemani et al., 2013). All these advantages make SU-8 one of the most popular materials for fabricating MNs. As an example, a single MN was fabricated from SU-8 for neural applications (Altuna et al., 2010). The MN in (Altuna et al., 2010) consists of the insertion area, the MN body, and a connection head. Fig. 5.6 shows the schematic of the fabricated MN and its insertion tip image under a scanning electron microscope (SEM).

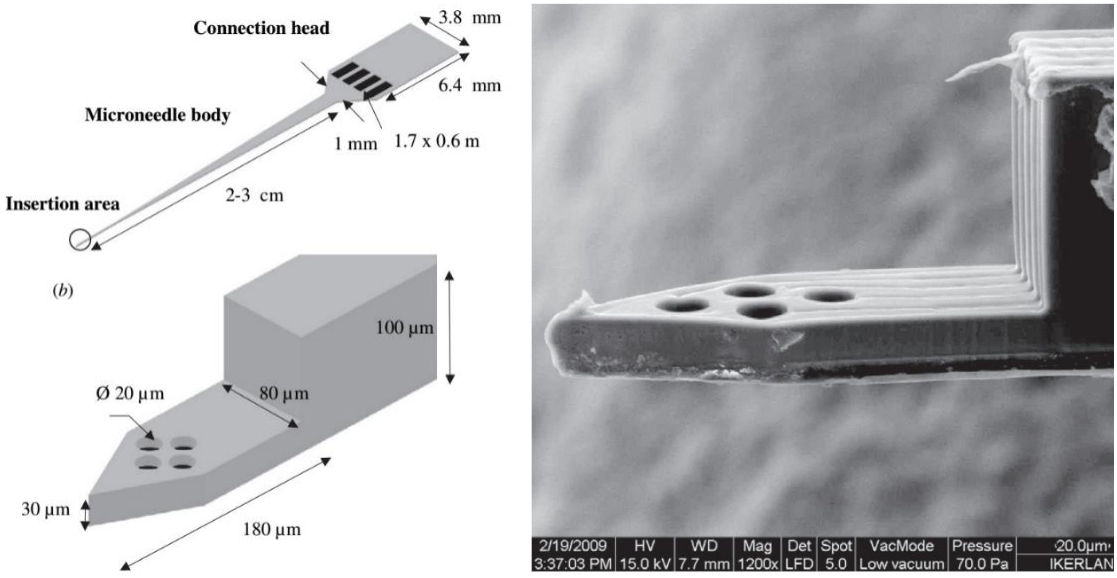


(a) (b)

**Fig. 5.6.** (a) The schematic of the fabricated MN (b) the SEM image of the MN tip (Altuna et al., 2010) [Used with permission]

In another study, SU-8 was used as a mold to fabricate hollow MNs for blood sampling (Lee et al., 2018, Li et al., 2013). The SU-8 was first spun on a glass wafer. In order to control the inner diameter of the fabricated MNs, they changed the thickness of the coated SU-8 by changing the speed of its spin deposition process. By sucking the coated SU-8 to give a pulling force, a wasp waisted structure was formed. Afterwards, a thin a layer of silver (Ag) was coated on the structure as the seed for nickel (Ni) electroplating by electrolyses. In the final step, the uncured SU-8 was removed from the fabricated metallic MN so as to make it hollow. Fig. 5.7 shows the described fabrication steps in detail. The tip of the fabricated metallic MN was cut to the desired angle (either 30° or 60°) by laser beam.

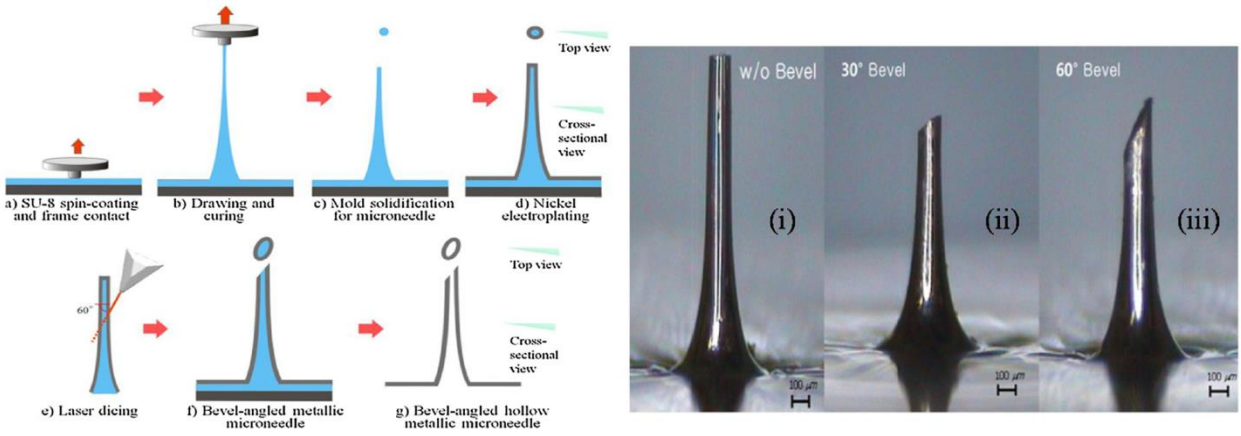


(a) (b)

**Fig. 5.7.** (a) Different fabrication steps of metallic hollow MN (b) The SEM image of the beveled fabricated MN (Lee et al., 2018) [Used with permission]

A similar technique was used to fabricate an arched MN in (You et al., 2014). As it is shown in Fig. 5.8, the coated SU-8 on the substrate was drawn by a hypodermic needle. To make the arched MN, a controlled air flow was blown on the lower part of the drawn MN to bend it slightly.

After solidifying, the formed SU-8 was used as a mold for Ni electroplating. When the Ni was coated on the MN, the uncured SU-8 was removed to make the hollow inner channel.

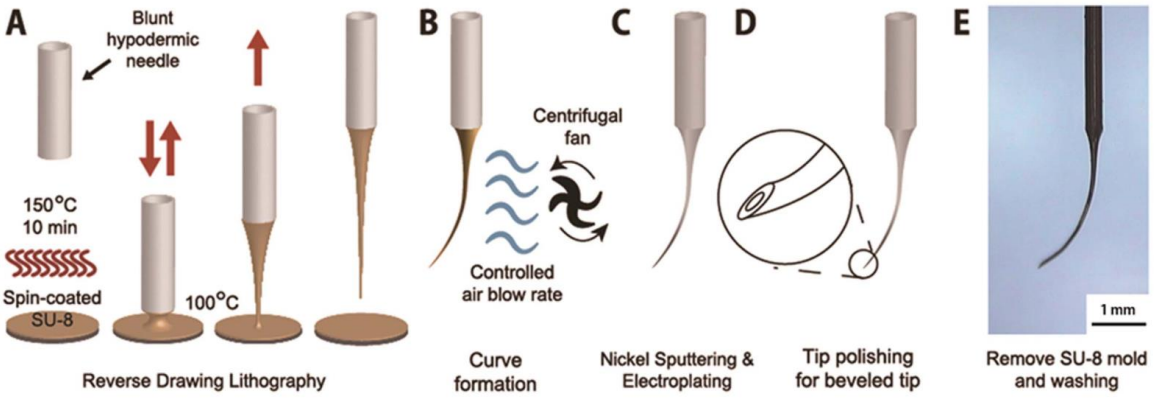


**Fig. 5.8.** The fabrication steps of the arched hollow MN (You et al., 2014) [Permission governed through Creative Commons Attribution (CC BY) license]

SU-8 was used as a sacrificial material in the above fabrication methods. However, because of its suitable mechanical strength, SU-8 can also be used as the main structural material. As an example, in (Vasylieva et al., 2015), a combination of silicon and SU-8 was used as the main material of a fabricated multi-electrode MN. Fig. 5.9a illustrates the fabrication steps and Fig. 5.9b shows the final fabricated MN used as an electrochemical sensor for three different materials. In Fig. 5.9b, SU-8 was used as the insulator between platinum wires (Römgens et al.). Although the main substrate in the suggested fabrication method is silicon, SU-8 was used permanently as a structural material.

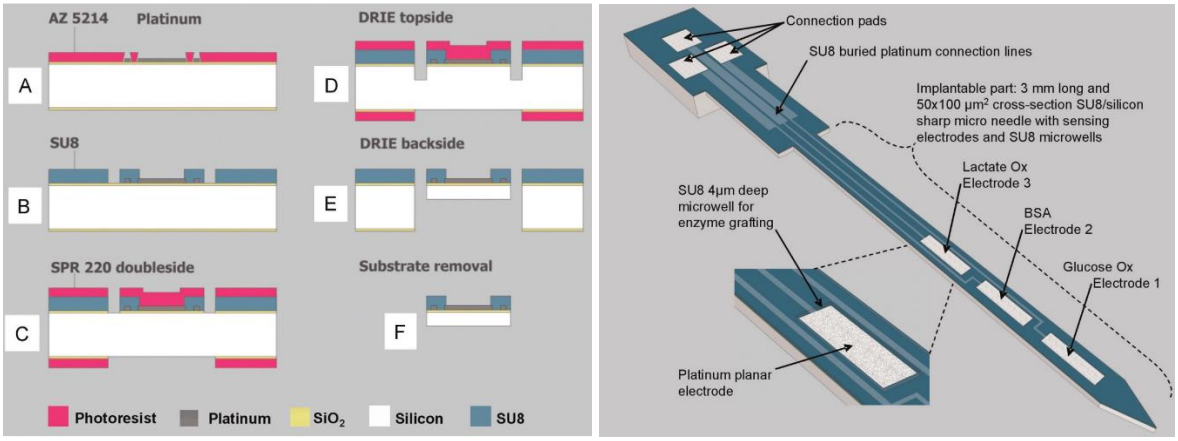


(a) (b)

**Fig. 5.9.**(a) Fabrication steps of the multi-sensor MN structure (b) finalized structure (the SU-8 was used as an insulator between the Pt wires) (Vasylieva et al., 2015) [Used with permission]

Another design of a standalone SU-8 structure was investigated in (Fernández et al., 2009). Like most of the single MN applications, the suggested MN design in (Fernández et al., 2009) was used in neuroscience applications. In the first step, the SU-8 was coated and patterned on a thin (125 µm) Kapton film on top of a Pyrex substrate. Kapton is a polyimide film that remains stable over a wide range of temperatures and has low adhesion to SU-8 (Films, Agirregabiria et al., 2005). The poor bonding between Kapton and SU-8 allowed the SU-8 to detach from the main substrate when the fabrication procedure was completed. A layer of Cr and Au was used as a protection layer for the un-exposed SU-8. Afterwards, the microchannel in the middle of the MN and the Pt/Ti recording electrodes beside the microchannel were patterned. To finalize the design, the cap of the microchannel, which was a 20 µm thick SU-8, was fabricated separately and placed on top of the fabricated MN channel. Fig 5.10, shows the different fabrication steps of the single SU-8 MN and the final design.

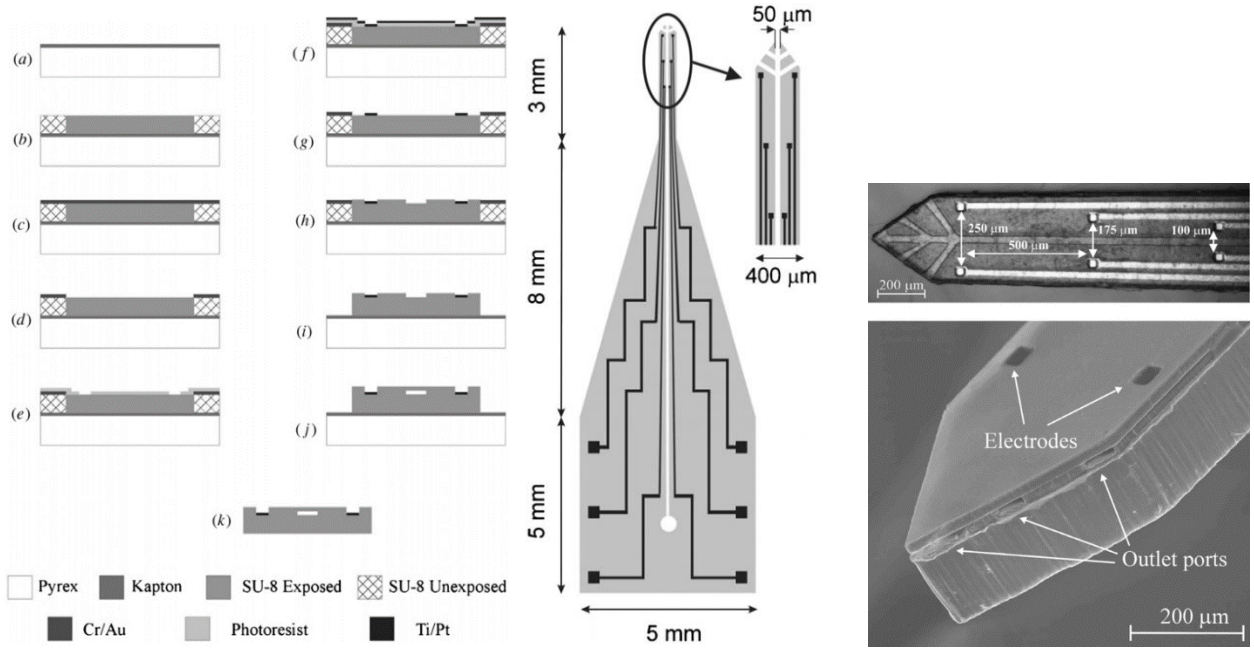


(a) (b) (c)

**Fig. 5.10.** Standalone SU-8 MN for injection and recording (a) fabrication steps (b) final design schematic (c) microscopic and SEM image of the fabricated SU-8 MN (Fernández et al., 2009) [Used with permission]

Overall, it has been shown that using the polymers for single MN fabrication is more popular and easier than using Si or any other common materials in MEMS. Biocompatibility, photo-patternability, high adhesion to metals, low adhesion to some other polymers like Kapton, high capability of fabricating HAR structures, relatively high mechanical strength (Hammacher et al., 2008) and the initial liquid state of most polymers, make them favorite materials for single MNs with or without a hollow microchannel. On the other hand, the requirement of a primary substrate, multi-level curing, poor adhesion to some surfaces like glass, oxides and nitrides, significant difference between the thermal expansion coefficients of SU-8 and its substrate (which can cause wrinkles on the SU-8 when the crosslinks are formed in it (Conradie and Moore, 2002)), and the

requirement of special temperatures and moisture level for storage conditions, are the disadvantages of SU-8 when applied to MN fabrication. Also, the curing condition of SU-8 affects its mechanical properties. For example, it has been shown that a longer post exposure bake (PEB) increases SU-8's mechanical strength, because it helps form more crosslinks in the exposed SU-8 (Feng and Farris, 2002).

### 5.2.2. Single Microneedle Application

In most of the MN investigations, the single MNs were used to access a very fine spot in the body or inside a cell. As mentioned earlier in the fabrication section, single MNs are usually used in neuroscience studies to stimulate or record from a specific cortex area in the central nervous system (CNS). A particular region in the brain or in the spinal cord may involve injection of a particular drug, be used for recording an action potential, or both at the same time (Seymour et al., 2017). In an interesting study, arched MNs were used to inject drugs to retinal tissue. Also, blood sampling, in-vitro fertilization (IVF) and the patch-clamp method for membrane studies can be considered as an application for single MNs. In some applications, the MNs needed to be conductive. Therefore, they were fabricated either directly from metal or coated by suitable metal, by either electroless methods or cold reactive sputtering.

Testing procedures for fabricated MNs depend on the application and should be done before the main experiment. For example, the mechanical strength of the fabricated MNs is one of the most important parameters, and this should be measured before any experiment particularly for in-vivo applications. Table 5.1 demonstrates some of the other materials, applications, and tested parameters of single MNs which have been studied in different investigations.

**Table 5. 1.** Different materials, applications and testing parameters of the fabricated single MNs

| Study | MN material | Type of the MN | Application | Testing parameters |
|---|---|---|---|---|
| Fiber microelectrodes for electrophysiological recordings (Reitboeck, 1983) | Tungsten-glass and platinum-rhodium-quartz fiber | Solid/Conductive | Electrophysiological recordings | Permissible axial force for various MN lengths/Electrical impedance |
| Microchip Technology for Automated and Parallel Patch-Clamp Recording (Brüggemann et al., 2006) | Borosilicate glass | Hollow | Patch-clamp for cell membrane studies | Measuring the "tip potential"(Okada and Inouye, 1975) / Electrical impedance of the electrode (Edelman et al., 2004) |
| New Rapid Method Of Producing MNs for Subzonal Sperm Insertion (Gordon et al., 1993) | Glass/Quartz/Silicon micropipette | Hollow | Subzonal sperm insertion (SUZI) | Flow rate of the fluid inside the MN |
| A self-powered one-touch blood extraction hollow MN (Li et al., 2015) | Replication with a Mixture of PVP, CMC and HA polymers | Hollow | Blood sampling | Mechanical strength |
| Brain activity mapping at multiple scales with silicon microprobes containing 1,024 electrodes (Shobe et al., 2015, Scholvin et al., 2016, Seidl et al., 2012, Jun et al., 2017) | Silicon | Solid MN with electrode arrays on it | Cortical recording | Electrical Impedance/potential measurement in the electrolyte (0.9% saline solution) |
| Development of electrical conductivity measurement technology for key plant physiological information using MN sensor (Wise and Najafi, 1991, Jeon et al., 2017) | Silicon | Solid MN with electrode arrays on it | Electrical impedance/pressure measurement in plants to monitor nutrient solutions. | Electrical Impedance/mechanical strength |
| Microneedle-Based Transdermal Sensor for On-Chip Potentiometric Determination of K+ (Miller et al., 2014) | PMMA | Hollow MN | Ion-selective-electrode to measure the $K^+$ concentration | Electrochemistry properties of the fabricated electrochemical cell |

From Table 5.1, it can be inferred that over time the application of single MNs approached towards neurological applications. Also, it is worthwhile to mention that the single MNs were usually fabricated from silicon. Although the silicon fabrication techniques are expensive, it provides a good quality substrate upon which to fabricate the accessories around the fabricated MN, like electrodes and amplifiers. Therefore, silicon is still favorite material particularly for single MN fabrication for special purposes.

For applications where high fluid rate or low electrical conductivity is needed, usually MN arrays were fabricated. In the next section of this review, the fabrication methods and applications of MN arrays are discussed in more detail.

## 5.3. Microneedle Arrays

There are many different fabrication methods and applications for MN arrays. Most of the studies employed MEMS techniques to fabricate disposable (or biodegradable) MN arrays for drug delivery purposes (Kim et al., 2012). In the discussion below, in the first section, different fabrication techniques that have been used to fabricate MN arrays is discussed. Since MN arrays consist of many MNs on the substrate, several different replication methods are investigated. Therefore, this discussion will also describe replication methods. Moreover, MN rolls, which are a new format of MN and being used mostly in dermatology applications, is introduced and explained. In the last part of this section, different applications are discussed.

### 5.3.1. Microneedles Array Fabrication

There are many different techniques to fabricate MN arrays. MN arrays might be fabricated in the format of single row (1-dimension (1D)) (Paik et al., 2004, Parker et al., 2007) or multiple rows (2-dimension (2D)) (Stoeber and Liepmann, 2005). In this review, 2D arrays of MNs will be addressed. Depending on the application, MN arrays are fabricated in either solid or hollow shape. Different materials were used as the structural material. Silicon, metals, and polymers are the most popular materials that have been used for the main structural material for the MN arrays. Different examples of the fabrication techniques of each of these materials for solid and hollow MN are discussed separately below.

#### 5.3.1.1. Solid Vertical Silicon Microneedle Array Fabrication

Making hollow channels inside the MNs array fabricated from Si is not easy. Therefore, most of the Si MNs, even for drug delivery purposes, are solid. As an example, one of the early studies on the fabrication of a silicon MN array was done by (Henry et al., 1998). Reactive ion etching (RIE) was used to etch the silicon and build the MN array. However, RIE has low throughput compared to the other fabrication techniques used to build HAR structures (Jansen et al., 1996). Since MN arrays are a HAR structure and the deep etching of silicon depends considerably on the side wall temperature, RIE cannot be suitable method for fabricating MN arrays (Jansen et al., 1996). In order to overcome this problem, other advanced methods like cryogenic deep reactive ion etching (Cryo-DRIE) (Laermer et al., 2015) have been used. As an example, in (Griss et al., 2001), through a sequence of isotropic (like the recipe that is mentioned in (Jansen et al., 1996)) and anisotropic etching procedures, MN spikes were etched on the surface of electrodes. In onrder to connect both sides of the electrodes and to connect a wire to them, a hole was etched on the

fabricated electrode using KOH wet etching of silicon. In the next step, the fabricated electrode was made conductive by evaporating silver on the electrode, using a tilting and rotating mechanism. Fig. 5.11 shows a schematic of the described fabrication steps and the Ag evaporation system.

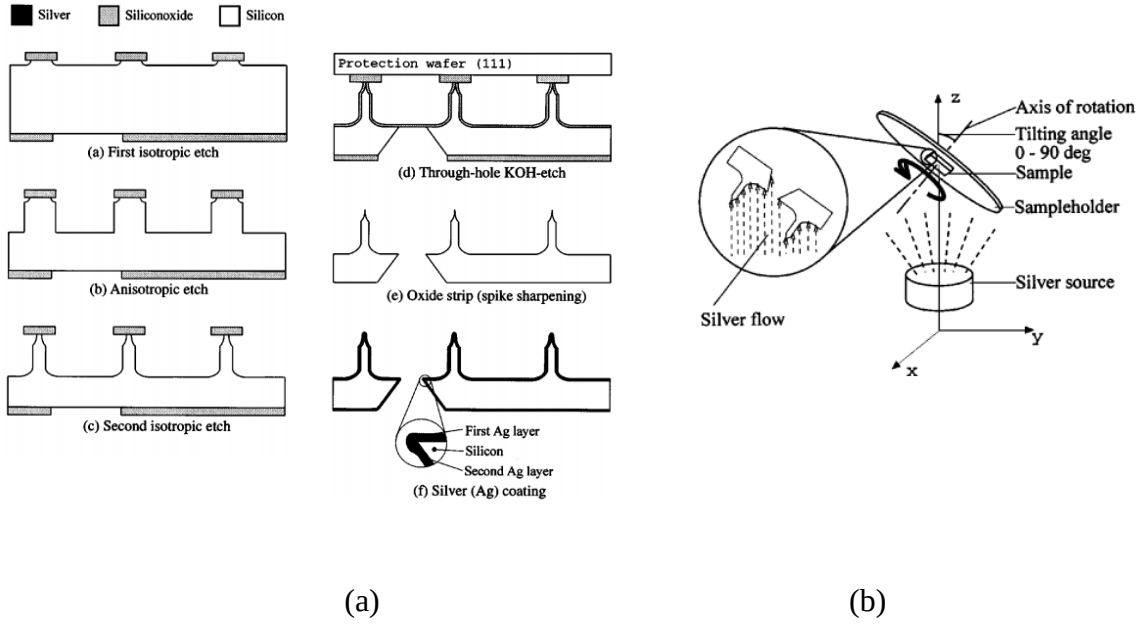


(a) (b)

**Fig. 5.11**. Solid MN electrode (a) fabrication steps (b) metallization (Griss et al, Micromachined Electrodes for Biopotential Measurements, Journal of Microelectromechanical Systems) IEEE copyright line © 2011 IEEE

In addition to the DRIE method, another HAR silicon etching method called the Bosch process, was used in some studies (Roxhed et al., 2007). The Bosch method is a procedure that consists of alternating RIE anisotropic and isotropic etch steps. The problem with the Bosch method is the poor quality of the MN sidewall. As it is shown in Fig. 5.12, the sidewall of the MNs are dentate. Therefore, the penetration depth for MN arrays fabricated with the Bosch method is not as clearly understood as the ones fabricated by the DRIE technique. Also, the processing time

of the Bosch method is significantly longer than the DRIE method, because it is a multi-step reactive ion etching technique.

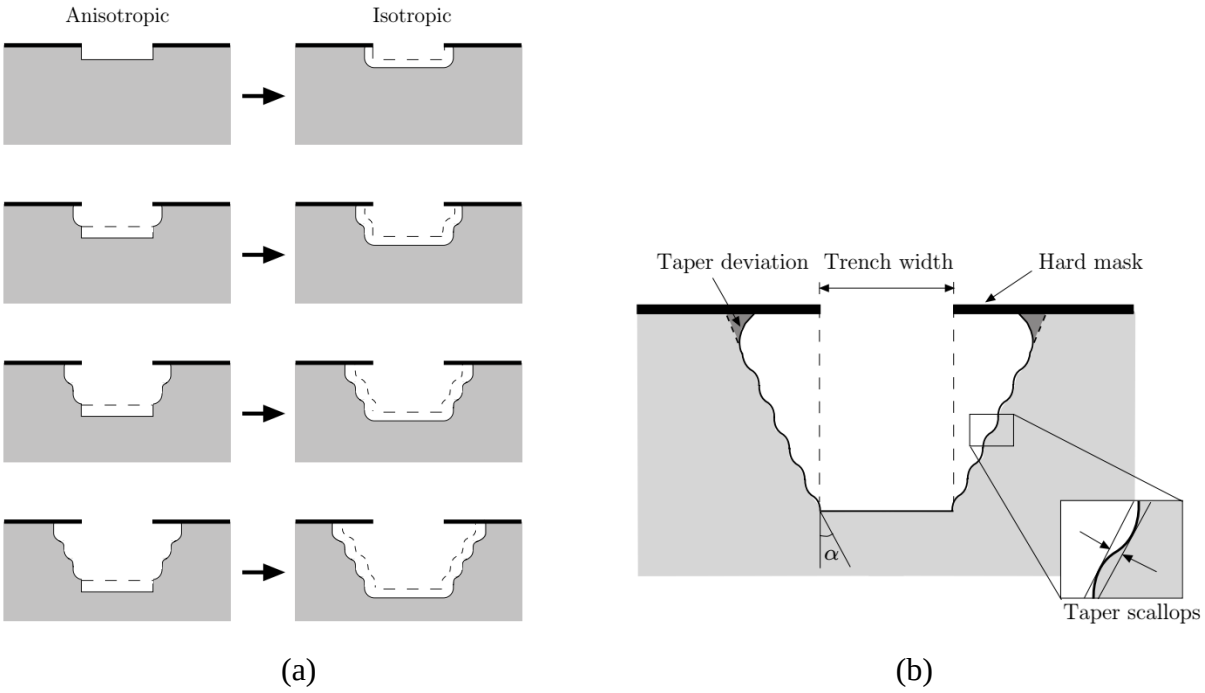


**Fig. 5.12.** (a) Bosch technique steps (b) the dentate walls (results of the Bosch method) [Used with permission]

There are some other techniques for fabricating MN arrays from silicon that have been used based on dicing the silicon and then using silicon wet etching to taper the micro rods. (Bhandari et al., 2010a, Bhandari et al., 2010b, Jones et al., 1992).

In some applications, it is needed to reach different depths of penetration in one MN insertion. Therefore, MN arrays have been fabricated in a slanted format which is described in the next section.

### 5.3.1.2. Solid Slanted Silicon Microneedle Array Fabrication

A bundle of peripheral nerves or capillary branches have different parts located at different depths that cannot be reached with vertical MN arrays. Therefore, a morphology for MN arrays was suggested that had slanted MN spikes on the surface of a substrate (Wark et al., 2013). This design was called the Utah slanted microelectrode array (USEA). As it is shown in Fig. 5.13, the slanted MN arrays were fabricated by different depth fine saw cut of Si wafers and followed by a wet etching process (Abaya et al., 2012, Bhandari et al., 2009).

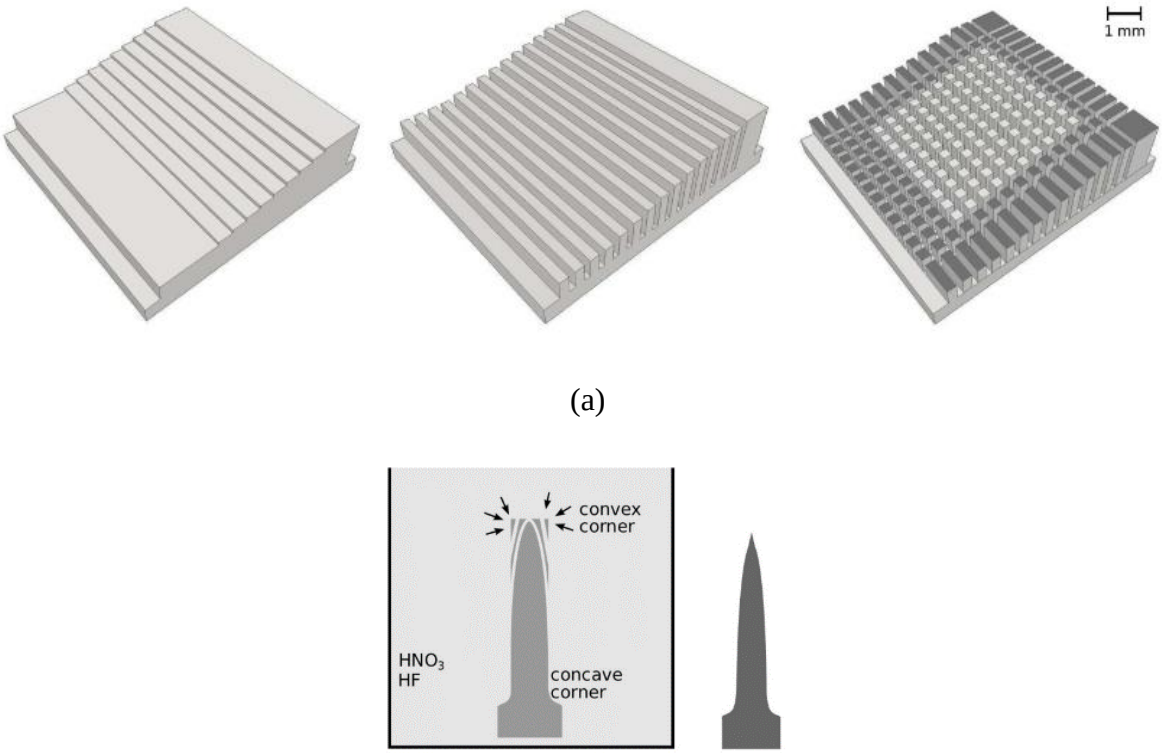


(a)

(b)

**Fig. 5.13.** Slanted MN array fabrication steps (a) Wafer saw in different depth (b) Wet etching process (Adapted with permission from (Abaya et al., 2012) [OSA publication])

In the application section, it was shown that the USEA is more effective than vertical MN arrays. However, the fabrication process of the USEA, particularly from Si, is more challenging than for regular MN arrays.

Although in many applications, solid silicon MNs array have been used, hollow MN arrays are more applicable in the drug delivery investigations. In the next section, some examples about hollow silicon MN arrays fabrication are described.

#### 5.3.1.3. Hollow Vertical Silicon Microneedle Array Fabrication

As mentioned earlier, hollow MNs are a popular structures in drug delivery studies. Therefore, much effort has been done to make them more efficient and disposable. One of the parameters that affects the efficiency of hollow MN arrays is their mechanical strength, which is needed to pierce the skin, and to remain intact until the whole drug dosage is applied, via either injection or polymer dissolve (Larrañeta et al., 2016). A recent study showed that a hollow MN array with smooth wall channels has the best performance in drug delivery (Bal et al., 2008). In order to make a silicon MN array hollow, the common fabrication method is DRIE. For example in (Ji et al., 2006a), as shown in Fig. 5.14, a combination of inductively coupled plasma (ICP) and DRIE etching techniques was used to fabricate a hollow MN array (Ji et al., 2006b).

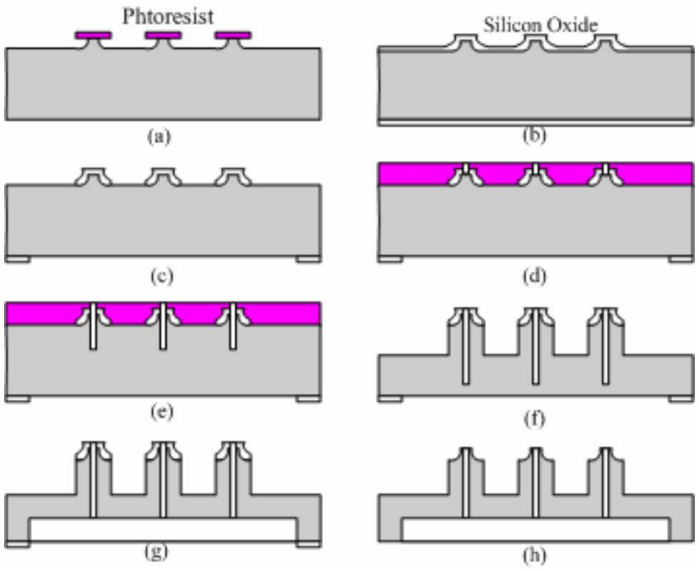


**Fig. 5.14.** Hollow MN fabrication using ICP and DRIE etching techniques (Ji et al., 2006a) [Used with permission] © IOP Publishing. Reproduced with permission. All rights reserved

As it shown in Fig. 5.14, the MNs' tips were tapered via the ICP method (Fig.14a). Afterwards, the needle shaft and the microchannel inside them were grooved by the DRIE technique (Fig 5.14d-f). By etching the backside of the array, enough space was created for the fluid drug (Fig. 5.14g). Noteworthy is that the $SiO_2$ is a suitable mask material in DRIE. There other studies that used similar techniques for fabricating the MN arrays from silicon (Resnik et al., 2018, Khanna et al., 2010).

#### 5.3.1.4. Solid Vertical Metallic Microneedle Array Fabrication

Working with the metals on the micro scale is difficult for fabricating MN arrays. In order to tackle this problem, usually other materials, like Si or polymers, were used as either the base for the MN arrays or a sacrificial material, and they are coated with a particular metal needed for the application. The techniques that used polymers as the base material for the metal coated MN is discussed in the polymer MN array section.

There are some studies that formed metals in the micro-scale to fabricate the metallic MN arrays directly from stainless steel, Al (coated with Pt), or Ti using photolithography and etching techniques (Cormier et al., 2001, Trautman et al., 2000, Peixoto et al., 2014). For example, in (Martanto et al., 2004), researchers used a laser to cut the MN array out of a stainless-steel substrate. In another study, a hollow MN array was fabricated by femtosecond laser etching from a bulk stainless steel substrate (Vinayakumar et al., 2016). Although the laser micromachining technique is simple and a one-step method, the high cost of the laser techniques is a disadvantage particularly for mass production and disposable structures. To date, no study was found that fabricated slanted metallic MNs directly from a bulk metallic material. However, as mentioned above, there are fabrication methods that involved polymers as either structural or sacrificial materials for fabricating hollow metallic MN arrays, particularly for drug delivery purposes.

#### 5.3.1.5. Solid Metallic Microneedle Rollers Structure

A microneedle rollers structure consists of a body with handle and a MN sheet which is wrapped around a detachable cylinder. The substrate of the MN sheet should be flexible to be able to bend it (Lee et al., 2010b). In terms of fabrication, different methods have been used depending on the application. In most of the cosmetic and dermatology applications, stainless steel or Ti MNs are fabricated in either a separate circular form or a row of MNs and inserted inside the sluts on a cylinder (Lee and Hong, 2008, Kim et al., 2009). It is worthwhile to mention that for dermatology applications, the lifetime of Ti alloy MNs is more than those fabricated from stainless steel (Kim et al., 2009, Altarac, 2016). Fig. 5.15 shows three different samples of MN rollers and the length of their MNs. Different applications of MN rollers will be discussed in the application section.

(a)

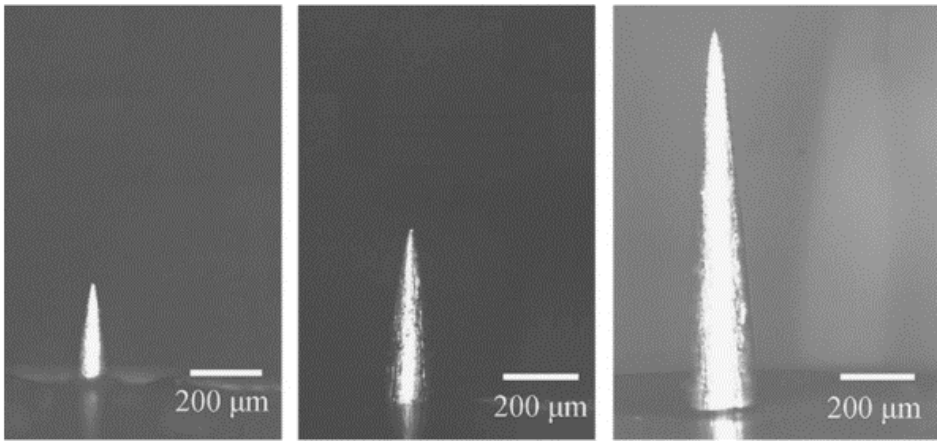


(b)

**Fig. 5.15.** (a) MN roller (b) a single MN of each roller (Zhou et al., 2010)
[Used with permission]

### 5.3.1.6. Solid Vertical Polymeric Microneedle Arrays Fabrication

Polymers are the most common material for fabricating MN arrays. The negative tone photoresist SU-8 and PDMS are the well-known materials used for structural and molding types respectively. However, other polymers, like polycarbonate (PC), PMMA, and acrylic, have been used as either sacrificial materials or the main structural materials in different investigations. For example, in a recent investigation (Nejad et al., 2018), an acrylic sheet was used as a substrate for a PDMS mold fabrication, and the desired MN shape was cut on it by laser beam. Afterwards, in a 2-step procedure, a PDMS mold was prepared. The prepared mold could be filled by any type of polymer to fabricate the MN array. Fig. 5.16, shows the mold fabrication from PDMS on an acrylic sheet by a laser beam etching technique.

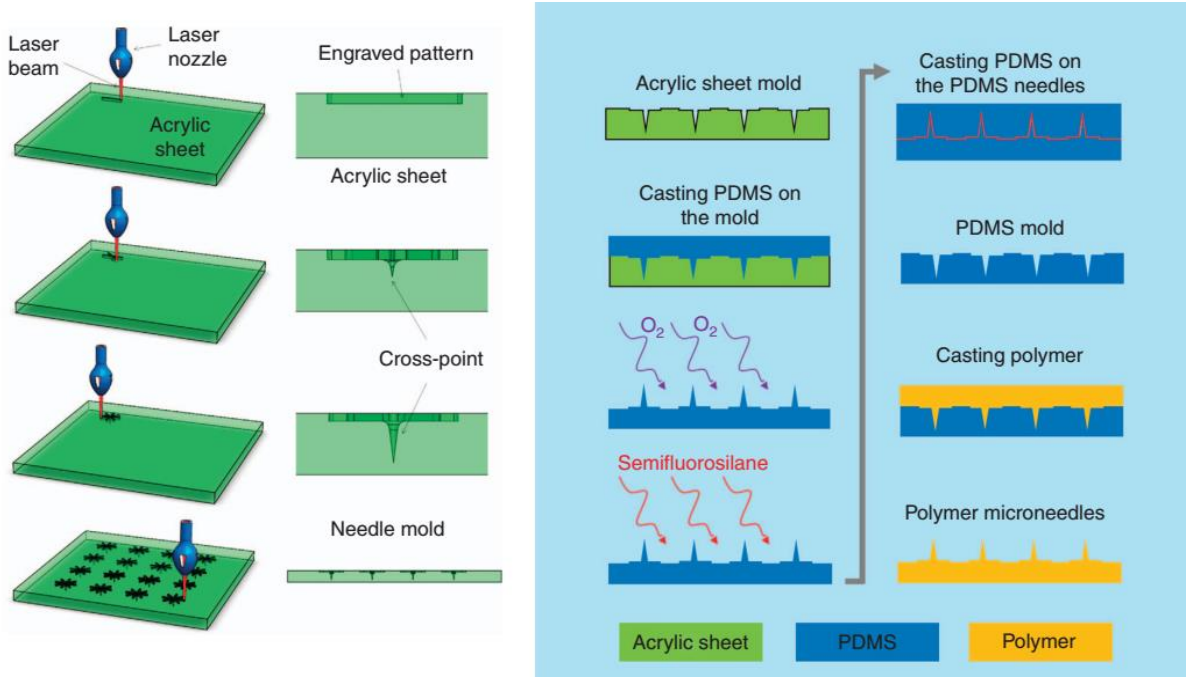


(a) (b)

**Fig. 5.16.** (a) Preparing the acrylic substrate for molding PDMS (b) Preparing the PDMS mold for the other polymers (Nejad et al., 2018) [Permission was governed through Creative Commons Attribution (CC BY) license]

A similar method was investigated in (Tu and Chung, 2016) using PMMA as a mold for poly-lactic-co-glycolic acid (PLGA) as the main material of the MNs. It is worthwhile to mention that a $CO_2$ laser was used in this study. Different laser powers (from 1.5 W to 10 W) and different scanning rate (from 11.4 mm/s to 114 mm/s) were adjusted for the laser to achieve the desired cutting depth in the micro-mold.

The other technique is called *"Lithograph Drawing"* (LD). LD was used to fabricate MNs from the polymers. In this technique, stainless steel drills were built to draw the coated polymer and make the MN pillars. For example in (Lee et al., 2010a, Paek and Kim, 2014), SU-8 was drawn by a drill (show in Fig. 5.17).

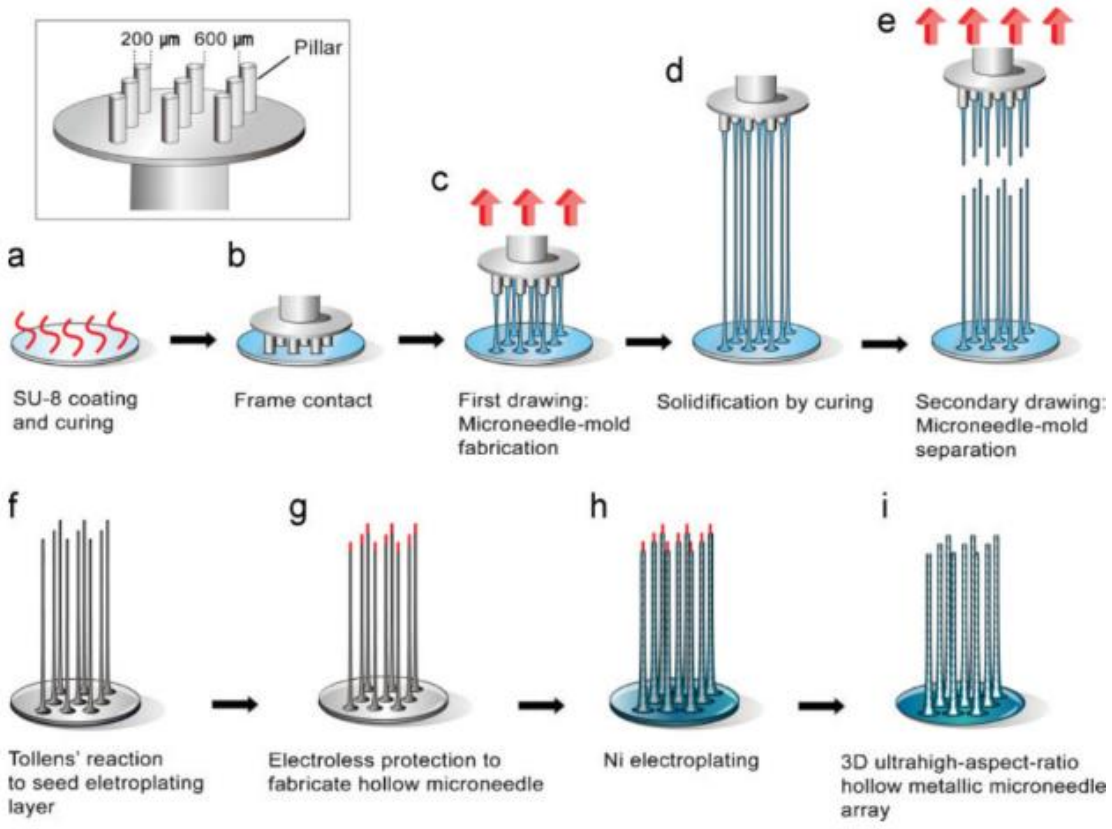


**Fig. 5.17.** The drawing drill (top left) and different steps of the LD fabrication technique (Lee et al., 2010a) [Used with permission]

One of the advantages of polymers is their flexibility and plasticity. The photoresist polymers, like SU-8, can be shaped based on the direction of the UV beam exposure direction. Based on the properties, many different studies were run by fabricating MN arrays from the SU-8 with a simple lithography step (Srivastava et al., 2015). Dependig on the length of the MNs, different types of SU-8 might be used in different studies. Usually, the type of SU-8 that has been used in different studies was SU-8-2025. The last two numbers in the SU-8 name, represents its increasing viscosity, and higher viscosities result in thicker coating layers on the substrate. For instance, SU-8-2025 is much thinner than SU-8-2075. Working with a thick layer of SU-8 is not easily practically, because the refractive index of the SU-8 is not a constant parameter (Lawes, 2005). It has been shown that at different depths the refractive index of SU-8 in the UV wavelength varies (Martham et al., 2014). Also, it was shown that the SU-8 preparation process (like its soft bake time) affects its refractive index (Parida and Bhat, 2009). Therefore, one may conclude that fabrication of HAR MN structures from SU-8 by means of a simple UV lithographic method is challenging. To tackle this problem and enable consistent UV exposure of the SU-8 over its entire depth, different solutions have been explored. For example, in (Park et al., 2005, Park et al., 2007b), first an array of micro-lenses were fabricated on a glass substrate using an etching process. The fabricated lenses helped the UV to converge to a point in the depth of the SU-8, and so make tapered MN arrays. It was reported that up to 600 µm length and 100 µm base have been fabricated by this method. However, their shape specifications depends on different parameters like the soft baking time and the initial concentration of the solvent in the SU-8. In another study, the intensity of the UV beam was alternated spatially. In the other words, it was tried to taper the tip of the MNs by exposing different UV intensities in different spots of the SU-8 substrate (Takahashi et al., 2016). Using lithography techniques to taper MNs' tips have been investigated in the other studies.

For example in (Ami et al., 2011), it was shown that UV diffraction can form the tapered shape of the MNs in an array. Moreover, SU-8 is not the only polymer that is used as a structural material. Different polymers, that might be doped by medications or specific chemical agents, have been used to fabricate the MNs. In (Caliò et al., 2016), poly(ethylene glycol) diacrylate (PEGDA) doped by enzyme was used as the structural material for sensing glucose and lactic acid. In another example, a researcher used polylactic acid (PLA), and which is biocompatible material and harmless for the body (Tomono, 2018). In this study, Tomon used a combination of imprint and tilted lithography to fabricate a master (from SU-8) for a slanted polymeric MN array mold (from PDMS). Afterwards, PLA was used as the main material of the MN array and filled the PDMS mold to form the MN array.

In summary, it can be inferred that polymers are more common materials for fabricating solid MN arrays. Flexibility, sufficient mechanical strength, biocompatibility, and their capability to be doped by other chemicals, are the advantages of polymers in fabricating solid MN arrays.

#### 5.3.1.7. Solid Slanted Polymeric Microneedle Arrays Fabrication

Simultaneous access to different specific spots at different depths in tissue is one of the challenging issues, particularly for drug delivery and neurosciences studies. For example in neuroprosthetic applications, it is necessary to either record or stimulate different nerve fibers at different depths of a nerve bundle simultaneously (Normann, 2007). There are two different techniques to build solid slanted MNs arrays. In one approach, the researchers fabricated MNs on a flexible substrate. Therefore, depending on the type of the surface and the depth that they wanted to penetrate, the suitable force was applied on the MNs over the tissue (Xiang et al., 2016). MNs with a flexible based were used in cortical recording; this will be discussed more in the application

section. In the other approach, the MNs were fabricated on a rigid substrate with varying lengths. An example of this type was fabricated from a droplet of a SU-8 and used backside lithograph to form the MNs (Kwon et al., 2014). However, this technique needs a very accurate droplet of the SU-8 to be placed on a substrate, like PDMS, and has a specific diameter to shape the MNs in the different desired lengths. In another investigation, an array of 10×10 MN were attached to an adhesive substrate inserted to a PDMS petri dish (Cha et al., 2014). The length of the fabricated MNs in this technique depended on the level of the liquid PDMS in the petri dish. Also, the micro-mold can be patterned in different shapes depending on the formation of the mold casts. The final structural material in this study was PLA, which is a biodegradable material. The fabrication processes is shown in Fig. 5.18.

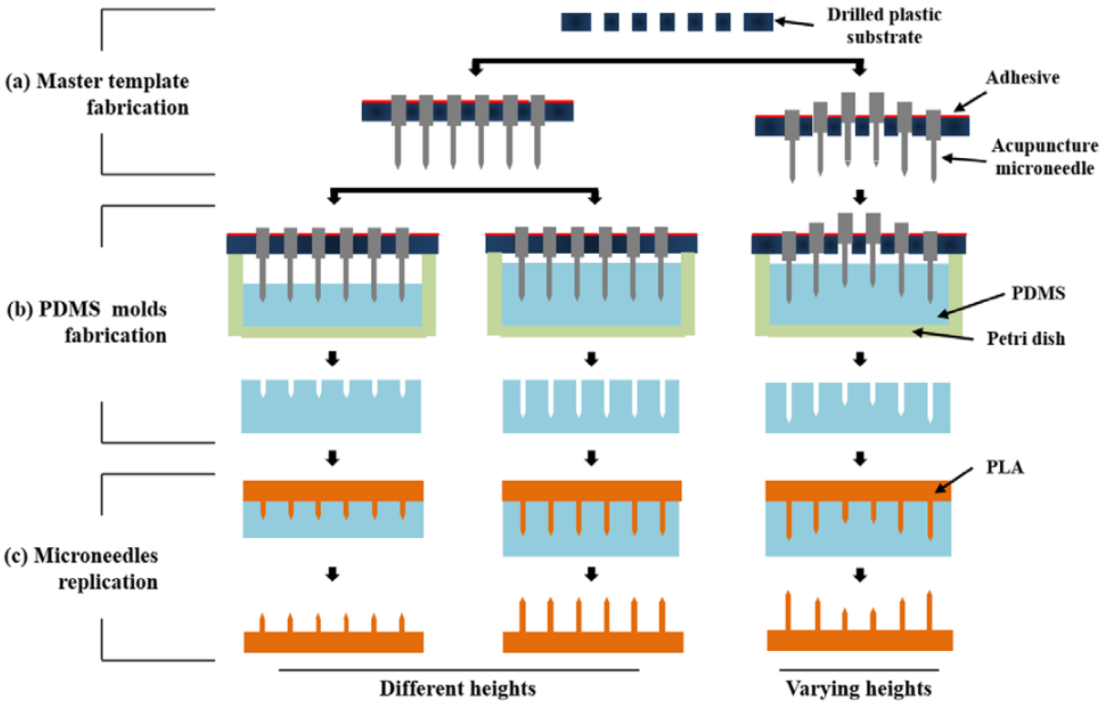


**Fig. 5.18.** Fabrication steps of slanted polymeric MN using PDMS as the micromold and the PLA is the main material of the MNs (Cha et al., 2014). [Used with permission]

From the discussion of this section, it can be inferred that the polymeric slanted MNs are the favourite designs particularly for the rapid prototyping and feasibility studies. In the mentioned studies, it was shown that the slanted polymeric MN arrays can be shaped by lithography methods readily. However, the throughput of methods like micro-molding would be more than the other fabrication techniques. Therefore, in most of the studies that used polymers to fabricate MNs, it was preferred to use the micro-molding techniques. This is discussed in detail in the replication section.

#### 5.3.1.8. Solid Polymeric Microneedle Rolls

Technically, polymeric rolls are flexible MN arrays which were wrapped around a cylinder. For example, in (Park et al., 2010), a flexible MN array was fabricated from PLA in a two-step molding procedure, where two other polymers (SU-8 and PDMS) were used. Afterwards, the fabricated PLA was wrapped around a cylinder to make a roller. Fig. 5.19 shows the fabrication processes of the described procedure.

The important fabrication point in this study is the method of preparing the PLA. As it is shown in Fig. 20, the PLA was treated by either a vacuum oven or only a thermal process without any pressure change. In the process with the vacuum oven, the prepared MN array was coated by water-soluble carboxy-methyl-cellulose (CMC). In the thermal PLA treatment, the PLA and CMC formed the main casting material. In this example, the main material of the MN cylinder was dissolved in the skin, which is the main purpose of the drug delivery application. In the other study, the MN arrays were fabricated on a flexible substrate that could be possibly used as a MN roller (Rajabi et al., 2016). The flexible substrates were fabricated from polystyrene and thiol-ene-epoxy-based thermoset film with a thickness of 250 µm. Also, the relatively long MNs (with 1.8 mm and

2 mm length) were assembled on the substrates by magnetic force applied by an external permanent magnet.

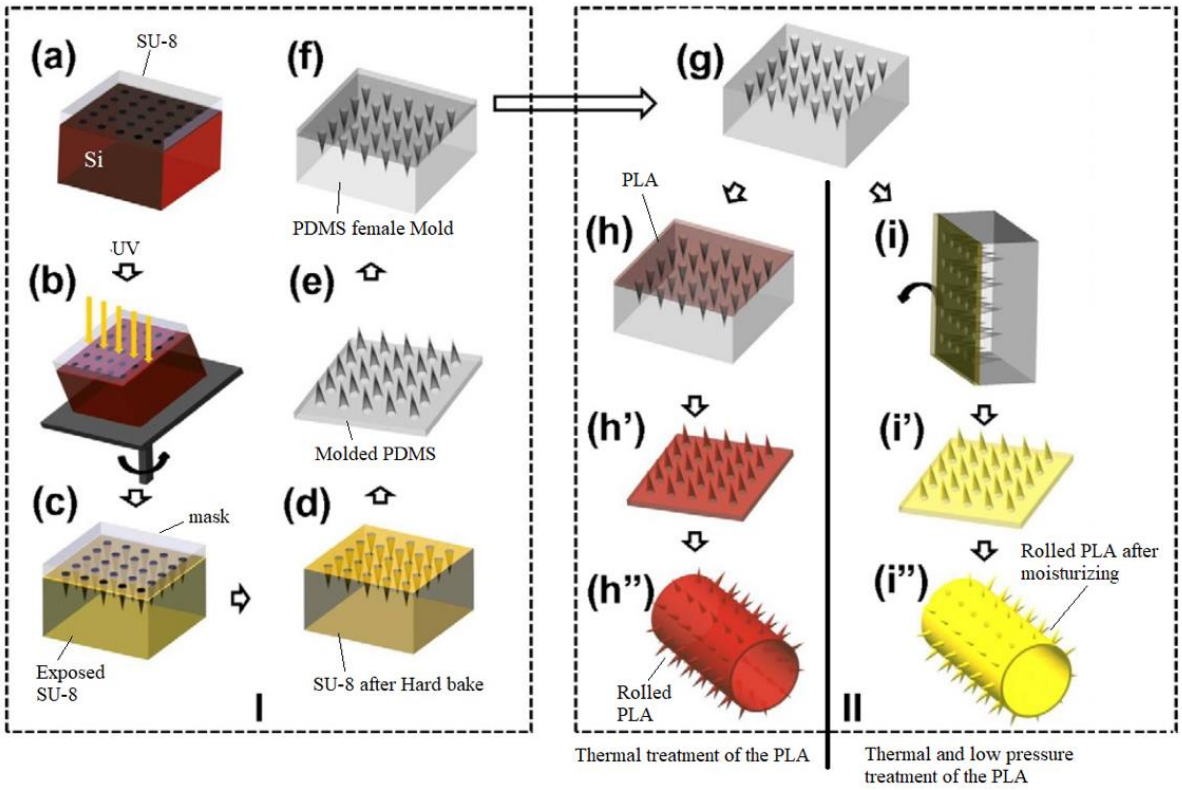


**Fig. 5.19.** Fabrication steps of an MNA roller fabricated from PLA (Park et al., 2010) [Used with permission]

The roller shape of a MN array makes it easier to use and facilitates multiple skin piercing while the roller is moving on the skin. These kinds of structures are being used either for cosmetic purposes or for drug delivery applications. It is worthwhile to mention that the long MNs are usually used for skincare purposes, particularly in the parts of the body were thick layer of tissue or scars are existed. This is the reason that some MN rollers are fabricated in relatively large lengths. However, the outer diameter of the fabricated MNs are around 200 µm to 250 µm to facilitate the skin piercing. Also, depending on the dosage of the drug that is needed to be delivered

to the body, some grooves or holes might be embedded inside the shaft of the MNs (Gill and Prausnitz, 2007).

#### 5.3.1.9. Hollow Vertical Polymeric Microneedle Arrays Fabrication

Fabricating a MN array from materials like Si and metals is a complicated procedure particularly when hollow MN arrays are required to deliver a fluid into the body. Therefore, in many studies researchers use the flexibility of the polymers to form their desired shape and use that polymeric structure either as the main material or a sacrificial one. In some studies, the finishing structure might be a metal that has been electroplated on the polymer or sputtered on it. For example, in (Kim et al., 2004), SU-8 was used as a sacrificial material to form the MNs structure by backside lithography method. Afterwards, Cr and Cu was sputtered on it as a seed for Ni electroplating on the SU-8 fabricated array. In the last step, the SU-8 was removed and the final Ni MN array was released. A similar technique was used in (Mansoor et al., 2013) to fabricate a conductive MN array. In some application, the SU-8 was directly used as the main material of the MNs and no finishing procedure was applied on the structure. For example in (Wang et al., 2009), PDMS was etched by plasma etching procedure and was used as a mold for SU-8. By doing backside lithography, the microchannel was grooved inside the fabricated needle shaft and made a hollow needle. Since SU-8 can be peeled off easily from PDMS, the final structure was released by mechanical force (Patel et al., 2008). It is worthwhile to mention that the RIE etching (1:3 mixture of $O_2$ to $CF_4$ gas) is the best way to etch the PDMS anisotropically and make almost vertical walls in the HAR structures (Garra et al., 2002). Instead of PDMS, Si was used as a substrate for SU-8 in another study (Ceyssens et al., 2013). Another other technique that used polymers as the main and sacrificial material was introduced in (Perennes et al., 2006). In this

technique PMMA was formed a saw tooth pattern via x-ray lithography which fabricated the tip of the MN array. Afterwards, polyvinyl alcohol (PVA) was used as the secondary material to build the negative mold of the MN array. In the third step, again PMMA was cast on top of the PVA. Finally, the surface of the fabricated needles was electroplated by an appropriate metal. Fig. 5.20 shows the different steps of the described fabrication method.

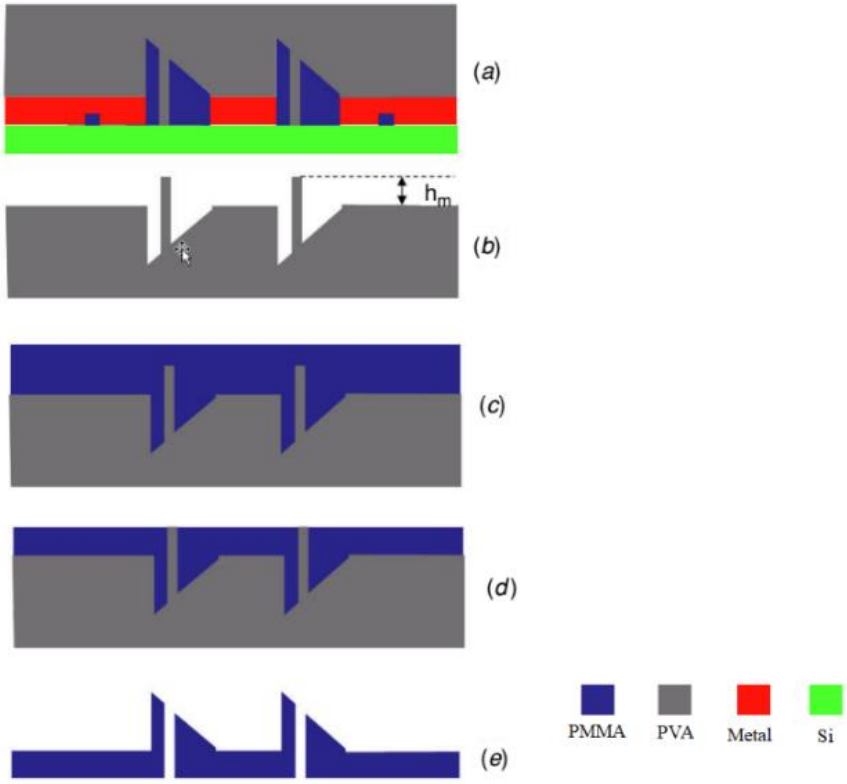


**Fig. 5.20.** MN fabrication steps using PMMA, PVA and metal (Perennes et al., 2006) [Used with permission]

In order to enhance the mechanical strength of the PMMA as the main material of a HAR structure like a MN array, different methods have been suggested in different applications. For example in (Choi et al., 2010), metal was coated on the PMMA structure via laser ablation patterning. In another study, the beveled tip MN array was fabricated from PMMA and inclined

X-ray lithography and Ni was electroplated on the arrays as the finishing surface to increase the mechanical strength of the structure (Lee, 2003).

The discussion of this section showed that polymers are more applicable than the traditional MEMS materials for MN array fabrication. Photoresists like SU-8 (with negative tonality), PMMA (with positive tonality) and PDMS are the common polymers used in MN array fabrication processes. The mentioned polymers are biocompatible and harmless for living tissue. This different properties determine their usage in specific applications. This will be discussed further in the application section.

#### 5.3.1.10. Hollow Slanted Polymeric Microneedle Arrays Fabrication

Inclined MN arrays are more interesting in some applications because they pierce the skin easier than the vertical ones (Kuo and Chou, 2006). Fabrication of slanted MNs from Si wafers is a complicated process. Therefore, fabricating slanted hollow MN arrays has been mostly from polymers. By reviewing the rational behind the design and fabrication of slanted and hollow MN arrays, one may understand that they were mostly used in the electrophysiological and drug injection investigations respectively. Therefore, having both hollow and slanted features at the same time brings up applications like studying the effects of specific drug injection on the physiological signals in mind. To date of this review, no study that investigated the fabrication methods of the hollow slanted MN arrays was found. However, in many articles and patents, researchers explored techniques for making hollow MNs via laser cut along the MNs' shafts (Allen et al., 2002, Sage Jr and Gillett, 2009, Gittard and Narayan, 2010, Duan et al., 2011). It is worthwhile to mention that in some drug delivery studies, solid slanted MNAs coated by the drugs

has been investigated, but drug injection through the hollow polymeric MN arrays have not been investigated.

#### 5.3.1.11. 3-Dimentsional printer Microneedle Arrays

3-Dimensional (3D) printer technologies are advancing rapidly and different designs for them are presented to the market. Depends on the type of nozzle used, different materials and resolutions can be obtained in the printed structure. In some cases, 3D printers can print the structures that could not be fabricated by conventional methods, like multi-step molding processes. Since molding is one of the most common methods in HAR structures fabrication, like MN arrays, and 3D printing is going to be replaced with the molding in many applications, 3D printers were engaged into printing MN arrays (Prasad and Smyth, 2016).

Generally, there are two common types of 3D printers; inkjet and powder based. The inkjet printers perform either in continuous inkjet (CIJ) or drop-on-demand (DoD) format (Economidou et al., 2018). To date of this review, no report was found employing printing MNs with 3D printers. However, Yanfeng Lu et al., developed a 3D printing method that can print MN arrays via layer by layer UV exposure, which is called microstereolithography (μSL) for drug delivery applications (Lu et al., 2015). The μSL has been used in many former studies to fabricate HAR structures, particularly MN arrays. For example, Shaun D. Gittard et al., coated fabricated MNs via μSL method with the antimicrobial drugs (Gittard et al., 2011). Also, there are several other studies that used the μSL technique to fabricate MNs (Choi et al., 2006, Boehm et al., 2012, Maruo et al., 2003, Choi, 2007). In an investigation, the DoD method was used for post-fabrication processing like coating MN arrays. For example, in (Boehm et al., 2013, Boehm et al., 2011), an inkjet piezoelectric printer was used to modify the surface of a prepared MN array for drug delivery

based on the DoD method. Besides µSL, there is a similar method called two-photon polymerization where two light beams in a proper wavelength is focused on specific points at different depths to enable polymerizeation at only in the focal point of these to beams (Kavaldzhiev et al., 2017, Gittard et al., 2009, Ovsianikov et al., 2007).

Another technique that has been introduced as a 3D printing technique was called direct laser writing, and is similar to µSL but it is performed by laser beams (Hwang et al., 2018). Likewise, the two-photon lithography can be performed by femtosecond lasers (Schmidt et al., 2007). The laser absorption can be controlled by parameters like the laser wavelength, laser pulse duration, exposure time, laser repetition rate and the material properties (Gittard and Narayan, 2010).

In this section, it was shown that 3D printing technology can be a pioneer in MN arrays fabrication at large scales. Techniques like µSL, two-photon polymerization and the laser writing techniques are the studied methods in the fabrication of the whole structure of the MN arrays. 3D printing is not only employed in fabrication, but has been used in surface modification of MN arrays. Many studies investigated coating a particular drug on the spikes of a MN array with different thicknesses, and will be discussed more in the application section.

### 5.3.2. Replication

Replication is used in many studies. In the ones were the application of the MNs is considered as the main topic of investigation, the MNs were replicated. Usually, during the replication, a liquid polymer fills a prepared mold from a fabricated master. The important practical issue about fabricating MNs through molding with liquid polymer is the way that the polymer fills the mold. Since the density of the liquid polymer (e.g. SU-8) is high, air bubbles will be trapped in the MNs' tip area and does not allow the polymer to form the MNs' tip completely. Therefore, in the molding

procedure, it is useful to either use diluted polymers or decrease the pressure while the polymer is filled in inside the mold (Heyderman et al., 2000).

*"Hot Embossing"* (HE) is a technique for MN array mold fabrication. As it is shown in Fig. 5.21, in this technique the micromachined embossing master, which was fabricated from Si or metals, is used to build the desired microstructure on a polymer substrate (Becker and Heim, 2000, Worgull, 2009). HE is known as a low-cost and flexible method for microstructures particularly HAR ones like the MN arrays (Heckele et al., 1998).

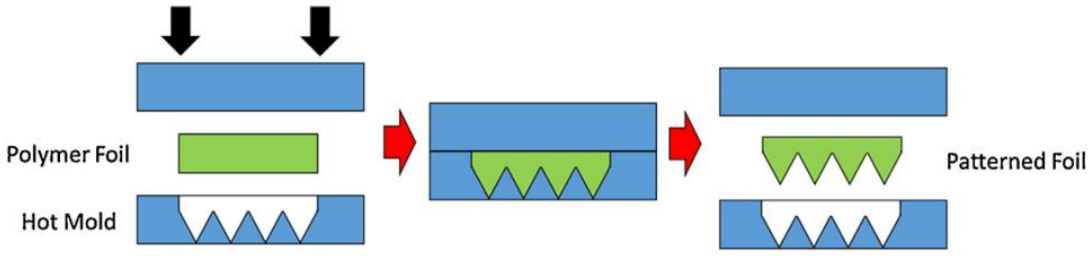


**Fig. 5.21.** The schematic of the HE process (Larraneta et al., 2016) [Used based on Creative common attribution license; DOI: 10.1016/j.mser.2016.03.001]

For example in (Jin et al., 2009), two different mold masters was used that were fabricated from Ni and PMMA for preparing a mold that were filled by melted PC. For fabricating the master from PMMA, deep X-ray lithography was needed which required long exposure time. Therefore, Jin et al. built a 1-dimension (1D) MN row and repeated on the surface to fabricate a 2D MN array. Repeating a 1D MN array on the surface is similar to what Moon et al. reported in (Moon et al., 2006). Using the HE method is not only restricted to specific polymers. Depending on the maximum heat and pressure that a polymer can tolerate and that can be provided, different polymers can be used in HE technique. For example, the HE method was used to build MNs from the Cyclic Olefin Copolymer (COC)(Trichur et al., 2002).

Replicating a hollow MN array is not as simple as the replication procedure of solid MN arrays. Lippmann et al. presented a method that used a sacrificial layer, which they called investing polymer, to replicate hollow MN arrays via molding techniques (Lippmann et al., 2007). In order to replicate a hollow MN array, in the first step Lippmann et al. inserted a sacrificial polymer in the middle of the MN mold. Afterwards, they molded the main shaft of the MNs and removed the sacrificial polymer in the last step.

Increasing the throughput of MN arrays is an advantage of replication methods. In (Lutton et al., 2015a), it was suggested that a rolling based replication can significantly increase the throughput of the MN array fabrication compared to the other common methods. Based on the experiments, it was shown that the replicated hydrogel MN arrays and the directly fabricated ones have almost same mechanical characteristics that can pierce the SC of the skin readily.

One can infer that replication can be done via either HE or a simple molding procedure. Although these two are different methods, they are being used in different studies as complimentary steps. In some studies, it was shown that replication can be used to commercialize specific MN array for particular applications. However, the commercialization of MN arrays needs to be investigated in detail through microstructure manufacturing hazard and cost assessment protocols, which is beyond the scope of this review (Martin et al., 2017).

### 5.3.3. Application and testing parameters of the Microneedle arrays

MN arrays have been used in different applications. Drug and vaccine delivery, electrophysiological signal recording, optical and electrical conduction through the MNAs are the most common applications. The common reasons for using MN arrays in almost all the applications is to bypass the SC. Also, the MN array length is usually short enough to avoid touching the pain percutaneous nerve (< 500 μm). Therefore, being painless is the other advantage of MN arrays. However, in some applications, particularly in cosmetic purpose and scare tissue removal, the MN length is chosen around to be 1 mm to pierce the thick tissue.

#### 5.3.3.1. Drug Delivery Applications

The majority of applications for the MN arrays is related to drug delivery which is called transdermal drug delivery (TDD) (Prausnitz, 2004). MN arrays are usually used to deliver vaccine, insulin and the other hormones (Marshall et al., 2016, Quan et al., 2013). As it is shown in Fig. 5.22, there are different approaches of drug delivery that used MN arrays (van der Maaden et al., 2012).

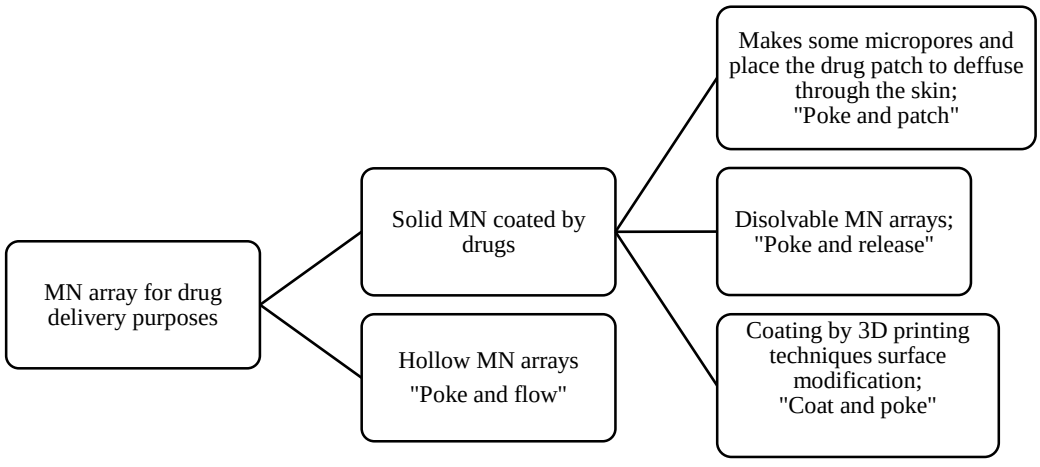


**Fig. 5.22.** Different methods of drug delivery via MN arrays

There are different advantages and disadvantages for each of the TTD approaches. For example, one of the advantages of the "coat and poke" method is that the MN is reusable. However, the "coat and poke" technique can only be used for small dosage of drugs. Depending upon the drug dosage, molecular weight and metabolizing propensity, an appropriate solid MN array is designed. In order to adjust the drug or vaccine dosage, MN arrays with either surface or hole and dents in their shafts might be fabricated. For example in (McGrath et al., 2011), the best parameter to spray hydroxypropylmethylcellulose (HPMC) and carboxymethylcellulose (CMC) through conventional film spray-coating process was investigated.

In drug injection applications, or "poke and flow" TTD approach, the flow regime of the fluid inside the microchannel of a hollow MN is critical. Because of the microscale of the MN arrays, the dominant flow regime in the MN arrays channel is laminar flow (Lhernould, 2013, Colin, 2004). However, the flow regime of a fluid in a MN channel depends on the geometry of the MNs, the viscosity of the fluid, number of the spikes that a MN array has on the surface, pressure drop in both sides of the MN channel, and the roughness of the internal walls of the MNs (Lhernould, 2013).

Dissolvable MNs for drug delivery are being used in the "poke and release" approach. The dissolvable MNAs are usually built from the water-soluble materials like maltose, dextran, albumin and etc.(Ita, 2017). By piercing the skin, the structural materials of the MNAs would be resolved in the water of the tissue, and the drug would be released into the patients' tissue and blood consequently (Chen et al., 2014, Chu et al., 2010, Thakur et al., 2016, Gujjar and Banga, 2014). In some structures, the drug is embedded between the layers of an MNA. By resolving each layer, the drug would be released and the next layer of the water-soluble material would be exposed to the tissue water (Ito et al., 2012). Since these types of MNAs are resolved in the water

completely, no hazardous residue will remain on the skin after usage (Lee et al., 2008). Furthermore, dissolvable MNAs are inexpensive and can be used for variety of the drugs (Chu et al., 2010).

In the "poke and patch" method, the role of an MNA is only in making pores on the skin and so to facilitate the drug diffusion into the deep skin layer. For this, the MNAs only pierce the skin and after that a drug sponge or patch will be replace by the MNAs. The "poke and patch" technique was used to deliver insulin by Mortanto et al. (Martanto et al., 2006).

Overall, among the different methods of TDD, it can be inferred that depending on the goal (dose and the placement of drug), the delivery method may vary. However, "poke and release" was known as the best method for subcutaneous drug delivery in different articles.

#### 5.3.3.2. Electrophysiological Signal Recording

Electroencephalography (EEG) is the brain electrical activity that is a resultant of millions of the nerve fibers inside the brain. EEG is a low-amplitude (~20 µV) and low-frequency (0.16 Hz to 30 Hz) signal. Therefore, to record the EEG, a high input impedance, high gain and high common mode rejection ratio (CMRR) amplifier is inevitable. Besides that, the efficiency of the electrodes plays a crucial role in the quality of the signal and its signal-to-noise ratio (SNR). Bypassing the SC in recording the EEG has a similar correspondence to bypassing a series resistor in a circuit, and so result in increasing the raw signal amplitude. Recording EEG with MNAs of different length and materials, particularly for long term recording, was investigated in many studies. In a recent study, MNAs with a length of 500 µm and circular base of 100 µm were fabricated from SU-8 and decreased the tissue-electrode interface resistance from 15 MΩ to 7 MΩ (Stavrinidis et al., 2016). However, no result was mentioned about SNR or total harmonic

distortion (THD) enhancement. MNAs with rigid substrate are fragile practically. To resolve this, Wang et al., designed an MNA with flexible substrate that could reshape slightly (Wang et al., 2012b, Wang et al., 2012a, Wang et al., 2017a).

MNAs were not only used to record EEG. Electrophysiological signals such as electrocardiography (ECG) and electromyography (EMG) have been recorded via MNA electrodes in different applications. For example in (Chen et al., 2016), an MNA constructed from a magnetic fluid and coated with Ti and Au, successfully recorded ECG and EMG. Also, they demonstrated that because of its secure and greater surface contact, the MNA can record ECG in dynamic situation better than the conventional Ag/AgCl electrodes. Similar investigation and results have been reported by Ren et al. in (Ren et al., 2016, Ren et al., 2017). Electrooculography (EOG) is the other biopotential that can be recorded with MNAs (Golparvar and Yapici, 2017). They revealed that MNAs are the favorite structures particularly for long term applications like the wearable technology and brain computer interface (BCI) applications. However, over short time usage, the recoded signals via the MNAs have higher SNRs compared to the surface electrodes.

#### 5.3.3.3. Optical and Electrical Conduction through MNAs

An interesting application of the MNAs is optical nerve stimulation. Since the refractive indices and the light reflection of different layers of the skin are different at specific wavelengths, bypassing a layer facilitates reaching the layers underneath. For example in (Ding et al., 2006), it was shown that the reflection of the epidermis in the wavelength of 633 nm is more than the other layers of the skin. Therefore, by bypassing the epidermis with an MNA that is transparent in this wavelength, one can obtain more data from the layer underneath. Another potential application of

MNAs is recording blood oxygen saturation using the photoplethysmography (PPG) technique. Studies showed that the skin colour pigments increase the bias of the obtained data through PPG, particularly in the dark skins and at low oxygen saturation levels (Bickler et al., 2005). Therefore, if MNAs can bypass the SC, where the most of the skin pigments are placed, then it can be speculated that robust results can be obtained. However, this should be studied clinically.

The depth of light penetration using MNAs was studied in (Kim et al., 2016). In that study, they fabricated an MNA with 11×11 MN on the surface from PLA. The length of the designed needles was 1.6 mm which is relatively large. Also, they fabricated a micro-lense on the back of the fabricated MNAs to focus the light beams toward the tips of the MNs. They showed that 7.5% of the input photons at the wavelength of 491 nm was delivered to the specific subcutaneous tissue, compared to 0.85% without the MNAs. In another study, Kwon et al. designed a slanted MNA that can deliver light to different depths of tissues, particularly the brain cortex (Kwon et al., 2013).

SC is the most resistive layer of the skin and has around 100 kΩ resistance (Miklavčič et al., 2006). Therefore, any surface stimulation should pass through this relatively high electrical resistance. Using MNAs will assist to bypass this high resistance layer and reach the lower layers that have more conductivity. Moreover, it was shown that bypassing the SC will increase the directivity of the current density toward a target nerve fiber. In long-term applications, using MNAs will reduce the hazard of skin burn (Soltanzadeh et al., 2018). In another application, MNAs were fabricated from PMMA to electroporate the epidermis layer of the skin and increase the transfection of the drugs and vaccines that enhances the “poke and patch” TTD method (Choi et al., 2010, Choi et al., 2005).

MNAs are being used in implantable stimulators. For example in (Patel et al., 2016), an MNA cuff-electrode was fabricated in which the length of each needle was 100 µm and they minimally

pierced the surface of a nerve fiber to stimulate it with a 0.95 mA lower current than the regular flat cuff-electrodes.

#### 5.3.3.4. Testing parameters

##### 5.3.3.4.1. Mechanical Parameters Testing

The main goal of testing an MN or an MNA is assessing its safety and efficiency (Lutton et al., 2015b). The testing parameters vary depending on the application. However, in all the applications, the mechanical strength of any type of MN is very important. Therefore, different studies investigated the needed mechanical requirements of an MN structure. Since the skin is the first barrier that a MN confronts, most of the investigations have addressed the mechanical interaction between the skin, particularly the SC, and the MN. A MN may experience different mechanical stresses. Different situations like an uneven insertion force, non-uniform skin surface and unexpected movements during insertion or removal are some of the mechanical stresses that a MN may experience.

The geometry and material of the MN play a crucial role in their failure from any of these forces (Park and Prausnitz, 2010). Studies showed that polymer MNs are more efficient and safer than other materials like Si and metals (Park et al., 2006, Han et al., 2007). In many cases, the tip of MNs are sharpened to facilitate their insertion. Meanwhile, the diameter of the MNs are increased to enhance their mechanical strength (Park et al., 2007a). Insertion and fracture forces of MNs in the skin were the mechanical parameters assessed in (Davis et al., 2004). It was concluded that the insertion force decreases by decreasing the tip radius and increasing the wall angles. It was demonstrated that the fracture force increases by thickening the MN. Also, in the

same study, the insertion force was measured in the range of 0.1 to 3 N, which supports the measurements of the other studies (Roxhed et al., 2008, Park et al., 2006).

#### 5.3.3.4.2. Fluidic Parameters Testing

In the "poke and flow" drug delivery method, the drug flow regime and the hydraulic resistance in the channel of a MN should be considered in any MN design. Lyle et al. estimated the fluid regime and hydraulic resistance of a silica MN (with 150 µm inner diameter). Their calculations based on Poiseuille's Law for deionized water with 69-621 kPa showed that in a MN channel the Reynold number is around 700 and the fluid regime is laminar (Hood et al., 2011). Also, they concluded that decreasing the MN tip will increase the hydraulic resistance 1 to 2 times. In another study, Chakraborty et al. fabricated very thin and tall MNAs (3.5 - 4 mm length and 30 µm inner diameters) to take blood samples (Chakraborty and Tsuchiya, 2008). To evaluate their sputtered titanium structure, they took a third fluidic regime into account which is called "*meniscus traction"* regime (Huang et al., 2001, Chakraborty, 2005).

#### 5.3.3.4.3. Electrical and Electrochemical Parameters Testing

In order to design MNAs as an electrode for either recording or stimulation, the electrical and electrochemical parameters should be assessed. Electrical impedance of the recording electrode at different frequencies is the most important parameter that should be measured, particularly in the biopotentials recording devices (Pini et al., 2012, Wang et al., 2012b). Low electrical impedance between the skin and the electrode will increase the SNR of the signal and enhance the quality of the recorded signal (Huigen et al., 2002). Also, electrical charge is transferred by ions inside the body, compared to the electrodes where this happens through electron

movement. This conversion happens in electrodes through a set of electrochemical process. Therefore, assessing the electrochemical properties of the electrodes is very crucial in the performance of MNAs used in the biological applications. The common test that is used for characterizing the electrochemical properties of the structures is cyclic voltammetry (CV) test that can determine the rate of the ion and electron charge transfer (Shih et al., 2007). In the other words, CV characterizes the properties of the electrode-electrolyte interface (Chen, 2016).

## 5.4. Discussion and Conclusion

MNs are micro-scale structures that can change the quality of different medical interventions like drug delivery, mechanical/electrical stimulations, etc.. The main purpose of the application of MNs is to bypass the SC, which is the first barrier of the skin and which has the highest electrical and mechanical resistance. Therefore, bypassing this layer may increase concerns about the safety of these components, and this is the topic of some investigations (Martin et al., 2017, Van Damme et al., 2009). In this review, the structure of MNs was categorized into single and array MNs. For each section, different methods of fabrication were described. Based this the research, one may understand that MNs are mostly fabricated (or mostly replicated) from polymers, because polymers are more flexible and biocompatible compared to the other materials like silicon or metals. However, depending on the application, the surface of MNs are coated either completely or patterned from different suitable metals, which are mostly biocompatible. The shape of MNs are either pyramidal or conical in most of the investigations, but the other shapes like rod, hexagonal, octagonal and rocket-shape have been investigated (Ashraf et al., 2011). The fabrication method and the application usually determines the shape of the electrodes. However, the main parameters that determine the shape needed for an MN is the amount of resistance that it

confronts during the insertion. For example, in the rod shapes, the resistance against the MNs during insertion is consistent. In contrast, in the cone and pyramid structures, because of increment in the surface area, more force is required to reach deeper layers of the skin than the surface layers. Pyramidal structures with a side length the same as the diameter of a conical structure, have a larger area. Therefore, the insertion force of a pyramidal structure is more than a conical one. In MNAs, not only the shape, but the increasing the space between the needle spikes will increase MNs penetration (Kochhar et al., 2013). By increasing the number of needle spikes on the surface, and decreasing the spacing between them, results in the insertion force increasing from 0.1 to 3 N. The tip sharpness of MNs is affects the insertion force. Sharp MNs need less effort to penetrate the skin and bypass the SC. Almost all of the investigations have been done on tapered MNs, as their primarily role is penetrating the SC (Chua et al., 2013). Also, in many applications the length of the MNs is between 100 µm to 500 µm, but in applications where access to capillaries and blood flow is required, the length of the MNs is increased to 1.5 mm. The number of MNs on the surface varies from 1 to 100 in an area less than 1 $cm^2$. The other application of long MNAs is the rollers that are used to stimulate scar tissue or thick layers of the tissue mechanically, and bring collagen to the skin surface.

In terms of application, it was realized that most of the single and one-row (also called in-plane) MNs are used in neurological applications to either record or stimulate a nerve fiber or the brain cortex. Single MNs are used in the applications where spatial accuracy is required, like reading from a single nerve fiber or a single cell (like patch-clamp technique). However, MNs with different lengths on a plane and MNAs (particularly ones with different lengths on the surface) were used in the neuroscience investigations too. MNAs have been used in different methods of drug delivery (described in Fig.22). In most of the TTD applications, the “poke and flow” method

was investigated through hollow MNAs. The other methods like “poke and release” and “poke and patch” need the MNAs.

Overall, it can be concluded that MNs, particularly MNAs, can enhance the quality of different medical interventions and monitoring. Many studies are on-going that apply MNs to scientific fields particularly medicine. The goals of these studies include increasing the throughput of the fabrication procedure and decreasing the cost to enable disposable low-priced MNs. In many fields of drug delivery, like vaccine and antibiotic delivery, MNAs are commercialized, but in the other fields like BCI, bionic limbs, and neuroscience studies, more clinical trials are needed to reach the level of the commercialization. The materials that MNs are fabricated from are still under investigation. Several different biocompatible polymers are studied and used for MN fabrication without any hazard for patients. One may reasonably call the MN field a major effort in micro-medical device investigation.

## References

ABAYA, T., DIWEKAR, M., BLAIR, S., TATHIREDDY, P., RIETH, L., CLARK, G. & SOLZBACHER, F. 2012. Characterization of a 3D optrode array for infrared neural stimulation. Biomedical optics express, 3, 2200-2219.

AGIRREGABIRIA, M., BLANCO, F., BERGANZO, J., ARROYO, M., FULLAONDO, A., MAYORA, K. & RUANO-LOPEZ, J. 2005. Fabrication of SU-8 multilayer microstructures based on successive CMOS compatible adhesive bonding and releasing steps. Lab on a Chip, 5, 545-552.

ALLEN, M. G., PRAUSNITZ, M. R., MCALLISTER, D. V. & CROS, F. P. M. 2002. Microneedle devices and methods of manufacture and use thereof. Google Patents.

ALTARAC, M. 2016. Microneedle roller. Google Patents.

ALTUNA, A., GABRIEL, G., DE LA PRIDA, L. M., TIJERO, M., GUIMERÁ, A., BERGANZO, J., SALIDO, R., VILLA, R. & FERNÁNDEZ, L. J. 2010. SU-8-based microneedles for in vitro neural applications. Journal of Micromechanics and Microengineering, 20, 064014.

AMI, Y., TACHIKAWA, H., TAKANO, N. & MIKI, N. 2011. Formation of polymer microneedle arrays using soft lithography. Journal of Micro/Nanolithography, MEMS, and MOEMS, 10, 011503.

ASHRAF, M. W., TAYYABA, S. & AFZULPURKAR, N. 2011. Micro electromechanical systems (MEMS) based microfluidic devices for biomedical applications. International journal of molecular sciences, 12, 3648-3704.

BAL, S. M., CAUSSIN, J., PAVEL, S. & BOUWSTRA, J. A. 2008. In vivo assessment of safety of microneedle arrays in human skin. european journal of pharmaceutical sciences, 35, 193-202.

BECKER, H. & HEIM, U. 2000. Hot embossing as a method for the fabrication of polymer high aspect ratio structures. Sensors and Actuators A: Physical, 83, 130-135.

BHANDARI, R., NEGI, S., RIETH, L. & SOLZBACHER, F. Wafer-scale processed, low impedance, neural arrays with varying length microelectrodes. Solid-State Sensors, Actuators and Microsystems Conference, 2009. TRANSDUCERS 2009. International, 2009. IEEE, 1210-1213.

BHANDARI, R., NEGI, S., RIETH, L. & SOLZBACHER, F. 2010a. A wafer-scale etching technique for high aspect ratio implantable MEMS structures. Sensors and Actuators A: Physical, 162, 130-136.

BHANDARI, R., NEGI, S. & SOLZBACHER, F. 2010b. Wafer-scale fabrication of penetrating neural microelectrode arrays. Biomedical microdevices, 12, 797-807.

BICKLER, P. E., FEINER, J. R. & SEVERINGHAUS, J. W. 2005. Effects of skin pigmentation on pulse oximeter accuracy at low saturation. Anesthesiology: The Journal of the American Society of Anesthesiologists, 102, 715-719.

BOEHM, R., MILLER, P., HAYES, S., MONTEIRO-RIVIERE, N. & NARAYAN, R. 2011. Modification of microneedles using inkjet printing. AIP advances, 1, 022139.

BOEHM, R. D., MILLER, P. R., SCHELL, W. A., PERFECT, J. R. & NARAYAN, R. J. 2013. Inkjet printing of amphotericin B onto biodegradable microneedles using piezoelectric inkjet printing. Jom, 65, 525-533.

BOEHM, R. D., MILLER, P. R., SINGH, R., SHAH, A., STAFSLIEN, S., DANIELS, J. & NARAYAN, R. J. 2012. Indirect rapid prototyping of antibacterial acid anhydride copolymer microneedles. Biofabrication, 4, 011002.

BRAZZLE, J. D., PAPAUTSKY, I. & FRAZIER, A. B. 2000. Hollow metallic micromachined needle arrays. Biomedical Microdevices, 2, 197-205.

BROWN, K. T. & FLAMING, D. G. 1974. Beveling of fine micropipette electrodes by a rapid precision method. Science, 185, 693-695.

BRÜGGEMANN, A., STOELZLE, S., GEORGE, M., BEHRENDS, J. C. & FERTIG, N. 2006. Microchip Technology for Automated and Parallel Patch-Clamp Recording. small, 2, 840-846.

BYSTROVA, S. & LUTTGE, R. 2011. Micromolding for ceramic microneedle arrays. Microelectronic engineering, 88, 1681-1684.

CALIÒ, A., DARDANO, P., DI PALMA, V., BEVILACQUA, M., DI MATTEO, A., IUELE, H. & DE STEFANO, L. 2016. Polymeric microneedles based enzymatic electrodes for electrochemical biosensing of glucose and lactic acid. Sensors and Actuators B: Chemical, 236, 343-349.

CEYSSENS, F., CHAUDHRI, B. P., VAN HOOF, C. & PUERS, R. 2013. Fabrication process for tall, sharp, hollow, high aspect ratio polymer microneedles on a platform. Journal of Micromechanics and Microengineering, 23, 075023.

CHA, K. J., KIM, T., PARK, S. J. & KIM, D. S. 2014. Simple and cost-effective fabrication of solid biodegradable polymer microneedle arrays with adjustable aspect ratio for transdermal drug delivery using acupuncture microneedles. Journal of Micromechanics and Microengineering, 24, 115015.

CHAEN, S., OIWA, K., SHIMMEN, T., IWAMOTO, H. & SUGI, H. 1989. Simultaneous recordings of force and sliding movement between a myosin-coated glass microneedle and actin cables in vitro. Proceedings of the National Academy of Sciences, 86, 1510-1514.

CHAKRABORTY, S. 2005. Dynamics of capillary flow of blood into a microfluidic channel. Lab on a Chip, 5, 421-430.

CHAKRABORTY, S. & TSUCHIYA, K. 2008. Development and fluidic simulation of microneedles for painless pathological interfacing with living systems. Journal of Applied Physics, 103, 114701.

CHEN, K., REN, L., CHEN, Z., PAN, C., ZHOU, W. & JIANG, L. 2016. Fabrication of micro-needle electrodes for bio-signal recording by a magnetization-induced self-assembly method. Sensors, 16, 1533.

CHEN, W., WANG, C., YAN, L., HUANG, L., ZHU, X., CHEN, B., SANT, H. J., NIU, X., ZHU, G. & YU, K. 2014. Improved polyvinylpyrrolidone microneedle arrays with non-stoichiometric cyclodextrin. Journal of Materials Chemistry B, 2, 1699-1705.

CHEN, Y.-H. 2016. Polymer-based Dry Electrodes for Biopotential Measurements.

CHOI, J.-W. 2007. Development of projection-based microstereolithography apparatus adapted to large surface and microstructure fabrication for human body application. Pusan National University.

CHOI, J.-W., PARK, I.-B., HA, Y.-M., JUNG, M.-G. & LEE, S.-H. Insertion force estimation of various microneedle array-type structures fabricated by a microstereolithography apparatus. SICE-ICASE, 2006. International Joint Conference, 2006. IEEE, 3678-3681.

CHOI, S.-O., KIM, Y. C., PARK, J.-H., HUTCHESON, J., GILL, H. S., YOON, Y.-K., PRAUSNITZ, M. R. & ALLEN, M. G. 2010. An electrically active microneedle array for electroporation. Biomedical microdevices, 12, 263-273.

CHOI, S.-O., PARK, J.-H., CHOI, Y., KIM, Y., GILL, H. S., YOON, Y.-K., PRAUSNITZ, M. R. & ALLEN, M. G. An electrically active microneedle array for electroporation of skin for gene delivery. Solid-State Sensors, Actuators and Microsystems, 2005. Digest of Technical Papers. TRANSDUCERS'05. The 13th International Conference on, 2005. IEEE, 1513-1516.

CHOWDHURY, T. 1969. Fabrication of extremely fine glass micropipette electrodes. Journal of Physics E: Scientific Instruments, 2, 1087.

CHU, L. Y., CHOI, S.-O. & PRAUSNITZ, M. R. 2010. Fabrication of dissolving polymer microneedles for controlled drug encapsulation and delivery: bubble and pedestal microneedle designs. Journal of pharmaceutical sciences, 99, 4228-4238.

CHUA, B., DESAI, S. P., TIERNEY, M. J., TAMADA, J. A. & JINA, A. N. 2013. Effect of microneedles shape on skin penetration and minimally invasive continuous glucose monitoring in vivo. Sensors and Actuators A: Physical, 203, 373-381.

COLIN, S. 2004. Microfluidique. Trait {é} Egem. Hermes Science Publications.

CONRADIE, E. H. & MOORE, D. F. 2002. SU-8 thick photoresist processing as a functional material for MEMS applications. Journal of Micromechanics and Microengineering, 12, 368.

CORMIER, M. J., NAT, A. S., NEUKERMANS, A. P. & BLOCK, B. 2001. Device for enhancing transdermal agent delivery or sampling. Google Patents.

DAI, W., LIAN, K. & WANG, W. 2005. A quantitative study on the adhesion property of cured SU-8 on various metallic surfaces. Microsystem technologies, 11, 526-534.

DAVIS, S. P., LANDIS, B. J., ADAMS, Z. H., ALLEN, M. G. & PRAUSNITZ, M. R. 2004. Insertion of microneedles into skin: measurement and prediction of insertion force and needle fracture force. Journal of biomechanics, 37, 1155-1163.

DEL CAMPO, A. & GREINER, C. 2007. SU-8: a photoresist for high-aspect-ratio and 3D submicron lithography. Journal of Micromechanics and Microengineering, 17, R81.

DING, H., LU, J. Q., WOODEN, W. A., KRAGEL, P. J. & HU, X.-H. 2006. Refractive indices of human skin tissues at eight wavelengths and estimated dispersion relations between 300 and 1600 nm. Physics in Medicine & Biology, 51, 1479.

DUAN, D., MOECKLY, C., GYSBERS, J., NOVAK, C., PROCHNOW, G., SIEBENALER, K., ALBERS, L. & HANSEN, K. 2011. Enhanced delivery of topically-applied formulations following skin pre-treatment with a hand-applied, plastic microneedle array. Current drug delivery, 8, 557-565.

ECONOMIDOU, S. N., LAMPROU, D. A. & DOUROUMIS, D. 2018. 3D printing applications for transdermal drug delivery. International Journal of Pharmaceutics.

EDELMAN, A., CHANSON, M. & HUG, M. J. 2004. Microelectrodes and their use to assess ion channel function. Journal of Cystic Fibrosis, 3, 113-117.

ERIKSSON, E. 1997. Gene delivery by microneedle injection. Google Patents.

FENG, R. & FARRIS, R. J. 2002. Influence of processing conditions on the thermal and mechanical properties of SU8 negative photoresist coatings. Journal of Micromechanics and Microengineering, 13, 80.

FERNÁNDEZ, L. J., ALTUNA, A., TIJERO, M., GABRIEL, G., VILLA, R., RODRÍGUEZ, M. J., BATLLE, M., VILARES, R., BERGANZO, J. & BLANCO, F. 2009. Study of

functional viability of SU-8-based microneedles for neural applications. Journal of Micromechanics and Microengineering, 19, 025007.

FILMS, D. High Performance Films: Kapton General Specifications. Bulletin GS-96-7, http://www. dupont. com/corp/markets/aerospace/products/kapton. html.

GARRA, J., LONG, T., CURRIE, J., SCHNEIDER, T., WHITE, R. & PARANJAPE, M. 2002. Dry etching of polydimethylsiloxane for microfluidic systems. Journal of Vacuum Science & Technology A: Vacuum, Surfaces, and Films, 20, 975-982.

GILL, H. S. & PRAUSNITZ, M. R. 2007. Coating formulations for microneedles. Pharmaceutical research, 24, 1369-1380.

GITTARD, S. D., MILLER, P. R., JIN, C., MARTIN, T. N., BOEHM, R. D., CHISHOLM, B. J., STAFSLIEN, S. J., DANIELS, J. W., CILZ, N. & MONTEIRO-RIVIERE, N. A. 2011. Deposition of antimicrobial coatings on microstereolithography-fabricated microneedles. Jom, 63, 59-68.

GITTARD, S. D. & NARAYAN, R. J. 2010. Laser direct writing of micro-and nano-scale medical devices. Expert review of medical devices, 7, 343-356.

GITTARD, S. D., OVSIANIKOV, A., MONTEIRO-RIVIERE, N. A., LUSK, J., MOREL, P., MINGHETTI, P., LENARDI, C., CHICHKOV, B. N. & NARAYAN, R. J. 2009. Fabrication of polymer microneedles using a two-photon polymerization and micromolding process. Journal of diabetes science and technology, 3, 304-311.

GOLPARVAR, A. J. & YAPICI, M. K. Wearable graphene textile-enabled EOG sensing. SENSORS, 2017 IEEE, 2017. IEEE, 1-3.

GORDON, J. W., LIH, C. H., NAVOT, D., ZETNER, B.-S. & LAUFER, N. 1993. A new rapid method of producing microneedles for subzonal sperm insertion. Journal of assisted reproduction and genetics, 10, 444-448.

GRISS, P., ENOKSSON, P., TOLVANEN-LAAKSO, H. K., MERILAINEN, P., OLLMAR, S. & STEMME, G. 2001. Micromachined electrodes for biopotential measurements. Journal of Microelectromechanical Systems, 10, 10-16.

GRISS, P., TOLVANEN-LAAKSO, H. K., MERILAINEN, P. & STEMME, G. 2002. Characterization of micromachined spiked biopotential electrodes. IEEE Transactions on Biomedical Engineering, 49, 597-604.

GUJJAR, M. & BANGA, A. K. 2014. Iontophoretic and microneedle mediated transdermal delivery of glycopyrrolate. Pharmaceutics, 6, 663-671.

HAMMACHER, J., FUELLE, A., FLAEMIG, J., SAUPE, J., LOECHEL, B. & GRIMM, J. 2008. Stress engineering and mechanical properties of SU-8-layers for mechanical applications. Microsystem Technologies, 14, 1515-1523.

HAN, M., HYUN, D.-H., PARK, H.-H., LEE, S. S., KIM, C.-H. & KIM, C. 2007. A novel fabrication process for out-of-plane microneedle sheets of biocompatible polymer. Journal of Micromechanics and Microengineering, 17, 1184.

HECKELE, M., BACHER, W. & MÜLLER, K. 1998. Hot embossing-the molding technique for plastic microstructures. Microsystem technologies, 4, 122-124.

HELD, J., GASPAR, J., RUTHER, P., HAGNER, M., CISMAK, A., HEILMANN, A. & PAUL, O. 2010. Design of experiment characterization of microneedle fabrication processes based on dry silicon etching. Journal of Micromechanics and Microengineering, 20, 025024.

HENRY, S., MCALLISTER, D. V., ALLEN, M. G. & PRAUSNITZ, M. R. 1998. Microfabricated microneedles: a novel approach to transdermal drug delivery. Journal of pharmaceutical sciences, 87, 922-925.

HEYDERMAN, L., SCHIFT, H., DAVID, C., GOBRECHT, J. & SCHWEIZER, T. 2000. Flow behaviour of thin polymer films used for hot embossing lithography. Microelectronic Engineering, 54, 229-245.

HOOD, R. L., KOSOGLU, M. A., PARKER, M. & RYLANDER, C. G. 2011. Effects of microneedle design parameters on hydraulic resistance. Journal of medical devices, 5, 031012.

HUANG, W., BHULLAR, R. S. & FUNG, Y. C. 2001. The surface-tension-driven flow of blood from a droplet into a capillary tube. Journal of biomechanical engineering, 123, 446-454.

HUIGEN, E., PEPER, A. & GRIMBERGEN, C. 2002. Investigation into the origin of the noise of surface electrodes. Medical and biological engineering and computing, 40, 332-338.

HWANG, H. H., ZHU, W., VICTORINE, G., LAWRENCE, N. & CHEN, S. 2018. 3D-Printing of Functional Biomedical Microdevices via Light-and Extrusion-Based Approaches. Small Methods, 2, 1700277.

ITA, K. 2017. Dissolving microneedles for transdermal drug delivery: Advances and challenges. Biomedicine & Pharmacotherapy, 93, 1116-1127.

ITO, Y., HIRONO, M., FUKUSHIMA, K., SUGIOKA, N. & TAKADA, K. 2012. Two-layered dissolving microneedles formulated with intermediate-acting insulin. International journal of pharmaceutics, 436, 387-393.

JAHNKE, M. T. 1982. Properties of a microcoaxial electrode designed for unit recording from human peripheral nerves. Journal of neuroscience methods, 6, 335-346.

JANSEN, H., GARDENIERS, H., DE BOER, M., ELWENSPOEK, M. & FLUITMAN, J. 1996. A survey on the reactive ion etching of silicon in microtechnology. Journal of micromechanics and microengineering, 6, 14.

JEON, E., CHOI, S., YEO, K.-H., PARK, K. S., RATHOD, M. L. & LEE, J. 2017. Development of electrical conductivity measurement technology for key plant physiological information using microneedle sensor. Journal of Micromechanics and Microengineering, 27, 085009.

JI, J., TAY, F. E. & MIAO, J. Microfabricated hollow microneedle array using ICP etcher. Journal of Physics: Conference Series, 2006a. IOP Publishing, 1132.

JI, J., TAY, F. E., MIAO, J. & SUN, J. Characterization of silicon isotropic etch by inductively coupled plasma etcher for microneedle array fabrication. Journal of Physics: Conference Series, 2006b. IOP Publishing, 1137.

JIN, C. Y., HAN, M. H., LEE, S. S. & CHOI, Y. H. 2009. Mass producible and biocompatible microneedle patch and functional verification of its usefulness for transdermal drug delivery. Biomedical microdevices, 11, 1195.

JONES, K. E., CAMPBELL, P. K. & NORMANN, R. A. 1992. A glass/silicon composite intracortical electrode array. Annals of biomedical engineering, 20, 423-437.

JUN, J. J., STEINMETZ, N. A., SIEGLE, J. H., DENMAN, D. J., BAUZA, M., BARBARITS, B., LEE, A. K., ANASTASSIOU, C. A., ANDREI, A. & AYDıN, Ç. 2017. Fully integrated silicon probes for high-density recording of neural activity. Nature, 551, 232.

KAVALDZHIEV, M., PEREZ, J. E., IVANOV, Y., BERTONCINI, A., LIBERALE, C. & KOSEL, J. 2017. Biocompatible 3D printed magnetic micro needles. Biomedical Physics & Engineering Express, 3, 025005.

KHANNA, P., LUONGO, K., STROM, J. A. & BHANSALI, S. 2010. Axial and shear fracture strength evaluation of silicon microneedles. Microsystem Technologies, 16, 973-978.

KIM, C.-H., HYUN, D.-H., LEE, S.-S. & HAN, M.-H. 2009. Micro needle roller assembly. Google Patents.

KIM, J. D., KIM, M., YANG, H., LEE, K. & JUNG, H. 2013. Droplet-born air blowing: Novel dissolving microneedle fabrication. Journal of controlled release, 170, 430-436.

KIM, K., PARK, D. S., LU, H. M., CHE, W., KIM, K., LEE, J.-B. & AHN, C. H. 2004. A tapered hollow metallic microneedle array using backside exposure of SU-8. Journal of Micromechanics and Microengineering, 14, 597.

KIM, K., PARK, S., LEE, J.-B., MANOHARA, H., DESTA, Y., MURPHY, M. & AHN, C. H. 2002. Rapid replication of polymeric and metallic high aspect ratio microstructures using PDMS and LIGA technology. Microsystem Technologies, 9, 5-10.

KIM, M., AN, J., KIM, K. S., CHOI, M., HUMAR, M., KWOK, S. J., DAI, T. & YUN, S. H. 2016. Optical lens-microneedle array for percutaneous light delivery. Biomedical optics express, 7, 4220-4227.

KIM, Y.-C., PARK, J.-H. & PRAUSNITZ, M. R. 2012. Microneedles for drug and vaccine delivery. Advanced drug delivery reviews, 64, 1547-1568.

KOCHHAR, J. S., QUEK, T. C., SOON, W. J., CHOI, J., ZOU, S. & KANG, L. 2013. Effect of microneedle geometry and supporting substrate on microneedle array penetration into skin. Journal of Pharmaceutical Sciences, 102, 4100-4108.

KUO, S.-C. & CHOU, Y.-K. 2006. Microneedle array device and its fabrication method. Google Patents.

KUO, S.-C. & CHOU, Y. 2004. A novel polymer microneedle arrays and PDMS micromolding technique. 淡江理工學刊, 7, 95-98.

KWON, K. Y., KHOMENKO, A., HAQ, M. & LI, W. Integrated slanted microneedle-LED array for optogenetics. Engineering in Medicine and Biology Society (EMBC), 2013 35th Annual International Conference of the IEEE, 2013. IEEE, 249-252.

KWON, K. Y., WEBER, A. & LI, W. 2014. Varying-length polymer microneedle arrays fabricated by droplet backside exposure. Journal of Microelectromechanical Systems, 23, 1272-1280.

LAERMER, F., FRANSSILA, S., SAINIEMI, L. & KOLARI, K. 2015. Deep reactive ion etching. Handbook of Silicon Based MEMS Materials and Technologies (Second Edition). Elsevier.

LARRANETA, E., LUTTON, R. E., WOOLFSON, A. D. & DONNELLY, R. F. 2016. Microneedle arrays as transdermal and intradermal drug delivery systems: materials science, manufacture and commercial development. Materials Science and Engineering: R: Reports, 104, 1-32.

LARRAÑETA, E., STEWART, S., FALLOWS, S. J., BIRKHÄUER, L. L., MCCRUDDEN, M. T., WOOLFSON, A. D. & DONNELLY, R. F. 2016. A facile system to evaluate in vitro drug release from dissolving microneedle arrays. International journal of pharmaceutics, 497, 62-69.

LAWES, R. A. 2005. Manufacturing tolerances for UV LIGA using SU-8 resist. Journal of Micromechanics and Microengineering, 15, 2198.

LEE, D.-S., LI, C. G., IHM, C. & JUNG, H. 2018. A three-dimensional and bevel-angled ultrahigh aspect ratio microneedle for minimally invasive and painless blood sampling. Sensors and Actuators B: Chemical, 255, 384-390.

LEE, J. & HONG, S. I. 2008. Electrically conductive microneedle roller. Google Patents.

LEE, J. W., PARK, J.-H. & PRAUSNITZ, M. R. 2008. Dissolving microneedles for transdermal drug delivery. Biomaterials, 29, 2113-2124.

LEE, K., LEE, H. C., LEE, D. S. & JUNG, H. 2010a. Drawing lithography: three-dimensional fabrication of an ultrahigh-aspect-ratio microneedle. Advanced Materials, 22, 483-486.

LEE, S. Fabrication of microneedle array using inclined LIGA process. TRANSDUCERS, Solid-State Sensors, Actuators and Microsystems, 12th International Conference on, 2003, 2003. IEEE, 1546-1549.

LEE, S. S., SUL, B. J. & HAN, M. H. 2010b. Microneedle roller and stamp adapted to enable the replacement of microneedles. Google Patents.

LEVICK, W. 1972. Another tungsten microelectrode. Medical and Biological Engineering, 10, 510-515.

LHERNOULD, M. S. 2013. Optimizing hollow microneedles arrays aimed at transdermal drug delivery. Microsystem technologies, 19, 1-8.

LI, C. G., DANGOL, M., LEE, C. Y., JANG, M. & JUNG, H. 2015. A self-powered one-touch blood extraction system: a novel polymer-capped hollow microneedle integrated with a pre-vacuum actuator. Lab on a Chip, 15, 382-390.

LI, C. G., LEE, C. Y., LEE, K. & JUNG, H. 2013. An optimized hollow microneedle for minimally invasive blood extraction. Biomedical microdevices, 15, 17-25.

LIN, L. & PISANO, A. P. 1999a. IC-processed microneedles. Google Patents.

LIN, L. & PISANO, A. P. 1999b. Silicon-processed microneedles. Journal of Microelectromechanical Systems, 8, 78-84.

LIPPMANN, J. M., GEIGER, E. J. & PISANO, A. P. 2007. Polymer investment molding: method for fabricating hollow, microscale parts. Sensors and Actuators A: Physical, 134, 2-10.

LIU, C. 2007. Recent developments in polymer MEMS. Advanced Materials, 19, 3783-3790.

LORENZ, H., DESPONT, M., FAHRNI, N., BRUGGER, J., VETTIGER, P. & RENAUD, P. 1998. High-aspect-ratio, ultrathick, negative-tone near-UV photoresist and its applications for MEMS. Sensors and Actuators A: Physical, 64, 33-39.

LORENZ, H., DESPONT, M., FAHRNI, N., LABIANCA, N., RENAUD, P. & VETTIGER, P. 1997. SU-8: a low-cost negative resist for MEMS. Journal of Micromechanics and Microengineering, 7, 121.

LU, Y., MANTHA, S. N., CROWDER, D. C., CHINCHILLA, S., SHAH, K. N., YUN, Y. H., WICKER, R. B. & CHOI, J.-W. 2015. Microstereolithography and characterization of poly (propylene fumarate)-based drug-loaded microneedle arrays. Biofabrication, 7, 045001.

LUTTON, R. E., LARRAÑETA, E., KEARNEY, M.-C., BOYD, P., WOOLFSON, A. D. & DONNELLY, R. F. 2015a. A novel scalable manufacturing process for the production of hydrogel-forming microneedle arrays. International journal of pharmaceutics, 494, 417-429.

LUTTON, R. E., MOORE, J., LARRAÑETA, E., LIGETT, S., WOOLFSON, A. D. & DONNELLY, R. F. 2015b. Microneedle characterisation: the need for universal acceptance criteria and GMP specifications when moving towards commercialisation. Drug delivery and translational research, 5, 313-331.

MAHADEVAN, G. 2011. Drug Delivery to the Posterior Eye Using Etched Microneedles.

MANSOOR, I., LIU, Y., HÄFELI, U. & STOEBER, B. Fabrication of hollow microneedle arrays using electrodeposition of metal onto solvent cast conductive polymer structures. Solid-State Sensors, Actuators and Microsystems (TRANSDUCERS & EUROSENSORS XXVII), 2013 Transducers & Eurosensors XXVII: The 17th International Conference on, 2013. IEEE, 373-376.

MARSHALL, S., SAHM, L. J. & MOORE, A. C. 2016. The success of microneedle-mediated vaccine delivery into skin. Human vaccines & immunotherapeutics, 12, 2975-2983.

MARTANTO, W., DAVIS, S. P., HOLIDAY, N. R., WANG, J., GILL, H. S. & PRAUSNITZ, M. R. 2004. Transdermal delivery of insulin using microneedles in vivo. Pharmaceutical research, 21, 947-952.

MARTANTO, W., MOORE, J. S., COUSE, T. & PRAUSNITZ, M. R. 2006. Mechanism of fluid infusion during microneedle insertion and retraction. Journal of Controlled Release, 112, 357-361.

MARTHAM, S. K., NAN, K. K. & SHAHIMIN, M. M. Refractive index modification of SU-8 polymer based waveguide via fabrication parameters. Research and Development (SCOReD), 2014 IEEE Student Conference on, 2014. IEEE, 1-5.

MARTIN, A., MCCONVILLE, A., ANDERSON, A., MCLISTER, A. & DAVIS, J. 2017. Microneedle Manufacture: Assessing Hazards and Control Measures. Safety, 3, 25.

MARUO, S., IKUTA, K. & KOROGI, H. 2003. Submicron manipulation tools driven by light in a liquid. Applied Physics Letters, 82, 133-135.

MCGRATH, M. G., VRDOLJAK, A., O'MAHONY, C., OLIVEIRA, J. C., MOORE, A. C. & CREAN, A. M. 2011. Determination of parameters for successful spray coating of silicon microneedle arrays. International journal of pharmaceutics, 415, 140-149.

MIKLAVČIČ, D., PAVŠELJ, N. & HART, F. X. 2006. Electric properties of tissues. Wiley encyclopedia of biomedical engineering.

MILLER, P. R., XIAO, X., BRENER, I., BURCKEL, D. B., NARAYAN, R. & POLSKY, R. 2014. Microneedle-Based Transdermal Sensor for On-Chip Potentiometric Determination of K+. Advanced healthcare materials, 3, 876-881.

MOON, S. J., JIN, C. Y. & LEE, S. S. A novel method of microneedle array fabrication using inclined deep x-ray exposure. Journal of Physics: Conference Series, 2006. IOP Publishing, 180.

MOON, S. J., LEE, S. S., LEE, H. & KWON, T. 2005. Fabrication of microneedle array using LIGA and hot embossing process. Microsystem technologies, 11, 311-318.

NEJAD, H. R., SADEQI, A., KIAEE, G. & SONKUSALE, S. 2018. Low-cost and cleanroom-free fabrication of microneedles. Microsystems & Nanoengineering, 4, 17073.

NEMANI, K. V., MOODIE, K. L., BRENNICK, J. B., SU, A. & GIMI, B. 2013. In vitro and in vivo evaluation of SU-8 biocompatibility. Materials Science and Engineering: C, 33, 4453-4459.

NORMANN, R. A. 2007. Technology insight: future neuroprosthetic therapies for disorders of the nervous system. Nature Reviews Neurology, 3, 444.

OKADA, Y. & INOUYE, A. 1975. Tip potential and fixed charges on the glass wall of microelectrode. Experientia, 31, 545-546.

OSTERELE, A. 2011. P-1000 & P-97 pipette cookbook. Sutter Instruments.

OVSIANIKOV, A., CHICHKOV, B., MENTE, P., MONTEIRO-RIVIERE, N., DORAISWAMY, A. & NARAYAN, R. 2007. Two photon polymerization of polymer–ceramic hybrid materials for transdermal drug delivery. International journal of applied ceramic technology, 4, 22-29.

PAEK, J. & KIM, J. 2014. Microsphere-assisted fabrication of high aspect-ratio elastomeric micropillars and waveguides. Nature communications, 5, 3324.

PAIK, S.-J., BYUN, S., LIM, J.-M., PARK, Y., LEE, A., CHUNG, S., CHANG, J. & CHUN, K. 2004. In-plane single-crystal-silicon microneedles for minimally invasive microfluid systems. Sensors and Actuators A: Physical, 114, 276-284.

PARIDA, O. P. & BHAT, N. Characterization of optical properties of SU-8 and fabrication of optical components. Int. Conf. on Opt. and Photon.(CSIO), 2009. 4-7.

PARK, J.-H., ALLEN, M. G. & PRAUSNITZ, M. R. 2005. Biodegradable polymer microneedles: fabrication, mechanics and transdermal drug delivery. Journal of Controlled Release, 104, 51-66.

PARK, J.-H., ALLEN, M. G. & PRAUSNITZ, M. R. 2006. Polymer microneedles for controlled-release drug delivery. Pharmaceutical research, 23, 1008-1019.

PARK, J.-H., CHOI, S.-O., KAMATH, R., YOON, Y.-K., ALLEN, M. G. & PRAUSNITZ, M. R. 2007a. Polymer particle-based micromolding to fabricate novel microstructures. Biomedical microdevices, 9, 223-234.

PARK, J.-H., CHOI, S.-O., SEO, S., CHOY, Y. B. & PRAUSNITZ, M. R. 2010. A microneedle roller for transdermal drug delivery. European journal of pharmaceutics and biopharmaceutics, 76, 282-289.

PARK, J.-H. & PRAUSNITZ, M. R. 2010. Analysis of mechanical failure of polymer microneedles by axial force. The journal of the Korean Physical Society, 56, 1223.

PARK, J.-H., YOON, Y.-K., CHOI, S.-O., PRAUSNITZ, M. R. & ALLEN, M. G. 2007b. Tapered conical polymer microneedles fabricated using an integrated lens technique for transdermal drug delivery. IEEE transactions on biomedical engineering, 54, 903-913.

PARK, J.-H., YOON, Y.-K., PRAUSNITZ, M. R. & ALLEN, M. G. High-aspect-ratio tapered structures using an integrated lens technique. Micro Electro Mechanical Systems, 2004. 17th IEEE International Conference on.(MEMS), 2004. IEEE, 383-386.

PARKER, E., RAO, M., TURNER, K., MEINHART, C. & MACDONALD, N. 2007. Bulk micromachined titanium microneedles. Journal of microelectromechanical systems, 16, 289-295.

PATEL, J. N., KAMINSKA, B., GRAY, B. L. & GATES, B. D. 2008. PDMS as a sacrificial substrate for SU-8-based biomedical and microfluidic applications. Journal of Micromechanics and Microengineering, 18, 095028.

PATEL, Y. A., WILLSIE, A., CLEMENTS, I. P., AGUILAR, R., RAJARAMAN, S. & BUTERA, R. J. Microneedle cuff electrodes for extrafascicular peripheral nerve interfacing. Engineering in Medicine and Biology Society (EMBC), 2016 IEEE 38th Annual International Conference of the, 2016. IEEE, 1741-1744.

PEIXOTO, A., GONCALVES, S., PINHO, F., SILVA, A., DIAS, N. & CORREIA, J. 2014. Flexible three-dimensional microelectrode array for neural applications. Sensors and Actuators A: Physical, 217, 21-28.

PERENNES, F., MARMIROLI, B., MATTEUCCI, M., TORMEN, M., VACCARI, L. & DI FABRIZIO, E. 2006. Sharp beveled tip hollow microneedle arrays fabricated by LIGA and 3D soft lithography with polyvinyl alcohol. Journal of Micromechanics and Microengineering, 16, 473.

PINI, F., O'MAHONY, C. & MCCARTHY, K. G. Electrical characterisation of dry microneedle electrodes for portable bio-potential recording applications. Microelectronic Test Structures (ICMTS), 2012 IEEE International Conference on, 2012. IEEE, 87-90.

PRASAD, L. K. & SMYTH, H. 2016. 3D Printing technologies for drug delivery: a review. Drug development and industrial pharmacy, 42, 1019-1031.

PRAUSNITZ, M. R. 2004. Microneedles for transdermal drug delivery. Advanced drug delivery reviews, 56, 581-587.

QUAN, F.-S., KIM, Y.-C., SONG, J.-M., HWANG, H. S., COMPANS, R. W., PRAUSNITZ, M. R. & KANG, S.-M. 2013. Long-term protective immunity from an influenza virus-like particle vaccine administered with a microneedle patch. Clinical and Vaccine Immunology, 20, 1433-1439.

RAJABI, M., ROXHED, N., SHAFAGH, R. Z., HARALDSON, T., FISCHER, A. C., VAN DER WIJNGAART, W., STEMME, G. & NIKLAUS, F. 2016. Flexible and stretchable microneedle patches with integrated rigid stainless steel microneedles for transdermal biointerfacing. PloS one, 11, e0166330.

REITBOECK, H. 1983. Fiber microelectrodes for electrophysiological recordings. Journal of neuroscience methods, 8, 249-262.

REN, L., JIANG, Q., CHEN, K., CHEN, Z., PAN, C. & JIANG, L. 2016. Fabrication of a micro-needle array electrode by thermal drawing for bio-signals monitoring. Sensors, 16, 908.

REN, L., JIANG, Q., CHEN, Z., CHEN, K., XU, S., GAO, J. & JIANG, L. 2017. Flexible microneedle array electrode using magnetorheological drawing lithography for bio-signal monitoring. Sensors and Actuators A: Physical, 268, 38-45.

RESNIK, D., MOŽEK, M., PEČAR, B., JANEŽ, A., URBANČIČ, V., ILIESCU, C. & VRTAČNIK, D. 2018. In Vivo Experimental Study of Noninvasive Insulin Microinjection through Hollow Si Microneedle Array. Micromachines, 9, 40.

RÖMGENS, A., BADER, D., BOUWSTRA, J. A., BAAIJENS, F. & OOMENS, C. 2014. Monitoring the penetration process of single microneedles with varying tip diameters. journal of the mechanical behavior of biomedical materials, 40, 397-405.

ROXHED, N., GRISS, P. & STEMME, G. 2007. A method for tapered deep reactive ion etching using a modified Bosch process. Journal of Micromechanics and Microengineering, 17, 1087.

ROXHED, N., SAMEL, B., NORDQUIST, L., GRISS, P. & STEMME, G. 2008. Painless drug delivery through microneedle-based transdermal patches featuring active infusion. IEEE Transactions on Biomedical Engineering, 55, 1063-1071.

SAGE JR, B. H. & GILLETT, D. 2009. Laminated sprinkler hypodermic needle. Google Patents.

SAWAHATA, H., YAMAGIWA, S., MORIYA, A., DONG, T., OI, H., ANDO, Y., NUMANO, R., ISHIDA, M., KOIDA, K. & KAWANO, T. 2016. Single 5 μm diameter needle electrode block modules for unit recordings in vivo. Scientific reports, 6, 35806.

SCHMIDT, V., KUNA, L., SATZINGER, V., JAKOPIC, G. & LEISING, G. 2007. Two-photon 3D lithography: A Versatile Fabrication Method for Com-plex 3D Shapes and Optical Interconnects within the Scope of Innovative Industrial Applications.

SCHOLVIN, J., KINNEY, J. P., BERNSTEIN, J. G., MOORE-KOCHLACS, C., KOPELL, N., FONSTAD, C. G. & BOYDEN, E. S. 2016. Close-packed silicon microelectrodes for scalable spatially oversampled neural recording. IEEE Transactions on Biomedical Engineering, 63, 120-130.

SEIDL, K., SCHWAERZLE, M., ULBERT, I., NEVES, H. P., PAUL, O. & RUTHER, P. 2012. CMOS-based high-density silicon microprobe arrays for electronic depth control in intracortical neural recording–characterization and application. Journal of Microelectromechanical Systems, 21, 1426-1435.

SEYMOUR, J. P., WU, F., WISE, K. D. & YOON, E. 2017. State-of-the-art MEMS and microsystem tools for brain research. Microsystems & Nanoengineering, 3, 16066.

SHARPE JR, W. & BAGDAHN, J. 2004. Fatigue testing of polysilicon—a review. Mechanics of Materials, 36, 3-11.

SHARPE, W. N., JACKSON, K. M., HEMKER, K. J. & XIE, Z. 2001. Effect of specimen size on Young's modulus and fracture strength of polysilicon. Journal of Microelectromechanical systems, 10, 317-326.

SHIH, C. C., SHIH, C. M., CHOU, K. Y., LIN, S. J., SU, Y. Y. & GERHARDT, R. A. 2007. Mechanism of degradation of AgCL coating on biopotential sensors. Journal of Biomedical Materials Research Part A, 82, 872-883.

SHIKIDA, M., ODAGAKI, M., TODOROKI, N., ANDO, M., ISHIHARA, Y., ANDO, T. & SATO, K. 2004. Non-photolithographic pattern transfer for fabricating arrayed three-dimensional microstructures by chemical anisotropic etching. Sensors and Actuators A: Physical, 116, 264-271.

SHIRTCLIFFE, N. J., AQIL, S., EVANS, C., MCHALE, G., NEWTON, M. I., PERRY, C. C. & ROACH, P. 2004. The use of high aspect ratio photoresist (SU-8) for super-hydrophobic pattern prototyping. Journal of Micromechanics and Microengineering, 14, 1384.

SHOBE, J. L., CLAAR, L. D., PARHAMI, S., BAKHURIN, K. I. & MASMANIDIS, S. C. 2015. Brain activity mapping at multiple scales with silicon microprobes containing 1,024 electrodes. Journal of neurophysiology, 114, 2043-2052.

SMART, W. H. & SUBRAMANIAN, K. 2000. The use of silicon microfabrication technology in painless blood glucose monitoring. Diabetes technology & therapeutics, 2, 549-559.

SOLTANZADEH, R., AFSHARIPOUR, E., SHAFAI, C., ANSSARI, N., MANSOURI, B. & MOUSSAVI, Z. 2018. Molybdenum coated SU-8 microneedle electrodes for transcutaneous electrical nerve stimulation. Biomedical microdevices, 20, 1.

SRIVASTAVA, A. K., BHARTIA, B., MUKHOPADHYAY, K. & SHARMA, A. 2015. Long term biopotential recording by body conformable photolithography fabricated low cost polymeric microneedle arrays. Sensors and Actuators A: Physical, 236, 164-172.

STAVRINIDIS, G., MICHELAKIS, K., KONTOMITROU, V., GIANNAKAKIS, G., SEVRISARIANOS, M., SEVRISARIANOS, G., CHANIOTAKIS, N., ALIFRAGIS, Y. & KONSTANTINIDIS, G. 2016. SU-8 microneedles based dry electrodes for Electroencephalogram. Microelectronic Engineering, 159, 114-120.

STOEBER, B. & LIEPMANN, D. Fluid injection through out-of-plane microneedles. Microtechnologies in Medicine and Biology, 1st Annual International, Conference On. 2000, 2000. IEEE, 224-228.

STOEBER, B. & LIEPMANN, D. 2005. Arrays of hollow out-of-plane microneedles for drug delivery. Journal of microelectromechanical systems, 14, 472-479.

SULLIVAN, S. P., MURTHY, N. & PRAUSNITZ, M. R. 2008. Minimally invasive protein delivery with rapidly dissolving polymer microneedles. Advanced materials, 20, 933-938.

TAKAHASHI, H., HEO, Y. J., ARAKAWA, N., KAN, T., MATSUMOTO, K., KAWANO, R. & SHIMOYAMA, I. 2016. Scalable fabrication of microneedle arrays via spatially controlled UV exposure. Microsystems & Nanoengineering, 2, 16049.

THAKUR, R. R. S., TEKKO, I. A., AL-SHAMMARI, F., ALI, A. A., MCCARTHY, H. & DONNELLY, R. F. 2016. Rapidly dissolving polymeric microneedles for minimally invasive intraocular drug delivery. Drug delivery and translational research, 6, 800-815.

TOMONO, T. 2018. Puncture performance of sharpen microneedles by using inclined contact UV lithography. Microsystem Technologies, 1-11.

TRAUTMAN, J. C., CORMIER, M. J., KIM, H. L. & ZUCK, M. G. 2000. Device for enhancing transdermal agent flux. Google Patents.

TRENTLER, T. J., HICKMAN, K. M., GOEL, S. C., VIANO, A. M., GIBBONS, P. C. & BUHRO, W. E. 1995. Solution-liquid-solid growth of crystalline III-V semiconductors: an analogy to vapor-liquid-solid growth. Science, 270, 1791-1794.

TRICHUR, R., KIM, S., ZHU, X., SUK, J. W., HONG, C.-C., CHOI, J.-W. & AHN, C. H. Development of plastic microneedles for transdermal interfacing using injection molding techniques. Micro Total Analysis Systems 2002, 2002. Springer, 395-397.

TU, K. & CHUNG, C. 2016. Rapid prototyping of biodegradable microneedle arrays by integrating CO2 laser processing and polymer molding. Journal of Micromechanics and Microengineering, 26, 065015.

VAN DAMME, P., OOSTERHUIS-KAFEJA, F., VAN DER WIELEN, M., ALMAGOR, Y., SHARON, O. & LEVIN, Y. 2009. Safety and efficacy of a novel microneedle device for dose sparing intradermal influenza vaccination in healthy adults. Vaccine, 27, 454-459.

VAN DER MAADEN, K., JISKOOT, W. & BOUWSTRA, J. 2012. Microneedle technologies for (trans) dermal drug and vaccine delivery. Journal of controlled release, 161, 645-655.

VASYLIEVA, N., MARINESCO, S., BARBIER, D. & SABAC, A. 2015. Silicon/SU8 multi-electrode micro-needle for in vivo neurochemical monitoring. Biosensors and Bioelectronics, 72, 148-155.

VINAYAKUMAR, K., KULKARNI, P. G., NAYAK, M., DINESH, N., HEGDE, G. M., RAMACHANDRA, S. & RAJANNA, K. 2016. A hollow stainless steel microneedle array to deliver insulin to a diabetic rat. Journal of Micromechanics and Microengineering, 26, 065013.

WAGNER, R. & ELLIS, W. 1964. Vapor-liquid-solid mechanism of single crystal growth. Applied Physics Letters, 4, 89-90.

WANG, P.-C., WESTER, B. A., RAJARAMAN, S., PAIK, S.-J., KIM, S.-H. & ALLEN, M. G. Hollow polymer microneedle array fabricated by photolithography process combined with micromolding technique. Engineering in Medicine and Biology Society, 2009. EMBC 2009. Annual International Conference of the IEEE, 2009. IEEE, 7026-7029.

WANG, P. M., CORNWELL, M., HILL, J. & PRAUSNITZ, M. R. 2006. Precise microinjection into skin using hollow microneedles. Journal of investigative dermatology, 126, 1080-1087.

WANG, R., JIANG, X., WANG, W. & LI, Z. 2017. A microneedle electrode array on flexible substrate for long-term EEG monitoring. Sensors and Actuators B: Chemical, 244, 750-758.

WANG, R., WEI, Z., WANG, W. & LI, Z. Flexible microneedle electrode array based-on parylene substrate. Proceedings of the 16th International Conference on Miniaturized Systems for Chemistry and Life Sciences, Okinawa, Japan, 2012a. 1249-1251.

WANG, R., ZHAO, W., WANG, W. & LI, Z. 2012b. A flexible microneedle electrode array with solid silicon needles. Journal of Microelectromechanical Systems, 21, 1084-1089.

WARK, H., SHARMA, R., MATHEWS, K., FERNANDEZ, E., YOO, J., CHRISTENSEN, B., TRESCO, P., RIETH, L., SOLZBACHER, F. & NORMANN, R. 2013. A new high-density (25 electrodes/mm2) penetrating microelectrode array for recording and stimulating sub-millimeter neuroanatomical structures. Journal of neural engineering, 10, 045003.

WISE, K. D. & NAJAFI, K. 1991. Microfabrication techniques for integrated sensors and microsystems. Science, 254, 1335-1342.

WORGULL, M. 2009. Hot embossing: theory and technology of microreplication, William Andrew.

WU, Y. & YANG, P. 2001. Direct observation of vapor− liquid− solid nanowire growth. Journal of the American Chemical Society, 123, 3165-3166.

XIANG, Z., LIU, J. & LEE, C. 2016. A flexible three-dimensional electrode mesh: An enabling technology for wireless brain–computer interface prostheses. Microsystems & Nanoengineering, 2, 16012.

YOU, Y. S., LEE, C. Y., LI, C., LEE, S. H., KIM, K. & JUNG, H. 2014. An arched micro-injector (ARCMI) for innocuous subretinal injection. PloS one, 9, e104145.

ZAHN, J. D., TALBOT, N. H., LIEPMANN, D. & PISANO, A. P. 2000. Microfabricated polysilicon microneedles for minimally invasive biomedical devices. Biomedical microdevices, 2, 295-303.

ZHANG, Y., LO, C.-W., TAYLOR, J. A. & YANG, S. 2006. Replica molding of high-aspect-ratio polymeric nanopillar arrays with high fidelity. Langmuir, 22, 8595-8601.

ZHOU, C.-P., LIU, Y.-L., WANG, H.-L., ZHANG, P.-X. & ZHANG, J.-L. 2010. Transdermal delivery of insulin using microneedle rollers in vivo. International journal of pharmaceutics, 392, 127-133.

# 6

# Fabricating High Aspect Ratio SU-8 Microneedle Array Electrodes Using Dry Etching Method

## Summary

The negative photoresist SU-8 is becoming more popular in MEMS applications particularly for fabricating the high aspect ratio structures. This chapter is a demonstration of a fabrication process of a microneedle array of tapered microneedles make using SU-8. The goal of this study was to fabricate a 5 × 5 mm patch with a 10 × 10 array of SU-8 pillars. Different MN lengths from 600 to 850 µm were fabricated. In order to determine the best fabrication process, different RIE recipes were investigated. However, it was found that only the length of 100 µm could be fabricated. The results revealed that plasma etching is not a suitable method to fabricate a high aspect ratio structure from SU-8. Because of this, in chapter 7 an SU-8 molding process is explored.

## 6.1. Introduction

SU-8 has been widely used in high aspect ratio (HAR) structures either for mold purposes or as a main material of a final design (Bogdanov and Peredkov, 2000). After UV exposure, a post-exposure bake (PEB) is done to form cross-links inside the SU-8 by eight epoxy groups at each molecule. A suitable PEB time, like 10 to 15 minutes, will result in an SU-8 structure with a suitable mechanical strength and chemical stability needed for a HAR structure (Anhoj et al., 2006). The mechanical strength of a cured SU-8 structure enables the required skin piercing needed for an MNA, with the tips' diameters in the range of 25 µm to 30 µm. In addition, the SU-8 fabrication methods have a relatively low-price compared to the other silicon-based techniques, which make it suitable for fabricating disposable MNAs.

In this study, a fabrication process for a dense MNA from SU-8 was investigated. In the first step, a smooth thick layer of SU-8 (~ 600 µm) was prepared on top of a silicon wafer. Afterwards, the SU-8 was coated with a thin layer of chrome (Cr) using vacuum sputter deposition. This Cr layer was used as a plasma etch mask in the reactive ion etching (RIE) technique. After coating, the Cr was patterned by optical lithography, and the samples were prepared for plasma etching to form the pillars of the microneedle from the SU-8. This chapter will explore all the steps of fabrication in detail.

## 6.2. Methods and Materials

The process to fabricate the MN is illustrated in Fig. 6.1, and summarized in Table 6.1. The following sections detail these processes.

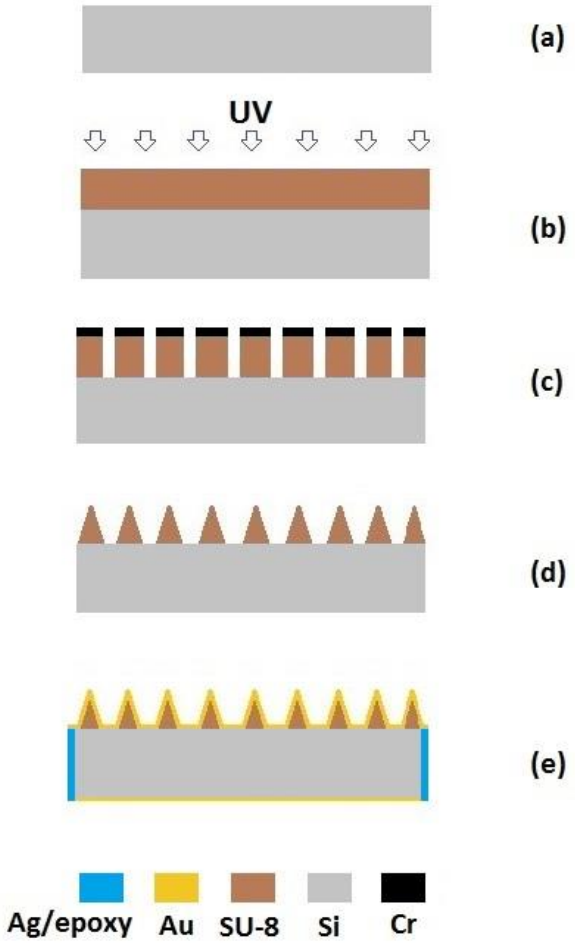


**Fig. 6. 1.** Fabrication process to form the SU-8 MNA.

**Table 6. 1.** Summarized fabrication processes

| Process name | Step |
|---|---|
| SU-8 preparation | Fig. 6.1.b |
| Preparing and patterning the metal mask | Fig. 6.1.c |
| Plasma etching form the needle pillars | Fig. 6.1.d |
| Metalizing the needles and connect them to the backside | Fig. 6.1.e |

### 6.2.1. Deposition of a thick layer of SU-8 on a silicon wafer

A silicon wafer was used as the substrate for the MNA fabrication. The un-polished side was chosen to increase the adhesion between the SU-8 and substrate, in order to avoid any shrinkage or wrinkle on the SU-8 surface. A thin layer (around 20 nm) of chromium could be sputtered on polished side of the silicon substrate in order to increase the adhesion of SU-8 to silicon. However, our experiments illustrated that the unpolished side of a silicon wafer is more adhesive to SU-8 than a thin layer of Cr.

A 3 inch diameter silicon wafer was cleaned by piranha solution (7:3 concentration ratio of $H_2SO_4/H_2O_2$). Afterwards, 10 ml of dense and highly viscose SU-8 MicroChem 2075 series, was spun on the at 50 rpm for 10 seconds, and spread thin at 1000 rpm for 30 seconds, to spread the photoresist evenly over the surface of the substrate. Since it was intended to work with a thick layer of SU-8, it is crucial to de-stress the material before any processing. Thus, the sample was left to rest at room temperature for 15 min to decrease the stress of the SU-8 in the superficial layers particularly.

In the soft-bake phase, the SU-8 solvent (cyclopentanone) is evaporated from the deep layers of the spun SU-8 completely. Otherwise, there will be trapped gas deep inside the SU-8, whereas

the upper layers lose the solvent. As shown in Fig. 6.2, the trapped gas will cause mechanical tension in the inner layers of the SU-8, which results in wrinkles on the surface of the photoresist. These wrinkles disappear after rewarming the sample, but they will remain at the surface of the sample permanently after exposure if the solvent is not evaporated in the deep layers.

**Fig. 6. 2.** Large wrinkles appear on the spun SU-8 surface due to solvent trapped in the inner layers of the coated SU-8.

To resolve this problem, all the solvent should be evaporated for the SU-8 during the soft bake procedure. This step must be done carefully to get rid of most of the solvent from the spun SU-8. In the suggested soft-bake procedure, to reduce the processing time and increase the quality of the photoresist, the pressure was gradually decreased while the temperature was rising. A study (Barhala et al., 2006) has shown that the evaporation temperature and pressure of cyclopentanone are relevant with the ratio 0.8. Using that result, the pressure was gradually decreased from almost $9.3\times10^4$ Pa to $1.01\times10^4$ Pa, while the temperature was increased from 25 °C to 95 °C. The samples were kept in these conditions for 30 minutes. If the soft bake was paused in this situation and the samples were inspected, the solvent bubbles could be seen in inner layers of SU-8 like what is shown in Fig. 6.3.a. After half an hour, the samples' weight decreased 1 gram, which implies that

1 gram of solvent was evaporated through the described procedure. At the end of the soft bake procedure, the coated SU-8 looked like what is shown in Fig. 6.3.b.

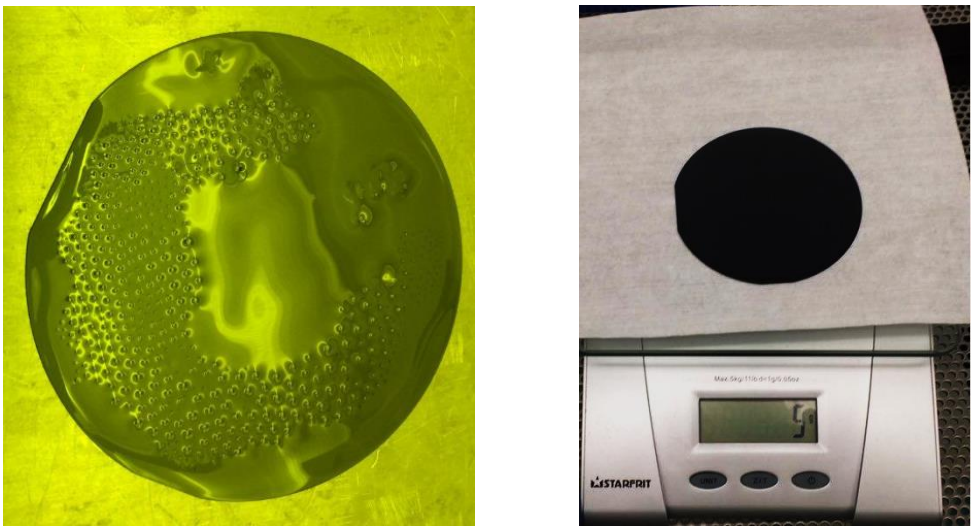


(a) (b)

**Fig. 6. 3.** (a) Solvent bubbles trapped in thick spun SU-8 on a silicon wafer (b) Uniform thick layer of SU-8 spun on the unpolished side of a silicon wafer.

### 6.2.2. Metal mask for plasma etching

In the next step, the soft-baked SU-8 was exposed to the ultraviolet (UV) light with the wavelength of 350 nm. Then, a layer of metal was sputtered on it that was patterned and used as a mask for plasma etching. Since the microneedle pillars were intended to be tall, a durable metal was needed that can tolerate the needed time required for the plasma etching. For this reason, two different metals were tried, Aluminum (Al) and Chrome (Cr), each with 45 nm thickness. During the experiments it was found that Cr resist was more than Al in the RIE plasma process, and the results of Cr mask are discussed in this chapter. The sputtered metal was lithographically patterned and then wet etched to form an array of circular Cr masks with 50 µm and 85 µm base diameter.

### 6.2.3. Plasma etching process

Different plasma etch recipes were investigated, with etching done in a Trion Phantom II ICP/RIE plasma etcher. The effect of changing 5 main parameters was explored. These parameters were etching pressure, plasma generator power (ICP), RF electric field (RIE), etching gas mixture of oxygen and $SF_6$ gases. Successful etching of the MN requires an appropriate balance between lateral undercut of the etch mask (isotropic etch), and vertical etching downwards (anisotropic etch), so as to make the needed tapered profile of the MN. This is illustrated in Fig.6.3b. In order to understand the best recipe for fabricating the SU-8 microneedles, 44 experiments were run. Fig. 6.3a shows one of the partially etched samples in which the mask was bombarded by the ions in plasma and its surface was roughened. We can also see some undercut of the chrome mask in this figure.

The 44 trials were run to study the relationships which control the lateral vs. vertical etch rate, which are needed to fabricate the tapered structure of the needle spike. The experiments are classified to 5 groups. In each group, one parameter was changed and the others were kept constant to investigate the effect of that particular parameter. Table 6.1 shows the base condition for all the sample groups. The results of the plasma etching were classified depending on the changed parameter and its influence on the etch rate. For example, if in an experiment the pressure was swept between from 20 - 100 mTorr, the other parameters were kept unchanged based on the principle values of Table 6.2. The results of the plasma etching are summarized in Table 6.3. In Table 6.3, the etch rates are separated into four categories: low etch rate (0.07-0.77 µm), mild etch rate (0.78-1.48 µm), moderate etch rate (1.49-2.19 µm) and the high etch rate (2.2-2.92 µm).

Amongst these experiments, 11 tries failed. In the failed efforts, either the metal mask peeled off or the sample was burned because of the high ICP power. In the cases where the mask was

peeled off, the speculated reasons were very high DC bias on the samples, or high $SF_6$ gas concentration that resulted in lots of (chemical based) isotropic etching that undercuts the mask a significant distance and so ends up in the removal of the metal mask (Fig. 6.4).

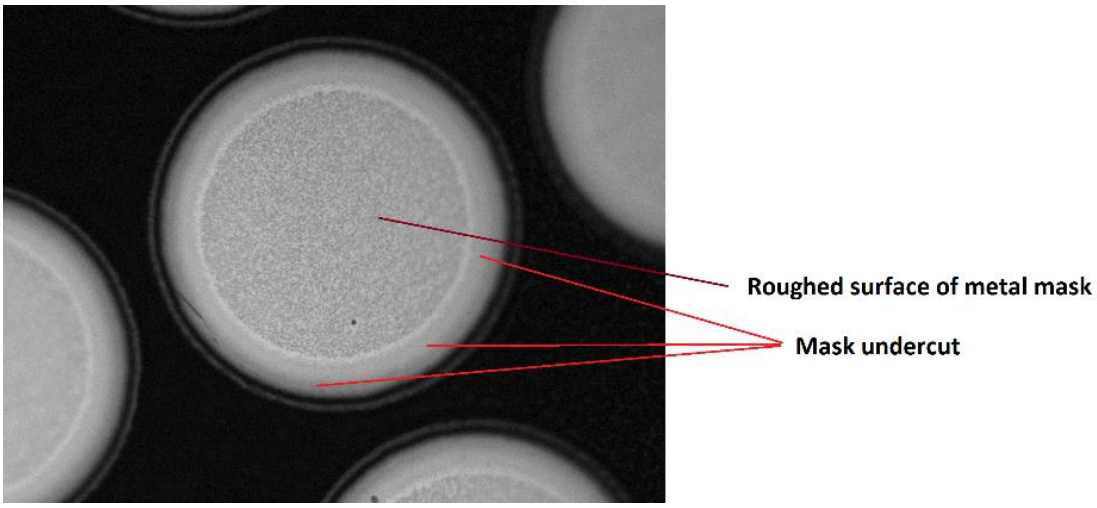


(a)

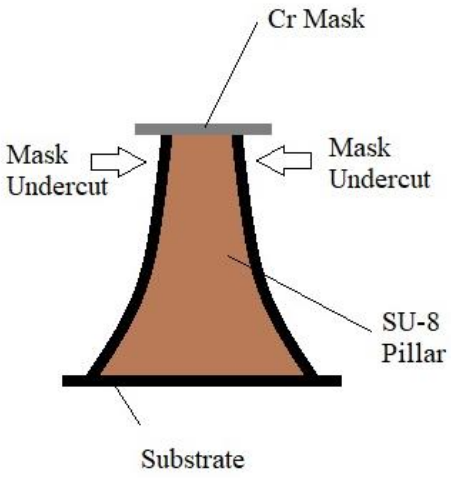


(b)

**Fig. 6. 4.** (a) Top view picture of the metal mask showing the visible undercut (the chrome metal has slight bending in the undercut region) during SU-8 plasma etching process. (b) Mask undercut (lateral view).

**Table 6. 2.** The initial value of the parameters

| Parameter | Base value |
|---|---|
| Pressure | 50 mTorr |
| ICP | 250 Watt |
| RIE | 100 Watt |
| % $O_2$ / $O_2$ + $SF_6$ | 90% |
| % $SF_6$ / $O_2$ + $SF_6$ | 10% |

**Table 6. 3.**The variation of each parameter and the resulting etch rate (E.R.)

| Parameters | Low E.R. | Mild E.R. | Moderate E.R. | High E.R. |
|---|---|---|---|---|
| Average of Pressure (mTorr) | 23 | 96 | 47 | 44 |
| $O_2$ flow percentage in the mixture of $O_2$ + $SF_6$ | 15-30 % | 90-93 % | 93-95 % | 80-90% |
| $SF_6$ flow percentage in the mixture of $O_2$ + $SF_6$ | 85-90 % | 70-75 % | 5-10 % | 20-10% |
| ICP (W) | 204 | 258 | 306 | 307 |
| RIE (W) | 50 | 152 | 206 | 104 |

### 6.2.4. Metallization of the MN

In the next step of fabrication, would have been the metallization of the MNs. However, since successful needles were not fabricated of appropriate length, this process was not done. The alternate process of Chapter 7 was used instead.

## 6.3. Discussion and Conclusion

This study was an attempt to fabricate a microneedle array through plasma etching of SU-8. The fabrication steps of this study were reviewed in Fig. 6.1 and Table 6.1 respectively. From the values of Table 6.3, one can understand that reducing pressure, will decrease the etch rate of the SU-8. There is a relationship between the oxygen gas ions and the etch rate, as the SU-8 etch rate reduces as the number of oxygen molecules reduce. The gas mixture ratio ($O_2$ / $O_2$ + $SF_6$) is an important factor in the anisotropic (formation of a more vertical slope angle) nature of the etc. This is also supporting the finding in (Bogdanov and Peredkov, 2000). High amounts of $SF_6$ gas resulted in isotropic etching and subsequently pealing of the mask. However, reducing the $SF_6$ gas will slow down the etching process. Therefore, a mixture of 80-90% oxygen and 20-10% $SF_6$ was found to be a suitable choice for having an anisotropic etch in a suitable time period.

A high ICP power generates a stronger plasma that has more ions in it, which impact the SU-8 and results in a high etch rate. On the other hand, the RIE which is connected to the substrate and by applying negative DC bias to it, helps the substrate to attract the positive oxygen ions and improves the anisotropy of etching process. However, high amounts of RIE causes high energy ions that strike the substrate, which can peel off the SU-8 from substrate and can even burn it. Therefore, one may conclude that an intermediate value of ICP and RIE will provide both a fast and more vertical etch.

After all the experiments, the deepest etch depth achieved was with the high etch rate process, and this depth could not go beyond 100 μm without resulting in damage (burning) of the sample. From this it was concluded that plasma etching of SU-8 could not be used to make HAR SU-8 structures. However, structures with low aspect ratio (around 5) can be fabricated with this etching

technique. Since HAR was needed for the MN under investigation, this etching process was abandoned, and the molding process of Chapter 7 was developed.

## References

ANHOJ, T. A., JORGENSEN, A. M., ZAUNER, D. A. & HÜBNER, J. 2006. The effect of soft bake temperature on the polymerization of SU-8 photoresist. Journal of Micromechanics and Microengineering, 16, 1819.

BARHALA, A., DRAGOESCU, D., TEODORESCU, M. & WICHTERLE, I. 2006. Isothermal (vapour+ liquid) equilibria in the binary mixtures (1, 2-dichloroethane and 1, 1, 1-trichloroethane with cyclopentanone) within the temperature range (298.15 to 313.15) K. The Journal of Chemical Thermodynamics, 38, 617-623.

BOGDANOV, A. & PEREDKOV, S. 2000. Use of SU-8 photoresist for very high aspect ratio x-ray lithography. Microelectronic Engineering, 53, 493-496.

# 7

# Molybdenum Coated SU-8 Microneedle Electrodes for Transcutaneous Electrical Nerve Stimulation

## Summary

In this chapter, design and replication of the microneedle electrodes for applications such as peripheral nerve stimulation is discussed. Molybdenum was coated on microneedle which is a biocompatible metal; it was used for the conductive layer of the needle array. In order to evaluate the performance of the fabricated electrodes, they were compared with the conventional surface electrodes in somatosensory nerve conduction velocity experiment. The recorded signals showed a much lower contact resistance and higher bandwidth in low frequencies for the fabricated microneedle electrodes compared to those of the conventional electrodes. These results indicate the electrode-tissue interface capacitance and charge transfer resistance have been increased in our designed electrodes, while the contact resistance decreased. These changes will lead to less harmful Faradaic current passing through the tissue during stimulation in different frequencies. Also, for more investigation, a 3-dimensional (3D) finite element simulation was run to analyze the performance of the surface electrodes and the microneedle array electrodes.

## 7.1. Introduction

Electrophysiological devices connect to the body using transcutaneous or subcutaneous electrodes. This chapter reports on the design, fabrication and evaluation of a micro-needle array for transcutaneous interface with peripheral nerves. Depending on the type of device, the electrodes may either convey a signal from the body to the device, or from the device to the body to stimulate local nerves in the body.

The electrodes are categorized based on their size into micro and macro-electrodes. If any part of an electrode structure is less than 10,000 μm2, the electrode is considered as a microelectrode (Cogan 2008). The shape of electrodes differs from one application to another, with common shapes being square and circular similar to the electrodes used in recording vital signals (Cogan 2008). In some cases, it is needed to penetrate the area of stimulation and contact an underlying region (Moses et al. 2007). Noteworthy, it has been shown that using conductive microneedle patches (MNPs) for physiological recordings increases the signal-noise-ratio (SNR) and obviates using any gel and surface preparation (Griss et al. 2002).

Different fabrication methods have been used to fabricate high aspect ratio (HAR) MNP structures. Many of these methods use micromachined and etched silicon as the main material of the needles, which are coated by biocompatible metals to make them conductive (L. Yu et al. 2009; P. Griss 2001 et al.; J.-C. Chiou 2006 et al.). However, microfabrication of silicon MNPs is not favorable for mass production due to its high cost. For low-cost electrodes a replication process would be more cost effective.

Polymers as the base material for MNPs have been explored recently, and different techniques have been proposed for fabricating HAR MNP structures (C. Liu 2007; M. Han et al.

2007). However, some of these techniques are not possible in many laboratories. For example, patterning and developing the photoresist polymers during HAR fabrication procedure is a complex process, and needs X-ray lithography which is not available in most fabrication laboratories. In the other investigations, researchers studied techniques like inclined rotational exposure of SU-8 (Y. K. Yoon et al. 2006). The inclined method is used to make the cone structure of each needle. Therefore, it confines the number of the electrodes that can be formed in a small area of a microneedle array and decreases the number of needles per unit. Moreover, in another investigation, the micro-lenses were designed on a glass substrate and it was tried to bend the exposed ultraviolet (UV) beam. That technique is not reliable in all the situations because it depends on the SU-8 optical parameter that may change during storage in the lab (J. H. Park et al. 2007). Other fabrication methods, like photochemical milling of metal for microneedle fabrication, were suggested to fabricate cylindric needle arrays with small number of needles in a unit area (G. S. Guvanasen et al. 2016). In this study, the molding and replication method was used as it can be done rapidly, at a low cost and by simple laboratory equipment. Also, the pyramidal structure of the fabricated needles will prevent deep penetration and touching the pain nerves.

To make a mold there are several methods. One is to use polydimethylsiloxane (PDMS) using lithographic technique followed by polycarbonate being casted in the mold, hardened by cooling, and the soft PDMS mold being removed (H. Becker et al. 2000). In most of the molding techniques, the mold is built by a master template, and the main material is injected inside the mold. Another molding method is to use laser (Aoyagi et al. 2007). For applications in need of conducting MNPs, the structure should be coated by a metal (M. Matteucci et al. 2007; Cogan 2008). The coated metal additionally enhances the mechanical strength of the HAR structure. For

example, K. Kim et al. (2004) fabricated hollow needle arrays for drug delivery. The needles were metallized to enhance their strength against insertion force.

Different metals or metal alloys have been explored for coating MNPs, such as stainless steel (SS), tungsten (W), platinum (Römgens et al.), platinum-iridium alloys (PtIr), iridium oxide (IrO), and titanium nitride (TiN) (A. Norlin et al. 2002; M. Schaldach et al. 1990; D. Zhou et al. 2003). Each of these materials has unique mechanical and electrical characteristics that can influence the stimulation parameters. For example, TiN has been explored for increasing the mechanical strength of the needles during penetration and enhancing the capacitance of the electrode-tissue interface (M. Schaldach et al. 1990; D. Zhou et al. 2003). Molybdenum (Mo) was proposed as a biocompatible metal for health care applications due to its low electrical resistance and robustness against corrosion (A. M. Ribeiro et al. 2016). Hence, Mo can be used as the surface material on top of TiN to reduce the electrical resistance and improve the stimulator electrodes capacitance effect.

The stimulation of underlying nerves is complicated by the impedance of the contact to the stratum corneum (SC). Studies have shown that the impedance of the SC drops for stimulation voltages above 30 V and the SC thickness varies in different parts of the body. (T. Keller et al. 2008; Y. A. Chizmadzhev et al. 1998). This non-linear impedance relationship can complicate prediction of the stimulation current on underlying nerves. However, MNP electrodes can offer benefit as they pierce the SC and epidermal minimally. Thus, they provide stimulation below the SC, thereby bypassing the contact impedance of the SC. This would provide the benefit of reduction in voltages; thus, it facilitates the design of an efficient low-power wearable peripheral nerve stimulator. Apart from the electrode tissue interface (ETI) resistance reduction, the ETI capacitance is another important parameter that should be taken into account for electrode design

(D. R. Merrill et al. 2005). A higher capacitance would reduce harmful Faradaic currents. As it is shown in Fig. 7.1.a, there two different charge injection from an electrode to a tissue: Capacitive and Faradaic. The Faradaic current can be either reversible or irreversible. The irreversible Faradaic currents are considered as the harmful current that ends up with net charge transfer and tissue pH change (D. R. Merrill et al. 2005). Different types of current in ETI are modeled like Fig. 7.1.b.

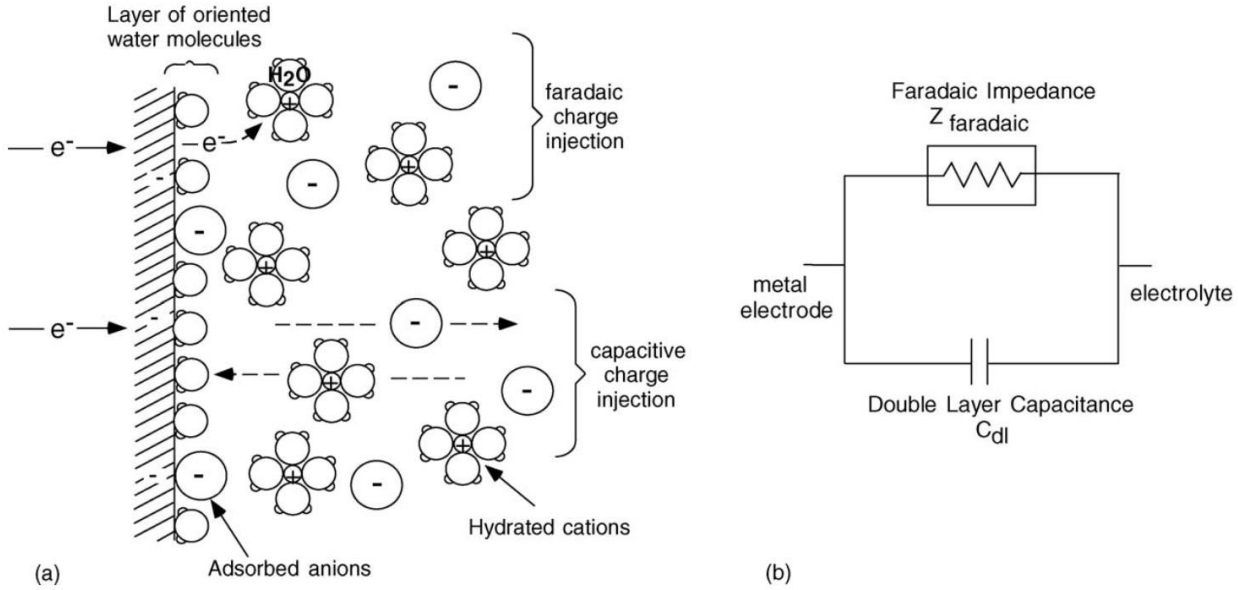


**Fig. 7.1.** (a) Electrode-Tissue-interface (ETI) ion diagram (b) equivalent electrical circuit of the ion diagram (D. R. Merrill et al. 2005). [Used with permission]

In this study, minimally piercing MNP electrodes with high ETI capacitance were fabricated to provide stimulation below SC. To reduce the fabrication cost, a replication technique was used to fabricate low cost MNPs components. MNPs with different lengths were fabricated from SU-8 and sputtered coated with TiN/Mo. Their effect on the current passed through the median nerve was measured and analyzed at different frequencies during a nerve conduction velocity (NVC) experiment. The frequency response of the fabricated microneedle arrays were compared with

conventional electrodes that are common for clinical somatosensory NCV examinations. Also, a 3-dimensional finite element modelling (FEM) of the current density at different depths of the tissue, heat dissipation and the directivity of the electrical field inside the tissue, were simulated using COMSOL® Multiphysics software. The FEM simulation was done for both conventional and micro-needle electrodes, and results were compared.

## 7.2. Fabrication process and Evaluations

In this study, the conductive MNPs with 410 µm lengths were fabricated. The MNPs with this length are tall enough to penetrate SC and reach the dermis layers underneath, which has lower electrical resistance. Since the needles are pyramidal, more penetration force will cause more penetration resistance from the skin. Therefore, the needles will penetrate a bit more than SC thickness. However, the depth of needles' penetration may not be consistent and depends on the individual's skin properties. In this section, the replication procedure of the MNP structure is described, followed by the NCV experiment and FEM simulation to evaluate the fabricated MNPs in comparison to the conventional electrodes.

### 7.2.1. MNP fabrication process

The fabrication of MNPs was done using a molding replication process. A MNP template, made of polycarbonate (H. Becker et al. 2000), was used to create the mold. Fig. 7.2, demonstrates the dimensions of the mold master that has been replicated. These dimensions are same as the final MNP design dimensions that has been examined in this study. As it is shown in Fig.1, the replicated MNPs has 100 pyramidal needles. Each needle has a 350×350 µm square base and almost 30 µm

radius sharpened tip. Also, the needles side-by-side pitch is 200µm. Overall, the fabricated MNPs is 8×8mm.

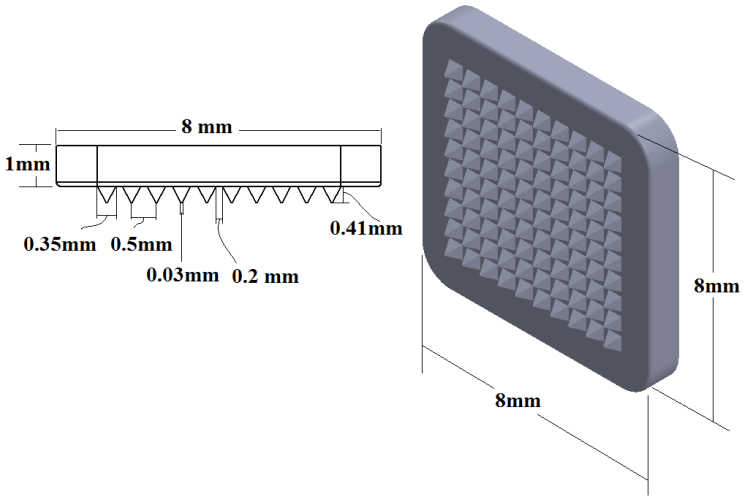


**Fig. 7.2.** Dimensions of the mold master and the final design of the fabricated MNPs (The total area of the mold template was estimated around 23 $mm^2$).

As shown in Fig. 7.3, the MNP template was first mounted on the bottom of a petri dish. Next, the petri dish was filled by PDMS (Fig. 7.3.a and Fig. 7.4a). After 10 minutes degassing at room temperature, the petri dish was heated up in 85℃ for 30 minutes. Once the PDMS became solid, the polycarbonate MNP template was easily peeled off, and the PDMS mold was ready (Fig. 7.3.b and Fig. 7.4.b).

The PDMS mold was then used to cast the SU-8 MNP structure. SU-8 2025 from Microchem® was diluted by SU-8 thinner solution with 1:1 ratio and used. Also, the biocompatibility of SU-8 was proved in a former study (K. V. Nemani et al. 2013). Therefore, any straight contact of SU-8 to the tissue is not biologically hazardous. After filling the PDMS mold with SU-8, it was heated up in a vacuum oven, where the pressure was decreased to 100 Torr for 45 minutes.

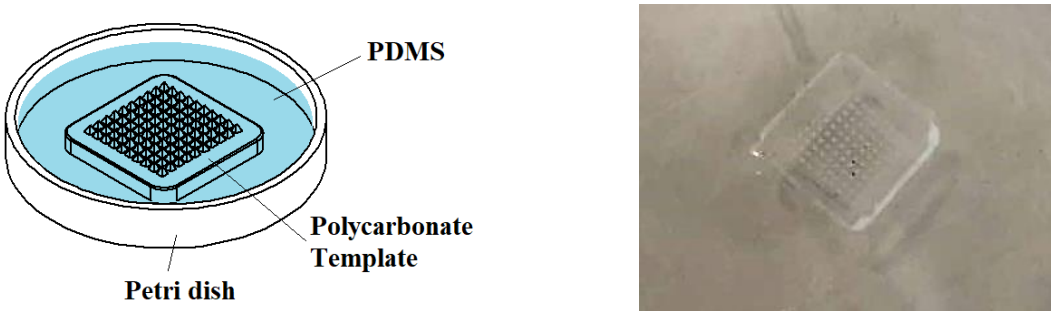


(a) (b)

**Fig. 7.3.** (a) Mold fabrication schematic before heat curing. (b) PDMS mold fabricated by the polycarbonate template after heat curing.

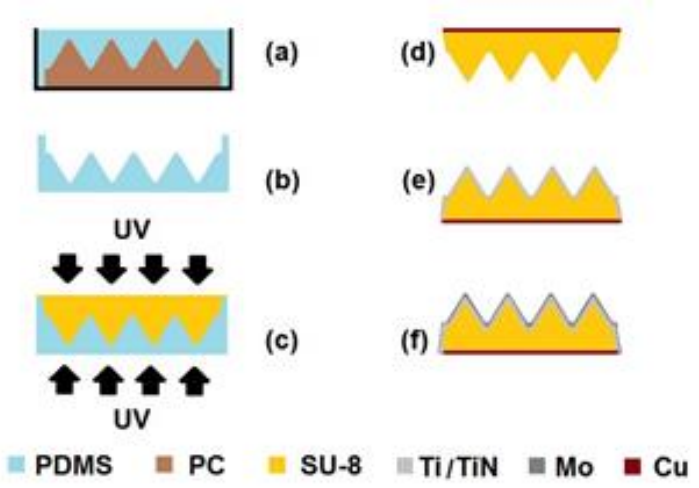


**Fig.7.4.** Fabrication process steps

The simultaneous pressure reduction and heating up to 95℃ increases the rate of evaporation of the SU-8's solvent during this soft-bake procedure; it also strengthens the cross-linking between SU-8 epoxy groups in next steps (T. A. Anhoj et al. 2006). Following this stage, both sides of the SU-8 filled mold were exposed to ultraviolet (UV) light of 350 nm wavelength for 20 seconds (Fig. 3.c). Then, a hard-bake step was done. This is the most important procedure in the hardening of the SU-8, and is where the SU-8 is cross-linked (M. B. Chan-Park 2004; C. Y. Jin et al. 2009).

The mold and SU-8 were baked for 30 minutes at 95℃. The PDMS has been reported that it could be used as a sacrificial layer for SU-8 (J. N. Patel et al. 2008). Likewise, in this study it was found that with a successful hard-bake process, the PDMS could be peeled-off the SU-8. However, it is important to note that if the hard-bake is not completed properly, the cross-linking of SU-8 in the narrow part of the structure, like the needle tips, is not sufficient. In such situation, both the structure and the mold will be destroyed during peel-off. In contrast, if the SU-8 cross-links are formed properly, the structure can be peeled-off with a small mechanical force without damaging the needle tips.

In the next fabrication step, a thin layer of copper (Cu) (<1µm) was sputtered on the back side of the SU-8 based MNP (Fig.4.d). As shown in Fig. 5, this was done to facilitate either binding wire with conductive epoxy or soldering the MNP directly to the stimulator circuit. Since the sputtered Cu is on the small area of the SU-8, its adhesion is high enough to connect the wire to the MNP (W. Dai et al. 2005). Moreover, the area where the wire is soldered (or glued by a conductive epoxy) to the MNP was already covered by solder. Therefore, it is not exposed to the air to be oxidized and change the electrical impedance of the connection.

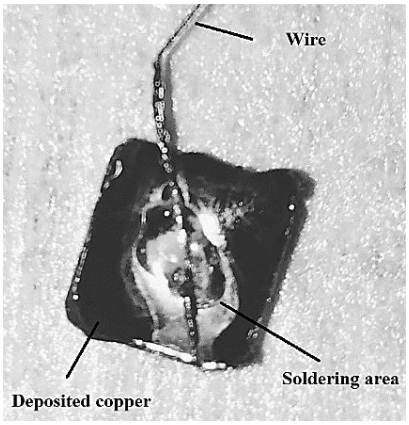


**Fig. 7.5.** Wire connection to the back side of the fabricated MNP

The surface of the needles was coated by a thin film of Ti/TiN by reactive sputtering using Argon (Ar) and Nitrogen (N) flowing at 40 sccm and 20 sccm, respectively, and at 7.6 mTorr working pressure. At the beginning of the sputtering process, a thin layer of Ti was deposited on the sample for about 2 minutes as an adhesion layer for TiN; then the nitrogen was applied to the sputtering chamber with the mentioned flow rate. Sputtering was done at the DC power of 150 W and for 16 minutes (A. Norlin et al. 2002; M. Schaldach et al. 1990). Since the thermal conductivity of the SU-8 substrate is not high enough to dissipate heat, a sputtering and cool down procedure was used with 2 minutes sputtering, followed by 2 minutes cool down (Fig. 7.4e). The average thickness of the sputtered Ti/TiN was around 300 nm. The Sputtered TiN will increase the mechanical strength of the structure. After this stage, the needles were then sputter coated with Mo using DC power of 150 W at 4.1 mTorr working pressure (Fig. 7.4f). The thickness of the sputtered Mo with the mentioned sputtering configuration was around 600 nm and overall thickness of the deposited metals was less than 1 μm. The Mo has higher electrical conductivity than TiN and it was chosen as the finishing surface of the MNPs. The scanning electron microscope (SEM) images of the fabricated MNPs are shown in Fig. 7.6. In these images, the adhesion and the side wall coverage of the sputtered metals on the needles are noticeable. Particularly in Fig. 7.6c it is shown that the sputtered metals adhered to the needles and the side walls of the needles are fairly covered.

Furthermore, the adhesion of the sputtered metals was examined three times based on "Scotch tape peel off test" qualitatively and the deposited layers were perfectly adhered to the SU-8 substrate (K. L. Mittal 1976). Also, in the former studies, it was shown that the Ti can be used as a proper adhesion layer for the other metals (W. Dai et al. 2005). The findings of this study

are confirming that the deposited metal can be tightly adhered even on the side walls of the needles after usage as shown in Fig. 7.6a-c.

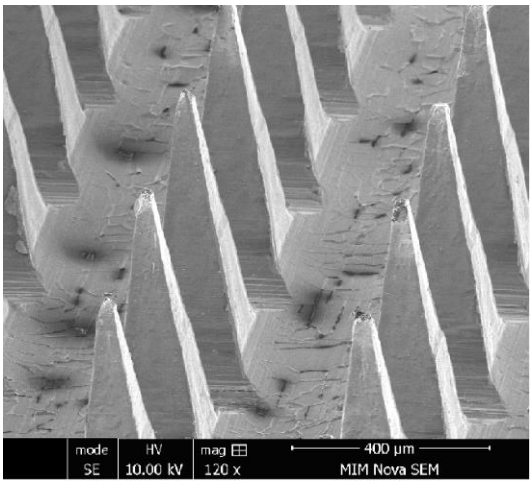


(a)

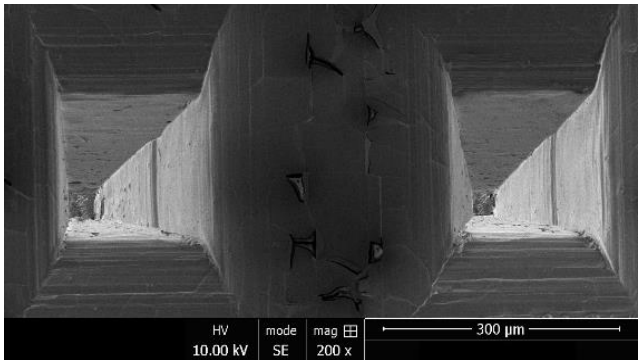


(b)

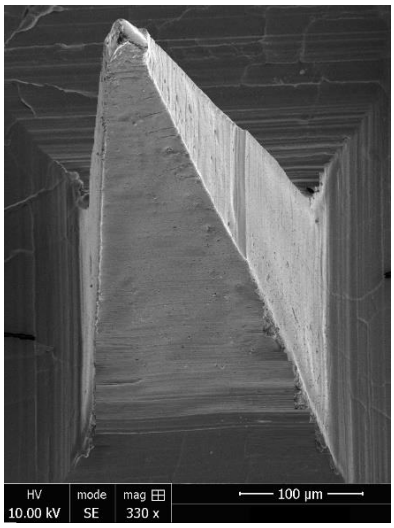


(c)

**Fig. 7.6.** (a) SEM images of two rows of fabricated MNPs. (b) Top view of two successive needles in a row. (c) Top view of a single needle. (Note: the black spots in the images are the impurities remained after alcohol wash; because the images were taken to inspect the mechanical strength of the needles after test)

## 7.3. MNPs Performance Evaluation

### 7.3.1. Nerve Conduction Velocity (NCV) experiment and MNPs characterization

The NCV is the most practical in-vivo examination that could be setup noninvasively to study the peripheral nerve conductivity. In an NCV experiment, the nerve stimulation current amplitude is gradually increased till the supramaximal voltage is reached. Hence, to evaluate the performance of the fabricated MNPs and estimate their different parameters, the sensory median conduction velocity examination was performed with VikingQuest® Electromyogram (EMG) machine by a neurologist. Two electrodes were connected to the amplifier and another two of them were connected to the stimulator (Fig. 7.7a). During the experiment, the stimulator electrodes, which was conventional metallic electrodes, were the same for testing both fabricated MNPs and carbon/AgCl gel (Fig. 7.6b) electrodes.

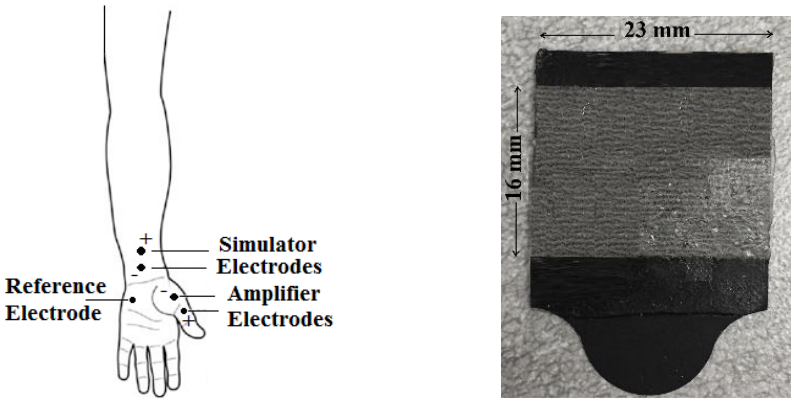


(a) (b)

**Fig. 7.7.** (a) The stimulator and electrode placement in the NCV test. (b) The conventional electrodes used for stimulation clinically. The effective area of the conventional electrode is 16mm×23mm=368 $mm^2$.

The stimulation signal was a square step pulse with 0.1 ms duration and in the range of 0 to 50 mA. During the test, the amplitude of the stimulation current was increased gradually to reach

the supramaximal stimulation current (a high enough strength stimulating signal) to activate all the nerve or muscle fibers in contact with the electrode (V. Parker et al. 2016). The recorder amplifier was filtered by a band-pass filter in the range of 20 Hz to 2 KHz. The test was repeated three times for each electrode type in the same condition to ensure reproducibility of the results; the variation of the results was found to be negligible.

### 7.3.2. 3-Dimension Finite Element Model (FEM) Simulation

In order to realize the role of the needles on the electrodes and compare the performance of the roughened surface electrodes to that of the electrodes without needles, a simple 3-D model was developed in FEM Multiphysics software, COMSOL® v5.2. With this model, the parameters like current density in different depths of a tissue, maximum heat loss and field directivity of the electrodes with and without needle spikes were analyzed. The skin tissue in this model had 4 layers, and the properties of each layer were adopted from (A. Kuhn et al. 2008; T. Maeda et al.) (Fig. 7.8).

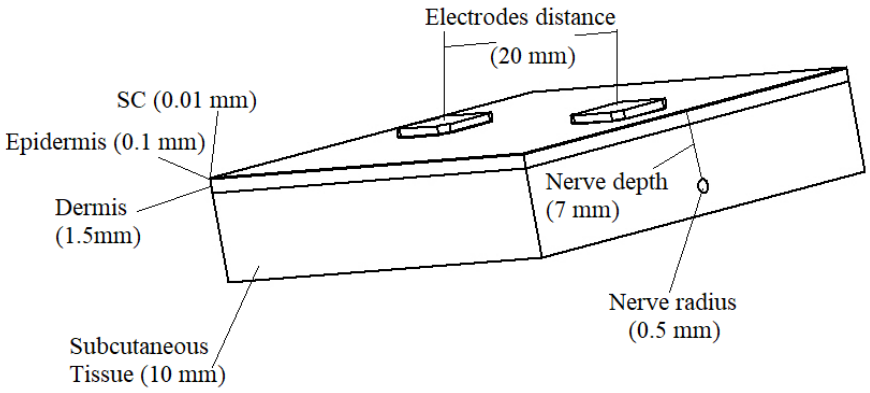


**Fig. 7.8.** The developed 3D model for FEM analysis

In the developed 3D model, the “electrical physics” were chosen to analyze the model in the frequency domain from 10 Hz to 1 kHz. Also, the stimulation amplitude was swept from 10 to 40

V. In the first simulation scenario, the MNPs were placed on the surface of the tissue model, while in the second simulation setting, the electrodes resembled to the fabricated MNPs but without any needle spikes. Since the frequency did not play a critical role in the desired parameters, the results are presented in the maximum analyzed frequency. Unlike the frequency, the simulation voltage was correlated with the resultant signal's amplitude. Thus, the results of maximum input, 40 V, were presented.

## 7.4. Results

### 7.4.1. Nerve Conduction Velocity experiment

The experiments of the conventional electrodes and the fabricated MNP were performed on the same hand. If the characteristic of the limb tissue was consistent during the experiment, investigating the order of the test was not considered in this experiment. However, a short relaxation time (around 10 minutes) was applied between testing each electrode. Fig. 7.9 shows the time response of both conventional electrode and the fabricated MNPs. They were found similar although the size of the conventional electrode was more than that of the MNPs. Moreover, the supramaximal current of the fabricated MNPs was almost half of that of the conventional electrode's one. Noteworthy is that supramaximal current is the stimulating current applied to the nerve incrementally to reach an almost constant voltage during the test. The plateau voltage (which is called supramaximal voltage) in Fig. 7.9 occurred in almost same voltage for both electrodes. However, the current that cause supramaximal voltage in the fabricated MNPs was almost twice of that for the conventional electrodes; this indicates the fabricated electrodes' resistance is almost half of the resistance of the conventional electrodes.

In order to interpret the result of the in-vivo NCV test, the electrical model of ETI, suggested by (Sawan et al. 2008; McAdams et al. 1991), was used. In that model (Fig. 7.9), the tissue is modeled by charge-transfer resistance ($R_{CT}$) and a double layer capacitor ($C_{dl}$). The estimation of complex impedance $C_{dl}$ between the electrode and tissue was addressed in the former studies (Beckmann et al. 2010, Oh et al. 2008). In this study, the cut-off frequency of the recorded NCV signal was used to estimate $C_{dl}$ (Fig. 7.10).

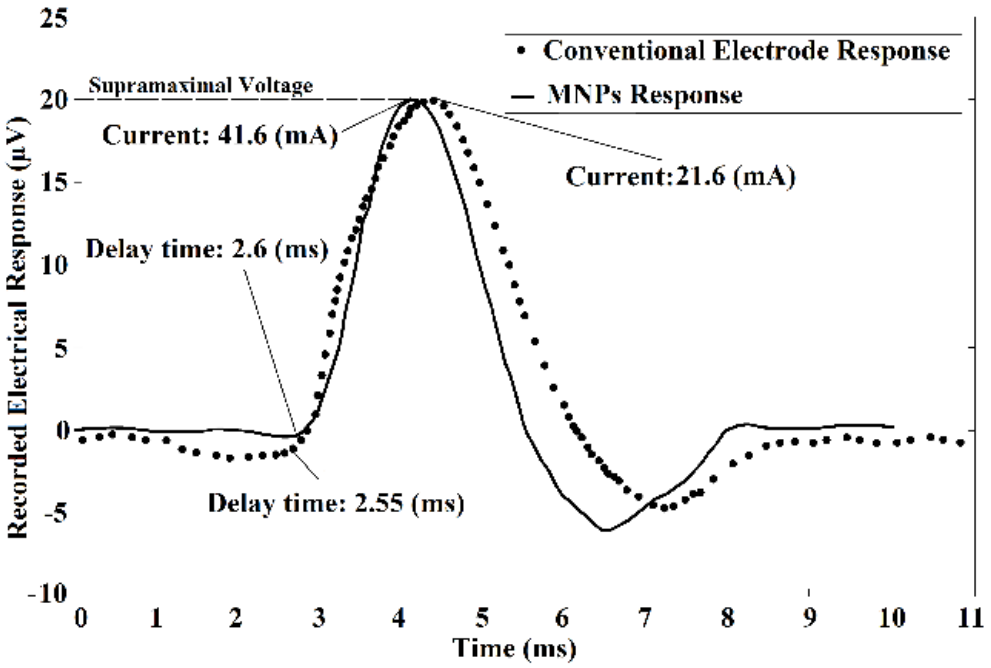


**Fig. 7.9.** A comparison between the time response and latency of the conventional electrodes and the fabricated MNPs

Besides the $R_{CT}$ and $C_{dl}$, like all other materials, biological tissues have a real resistance against the electrical current that is presented by $R_{TOTAL}$ in the ETI model. Moreover, the polarity characteristics of the nerve is modeled by Erev (Bard et al. 2001). For simplicity, it was assumed that the nerve below the skin corresponds to a simple linear resistor ($R_{el}$) (McAdams et al. 1991).

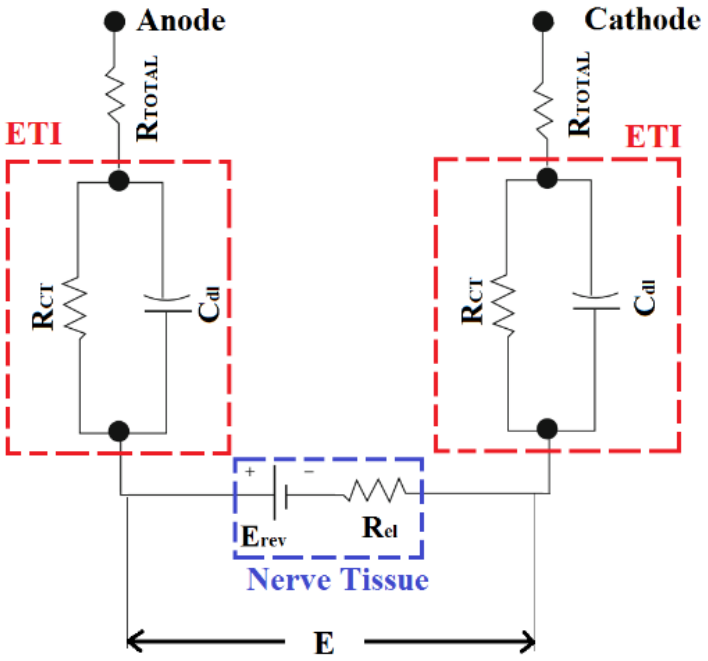


**Fig.7.10.** Electrical model of ETI in TENS (D. R. Merrill et al. 2005)

In order to compare the performance of the fabricated MNPs in different frequencies and estimate the parameters of the ETI model, the response of the nerve was analyzed in the frequency domain. For this purpose, the recorded voltage from the electrodes was converted to frequency domain and its magnitude Bode diagram was plotted. Fig. 7.11 shows the differences between the impedance of the fabricated MNPs and the conventional surface electrodes. In regard to the circuitry model of the ETI, at zero frequency (dc currents) the voltage would be across the two $R_{CT}$ and $R_{el}$. In contrast, in high frequencies, it is assumed that the $C_{dl}$ is short circuit and the voltage would be across the two $R_{TOTAL}$ and Rel.

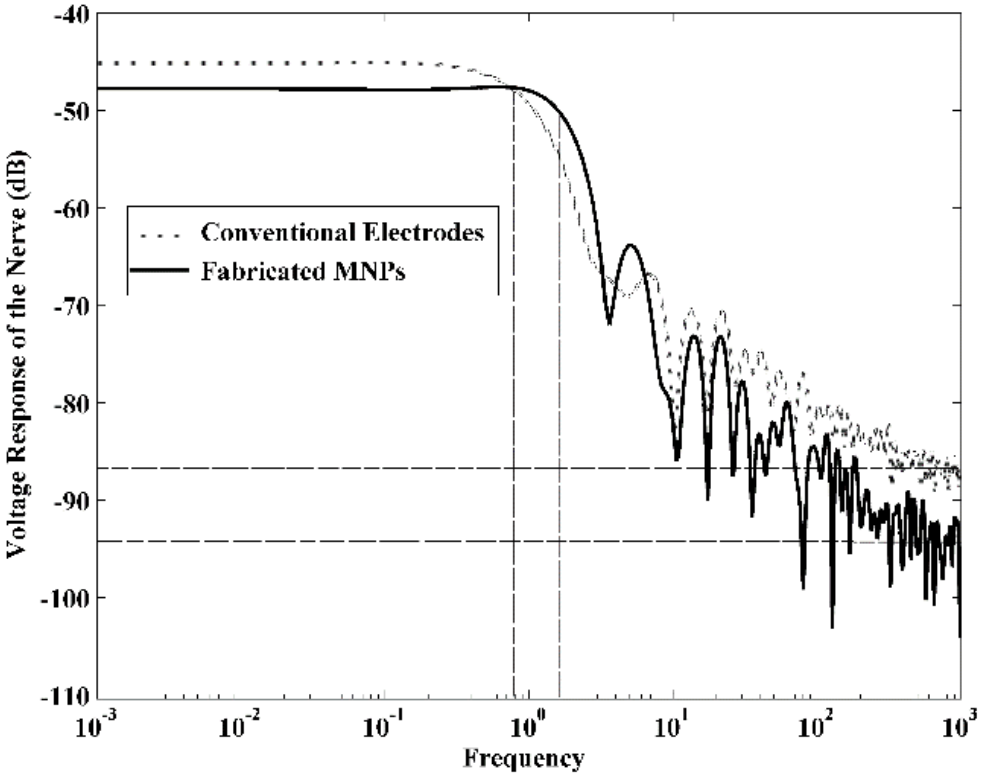


**Fig. 7.1.** Bode plot of the Nerve Voltage Response

If it is assumed that the resistance of the nerve ($R_{el}$) is negligible, then the voltage response of the nerve to the step current is presented by equation (1) (McAdams 2011)

$$V(t) = I_{dc}R_{TOTAL} + I_{dc}R_{CT}(1 - e^{\frac{-t}{R_{CT}C_{dl}}}) \qquad (1)$$

In Equation (1), when t → 0, it is corresponding to the high-frequency part of the Bode plot in Fig. 7.11. On the other hand, as t→ + ∞, it is corresponding to low-frequency part of the Bode plot. Using Equation (1) and data presented in Figs. 7.9 and 7.11, different parameters of the model (Fig. 7.10) were calculated; they are presented in Table 7.1. Note that the value of the $C_{dl}$ was

calculated in the cuff-off frequency of the electrodes, where the amplitude of the voltage decreased 3dB compared to the initial magnitude.

**Table 7. 1.** Calculated parameter for the ETI model in conventional and fabricated MNPs

| **Parameters** | **Conventional Electrodes** | **Fabricated MNPs** |
|---|---|---|
| $R_{TOTAL}$ (kΩ/m2) | 190.2 | 64.3 |
| $R_{CT}$ (kΩ/m2) | 18.2 | 143.7 |
| $C_{dl}$ (µF/ mm2) | 700 | 3200 |
| E (µV) | 40.4 | 42.2 |

Furthermore, the electrical impedance spectrum (EIS) of the fabricated MNPs were compared with the surface electrodes in Fig. 7.12 for three different test the same subject. In Fig. 7.12, it is shown that the impedance of the conventional electrodes is higher than the fabricated needles particularly in the low frequencies. However, in the high frequencies the resistance of the fabricated MNPS is higher that matches the results of Table 7.1.

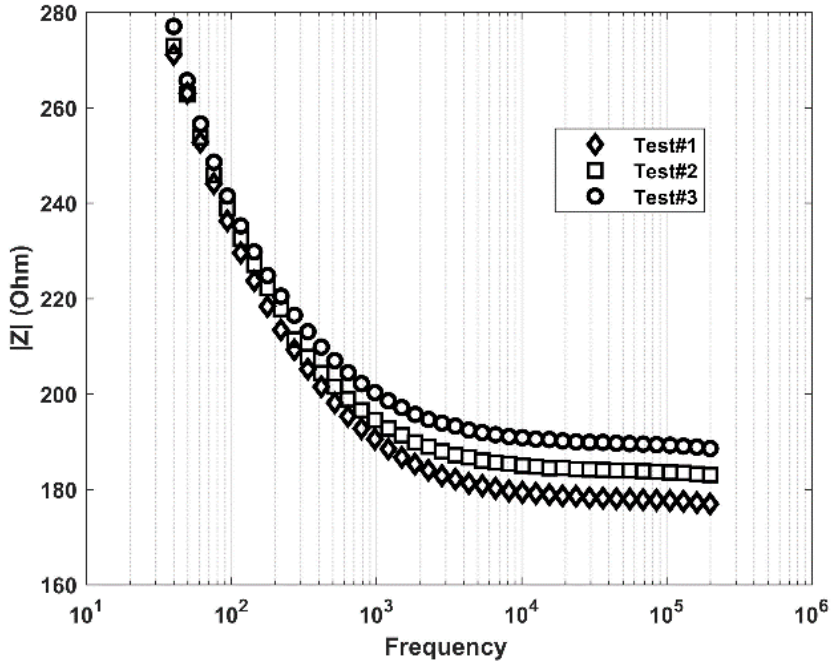


(a)

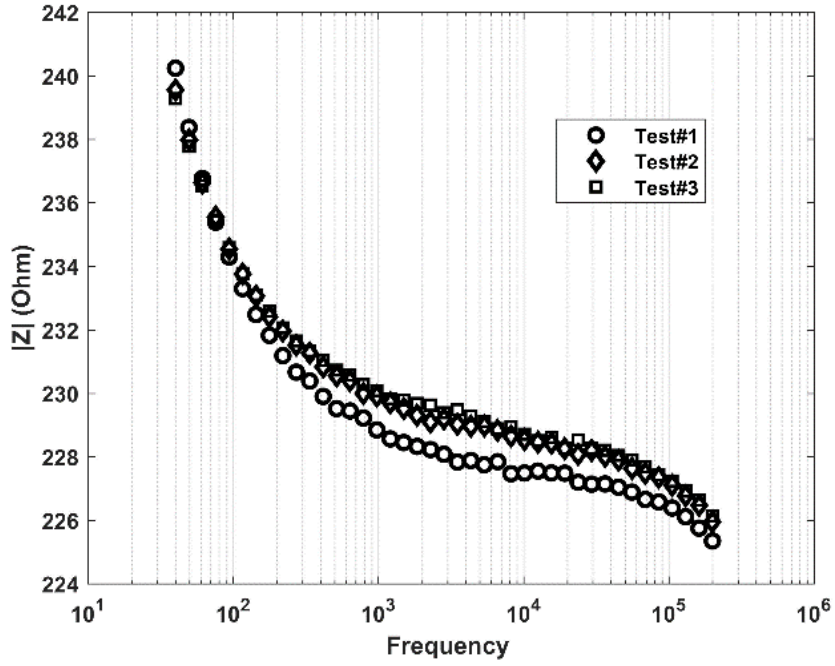


(b)

**Fig. 7.2.** The electrical impedance spectrum of (a) the conventional surface electrodes (b) the fabricated MNPs

### 7.4.2. Simulation Results

The electrodes' heat dissipation is important, particularly for the long-term stimulations. If the area underneath the electrode is exposed to high heat for a long period of time, it may burn and damage the tissue. Aforementioned, in this study the simulation was used to analyze and compare the current density, the maximum heat dissipation of the electrodes with and without needle spikes and the directivity of the electrical field within the tissue. It was assumed that the simulated electrodes have the same base area. However, in two different scenarios, the fabricated MNPs and smooth surface electrodes were used as the working and counter electrodes separately. The models with fabricated MNPs and smooth surface were solved for 580,112 and 98,184 elements, respectively. Fig. 7.13 shows that the maximum heat dissipation underneath (in the depth of ~400μm from the top of the skin model) of the two electrode types. The heat dissipation in the spiked electrodes occurred on tip of the needles, while the power was dissipated in the large middle area of the smooth electrode.

In the next step of the simulation, the current density underneath of the MNPs and smooth surface electrodes were compared. The graph in Fig. 7.14, depicts that the maximum current density of the fabricated MNPs in 40 V amplitude and 1 KHz stimulation is remarkably higher than that of the smooth surface electrodes. Although there might be concerns about the nerve damage because of the high charge delivery around the nerve, the former studies showed that in the microelectrodes, short time pulses would be safe for the tissue (Merrill et al. 2005). Furthermore, the directivity of the electrical field within the tissue is one of the important factors that analyzed in the simulation. It was found that the fabricated MNPs caused more directive electrical field towards the nerve within the tissue in comparison to the smooth surface electrodes. In Fig. 7.15, the lines show the electrical field between the working and counter electrodes.

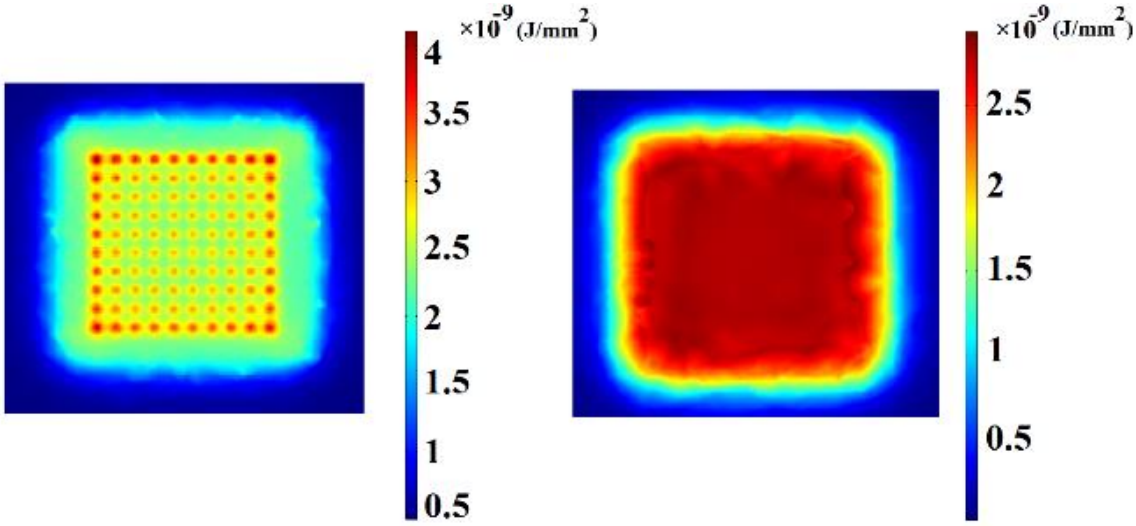


(a) (b)

**Fig. 7.3.** (a) Maximum planar heat dissipation of working electrodes; input: 40 V and 1 kHz in fabricated MNPs model (max: 3.8 J/mm$^2$ on some spots). (b) Smooth surface electrode (max: 3.2 J/mm$^2$ on the major part of the surface).

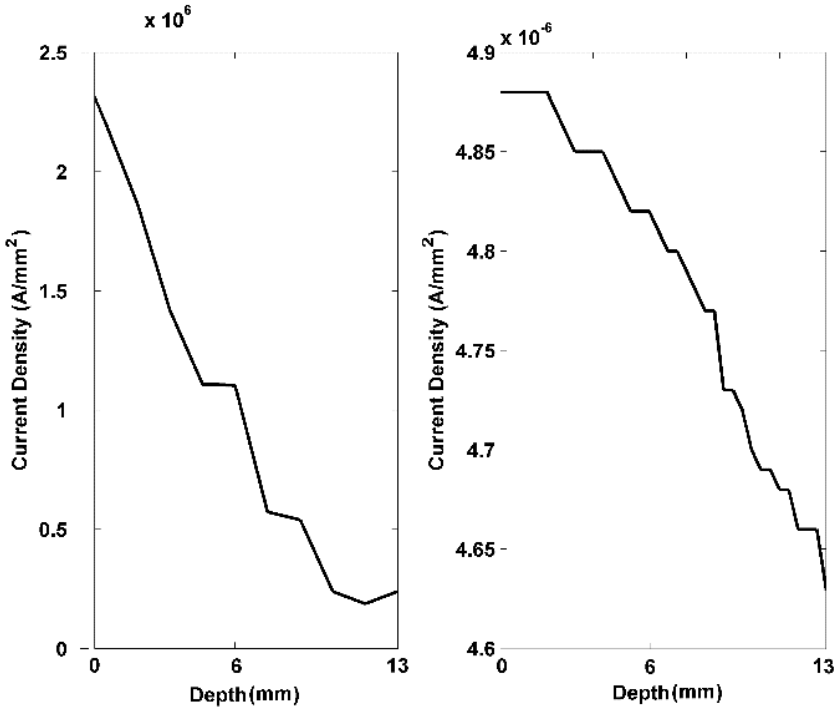


(a) (b)

**Fig. 7.4.** (a) Current density of the fabricated MNPs. (b) Current density of the electrodes without needle spikes on the surface.

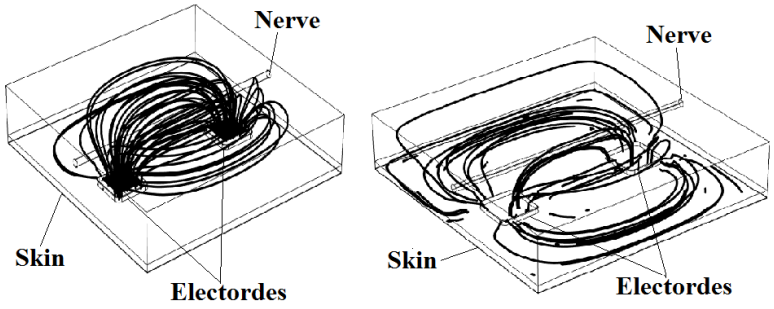


(a) (b)

**Fig. 7.5.** Field spatial distribution inside between (a) two MNPs and (b) Smooth surface electrodes

## 7.5. Discussion

In this study, a new MNPs sample was developed and examined by NCV experiment (base on 2 stimulation electrodes and 2 recording electrodes) for nerve stimulation applications. Also, the characteristics of the electrical field within the tissue was analyzed by a 3D FEM simulation. The main material of the fabricated MNPs was SU-8, and it was coated by Ti/TiN and Mo. The Ti/TiN layer was used to increase the mechanical strength of the needles and plays as adhesion layer. However, in other applications than nerve stimulation, it might be replaced by iridium oxide (IrO) or any other similar material that has almost same mechanical characteristics. The top layer was chosen from Mo, which has been extensively studied. Mo has a lower cost and is more reliable than other regular metal like tungsten (Merrill et al. 2005; Ribeiro et al. 2016).

In comparison to conventional electrodes, the roughness of MNPs surface was higher because of the shape of electrode; this causes remarkable increases in the capacitance of electrodes as each needle forms a capacitor; as these capacitors are all in parallel to each other, the resultant

overall capacitance of the MNP would be much higher than that of conventional electrodes. To study these characteristics, the NCV test was run. As seen in Fig. 7.9, the MNPs time response resembles to that of the conventional carbon/AgCl gel electrodes. In contrast, the MNPs frequency response showed to have a much wider bandwidth in the lower frequencies and lower contact resistance (leading to lower dc gain) compared to that of the conventional electrodes (Fig. 7.11). The calculated values shown in Table 7.1, indicates that the fabricated MNPs increased the ETI capacitance more than 4 times and decreased the contact resistance down to almost 3 times. Simultaneously, the charge transfer resistance ($R_{CT}$) was increased remarkably; it is an advantage particularly in TENS stimulation (E.McAdams et al. 2011). Overall, the measured and calculated parameters from the in-vivo test showed that the $C_{dl}$ and $R_{CT}$ were increased and the RTOTAL decreased simultaneously. Therefore, the suggested MNPs passed less faradaic current compared to the regular electrodes. Thus, MNPs would be less harmful for the long-term applications.

Moreover, the electrical EIS graph (Fig. 7.12) shows that in the lower frequencies, where the double layer capacitor is being charged through $R_{TOTAL}$, the resistance of the fabricated MNPs is lower than the conventional electrodes. This is also demonstrated in the values of the Table 1 where the RTOTAL in the fabricated MNPs is less than the conventional electrodes. In the high frequencies, the impedance of the fabricated MNPs is more than the conventional electrodes. It means that the MNPs eliminate the harmful Faradaic current more than the conventional electrodes by charging the $C_{dl}$. Also, the EIS graph in Fig. 7.12 was measure from the opposite hand where the NCV test was performed and proved the reproducibility of the test experiments.

The result of the heat dissipation shows that the overall dissipated heat underneath of a fabricated MNP electrode is slightly more than that of the surface electrodes. The simulated average volumetric density of the energy in the maximum input (40 V at 1 KHz) in a fabricated

MNP (~ 2.66×10-8 J/mm$^3$) was slightly higher than that of the smooth regular stimulation electrode (~ 8.28×10-9 J/mm$^3$); this was observed more in the needle spikes, which are located on the edges of the electrode. Although there is more heat dissipation at the tip of the needles in the MNPs, long-term stimulation through the MNPs with maximum input will not be hazardous for the tissue because the needles are periodically spaced on the surface; that helps the dissipated energy to distribute on the surface evenly. In contrast, using long-term the regular high impedance carbon/gel stimulator pads may result in serious injury of the skin surface (DeMonte et al. 2005). Moreover, in the real experiments, the pyramidal shape of the needles does not allow the needles to penetrate through the skin completely. Thus, the heat dissipation on the skin will be less. Also, in case of any damage on the surface of the fabricated MNPs, like breaking of the Mo or TiN, because of the short stimulation pulse, the skin will not be affected thermally. The 3D simulation revealed that the MNPs delivered higher current density in comparison to that of the similar electrodes without spikes. As shown Fig. 7.14, the current density of the smooth surface electrode was attenuated considerably in lower depth in comparison to that in the MNPs. Moreover, the simulation results show that the current density in the deep layer of the tissue mostly depends on the amplitude of the stimulation voltage rather than its frequency. However, the current density on the skin surface, particularly SC, is fairly correlated with the frequency.

Lastly, the directivity of a stimulator electrodes is quite important. Fig. 7.15 demonstrates the differences between the electrical field of the fabricated MNPs and the one without spike. Clearly, the generated field by the MNP is quite directive towards the nerve, which is intended to be excited. In contrast, the regular smooth surface electrode generated a wide electrical field on the SC that has lower resistance than fat layer; therefore, the electrical field within the tissue passed

mostly through the SC. The may lead to an increase in the SC temperature, and burn it in long-term applications.

Overall, one may conclude that compared to conventional electrodes such as smooth surface carbon/AgCl gel or metallic/AgCl gel electrodes, the developed MNPs results in power consumption reduction, low Faradaic current rate, less tissue damage hazardous and more directivity toward the target nerve. Furthermore, in this study, Mo was used for coating electrodes, which can be considered as a new step toward using Mo in health care applications.

## 7.5. Conclusion

In this study, double-layer (Ti/TiN/Mo) painless (which do not touch the pain nerve in the skin dermis) microneedle electrodes were fabricated for electrical peripheral nerve stimulation. In terms of fabrication, it was shown that polycarbonate can be used as a master for PDMS molding process instead of silicon, and it can be detached from the cured PDMS readily. Also, it was successfully demonstrated that the fabricated electrodes increased the capacitance and the charge transfer resistance of ETI; that substantially reduces the harmful Faradaic current passing through the tissue. By developing a 3D tissue model and FEM simulation, it was shown that the fabricated electrodes had better performance and current density delivery in different layers and electrical field directivity toward the target nerve than the conventional surface electrodes. However, clinical long-term experiments are required to characterize the performance of the fabricated electrodes practically.

## References

ANHOJ, T. A., JORGENSEN, A. M., ZAUNER, D. A. & HÜBNER, J. 2006. The effect of soft bake temperature on the polymerization of SU-8 photoresist. Journal of Micromechanics and Microengineering, 16, 1819.

AOYAGI, S., IZUMI, H., ISONO, Y., FUKUDA, M. & OGAWA, H. 2007. Laser fabrication of high aspect ratio thin holes on biodegradable polymer and its application to a microneedle. Sensors and Actuators A: Physical, 139, 293-302.

BARD, A. J. & FAULKNER, L. R. 2001. Fundamentals and applications. Electrochemical Methods, 2, 482.

BECKER, H. & HEIM, U. 2000. Hot embossing as a method for the fabrication of polymer high aspect ratio structures. Sensors and Actuators A: Physical, 83, 130-135.

BECKMANN, L., NEUHAUS, C., MEDRANO, G., JUNGBECKER, N., WALTER, M., GRIES, T. & LEONHARDT, S. 2010. Characterization of textile electrodes and conductors using standardized measurement setups. Physiological measurement, 31, 233.

BERGER, A.J., BAYLISS, D.A. AND VIANA, F. 1992. Modulation of neonatal rat hypoglossal motoneuron excitability by serotonin. Neuroscience letters, 143, 164-168.

CHAN-PARK, M.B., ZHANG, J., YAN, Y. AND YUE, C.Y. 2004. Fabrication of large SU-8 mold with high aspect ratio microchannels by UV exposure dose reduction. Sensors and Actuators B: Chemical, 101(1-2), 175-182.

CHAHAT, N., ZHADOBOV, M. AND SAULEAU, R. 2012. Broadband tissue-equivalent phantom for BAN applications at millimeter waves. IEEE Transactions on Microwave Theory and Techniques, 60(7), 2259-2266.

CHIOU, J.C., KO, L.W., LIN, C.T., HONG, C.T., JUNG, T.P., LIANG, S.F. AND JENG, J.L. 2006, November. Using novel MEMS EEG sensors in detecting drowsiness application. In 2006 IEEE Biomedical Circuits and Systems Conference IEEE, 33-36.

CHIZMADZHEV, Y.A., INDENBOM, A.V., KUZMIN, P.I., GALICHENKO, S.V., WEAVER, J.C. AND POTTS, R.O. 1998. Electrical properties of skin at moderate voltages: contribution of appendageal macropores. Biophysical Journal, 74, 843-856.

COGAN, S.F. 2008. Neural stimulation and recording electrodes. Annu. Rev. Biomed. Eng., 10, 275-309.

DAI, W., LIAN, K. AND WANG, W. 2005. A quantitative study on the adhesion property of cured SU-8 on various metallic surfaces. Microsystem Technologies, 11, 526-534.

DEMONTE, T.P., GADSBY, P.D., MEYER, P.F. AND JOY, M.L.2005. Measurement of edge effects in automatic external defibrillation electrodes using current density imaging. In Proc. 13th Annu. ISMRM Int. Conf.

FRANKS, W., SCHENKER, I., SCHMUTZ, P. AND HIERLEMANN, A. 2005. Impedance characterization and modeling of electrodes for biomedical applications. IEEE Transactions on Biomedical Engineering, 52, 1295-1302.

GONG, C.S., LAI, H.Y., HUANG, S.H., LO, Y.C., LEE, N., CHEN, P.Y., TU, P.H., YANG, C.Y., LIN, J. AND CHEN, Y.Y. 2015. A programmable high-voltage compliance neural stimulator for deep brain stimulation in vivo. sensors, 15, 12700-12719.

GRISS, P., TOLVANEN-LAAKSO, H.K., MERILAINEN, P. AND STEMME, G. 2002. Characterization of micromachined spiked biopotential electrodes. IEEE Transactions on Biomedical Engineering, 49, 597-604.

GRISS, P., ENOKSSON, P., TOLVANEN-LAAKSO, H.K., MERILAINEN, P., OLLMAR, S. AND STEMME, G. 2001. Micromachined electrodes for biopotential measurements. Journal of Microelectromechanical Systems, 10, 10-16.

GUVANASEN, G.S., GUO, L., AGUILAR, R.J., CHEEK, A.L., SHAFOR, C.S., RAJARAMAN, S., NICHOLS, T.R. AND DEWEERTH, S.P. 2017. A stretchable microneedle electrode array for stimulating and measuring intramuscular electromyographic activity. IEEE Transactions on Neural Systems and Rehabilitation Engineering, 25, 1440-1452.

HAN, M., HYUN, D.H., PARK, H.H., LEE, S.S., KIM, C.H. AND KIM, C. 2007. A novel fabrication process for out-of-plane microneedle sheets of biocompatible polymer. Journal of Micromechanics and Microengineering, 17, 1184.

JIN, C.Y., HAN, M.H., LEE, S.S. AND CHOI, Y.H. 2009. Mass producible and biocompatible microneedle patch and functional verification of its usefulness for transdermal drug delivery. Biomedical microdevices, 11, 1195.

KELLER, T., MICERA, S., LAWRENCE, M., MORARI, M. AND POPOVIC, D.B. 2010. Wearable neural prostheses. IEEE Engineering in Medicine and Biology Magazine, 29, 64-69.

KIM, K., PARK, D.S., LU, H.M., CHE, W., KIM, K., LEE, J.B. AND AHN, C.H. 2004. A tapered hollow metallic microneedle array using backside exposure of SU-8. Journal of Micromechanics and Microengineering, 14, 597.

KUHN, A., KELLER, T., LAWRENCE, M. AND MORARI, M. 2009. A model for transcutaneous current stimulation: simulations and experiments. Medical & biological engineering & computing, 47, 279.

LIU, C. 2007. Recent developments in polymer MEMS. Advanced Materials, 19, 3783-3790.

MCADAMS, E.T., LACKERMEIER, A., MCLAUGHLIN, J.A., MACKEN, D. AND JOSSINET, J. 1995. The linear and non-linear electrical properties of the electrode-electrolyte interface. Biosensors and Bioelectronics, 10, 67-74.

MCADAMS, E.T., LACKERMEIER, A., MCLAUGHLIN, J.A., MACKEN, D. AND JOSSINET, J. 1995. The linear and non-linear electrical properties of the electrode-electrolyte interface. Biosensors and Bioelectronics, 10, 67-74.

MCADAMS, E. 2011. Biomedical electrodes for biopotential monitoring and electrostimulation. In Bio-Medical CMOS ICs, 31-124. Springer, Boston, MA.

MCCREERY, D.B., AGNEW, W.F., YUEN, T.G. AND BULLARA, L. 1990. Charge density and charge per phase as cofactors in neural injury induced by electrical stimulation. IEEE Transactions on Biomedical Engineering, 37, 996-1001.

MAEDA, T., ARAKAWA, N., TAKAHASHI, M. AND AIZU, Y. 2010. Monte Carlo simulation of spectral reflectance using a multilayered skin tissue model. Optical review, 17, 223-229.

MATTEUCCI, M., CARABALONA, R., CASELLA, M., DI FABRIZIO, E.N.Z.O., GRAMATICA, F., DI RIENZO, M., SNIDERO, E., GAVIOLI, L. AND SANCROTTI, M. 2007. Micropatterned dry electrodes for brain–computer interface. Microelectronic Engineering, 84, 1737-1740.

MERRILL, D.R., BIKSON, M. AND JEFFERYS, J.G. 2005. Electrical stimulation of excitable tissue: design of efficacious and safe protocols. Journal of neuroscience methods, 141, 171-198.

MOSES, H.W. AND MULLIN, J.C. 2007. A practical guide to cardiac pacing. Lippincott Williams & Wilkins.

NORLIN, A., PAN, J. AND LEYGRAF, C. 2002. Investigation of interfacial capacitance of Pt, Ti and TiN coated electrodes by electrochemical impedance spectroscopy. Biomolecular Engineering, 19, 67-71.

OH, T.I., KOO, H., LEE, K.H., KIM, S.M., LEE, J., KIM, S.W., SEO, J.K. AND WOO, E.J. 2008. Validation of a multi-frequency electrical impedance tomography (mfEIT) system KHU Mark1: impedance spectroscopy and time-difference imaging. Physiological measurement, 29, 295.

PARK, J.H., YOON, Y.K., CHOI, S.O., PRAUSNITZ, M.R. AND ALLEN, M.G. 2007. Tapered conical polymer microneedles fabricated using an integrated lens technique for transdermal drug delivery. IEEE transactions on biomedical engineering, 54, 903-913.

PARKER, V., WARMAN CHARDON, J., MILLS, J., GOLDSMITH, C. AND BOURQUE, P.R. 2016. Supramaximal Stimulus Intensity as a Diagnostic Tool in Chronic Demyelinating Neuropathy. Neuroscience journal.

PATEL, J.N., KAMINSKA, B., GRAY, B.L. AND GATES, B.D. 2008. PDMS as a sacrificial substrate for SU-8-based biomedical and microfluidic applications. Journal of Micromechanics and Microengineering, 18, 095028.

RIBEIRO, A.M., FLORES-SAHAGUN, T.H. AND PAREDES, R.C. 2016. A perspective on molybdenum biocompatibility and antimicrobial activity for applications in implants. Journal of materials science, 51, 2806-2816.

SAWAN, M., MOUNAIM, F. AND LESBROS, G. 2008. Wireless monitoring of electrode-tissues interfaces for long term characterization. Analog Integrated Circuits and Signal Processing, 55, 103-114.

SCHALDACH, M., HUBMANN, M., WEIKL, A. AND HARDT, R. 1990. Sputter-deposited TiN electrode coatings for superior sensing and pacing performance. Pacing and Clinical Electrophysiology, 13, 1891-1895.

SUHONEN, T.M., BOUWSTRA, J.A. AND URTTI, A. 1999. Chemical enhancement of percutaneous absorption in relation to stratum corneum structural alterations. Journal of controlled release, 59, 149-161.

VIANA, F., BAYLISS, D.A. AND BERGER, A.J. 1994. Postnatal changes in rat hypoglossal motoneuron membrane properties. Neuroscience, 59, 131-148.

YU, L.M., TAY, F.E.H., GUO, D.G., XU, L. AND YAP, K.L. 2009. A microfabricated electrode with hollow microneedles for ECG measurement. Sensors and Actuators A: Physical, 151, 17-22.

YOON, Y.K., PARK, J.H. AND ALLEN, M.G. 2006. Multidirectional UV lithography for complex 3-D MEMS structures. Journal of microelectromechanical systems, 15, 1121-1130.

ZHOU, D.M. AND GREENBERG, R.J. 2003, September. Electrochemical characterization of titanium nitride microelectrode arrays for charge-injection applications. In Proceedings of the 25th Annual International Conference of the IEEE Engineering in Medicine and Biology Society (IEEE Cat. No. 03CH37439) ,2,1964-1967.

# 8

# Structural and Performance Comparison between SU-8 Microfabricated and 3D-Printed Microneedle Electrodes


## Summary

3-dimensional (3D) printing technology is one of the most popular technologies these days. There are tons of application of 3D printing in medicine. Relatively fast, easy design and reliable output are the most important features of the 3D printing technology. In this chapter, the 3D-printed microneedle arrays are compared with the microfabricated one to show their structural difference based on their scanning electron microscopy (SEM) images. Also, the performance of the two different types of the microneedles was investigated both in time domain and frequency domain. Results showed that the 3D printed microneedles can have higher gain than the microfabricated ones in the high frequencies. Also, SEM image comparison showed significant differences between the outputs of the 3D printed microneedles compare to the microfabricated ones and the primary design.

## 8.1. Introduction

3-dimensional (3D) printing technology is one of the pioneer technologies in medicine. From artificial organs to alive tissues have been printed with 3D printing technologies since mid-1990s (Michalski and Ross, 2014). Regardless of the type of 3D printer, almost all of them are common in the method that converts a 3D drawing to a physical prototype which is based on the layer by layer additive manufacturing technology (Standard, 2013). All of them convert the geometry of a drawing to Standard Tessellation Language (STL) file and a geometry file (called G-code) and transfer the G-code to the 3D printer machine (Brown and de Beer, 2013). However, the precision of the exported file in each of the mentioned conversion steps depends on the type of the 3D printer and its capabilities. Therefore, most of the 3D printer manufacturers provide a convertor with their machines. There are 5 different types of 3D printer technologies and almost all of them have been used for medical purposes to print artificial organs (Rybicki and Grant, 2017). These technologies are summarized in Fig. 8.1 diagram. Among all these technologies, stereolithography (SLA), is one the most accurate and high resolution technology that is progressed significantly in the recent years (Wang et al., 2017b). Also, preparing biocompatible light-cure resin materials, for SLA printers is more feasible compare to the other types of the 3D printing technologies (Chia and Wu, 2015).

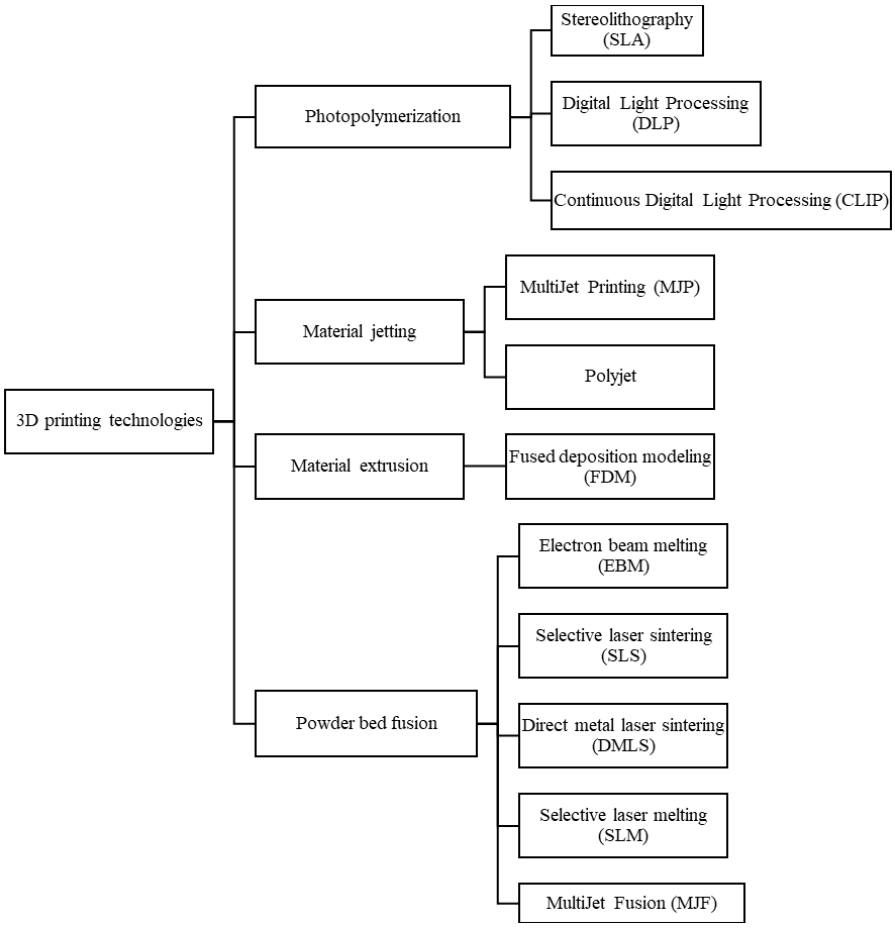


**Fig. 8.1.** 3D printing technologies

Digital light processing (DLP) and SLA work based on photopolymerization method but there are some differences between them. In DLP printers, the resin is exposed to the pattern of each layer at once using an array of micromirrors that selectively reflect the light beams onto the resin. In contrast, in the SLA printers, the pattern of each layer is drawn by only one scanning micromirror that reflect a laser beam onto one point of the resin at each step (Groth et al., 2014). The main difference between the SLA and DLP technologies is the exposure time. Different types of resins vary in the exposure time that is required for photopolymerization. The importance of the exposure time becomes noticeable in the quality difference between the SLA and DLP 3D-printed

samples that posses specific features. However, generally, the printing time in DLP is shorter than SLA.

Several articles have been published on the effect of using different materials or employing various 3D printing techniques on a 3D-printed medical device or body organ (Au et al., 2015, Mannoor et al., 2013, Ho et al., 2015, Mironov et al., 2003). However, not many researches can be found that compare a micromedical device that is fabricated by microfabrication techniques with the same micromedical device that is printed by a 3D printer.

Microneedle Arrays (MNA) are one of the micromedical devices that have several applications including biopotential recording and drug delivery (Forvi et al., 2012, Yu et al., 2009, Prausnitz, 2004, Lee et al., 2008). By advancing polymer technology, most of the microfabrication procedures were modified to enable fabricating structures in the scale of micrometers, by forming photopolymers like SU-8. For example (Stavrinidis et al., 2016) reported MNAs that were made of SU-8 for recording electroencephalogram (EEG). In other studies (Pere et al., 2018, Luzuriaga et al., 2018) reported water solvable 3D printed MNAs that were developed for drug delivery purposes. However, these studies do not include the comparison between the microfabricated MNAs with the 3D printed version of the device.

Fabrication challenges caused most of the studies about the 3D printed MNAs, investigated on the drug delivery application rather than using MANs as dry electrodes for biopotential recording or electrical stimulation. Making MNAs conductive with a biocompatible and low resistance metal (or alloy) for biopotential recording application is one of the major challenges in fabricating (or printing) conductive MNAs from the polymers. In this study $8 \times 8$ mm$^2$ MNAs (with 100 microneedles) was printed using a SLA printer. Then, it was coated with Molybdenum (Mo) to make it conductive using a direct current (DC) magnetron sputtering method. The structure

and the performance of the 3D printed MNA were compared with the replicated ones made from SU-8 in different experiments. Results showed that the structure of the replicated MNAs is significantly different from the 3D printed one with an identical geometry. The structural differences were observed in the sidewalls, edges and the microneedle tips. Also, in the method and material section, the type of 3D printing resin and its properties were compared with SU-8. Furthermore, the advantages and limitations of 3D printing MNAs were discussed and compared with the microfabricated ones in the discussion section.

## 8.2. Methods and Materials

In this section, first the 3D printing procedure for MNA is described and its properties are described. Afterwards, the resin that was used for 3D printing the MNA is compared with SU-8 which is a well-known photoresist in microfabrication processes. Then, in the second part of this section, the impedance characteristics and final structure of the 3D printed MNA are compared.

### 8.2.1. 3D printed MNA Material

In this study, 3D printer model Form II from Formlabs Company was used to print the MNA. The MNA was printed out of Clear V4 ® resin (FLGPCL04) whose properties are tested in (Zguris, 2016). Clear resin V4 is an acrylonitrile-butadiene-styrene (FormLabs) material that has been used in the other studies for 3D printing precise geometries (Chen et al., 2018, Etheredge et al., 2018). Regardless of 3D printer technology, the *solidification* process of the 3D printing materials plays a key role in the quality of the printed structure (Maniruzzaman, 2019). In the SLA printer resins, chemical solidification happens. Chemical solidification is a set of the chemical reactions inside

the resin that causes the phase change of the resins from liquid to solid state. The transition time from liquid to solid state is a determinant factor in the quality of a feature in a structure when it is printed with a polymer like Clear resin V4. For instance, if the material state transition happens slowly in photopolymer, a fine feature like the sharp edges cannot be formed and they collapse consequently. A fast solidification can result in a high-quality printed sample, however, it may weaken the adhesion of the sample to the printing substrate. Clear resin V4 is an amorphous polymer. Hence, it has a reasonable transition time from liquid state to solid one (Piorkowska and Rutledge, 2013).

Besides the material state transition time, the mechanical properties of a photopolymer (3D printer resin) play important roles on the mechanical strength of the printed structure. A weak mechanical structure cannot pierce the skin or it may break inside the tissue. The mechanical properties of Clear resin V4 are shown in Table 8.1. The values in Table 8.1 are for the post cured samples in 405 nm wavelength in 60º C for 60 minutes.

**Table 8. 1.** Mechanical properties of Clear Resin V4 (FormLabs).

| **Property Name** | **Value** |
|---|---|
| Tensile Modulus | 2.8 GPa |
| Ultimate Tensile Strength | 65 MPa |
| Flexural Modulus | 2.2 GPa |

These parameters are compared with the mechanical properties of SU-8, which is used for microfabricated microneedles, in section 8.2.4.

### 8.2.2. 3D printed microneedle geometry

The 10×10 array of needles was printed on an 8 mm × 8mm substrate. The length of the 3D printed needles is 450 µm. Each microneedle spike is 30×30 $\mu m^2$ at tip and 450×450 $\mu m^2$ at base. The walls of each microneedle spike are extended from the base to the tip with the angle of 26º. Fig. 8.2, shows the geometry of an array of 3D printed microneedles that contains 100 microneedle.

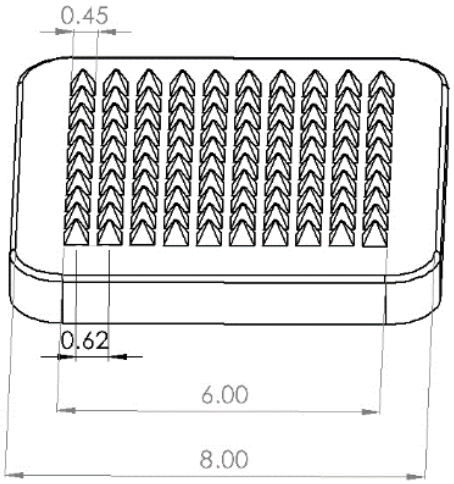


**Fig. 8.2.** The geometry of the 3D printed microneedles (all the dimensions are in mm)

### 8.2.3. 3D printed microneedle array Metallization

After printing, the samples were washed with isopropanol alcohol for 10 minutes and cured with ultraviolet (UV) light (wavelength ~305 nm) for 5 minutes. The printed microneedles were metalized using sputtering technique. The microneedles were first coated with a 250 nm layer of Titanium Nitride (TiN) to increase the mechanical strength of the microneedle spikes. The metallization process was followed by depositing a layer of 300 nm-thick Molybdenum (Mo) on top of the Ti layer to increase the electrical conductivity. Then, the sample was flipped over and a

layer of copper with 200 nm thickness was deposited on the backside of the microneedles substrate (Panescu et al.) to facilitate the wire connection on the back side of the printed MNA.

In the sputtering process, the samples were placed in the sputtering machine chamber and the chamber pressure was decreased down to $3.2 \times 10^{-6}$. In order to increase the mechanical strength of the microneedle spikes, an alloy of Ti and Nitrogen (N) was coated on the needles in a situation that the flow of Argon (Ar) and N were selected on 60 sccm and 20 sccm (working pressure 9.2 mT) and 150 W DC power. After sputtering TiN for 15 minutes with the described setting, the average thickness of the TiN was measured around 250 nm. The Mo was sputtered in the next step to increase the conductivity of the microneedles. After 30 minutes sputtering of Mo with 200 W DC power and Ar flow 78 sccm (while the working pressure was 8.3 mT), 300 nm of the metal was coated on the samples. Also, to avoid any thermal defect, all the described metal sputtering process was done with the periods of 10 minute sputtering and 5 minutes cool down.

### 8.2.4. SU-8 Microneedle Electrodes Replication and Metallization

The methods of replication and metalizing of the SU-8 microneedle electrodes were adapted from our former study (Soltanzadeh et al., 2018). In summary, an MNA template was used to build the mold of MNA from polydimethylsiloxane (PDMS). In the next step, the mold was filled by SU-8 and after proper cure procedures, the MNA was replicated. The SU-8 that was used in this study was from 2000 family. The geometry of the replicated microneedles is same as what is shown in Fig. 8.2. Also, Table 8.2, shows the mechanical properties of SU-8.

**Table 8.2.** Mechanical properties of SU-8(MicroChem)

| Property Name | Value |
|---|---|
| Tensile Modulus | 2.0 GPa |
| Ultimate Tensile Strength | 60 MPa |

A comparison between Tables 8.1 and 8.2 shows that the mechanical strength of the Clear resin is slightly more than the SU-8. However, by increasing the post exposure bake (PEB) time, the mechanical strength of the SU-8 will increase more than the typical values in Table 8.2.

### 8.2.5. Structural Comparison between the Replicated and 3D printed Microneedle Arrays

Scanning electron microscopy (SEM) images of both microfabricated and 3D printed microneedles were investigated. Energy Dispersive Spectroscopy (EDS) test was run on both of the MNAs, to ensure that the major coated material on top of the samples was Mo.

### 8.2.6. Impedance Characteristics of the Microfabricated and 3D printed Microneedle Arrays

In order to compare the functionality of the 3D printed MNAs with the microfabricated ones, their impedance characteristics were measured in the frequency range of 20 Hz to 200 KHz. Fig. 8.3 shows the location of the MNA electrodes for impedance spectroscopy. Two identical MNAs were placed on the forearm and the impedance spectroscopy was performed between them. The test was run while the electrodes were secured on the skin by pieces of medical tape. Also, before placing the electrodes, the skin was not cleaned to remove the stratum corneum.

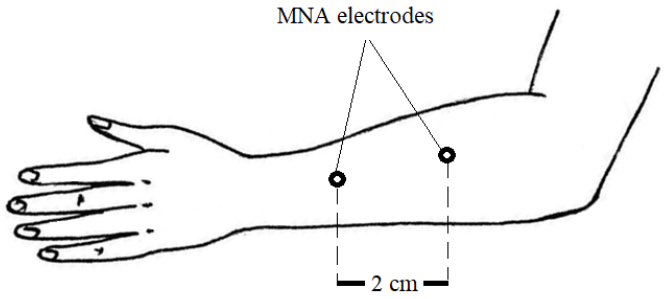


**Fig. 8.3.** MNA placement on the forearm skin

### 8.2.7. Nerve Fiber Action Potential Recording

In a clinical experiment, the signal recording ability of the 3D printed MNAs were compared with the microfabricated and conventional surface electrodes. The recorded action potential of the median nerve was studied in both time and frequency domains. The details of this experiment was described in Chapter 7 (Soltanzadeh et al., 2018). Fig. 8.4, shows the electrode placements. The MNA electrodes were connected to the amplifier setup. The test was run with VikingQuest® Electromyogram (EMG) machine with a sampling rate of 1000 sample per second and was supervised by a neurologist.

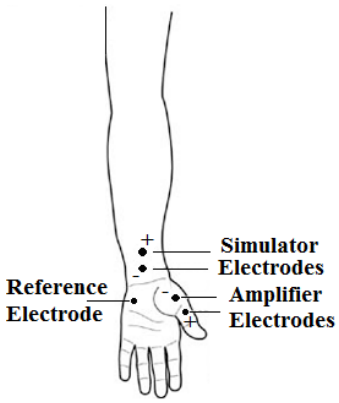


**Fig. 8.4.** Nerve conduction velocity (NCV) test electrode setup (Soltanzadeh et al., 2018)

## 8.3. Results

The results of the experiments on the microneedles are presented into three sections. In section 8.3.1, the SEM images of both 3D printed and microfabricated MNAs are compared. In section 8.3.2, the EDS graphs of the 3D printed and microfabricated MNAs are compared to ensure that the expected metal (which is Mo) is the major material on top of the MNAs. In sections 8.3.3 and 8.3.4, the impedance spectroscopy and the clinical measurement of the microfabricated MNA and 3D printed one are compared respectively.

### 8.3.1. Structural Comparison of Microfabricated and 3D printed MNAs

The SEM images of the 3D printed MNA and microfabricated MNAs are shown in Fig. 8.5a and Fig. 8.5b. Through the SEM images, some differences could be understood in the details of the MNA structures. The major structural difference that can be seen it the SEM images is the side walls of the needle spikes. Fig. 8.5 shows that the side walls of the microfabricated needles are sharper than the 3D printed ones. The quality of the microneedles' walls will affect the depth of penetration of an MNA electrode.

In the process of microfabrication, a PDMS mold was used to replicate the microneedles. The side walls of the PDMS mold provide the sufficient support for the SU-8 microneedles in the molding procedure. This support does not exist in the 3D printing process, therefore the walls of the microfabricated MNAs are sharper than the 3D printed one. Another reason is the difference between the solidification time of the SU-8 and the Methyl Methacrylate oligomer (MMA) which is the main material of the Clear resin (Tontowi et al., 2016).

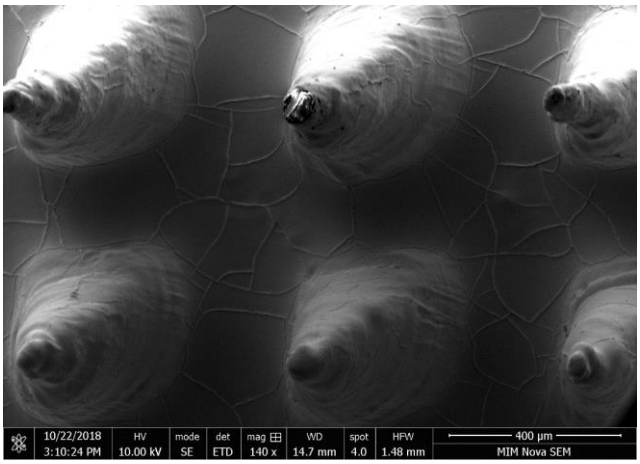


(a)

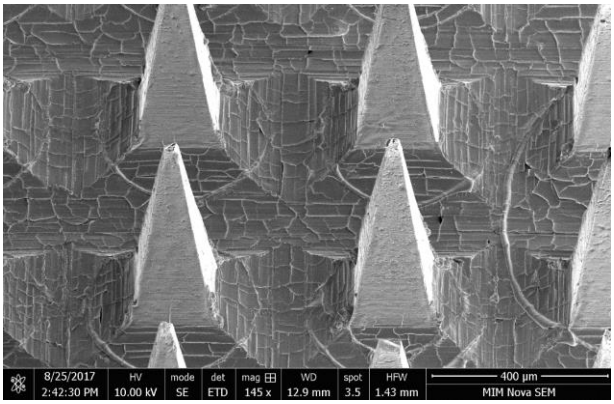


(b)

**Fig. 8.5.** SEM image of (a) 3D printed MNA electrode (b) Microfabricated MNA electrode

The effect of sharp tips and walls of an MNA on its performance was investigated by developing a 3D multilayer model. The developed model was analyzed using a finite element analysis (FEA) simulation in COMSOL Multiphysics 5.3 software. In the developed model, a microneedle spike was segmented into 3 equal lengths. It was assumed that in a proper MNA penetration, two third of the needles on its surface pierced the skin which equals to 300µm for a 450µ-tall needle. In another simulation scenario, only one third of the needles lengths pierced the skin which equals to 150µm for a 450µm-tall needle. The simulation was run for the described

scenarios with different depths of penetrations. The frequency of the input voltage was swept from 20 Hz to 200 kHz and the impedance between the MNA electrodes was calculated. The simulated MNAs contained 100 microneedles on the surface. The parameters of the model like the geometry and electrical properties were adapted from former investigations and the model developed in Chapters 3 and 4 (Comsol, 2011, Elder and Yoo, 2018, Panescu et al., 1995). Fig. 8.6, shows the developed 3D model that consists of different layers of the skin, two never fibers and a blood capillary in the subcutaneous layer. Simulation in the frequency domains showed that the depth of penetration affects the impedance between the electrode and the first layers of the skin. As it is shown in Fig. 8.7, particularly in lower frequencies, the impedance of the MNA that pierced skin with the depth of 150 µm is higher than the one that pierced the skin with depth of 300 µm. In practice, the impedance in the interface of the MNAs and skin can be more than what is simulated. The reason is that the MNAs will not be inserted evenly when an individual wants to use it. Therefore, some spikes may not even pierce the skin and some may fully penetrate and this ends to an inconsistent impedance in the interference of an MNA and the first layer of the skin.

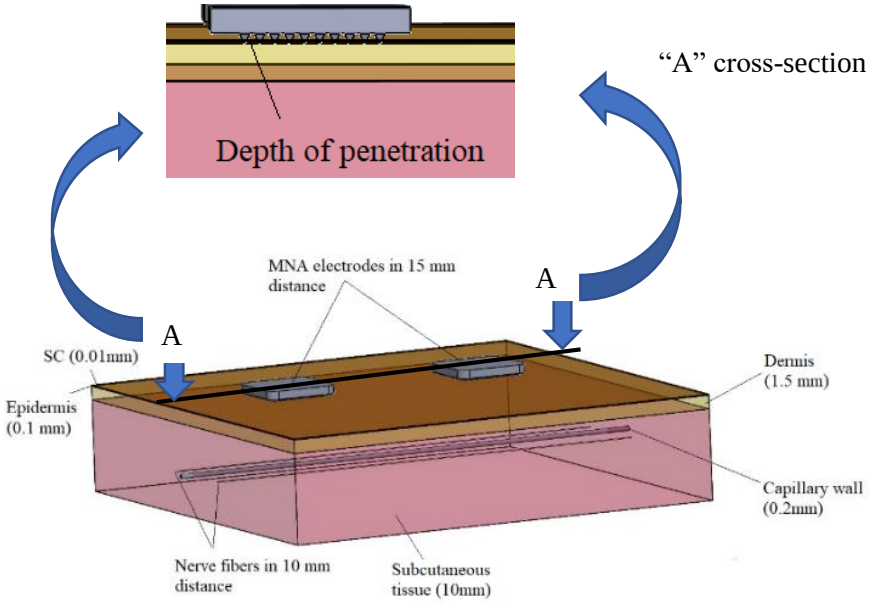


**Fig. 8.6.** Developed 3D model to investigate the effect of different depths of penetration by MNAs

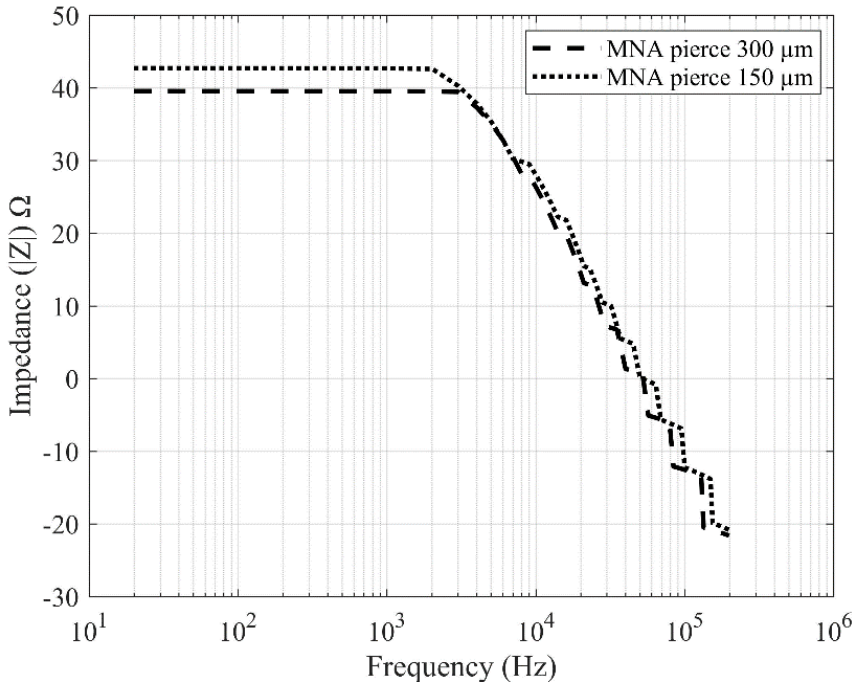


**Fig. 8.7.** Simulated impedance spectroscopy of the MNA pierced the skin in different depths of penetration.

The microfabricated electrodes have sharper edges than the 3D printed ones but sometimes molding procedures may defect the fabricated structure. Since the molding procedure was done in medium vacuum chamber, the main material of the SU-8 damages the PDMS mold can causes the structural defects that is shown in Fig. 8.8a. Furthermore, peeling the molded sample of the mold may cause some defects itself. Most of the time, peel off defects affect the fine parts of the microstructures like their tips as it is shown in Fig. 8.8b.

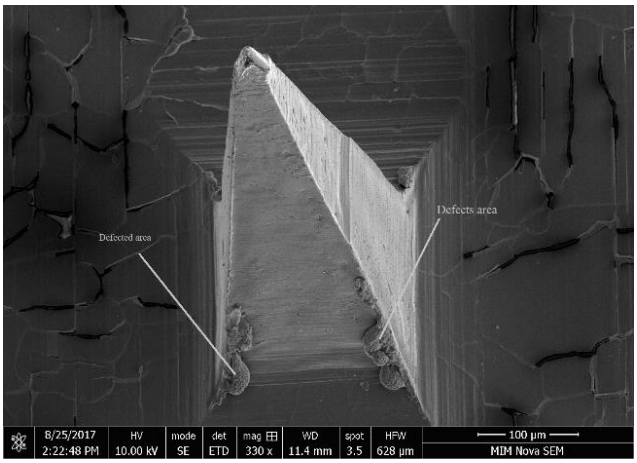


(a)

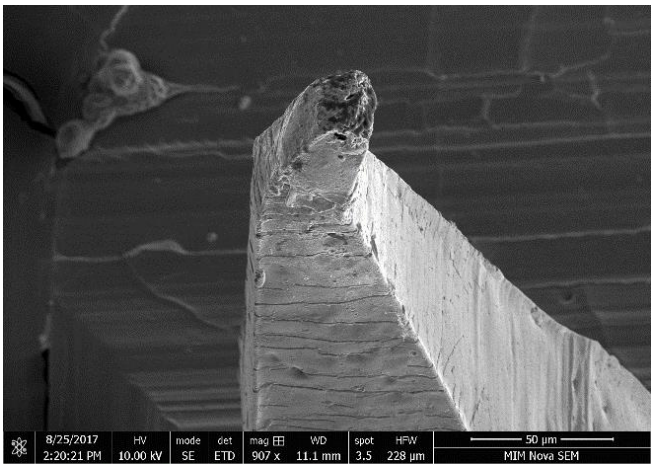


(b)

**Fig. 8.8.** (a) Defected parts on the edges of a microneedle because of the solvent evaporation during low pressure molding procedure (b) Damaged microneedle tip during peel off of the sample from micromold.

### 8.3.2. Energy Dispersive Spectroscopy

As mentioned above, the fabricated and 3D printed MNA arrays were sputtered with Mo as the finished conductive layer. However, because of the plasma formation during sputtering process, there is a risk that the Mo reacts chemically or make an alloy with the elements of the SU-8 and Clear resin. In order to make sure about the dominant element on top of the MNA arrays, the EDS measurement was run on both fabricated and printed MNA. Fig. 8.9 shows the EDS result of the coated and uncoated area of a 3D printed MNA and the microfabricated one form SU-8.

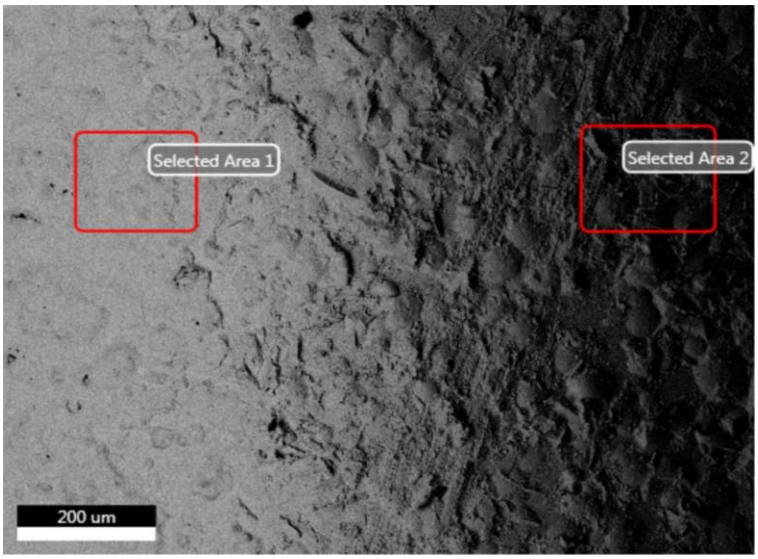


**Selected Area 1**

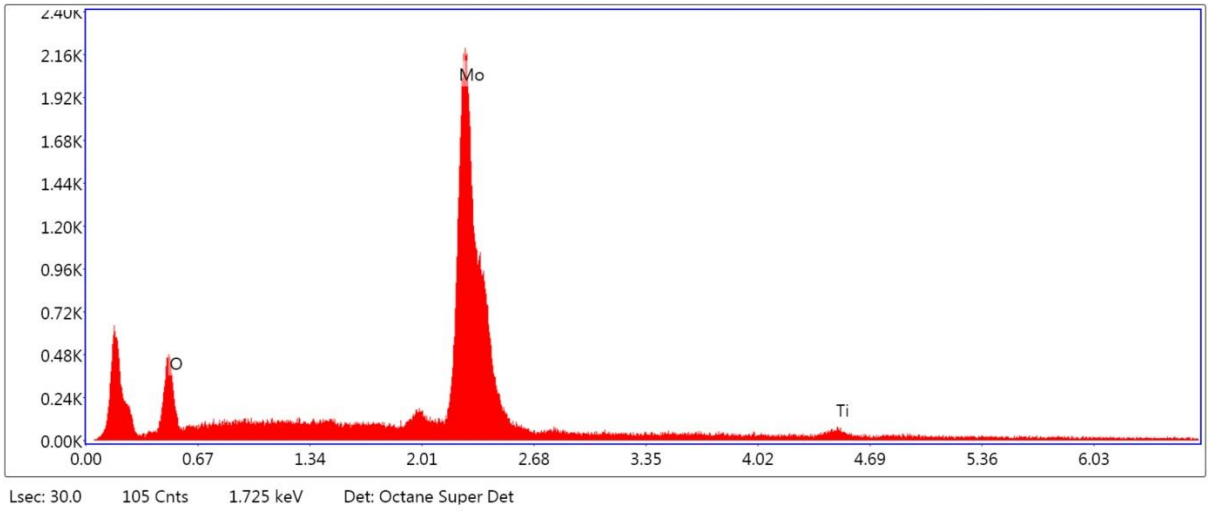

**Selected Area 2**

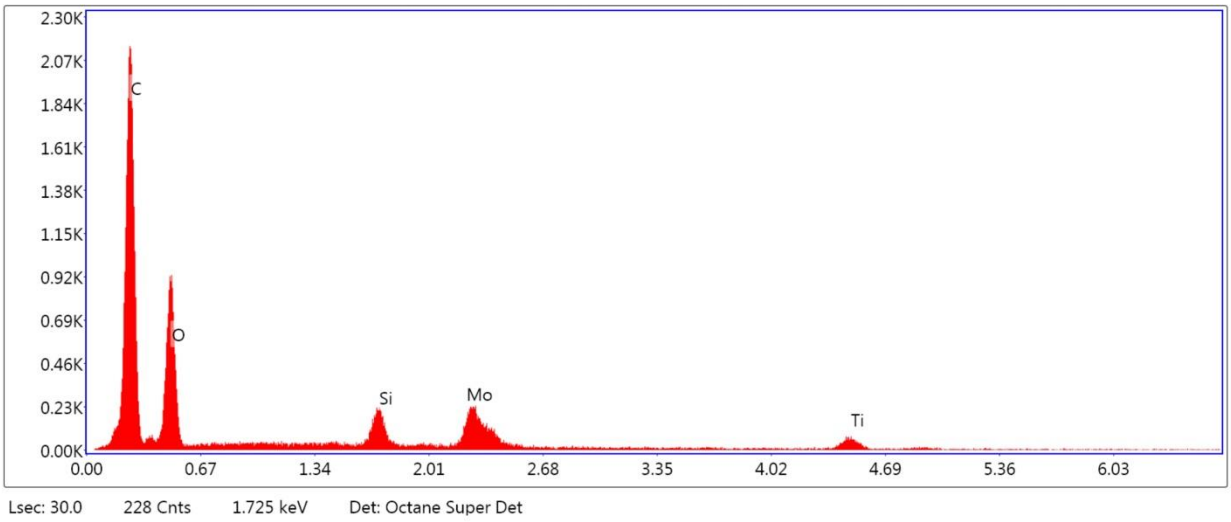


(a)

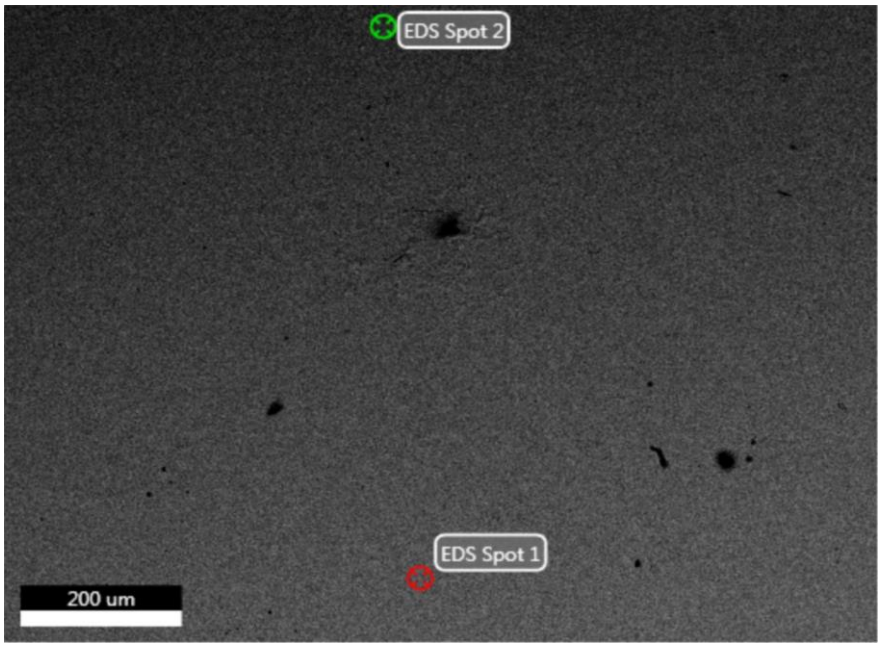

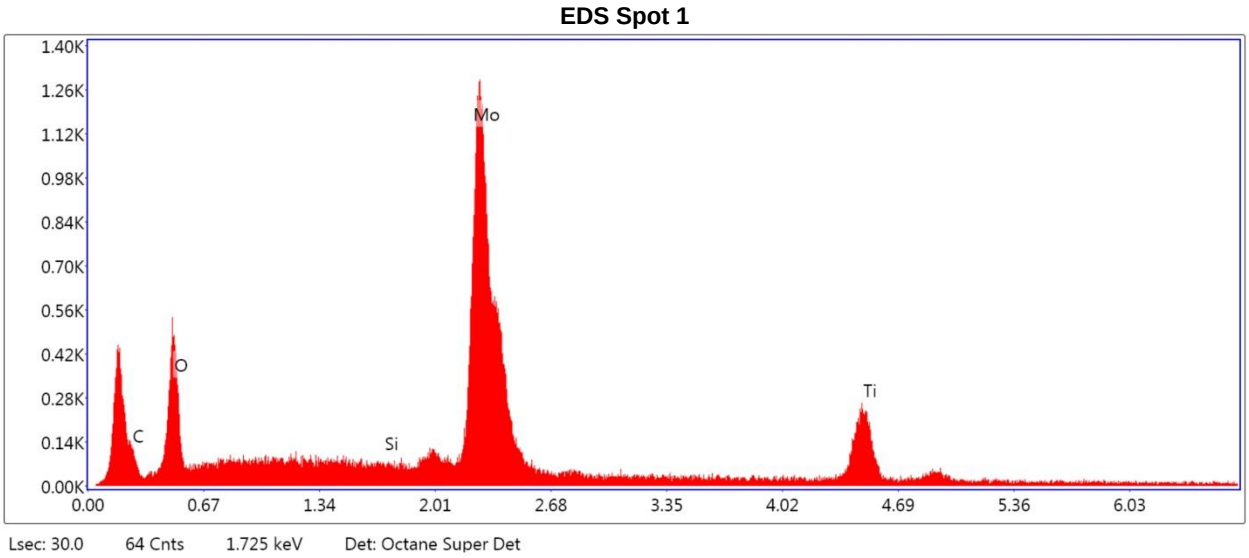


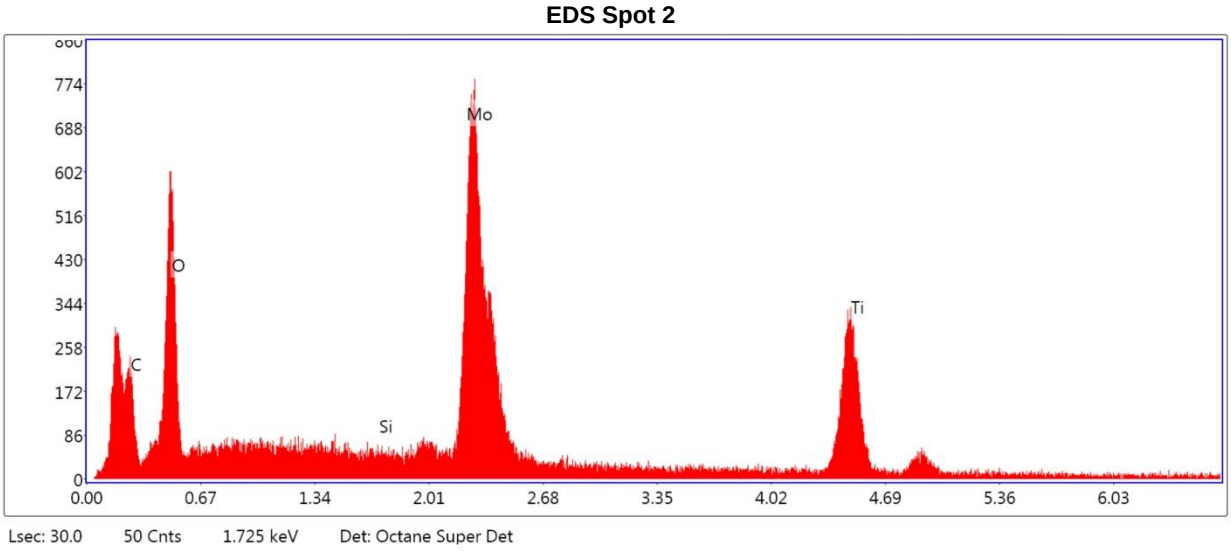


(b)

**Fig. 8.9.** EDS analysis of (a) 3D printed MNA (b) microfabricated MNA

The graphs of Fig. 8.9 show that the after sputtering, the Mo coated the surface of the samples properly and it is the dominant element of the finished surface of the microneedles. Likewise, in the non-sputter coated area, the major element is carbon which is the main material of the polymers.

### 8.3.3. Electrical Impedance Spectroscopy of the Microfabricated and 3D printed MNAs

The impedance of the microfabricated MNAs and the 3D printed ones were measured in the range of 20 Hz to 200 kHz with 4294A Agilent™ Impedance Analyser with the step of 10 Hz. Fig. 8.10 shows the absolute value and the phase of the impedance for the samples that built with different methods. The test was run 3 times and there was not any significant difference between the results of each time.

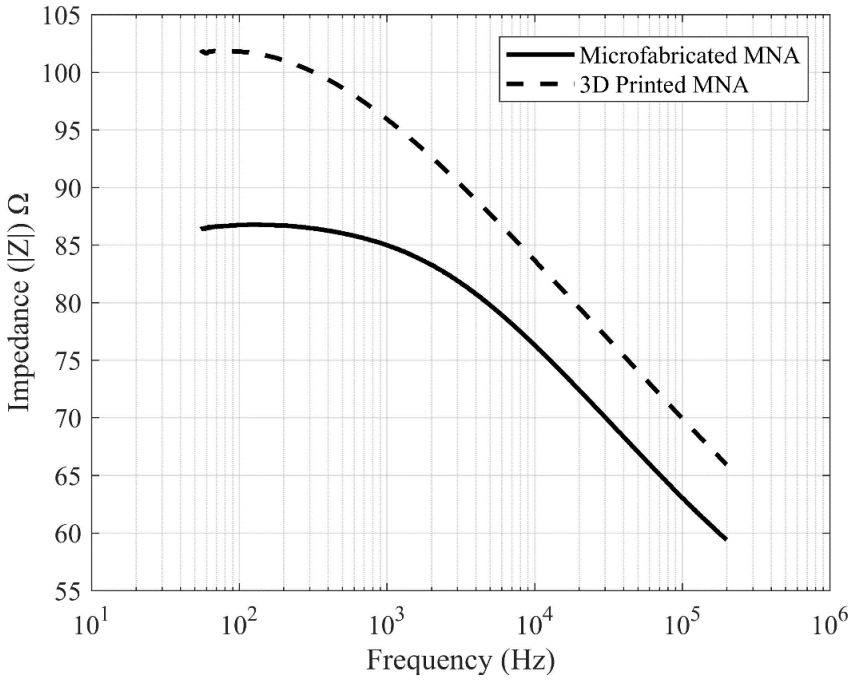


(a)

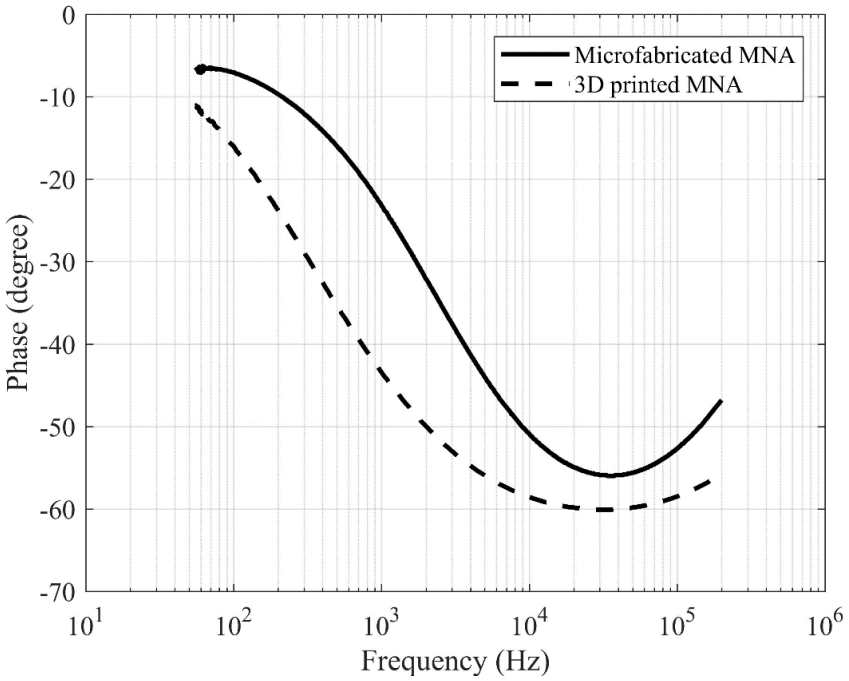


(b)

**Fig. 8.10.** A comparison between impedance (a) magnitude (b) phase of microfabricated and 3D printed MNAs

From Fig. 8.10, it can be inferred that the impedance difference between the 3D printed and microfabricated MNAs is significant particularly in the lower frequencies. Also, the phase of the 3D printed MNA is less than the phase of the microfabricated ones. It means that the 3D printed MNAs have more capacitance effect than the microfabricated ones.

### 8.3.4. Nerve Action Potential Recording

The performance of the 3D MNAs was compared with the microfabricated one in an extra experiment which was NCV test. As it was described in section 8.2.7, two electrodes were used to stimulate the median nerve and two MNAs were used to record the response of the nerve with respect to a reference electrode.

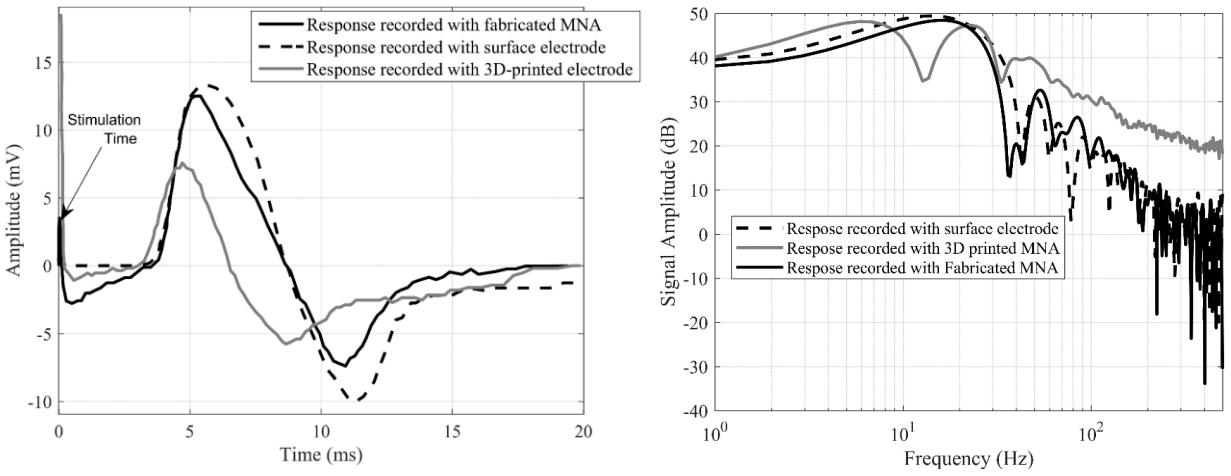


(a) (b)

**Fig. 8.11.** (a) Time domain (b) frequency domain of the median nerve response

From the time and frequency responses of Fig. 8.11, it can be understood that the 3D printed MNAs' performance is similar to the microfabricated ones. Also, because the skin was properly prepared in this test (cleaned with an alcohol pad), the surface electrodes have similar response to the MNAs. However, amplitude of the high frequencies in the 3D printed MNAs is higher than the other types of the MNA. This supports the results that obtained from electrical impedance spectroscopy section where it was showed that the capacitance of the 3D printed MNAs is higher than the microfabricated one. In the other word, the 3D printed MNAs can pass the high frequency signals more than the microfabricated ones. There are more discussions about the differences between different electrodes in the discussion section. It is worthwhile to mention that the nerve response signal was recorded 3 times in identical recording setup and situation and no significant difference was observed.

## 8.4. Discussion

Nowadays, 3D printing technology has engaged into different field of science and medicine. However, there is not enough studies to show its effectiveness particularly in microstructure printing. In this study the structure and the performance of a 3D printed and microfabricated MNA were compared. The design of the structure was identical but one was built with micromolding and the other was printed with a SLA 3D printer. In the structural comparison, it was shown that the structure of the needles' spikes changed during the printing procedure. The reason is relatively long solidification time of the 3D printing resin. Changing the structure of a needle spike from pyramid to cone can affect the needle's depth of penetration and it was shown in the simulation at the end of section 8.3.1.

Besides the solidification, in the micromolding technique the area around each spike is confined and the main material (SU-8) has enough time to keep its shape. However, due to the fact that the micromolding technique was performed in a medium vacuum chamber, some defects were seen on the body of the needles like what is shown in Fig. 8.8. Regardless of the quality of the structure, the building time is another important factor that distinguish between the microfabricated and 3D printed MNA. In order to print an MNA that has 220 layers with 0.02 mm thickness, it needs 42 minutes and 15 seconds. This time is relatively constant for printing up to 5 needles on a substrate. However, micromolding needs more than an hour and vacuum oven. Therefore, 3D printing would be faster and easier than microfabrication techniques.

Difference in the main material of the 3D printed and microfabricated MNAs did not affect the results of sputtering. In graphs of section 8.3.2, it was shown that the results of EDS measurements are consistent in both sputtered 3D printed MNA and the microfabricated one.

As a part of performance comparison, the impedance of the microfabricated and 3D printed MNAs were measured in different frequencies from 20 Hz to 20 kHz. It was shown that the impedance of the 3D printed MNAs is significantly higher than the microfabricated MNA. The reason can be found in the images of Fig 8.9. In these images, it is shown that the surface of the 3D printed structure is rougher than the microfabricated ones. Therefore, the connectivity between the sputtered metal spots on the surface of the 3D printed structure is weaker than the microfabricated ones that ends to lower conductivity. Also, the depths of penetration can be another reason. Because of the sharp wall edges in microfabricated needles, it can be speculated that the 3D printed MNA cannot pierce the skin as deep as the microfabricated ones.

The last performance comparison was done based on a clinical study that its results were described in section 8.3.4. In the graphs of both tine and frequency domains, it is shown that the microfabricated MNAs performed so close to the surface electrode when the skin was prepared by an alcohol pad. However, the 3D printed MNAs can record high frequency components of the signal with higher gain. This shows that a 3D printed MNA increase the capacitance in the interface of the recorder and the tissue. The reason of this increase can be higher relative permittivity of MMA (main material of the 3D printed MNAs) compared to SU-8 (main material of the microfabricated MNA) in the measured range (Thomas et al., 2012, MicroChem). Although it is a suitable feature for recording the bio-signal with high frequency components like electromyogram (EMG), it cannot be considered as a benefit for low frequency signals like EEG. The notch in the frequency range from 10 Hz to 20 Hz (where the most of the EEG component existed (Georgopoulos and Vaporidi, 2019)) supports the idea that the 3D printed MNAs are not suitable for recording low frequency signals like EEG.

Overall, it can be concluded that neither structure nor performance of the microfabricated and 3D printed MNAs are similar. Microfabricated MNAs can be used for recording different bio-signals. Also, they can be used for stimulation of the nerve percutaneously. However, the 3D printed MNAs, are not good choice for low frequency bio-signal. It can be predicted that the performance of the 3D printed MNAs will not be as good as the microfabricated ones in stimulation but it needs to be studies separately.

## 8.5. Conclusion

In this study the feasibility of print MNAs was investigated and it was understood that the microneedles with the length more then 0.5 mm can be printed with the SLA printers. Then, the printed MNAs were coated with metal to be conductive. In order to find the difference between the 3D printed MNAs and the microfabricated ones, SEM images were taken from both 3D printed and microfabricated MNAs. The images revealed that the structure of the 3D printed MNAs was not exactly what was expected. Also, the roughness of the surface in the 3D printed structures is more than the microfabricated ones. This ends to the fact that 3D printed MNAs have higher impedance and they are not suitable for direct current stimulation and some biosignal recordings. However, more clinical studies are required to determine the exact advantages and disadvantage of MNA applications and particularly 3D printed MNAs in medicine.

## References

AU, A. K., BHATTACHARJEE, N., HOROWITZ, L. F., CHANG, T. C. & FOLCH, A. 2015. 3D-printed microfluidic automation. Lab on a chip, 15, 1934-1941.

BROWN, A. C. & DE BEER, D. Development of a stereolithography (STL) slicing and G-code generation algorithm for an entry level 3-D printer. AFRICON, 2013, 2013. IEEE, 1-5.

CHEN, P., ALBERT, B. J., GAO, C., ALANIVA, N., PRICE, L. E., SCOTT, F. J., SALIBA, E. P., SESTI, E. L., JUDGE, P. T. & FISHER, E. W. 2018. Magic angle spinning spheres. Science advances, 4, eaau1540.

CHIA, H. N. & WU, B. M. 2015. Recent advances in 3D printing of biomaterials. Journal of biological engineering, 9, 4.

COMSOL, A. 2011. AC/DC Module–User's Guide. COMSOL, 3, 151.

ELDER, C. W. & YOO, P. B. 2018. A finite element modeling study of peripheral nerve recruitment by percutaneous tibial nerve stimulation in the human lower leg. Medical engineering & physics, 53, 32-38.

ETHEREDGE, A., ELLETT, T., POOLE, G. & REICHERT, W. M. 2018. Plasticization of PMMA Components Using Imidazolium-Based Ionic Liquids in Stereolithography Additive Manufacturing. ECS Transactions, 86, 239-245.

FORMLABS. Clear Resin V4, datasheet

FORVI, E., BEDONI, M., CARABALONA, R., SONCINI, M., MAZZOLENI, P., RIZZO, F., O'MAHONY, C., MORASSO, C., CASSARÀ, D. G. & GRAMATICA, F. 2012. Preliminary technological assessment of microneedles-based dry electrodes for biopotential monitoring in clinical examinations. Sensors and Actuators A: Physical, 180, 177-186.

GEORGOPOULOS, D. & VAPORIDI, K. 2019. Sleep and Wakefulness Evaluation in Critically Ill patients: One Step Forward. American journal of respiratory and critical care medicine.

GROTH, C., KRAVITZ, N. D., JONES, P. E., GRAHAM, J. W. & REDMOND, W. R. 2014. Three-dimensional printing technology. J Clin Orthod, 48, 475-85.

HO, C. M. B., NG, S. H., LI, K. H. H. & YOON, Y.-J. 2015. 3D printed microfluidics for biological applications. Lab on a Chip, 15, 3627-3637.

LEE, J. W., PARK, J.-H. & PRAUSNITZ, M. R. 2008. Dissolving microneedles for transdermal drug delivery. Biomaterials, 29, 2113-2124.

LUZURIAGA, M. A., BERRY, D. R., REAGAN, J. C., SMALDONE, R. A. & GASSENSMITH, J. J. 2018. Biodegradable 3D printed polymer microneedles for transdermal drug delivery. Lab on a Chip, 18, 1223-1230.

MANIRUZZAMAN, M. 2019. 3D and 4D printing in biomedical applications: process engineering and additive manufacturing, Wiley-VCH.

MANNOOR, M. S., JIANG, Z., JAMES, T., KONG, Y. L., MALATESTA, K. A., SOBOYEJO, W. O., VERMA, N., GRACIAS, D. H. & MCALPINE, M. C. 2013. 3D printed bionic ears. Nano letters, 13, 2634-2639.

MICHALSKI, M. H. & ROSS, J. S. 2014. The shape of things to come: 3D printing in medicine. Jama, 312, 2213-2214.

MICROCHEM.SU-8, 2000 family datasheet

MIRONOV, V., BOLAND, T., TRUSK, T., FORGACS, G. & MARKWALD, R. R. 2003. Organ printing: computer-aided jet-based 3D tissue engineering. TRENDS in Biotechnology, 21, 157-161.

PANESCU, D., WHAYNE, J. G., FLEISCHMAN, S. D., MIROTZNIK, M. S., SWANSON, D. K. & WEBSTER, J. G. 1995. Three-dimensional finite element analysis of current density and temperature distributions during radio-frequency ablation. IEEE Transactions on Biomedical Engineering, 42, 879-890.

PERE, C. P. P., ECONOMIDOU, S. N., LALL, G., ZIRAUD, C., BOATENG, J. S., ALEXANDER, B. D., LAMPROU, D. A. & DOUROUMIS, D. 2018. 3D printed microneedles for insulin skin delivery. International journal of pharmaceutics, 544, 425-432.

PIORKOWSKA, E. & RUTLEDGE, G. C. 2013. Handbook of polymer crystallization, John Wiley & Sons.

PRAUSNITZ, M. R. 2004. Microneedles for transdermal drug delivery. Advanced drug delivery reviews, 56, 581-587.

RYBICKI, F. J. & GRANT, G. T. 2017. 3D Printing in Medicine: A Practical Guide for Medical Professionals, Springer.

SOLTANZADEH, R., AFSHARIPOUR, E., SHAFAI, C., ANSSARI, N., MANSOURI, B. & MOUSSAVI, Z. 2018. Molybdenum coated SU-8 microneedle electrodes for transcutaneous electrical nerve stimulation. Biomedical microdevices, 20, 1.

STANDARD, A. 2013. F2792-12a: Standard Terminology for Additive Manufacturing Technologies (ASTM International, West Conshohocken, PA, 2012). P. Jain, AM Kuthe,

Feasibility study of manufacturing using rapid prototyping: FDM approach, Procedia Eng, 63, 4-11.

STAVRINIDIS, G., MICHELAKIS, K., KONTOMITROU, V., GIANNAKAKIS, G., SEVRISARIANOS, M., SEVRISARIANOS, G., CHANIOTAKIS, N., ALIFRAGIS, Y. & KONSTANTINIDIS, G. 2016. SU-8 microneedles based dry electrodes for Electroencephalogram. Microelectronic Engineering, 159, 114-120.

THOMAS, P., RAVINDRAN, R. E. & VARMA, K. Dielectric properties of Poly (methyl methacrylate)(PMMA)/CaCu 3 Ti 4 O 12 composites. 2012 IEEE 10th International Conference on the Properties and Applications of Dielectric Materials, 2012. IEEE, 1-4.

TONTOWI, A. E., KUSWANTO, D., SIHALOHO, R. I. & SOSIATI, H. Composite of [HA/PMMA] for 3D-printer material application. AIP Conference Proceedings, 2016. AIP Publishing, 150020.

WANG, X., JIANG, M., ZHOU, Z., GOU, J. & HUI, D. 2017. 3D printing of polymer matrix composites: A review and prospective. Composites Part B: Engineering, 110, 442-458.

YU, L., TAY, F., GUO, D., XU, L. & YAP, K. 2009. A microfabricated electrode with hollow microneedles for ECG measurement. Sensors and Actuators A: Physical, 151, 17-22.

ZGURIS, Z. 2016. How mechanical properties of stereolithography 3D prints are affected by UV curing. Formlabs Inc., Somerville, MA, accessed Mar, 7, 2017.

# 9

# Conclusion and Future works

## Summary

In this thesis new type of electrodes were suggested for electrical nerve stimulation and recording. Through different analysis and simulations, it was shown that the suggested microneedle array electrodes are working better than the conventional surface electrodes for both stimulation and recording. However, thee geometry of the microneedles should be modified depends on the type of application. Also, different low-cost methods were suggested to build the microneedle arrays. One may continue working on this topic with using the suggested electrodes in different application like electrical impedance tomography and compare the results with the conventional electrodes. More clinical and animal studies can also be recommended as a part of future work.

## 9.1. Conclusion

In this thesis, the performance of microneedle arrays was assessed for their performance in stimulation and recording. The focus was to investigate these new electrodes for nerve stimulation in terms of their ability to provide enhanced performance in different parameters like distinguishability between two nerves and avoid co-stimulation. This is very important particularly when the stimulation is used as a treatment method to moderate chronic syndromes like apnea and overactive bladder. Efforts included both simulation and clinical experimentation, so as to provide a comprehensive analysis on the functionality of the MNAs on both recording and stimulation. Also, a complete review on different methods of microneedle fabrication was presented. In the fabrication part, two low-cost methods for building MNAs were presented.

In chapter 2, a brief review on the nervous system in human body was presented. Since the skin is the first layer in TENS that electrical current should pass by, its mechanical and electrical properties were reviewed in a part of chapter 2. Also, depends on the application, different protocols are existed for TENS that has been reviewed in chapter 2.

In chapter 3, the parameters of stimulation like distinguishability, SAR, current density and others were analyzed for both microneedle electrodes and the conventional surface ones. Through a multiphysics simulation, it was shown that the suggested electrodes can increase the distinguishability while the SAR and temperature of the inner layers of the tissues from the skin surface and the nerve are not increasing. Therefore, using the microneedle electrodes can increase the efficiency of the stimulation. In the other words, the explorations of this study have shown that MNAs are suitable electrodes that can replace conventional surface stimulation electrodes. More robust and uniform current density, better distinguishability, and effective thermal behaviour for long term usage are the advantages of MNAs that are highlighted in this study through different

simulation scenarios. Besides the stimulation parameters, it was shown that the presence of any blood vessel in vicinity of a nerve fiber does not have a significant impact on the results stimulation while the electrical current is applied via microneedle electrode. In contrast, presence of a material with high conductivity, like blood, can drastically have negative impact of the stimulation. It was shown that the existence of blood capillaries can make the current density inconsistent in different depth of the tissue. Although the performance of microneedle electrodes is more consistent in different limbs with different variant types of tissue, the structure of the microneedle arrays is really important.

Investigations in chapter 4 showed that the tip-to-tip pitch of the microneedle arrays and the area that microneedles occupied on the electrode surface will affect the calculated stimulation parameters. Different scenarios of simulation showed that the tip-to-tip pitch around 0.62 mm and 100 microneedle on a surface was the best feasible geometry configuration. Increasing the pitch further or decreasing the pitch and increasing the number of needle spikes on surface was found approaching to the situation of a continuous surface and so the results of the surface electrodes. In the scenarios where the number of electrodes were decreased, because the current density was also decreased, the distinguishability of stimulation between a nerve fiber and its adjacent fiber was poor. Microneedle spikes strength the electric field along the z-axis that makes the electric field more directive and uniform toward the target nerve.

Using MNAs is altering the electrical parameters between the tissue and the electrode. Therefore they deliver more focused electric field to a target nerve. Loosely speaking, increasing the depth of penetration by microneedles will increase the distinguishability of a specific target nerve because it is decreasing the capacitance and resistance between the electrode and tissue. However, decreasing the length of the microneedle spikes will increase current density in different

depth because of increasing both resistance and capacitance (much more than resistance) between the tissue and electrode. This conclusion is supported while one is using surface electrode for stimulation that generates a widely distributed electric field (with singularities on the edges of the electrodes), extended along the underlying SC layer and does not specifically target a below nerve fiber. One should keep this in mind that depends on application, the geometry of the microneedles, their distribution on the surface and their structural material should be determined properly based on these findings.

After analyzing the performance of various MNA designs, and finding the best ones, the techniques for fabrication were reviewed. A complete review on the fabrication of different types of microneedles was presented in chapter 5. Since the application of the microneedle may affect the fabrication process, the application of different fabrication methods was also reviewed in this chapter. It was understood that the most flexible materials for microneedle fabrication are photopolymers. SU-8 is a negative tone biocompatible photoresist that has enough mechanical strength to be used as the main structural material. In the first fabrication effort of this thesis, various SU-8 etching recipes for building an MNA were investigated. However, problems like metal mask peel-off and SU-8 burning were encountered, and so it was not possible to build MNAs by etching SU-8.

Different methods of fabrication were explored, and it was realized that the best way to fabricate a high aspect ratio microstructure is molding. Therefore, a PDMS mold was built from a polycarbonate master (that was built in another study through hot embossing method) and an MNA was replicated from SU-8 and metalized with Mo. The experimental clinical studies and impedance spectroscopy measurement showed that the microfabricated MNA enhances the tissue-

electrode interface parameters, such as decreasing the resistance and increasing the double-layer capacitance.

Since microfabrication procedures are time consuming and difficult, this thesis also explored 3D printed MNAs, which were printed with SLA printers and Clear resin V4 commercial resin from Formlabs Company. The dominant material in Clear resin is methyl methacrylate. However, because of longer solidification time and lack of support, the structure of the 3D printed MNAs was different from the main design and microfabricated ones. Analysis and measurement showed that the 3D printed MNAs perform better than the microfabricated ones in high frequency signal recoding like EMG. For low frequency signals like EEG, the microfabricated MNAs perform better than the conventional surface electrodes. Since the stimulation signals are usually low frequency square waves, the 3D printed MNAs cannot be suitable choice for stimulation.

## 9.2. Future work

This study showed that the tip-to-tip pitch of the microneedles plays important role in distinguishability (or selectivity) of a specific nerve beside the adjacent ones. Therefore, design and optimizing a model that can link all the geometrical and stimulation parameters can be a good start point for the future work. Geometry optimization can be the next step that optimizes the shape, length of the fabricated MNAs based on the depth of the target nerve fiber and adjacent tissues.

In order to strengthen the results of the optimized model, a complete animal study is suggested. Two adjacent nerve can be picked in a rodent and current sensing sensor can be implemented inside the animal body. The current around each nerve fiber and the adjacent tissue can be measured while the tissue is stimulated transcutaneously. The described animal study can

assess the performance of different electrodes and verify any 3D model that is developed for stimulation. A preliminary animal study was done to study the effect MNAs stimulation on HGN but it was not completed to report (for more detail see the Appendix).

The skin is the first protection barrier for the internal organs. Among the skin layers, the first layer, SC, has the highest electrical impedance. Therefore, bypassing SC will end higher signal-noise-ratio (SNR) in the application like electrical impedance tomography (EIT). One of the future studies can be assessment of the EIT images of the surface and MNA electrode and compare the peak of SNA in reconstructed images.

Different clinical applications for recoding and stimulating through MNAs can be explored, as well as using the MNAs for medical devices, wearable devices, etc.. MNAs potentially represent the next generation of reusable electrodes (because they can be washed with alcohol and sterilized in oven) for medical devices. However more clinical and experimental works are required.

Though electrode type and geometry are very critical in stimulation results, the configuration of stimulation signal and the stimulation protocol is another key factor that should be considered in targeting a specific nerve. Developing a general model that can discuss the performance of different MNA geometries with different stimulation configuration can also be suggested as a future study in this field.

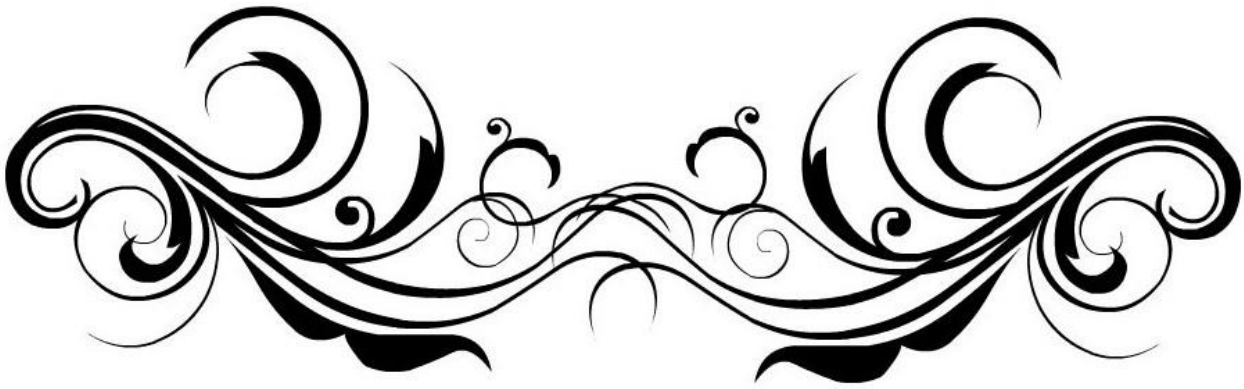

# Appendix

**Hypoglossal nerve stimulator development project – Pilot project animal study proposal**

**INTRODUCTION**

Obstructive sleep apnea (OSA) is a common, serious disorder defined as episodic obstruction of the airway during sleep. Obstructive episodes are caused by relaxation of the muscles of the tongue and pharynx, particularly in deeper stages of sleep – stages III and IV. The episodes may be brief and of little consequence or prolonged and of serious consequence. OSA is more common in males than females. OSA is highly correlated with obesity, excessive daytime sleepiness with loss of productivity, motor vehicle accidents, cardiomyopathy and a variety of health disorders.

Lee et al (2008) report that Obesity is a well-recognized risk factor for a variety of medical conditions such as type 2 diabetes, cardiovascular diseases, hyperlipidemia, metabolic syndrome, and nonalcoholic fatty liver disease. OSA greatly increases the odds of cardiovascular disease. It is a major health problem and will increase in importance as the obesity epidemic continues. Using in-laboratory polysomnography, Young et al (1993) reported that the prevalence of OSA (AHI ≥ 5) in 602 middle-aged adults between 30 and 60 years of age was 9% for women and 24% for men.

The fundamental pathophysiology of OSA is a loss of muscle tone in the base of tongue muscles during the deep stages of sleep which causes the airway to collapse, obstructing airflow. This obstruction is relieved by partial alerting so that the muscle tone is increased, opening the airway until the cycle repeats again. When this occurs hundreds of times per night, poor oxygenation and cardiovascular complications are likely.

Although the pathophysiology is strait forward, treatment is not. Tracheotomy is highly effective, but very few people would tolerate a tracheotomy for this disorder. Other forms of nasal, dental and oropharyngeal surgery and appliances have limited success. Standard therapy today is continuous positive airway pressure (CPAP) delivered via a mask, tightly applied during sleep. CPAP is uncomfortable and non-compliance rates are high. Many patient simply stop using the machine and tolerate the disease.

This project seeks to develop a new approach to treating OSA by maintaining muscle tone in the muscles of the tongue with a newly developed type of electrode. The new electrode is a patch that can be worn like a Band-Aid and has a special design that offers much lower resistance than other types of electrode. It can be predicted that this should prevent the obstructive episodes. Although muscle stimulation has been tried in the past it has not been successful because the method of stimulating the muscles using needle or surface electrodes is unpleasant. Large current densities are required for surface electrodes to stimulate the nerve and/or muscle percutaneously. Needle electrodes and various electrified oral appliances can stimulate the tongue but these devices are painful and not feasible for routine use. For this project the evidences were explored that showed the surface electrode system can increase muscle tone when the hypoglossal nerve is stimulated by wearing a wearable stimulator circuit (WSC). The electrode array consists of microneedle patches (MNP) that do not pierce the skin, yet should deliver reliable stimulation to the nerve and muscle. Later projects will refine the parameters more fully, if this pilot study shows promise.

## HYPOTHESIS

The wearable hypoglossal nerve stimulator (WHGNS) with the MNPs will increase muscle tone in a controlled manner.

## METHODS

A custom-made apparatus will be constructed that consists of two components, 1) a recording system that records spontaneous firing rates of muscle and 2) two stimulation systems that stimulation of muscle of the tongue. One of the stimulation systems will be our WHGNS and the other will be a commercially available stimulator that stimulates muscle by transcutaneous needle electrodes.

Tongue muscles demonstrate natural myoelectric impulse patterns that are modulated by the stage of sleep and respiratory cycle. The sensor system will record the pattern and frequency of these impulses in the tongue and permit synchronization of the stimulation, if desired, with respiratory cycle. The sensor will employ a clip-type of electrode, clipped to the frenula in the midline of the tongue. A thermistor will be available to permit recording of the respiratory cycle.

Two types of stimulator will be compared – ours and a commercially available system (Agilent 33220A). The commercially available standard stimulator utilized needle electrodes inserted into the hypoglossal muscles. Our new WHGNS stimulator looks like a 1 cm3 patch of material but it actually has hundreds of tiny projections that increase the surface area. These projections are molybdenum (Mo) coated in tungsten (W) that results in a very low. Hypothetically this low impedance will permit effective simulation with small current densities, reducing the unpleasant sensation of other types of electrode systems. The sensor will be placed in the submandibular area directly on the skin after shaving. It will be held in place with tape. There is some evidence that

a reasonable set of electrical parameters for this application utilizes electrical pulses every 5 sec, 2 ms length, 20 mV (Koizumi, Hidehiko et al.[2008]).

**Questions to be addressed in this pilot study**

1. Does single stimulation or sustained stimulation for a minute alter the muscle tone in the tongue as measured by spontaneous firing rate of muscles?
2. Does single stimulation or sustained stimulation for a minute alter the synchrony of muscle tone in the tongue with respiratory cycle as measured by spontaneous firing rate of muscles?

Depending on the findings of this study we may propose other studies to optimize our device.

**Testing parameters**

Each guinea pig will serve as its own control and each sensory / stimulation combination will be tested in all guinea pigs. All testing will be performed under ketamine/xylazine (10:1) general anesthesia so the animal will not move and so that sleep and OSA is mimicked.

1. Baseline recording – no stimulation. Parameters of interest are the firing rate and modulation with the respiratory cycle for one minute.
2. Single, short, 2 ms, 20 mV stimulation from 0 to 1 mA stimulation of the tongue with the commercial stimulator, followed by recording for one minute to establish the threshold parameters for modulating the myogenic firing rate.

3. Single, short, 2 ms, 20 mV stimulation from 0 to 1 mA stimulation of the tongue with our WHGS device, followed by recording for one minute for comparison to the commercially available system.
4. Sustained 1 mA stimulation with pulses every 5 sec, 2 ms length, 20 mV of the tongue with the commercial stimulator for one minute, followed by recording for one minute
5. Sustained 1 mA stimulation with pulses every 5 sec, 2 ms length, 20 mV of the tongue with our WHGS device for one minute, followed by recording for one minute for comparison with the commercially available device.
6. Post-testing recording for one minute to assess the effects of stimulation on spontaneous firing rates.

Animal numbers. We propose to use three animals, repeating the sequence of recordings outline above in each 3 times so that we may learn if the responses are consistent and predictable across different times and individuals.

**References**

LEE W, NAGUBADI S, KRYGER, MH, MOKHLESI, B. Epidemiology of Obstructive Sleep Apnea: a Population-based Perspective. Expert Rev Respir Med. 2008 Jun 1; 2(3): 349–364.

YOUNG T, PALTA M, DEMPSEY J, SKATRUD J, WEBER S, BADR S. The occurrence of sleep-disordered breathing among middle-aged adults. N Engl J Med. 1993;328:1230–1235.

KOIZUMI, HIDEHIKO ET AL. Functional imaging, spatial reconstruction and biophysical analysis of a respiratory motor circuit isolated in vivo. The Journal of Neuroscience 28: 10 (2008) 2352-2365.